Filamentation of femtosecond laser pulses in nonlinear transparent media

Stelios Tzortzakis

ÉCOLE POLYTECHNIQUE

FILAMENTATION D'IMPULSIONS LASER FEMTOSECONDE DANS DES MILIEUX NONLINEAIRES TRANSPARENTS

par

Stelios Tzortzakis

Thèse présentée pour obtenir le grade de

Docteur de l'Ecole Polytechnique

Spécialité: Optique Nonlinéaire

2001

Soutenue le 12 juin 2001 devant le jury composé de:

Messieurs:	**Pierre Agostini**	**(Rapporteur)**
	See Leang Chin	**(Rapporteur)**
	Patrick Mora	**(Président du jury)**
	André Mysyrowicz	**(Directeur de Thèse)**
	Bernard Prade	
	Roland Sauerbrey	

Ecole Polytechnique

Ph.D. Thesis

FEMTOSECOND LASER PULSE FILAMENTATION IN NONLINEAR TRANSPARENT MEDIA

by Stelios Tzortzakis

Σε όσους αγαπώ και μ'αγαπούν…

ACKNOWLEDGMENTS

The author wishes to thank a certain number of people that have helped in one way or another during the last three years and contributed significantly to the realization of this thesis work.

André Mysyrowicz, my thesis supervisor and mentor showed me the way to progress. I deeply appreciate his support both scientific and human. Thanks André.

Bernard Prade, Brigitte Lamouroux, Michel Franco, Arnaud Chiron, Yves Bernard André and Lionel Sudrie, members of our research group have contributed in different ways and provided solutions to numerus problems, allowing to the good continuity of my work. I thank them all.

Many thanks to Arnaud Couairon and Luc Bergé, from the CEA, for a great collaboration realizing direct comparisons between experiments, numerical simulations and analytical predictions on the propagation of filaments.

Thanks to Stefan Hüller and Patrick Mora, from the center of theoretical physics at the Ecole Polytechnique, for our collaboration on the research of the guiding of electric discharges and the beautiful results produced.

I am grateful to Stavros Moustaizis for a pleasant collaboration and for initiating a series of experiments in Crete that gave many interesting results using ultraviolet femtosecond laser pulses.

I acknowledge the help of the people participating in the French-German project "Teramobile" and the four coordinators: R. Sauerbrey, A. Mysyrowicz, J.-P. Wolf, and L. Wöste.

I thank Pierre Breger and Pierre Agostini for the experiments we did together. Even if they did not work the first time they gave us important experience that can be used to achieve the final goal in the near future.

Special thanks to Pierre Agostini and See Leang Chin for making me the great honour to act as referees for my thesis. The same goes to Patrick Mora and Roland Sauerbrey for participating in my defence jury.

In the laboratory of applied optics of the Ecole Polytechnique where I spend the last three years many people have assisted me. I thank D. Hulin, director of the laboratory, for the hospitality and the secretaries for the great assistance with all the administration issues. Thanks to our laser technicians G. Hamoniaux and G. Mullot, our informatics technicians A. Paris and R. Gaudemer and our mechanic technicians J.-L. Charles and D. Milly.

Finally, all my love and gratitude goes to my family and friends for assuring an ideal equilibrium in my life.

TABLE OF CONTENTS

PREFACE **1**

1. FEMTOSECOND FILAMENTATION IN AIR – IONIZATION **5**

1.1. INTRODUCTION 5
1.2. IONIZATION 6
1.2.1 Electric conductivity technique *6*
1.2.2 Temporally Resolved Optical Diffractometry *6*
REFERENCES 15
APPENDIX 1.1 "FORMATION OF A CONDUCTING CHANNEL IN AIR BY SELF-GUIDED FEMTOSECOND LASER PULSES", PRE **60**, R3505 (1999) 17
APPENDIX 1.2 "TIME-EVOLUTION OF THE PLASMA CHANNEL AT THE TRAIL OF A SELF-GUIDED IR FEMTOSECOND LASER PULSE IN AIR", OPT. COMMUN. **181**, 123 (2000) 23

2. MULTI-FILAMENTATION: BREAK-UP AND COALESCENCE **31**

2.1. INTRODUCTION 31
APPENDIX 2.1 "BREAK-UP AND FUSION OF SELF-GUIDED FEMTOSECOND LIGHT PULSES IN AIR", PRL **86**, 5470 (2001) 33
APPENDIX 2.2 "INFRARED FEMTOSECOND LIGHT FILAMENTS IN AIR: SIMULATIONS AND EXPERIMENTS" 39

3. ULTRAVIOLET LASER PULSE FILAMENTATION IN AIR **81**

3.1. INTRODUCTION 81
APPENDIX 3.1 "NON-LINEAR PROPAGATION OF SUB-PICOSECOND UV LASER PULSES IN AIR", OPT. LETT. **25**, 1270 (2000) 83
APPENDIX 3.2 "FEMTOSECOND AND PICOSECOND ULTRAVIOLET LASER FILAMENTS IN AIR: EXPERIMENTS AND SIMULATIONS" 89

4. FEMTOSECOND FILAMENT-GUIDED ELECTRIC DISCHARGES **117**

4.1. INTRODUCTION 117
APPENDIX 4.1 "FEMTOSECOND LASER-GUIDED ELECTRIC DISCHARGE IN AIR" 119

5. FILAMENTATION IN TRANSPARENT SOLIDS **135**

5.1. INTRODUCTION 135
APPENDIX 5.1 "SELF-GUIDED PROPAGATION OF ULTRASHORT IR LASER PULSES IN FUSED SILICA" 137

6. CONTINUUM GENERATION: "TERAMOBILE" 155

6.1. INTRODUCTION 155
6.2. CONTINUUM GENERATION 155
APPENDIX 6.1 "INFRARED EXTENSION OF THE SUPERCONTINUUM GENERATED BY FEMTOSECOND TERAWATT LASER PULSES PROPAGATING IN THE ATMOSPHERE", OPT. LETT. **25**, 1397 (2000) 157

FINAL REMARKS 163

RESUME EN FRANÇAIS 165

INTRODUCTION 165
1. IONISATION 168
1.1 Technique de conductivité électrique 168
1.2 Diffractometrie Résolue dans le Temps 173
2. DIVISION ET COALESCENCE D'IMPULSIONS AUTO-GUIDEES 177
3. FILAMENTATION D'IMPULSIONS ULTRAVIOLETTES 180
4. DECHARGES INITIEES ET GUIDEES PAR DES FILAMENTS FEMTOSECONDE 187
5. FILAMENTATION FEMTOSECONDE DANS LES SOLIDES 194
6. GENERATION DE CONTINUUM – "TERAMOBILE" 200
CONCLUSION 204
REFERENCES 205

BIBLIOGRAPHY 207

PERSONAL REFERENCES 219

PUBLICATIONS 219
INTERNATIONAL CONFERENCES 220

Preface

Propagation of electromagnetic pulses is of fundamental importance in pure and applied science, and the recent development of sources of intense ultra-short laser pulses has added many interesting twists to this long standing problem. The broad spectral bandwidths, high peak powers, and (3+1)-dimensional nature of these fields give rise to complex linear and nonlinear effects that have posed significant challenges to researchers.

In the last years an important effort has been devoted to the study of the propagation of powerful laser beams in atmosphere as well as in other transparent media, i.e. glasses. A particular interest has focused on femtosecond laser systems, able to deliver very high peak powers with a modest energy output. Due to the high power the nonlinear response of the medium plays a key role in the propagation. A very unusual and spectacular propagation of light has been observed recently [1-3]. Intense ultrashort laser pulses launched in air self-organize into filaments, which persist over very long distances. Complementary to the experiments are many numerical simulations solving complex extended nonlinear Schrödinger equations (NLS) including: linear diffraction, the optical Kerr effect, plasma generation from multiphoton absorptions (MPI), normal group velocity dispersion (GVD) or even other higher order terms of temporal dispersion.

This thesis reports on femtosecond self-guiding (also called hereafter filamentation) studies I have performed during the last three years. Even from the early work on beam filamentation, using IR femtosecond powerful laser pulses, it was generally accepted that ionization played the next most important role after self-focusing for the fs filamentation in air. However no experimental evidence of ionization was available at the early beginning of my dissertation work. We have developed and applied two original experimental techniques, that allowed as to give precise estimations of the electron density in the filaments. The results of those experiments with a complete analysis is presented in *Chapter 1*. Together with the work from Schillinger and Sauerbrey [4] these studies were the first to provide direct evidence for ionization of air by filaments.

Spatiotemporal propagation dynamics of ultra-short pulses at high powers require a sophisticated and multi-parameter approach. Sharp temporal features, small beam diameters, and broad bandwidths require that space-time coupling, group velocity dispersion, ionization effects,

and absorption losses be included in the theoretical analysis aimed at quantitative comparison with experiments. However, such complex effects lead to nonintegrable equations, making analytical predictions impossible. For this reason only numerical approaches are possible. Mlejnek *et al.* reported recently [5] a real 3-dimension (3D) numerical simulation where introducing a large laser beam (7 mm diameter) with power more than $35P_{cr}$ they observed multi-break-up and multi-filamentation. In *Chapter 2* we present the different stages leading to fs filamentation. We show for the first time clearly, the initial break-up of a fs pulse into two light channels in the Kerr regime. Those two channels further on coalesce to a single self-guided beam that propagates in the form of a robust filament over many Rayleigh distances. An analytic description of our numerical code used to simulate the self-guiding of ultrashort intense laser pulses in air is given in appendix 2.2.

Commonly most research on fs filaments is done with infrared laser pulses and very little information was available, at the beginning of my thesis, on the fs ultraviolet nonlinear propagation. In *Chapter 3* we present the first detailed experimental study on the nonlinear propagation of short ultraviolet pulses in air. Self-guiding of UV pulses is demonstrated with robust filaments propagating over several meters.

Laser-triggered discharges using powerful femtosecond IR lasers is an active domain of research. In *Chapter 4* we report the first experimental demonstration of a (short-scale) guided electric discharge triggered by a femtosecond laser filament. We analyze and give a concrete physical explanation of the mechanisms involved in this special kind of electric discharge.

Ranka *et al.* [6] Zozulya *et al.* [7] and Diddams *et al.* [8] have reported on pulse break-up when intense femtosecond pulses propagate in transparent glasses (BK7). Henz and Herrmann [9] have presented a numerical simulation that shows the existence of a soliton-like filament propagating in fused silica. This filament is the result of the equilibrium between self-focusing and multiphoton ionization with the group velocity dispersion playing a negligible minor role. In *Chapter 5* we present the first experimental evidence of a self-guided ultrashort filament propagating over many Rayleigh distances in fused silica. We show that there is pulse breakup and temporal compression in the nonlinear propagation.

Brodeur and Chin [10] have reported on the mechanisms of white light continuum generation when intense ultrashort pulses pass through transparent solids. Latter they demonstrated that the white light is coherent radiation (white-light laser) [11,12]. Nishioka *et al.* [13] have measured the

spectral content of fs filaments in the UV and visible ranges from 150 nm to 900 nm. In *Chapter 6* we present the first measurement on the infrared extension in the spectrum of fs filaments, from the visible up to 4.5 μm, and we discuss on applications to LIDAR.

Finally a summary in French of the most important results described in the previous chapters is given at the end of this thesis followed by an analytic bibliography and a complete list of personal references relative to this work.

References

[1] A. Braun, G. Korn, X. Liu, D. Du, J. Squier, and G. Mourou, Opt. Lett. **20**, 73 (1995).

[2] E. T. J. Nibbering, P. F. Curley, G. Grillon, B. Prade, M. Franco, F. Salin, and A. Mysyrowicz, Opt. Lett. **21**, 62 (1996).

[3] A. Brodeur, C. Y. Chien, F. A. Ilkov, S. L. Chin, O. G. Kosareva, and V. P. Kandidov, Opt. Lett. **22**, 304 (1997).

[4] H. Schillinger and R. Sauerbrey, Appl. Phys. B **68**, 753 (1999).

[5] M. Mlejnek, M. Kolesik, J. V. Moloney, and E. M. Wright, Phys. Rev. Lett. **83**, 2938 (1999).

[6] J. K. Ranka, R. W. Schirmer, and A. L. Gaeta, Phys. Rev. Lett. **77**, 3783 (1996).

[7] A. Zozulya, S. A. Diddams, A. G. Van Engen, and T. S. Clement, Phys. Rev. Lett. **82**, 1430 (1999).

[8] S. A. Diddams, H. K. Eaton, A. A. Zozulya, and T. S. Clement, Opt. Lett. **23**, 379 (1998).

[9] S. Henz and J. Herrmann, Phys. Rev. A **59**, 2528 (1999).

[10] A. Brodeur and S. L. Chin, J. Opt. Soc. Am. B **16**, 637 (1999).

[11] S. L. Chin, A. Brodeur, S. Petit, O. G. Kosareva, and V. P. Kandidov, J. Nonlinear Opt. Phys. & Materials **8**, 121 (1999).

[12] S. L. Chin, S. Petit, F. Borne, and K. Miyazaki, Jpn. J. Appl. Phys. **38**, L126-L128 (1999).

[13] H. Nishioka , W. Odajima, K.-I. Ueda, and H. Takuma, Opt. Lett. **20**, 2503 (1995).

Chapter 1

1. Femtosecond filamentation in air – ionization

1.1. Introduction

Interesting effects recently seen with high power femtosecond laser pulses propagating in solids, gases, and liquids include temporal breakup of the pulse [1,2], extreme spectral-broadening (commonly called continuum generation) [3,4], and self-guiding of the pulse in long distances [5-7]. To a large extent, these phenomena rely on the basic process of self-focusing, which is due to an intensity-dependent index of refraction in the propagation medium and appears when the input laser power is higher than a critical value. The critical power can be expressed as $P_{cr} = \lambda_0^2 / 2\pi n_0 n_2$ where λ_0 is the laser wavelength while n_0 and n_2 is the linear and the nonlinear index of refraction respectively. If the input power is lower than the critical value then the beam cannot overcome the normal tendency of the beam to spread due to diffraction. It is equally true, however, that these phenomena exist solely because physical mechanisms other than self-focusing are also involved. Were this not the case, one would predict the field to collapse to a spatial singularity after a finite propagation distance in the medium. Because of the associated broad spectral bandwidth, material dispersion typically plays an important role in the propagation of ultra-short pulses. Material dispersion is the frequency dependence of the refractive index, which in turn leads to different propagation speeds of the different frequency components (group velocity dispersion) and thus to a broadening of the pulse duration and diminution of the pulse peak intensity. Both self-focusing and material dispersion are accounted for in the formalism of the (3+1)-dimensional nonlinear Schrödinger equation (NLS), where it has been shown that for moderate powers normal group velocity dispersion may act to arrest catastrophic spatial collapse with the result of temporal splitting of the input pulse into two. Another potential mechanism to prevent collapse is ionization. The generation of free carriers (electrons) resulting from ionization processes lead to a diminution of the refractive index that can spread the laser beam. It is generally agreed that this is the most important effect for the fs filamentation in air. However no experimental evidence of ionization was available at the early beginning of my dissertation work. In the framework of my thesis I have applied two original experimental techniques, that allowed as to give precise estimations of the electron density in the

filaments. In the present chapter we will present those two experimental techniques together with their complementary numerical approach.

1.2. Ionization

The importance of ionization as an intensity limiter and stabilizer to the self-guiding of ultrashort pulses is commonly recognized. The numerical simulations predict a mean electron density in the filament about 10^{16} cm^{-3}. These density levels are quite low and make experimental observations very difficult, especially at atmospheric pressure air. As a result at the beginning of my thesis work no experimental results were reported in literature. In what follows we describe two experimental techniques used to detect such low level electron densities. The first one is a pure electric one and the second an all-optical one. A combination of the two is able to provide us with sensitive and precise measurements.

1.2.1 Electric conductivity technique

A detailed presentation of this technique can be found in appendix 1.1. This is a simple and sensitive technique to measure electron densities with a lower density threshold around 10^{14} to 10^{15} cm^{-3}. Schillinger and Sauerbrey [8] have performed an experiment that determines the existence of free charges by a capacitive coupling to a pick-up capacitor. They have demonstrated the existence of free charges in the channel and have given a lower limit value for the free electron density of $n_e \geq 6\times10^{11}\,\mathrm{cm}^{-3}$. That value is many orders of magnitude lower than the one we have reported [9,10] as well as the one of other groups [11,12], which is in the range of $n_e \sim 10^{16}\,\mathrm{cm}^{-3}$. A plausible explanation for this difference can be the estimation of the channel diameter. In our case as well as this of La Fontaine [11] and Ladouceur [12] a single filament with a diameter of ~100 μm is used while in the experiments of Schillinger the results are integrated over 10 – 20 channels of ~100 μm spread over a total surface of ~1 cm^2.

1.2.2 Temporally Resolved Optical Diffractometry

We want to determine the electron density of the plasma generated at the trail of a self-guided filament as well as to follow its temporal evolution. The pump-probe configuration used in our experiments is shown in Fig. 1. The pump beam produces the self-guided filament while the, less intense, probe beam visualizes the plasma created at the trail of the filament. The probe beam is focused near the plasma channel but not on it. We record the far field diffraction image of the probe beam, using a linear CCD camera. The presence of a plasma on the path of the beam

induces changes on the index of refraction and thus on the diffraction images as well. By changing the delay between the pump and probe beam one is able to follow the temporal evolution of the plasma and thus estimate its lifetime. With this technique one can also measure the diameter of the filament.

Numerical modelization

A numerical modelization of the experiment allows the reproduction of the results and the extraction of the plasma electron density. There are three stages in the modelization, namely the propagation of the Gaussian laser beam, the plasma evolution, and the reproduction of the diffraction images.

Fig. 1 shows the two coordinate systems that are used here. The plasma is defined on the axis system xyz. We make the assumption that the plasma is of cylindrical revolution and its density is constant along the z-axis. The pump beam induces an index of refraction $n\left(x^2+y^2\right)$ via plasma generation.

The probe beam is defined on the XYZ coordinates and propagates towards positive values of Z. From the two coordinate systems one has:

$$\begin{aligned} X &= x\cos\theta - z\sin\theta \\ Y &= y - y_0 \\ Z &= x\sin\theta + z\cos\theta \end{aligned}$$

or

$$\begin{aligned} x &= X\cos\theta + Z\sin\theta \\ y &= Y + Y_0 \\ z &= -X\sin\theta + Z\cos\theta \end{aligned}$$

the quantity $y_0 = Y_0$ represents the off-center distance as will be discussed below.

In the following we are interested on underdense plasmas (electron densities well below the critical density) that don't absorb nor reflect the laser beam. Thus one can simulate the effect of the plasma by a dephasing $\phi\left(X,Y\right)$:

$$\phi(X,Y)=\frac{2\pi}{\lambda}\int\left[n(X,Y,Z)-n_{\infty}\right]dZ,$$

where n_{∞} is the index of refraction of the medium.

If we call $g(X,Y,Z)$ the function describing the amplitude of the probe beam, then the amplitude of the field at a point Z_0 of crossing between the probe and the plasma can be expressed as:

$$E(X,Y)=g(X,Y,Z_0)e^{i\phi(X,Y)}.$$

The far-field intensity image recorded on the CCD camera of the experiment can be obtained calculating the Fourier transform of the following expression

$$I(p,q)=\left|\iint_{R^2} g(X,Y,Z_0)e^{i\phi(X,Y-Y_0)}e^{i(pX+qY)}dXdY\right|^2.$$

We calculate the above expression accepting the following

- The probe beam amplitude $g(X,Y,Z)$ has a Gaussian distribution.
- The refraction index of the plasma is axial symmetric, it does not depend on z and can be expressed in the form: $n(x,y)=1-n_0e^{-\left(x^2+y^2\right)/w^2}$, where n_0 is the plasma density magnitude and w is its characteristic radius.

The analytic expression of the probe beam can be written as:

$$g(X,Y)=\frac{1}{1+i(Z_0/Z_R)}\exp\left[i\frac{X^2+Y^2}{W_0^2}\frac{Z_0}{Z_R}\frac{1}{1+(Z_0/Z_R)^2}\right]\exp\left[-\frac{X^2+Y^2}{W_0^2}\frac{1}{1+(Z_0/Z_R)^2}\right]$$

where Z_R defines the Rayleigh distance $Z_R=kW_0^2/2$, and W_0 is the probe waist.

Now, we calculate the variation of the phase integral along the Z-axis

$$\phi(X,Y)=\frac{2\pi n_0}{\lambda}\int_R \exp\left[-\left(x^2+y^2\right)/w^2\right]dZ$$

or in the XYZ-coordinates system

$$\phi(X,Y)=\frac{2\pi n_0}{\lambda}\exp\left[-Y^2/w^2\right]\int_R \exp\left[-\left(X\cos\theta+Z\sin\theta\right)^2/w^2\right]dZ\,.$$

The observed images can be expressed in the form

$$I(p,q)=\left|F(p)\right|^2\left|G(q)\right|^2$$

with

$$F(p)=1/\left[1+i\left(Z_0/Z_R\right)\right]\exp\left[-X^2/W_t^2\right]\exp\left[iX^2Z_0/W_t^2Z_R\right]\exp\left[ipx\right]$$

and

$$G(Y_0,q)=\int_R \exp\left[-Y^2/W_t^2\right]\exp\left[iY^2Z_0/W_t^2Z_R\right]\exp\left[i\phi\left(Y-Y_0\right)\right]\exp\left[iqY\right]dY$$

where W_t defines the waist of the probe beam at the point Z_0 where it crosses the plasma channel.

What we measure in the experiments are the values of $I(q)$ at $p = 0$ for different delays or/and different Y_0, W_t is also measured. The only adjustable parameters in the numerical analysis are the value n_0 of the electron density and the radius of the plasma channel w. We adjust those two parameters to the best fit of the experimental results.

Results and discussion

Characteristic diffraction images in the presence of a plasma channel are shown in Fig. 1. On the left side is shown the case when the probe beam is focused 3 cm in front of the plasma channel (L = -3 cm, the sign is a convention with minus for in front and plus for ahead) and is characterized by a dark fringe at the center surrounded by two bright ones. On the right side is shown the case where the focus is placed 3 cm ahead the plasma channel (L = +3 cm). In this case the image is inversed and there is one bright fringe at the center surrounded by two dark. On both cases, depending on the electron density of the plasma, more secondary dark and bright fringes can appear. Fig. 2 shows the results of the fringe contrast at two time delays, just after the passage of the fs laser pulse and 69 ps latter. The diminution of the contrast with time reflects the electron recombination and thus the electrons lifetime can be estimated. An application of

this technique to measure the plasma density and lifetime in a fs laser filament is discussed in appendix 1.2.

In Fig. 3 is shown a case where the focus of the probe is in front of the plasma channel but this time it in not centered precisely on the channel. In this case the diffraction image is also decentralized. In Fig. 4 several diffraction images for different decentralization distances are shown. Such measurements provide more information on the plasma channel, such as its diameter. Another possibility using those images is to invert the solution. If one knows for different Y_0 the values of $I_{Y_0}(q)$ can probably retrieve the $\phi(Y)$ and from that the $n(r)$. This is a problem still open.

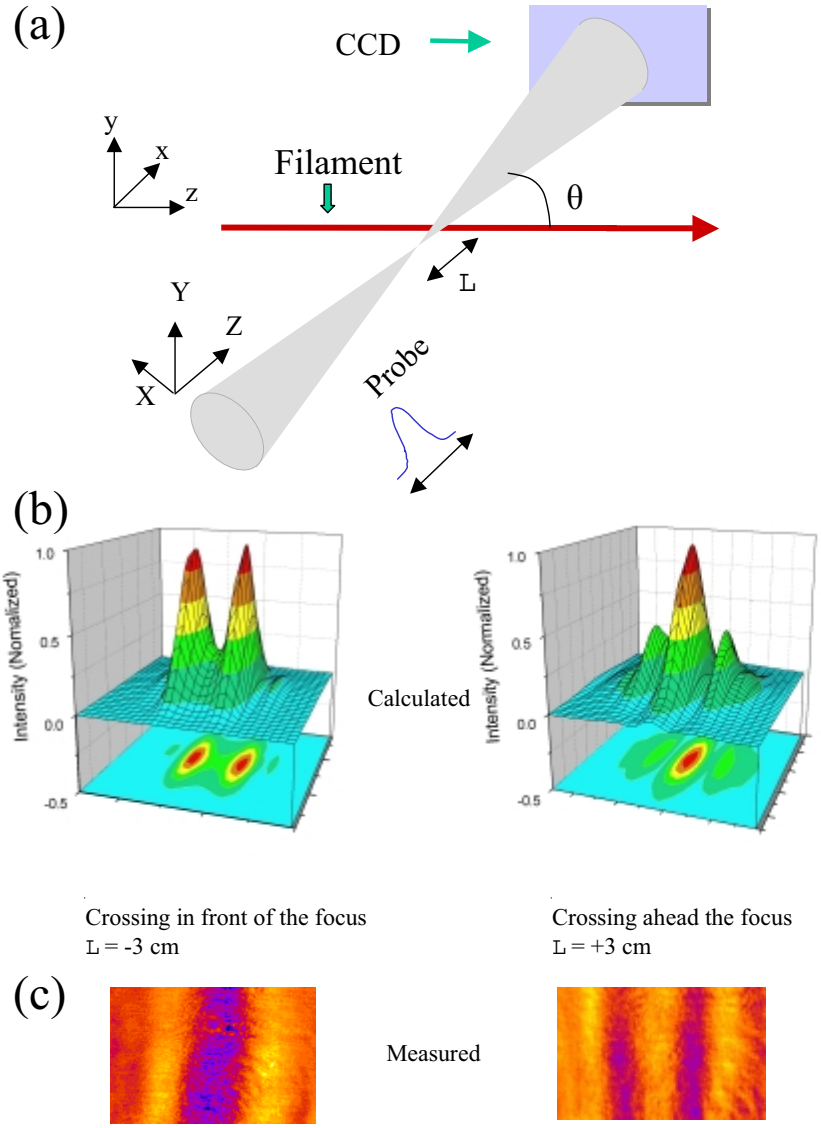

Fig. 1. (a) Schema of the experimental setup, the probe beam crosses the filament plasma and the modified diffraction images are recorded with a linear CCD camera. (b) Calculated diffraction patterns for L = -3 cm and L = +3 cm. (c) Measured diffraction patters for the same distances as (b).

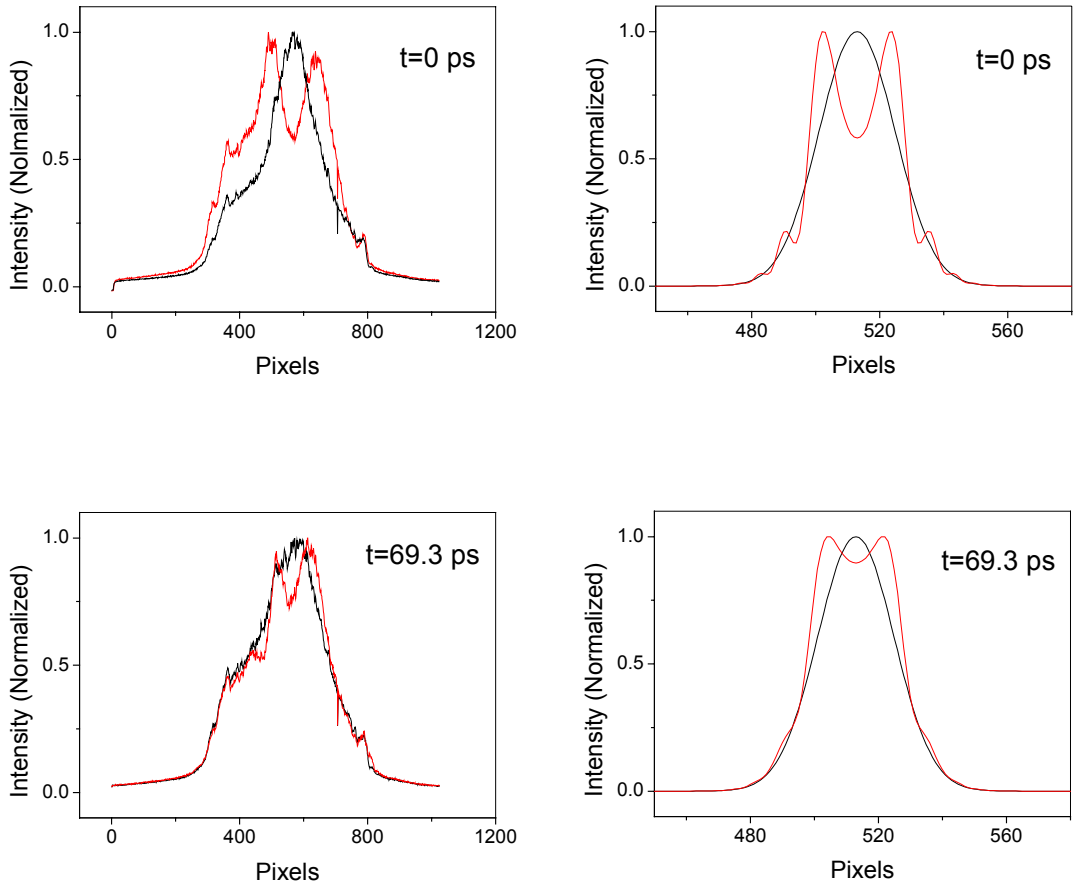

Fig. 2. In black is the probe profile without the pump and in red is with the pump for different probe delays. On the left are the experimental results and on the right the simulations.

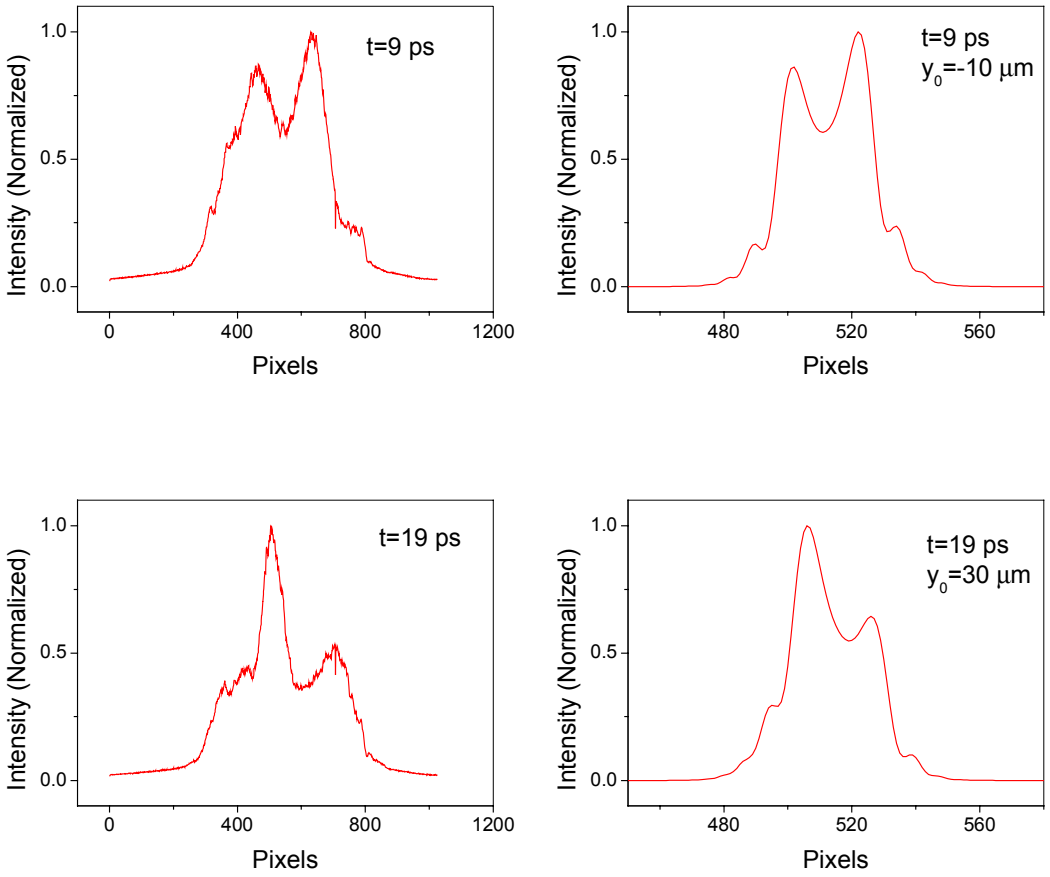

Fig. 3. Asymmetric profile revealing the off-axis crossing of the pump and probe beams. On the left are the experimental results and on the right the simulations.

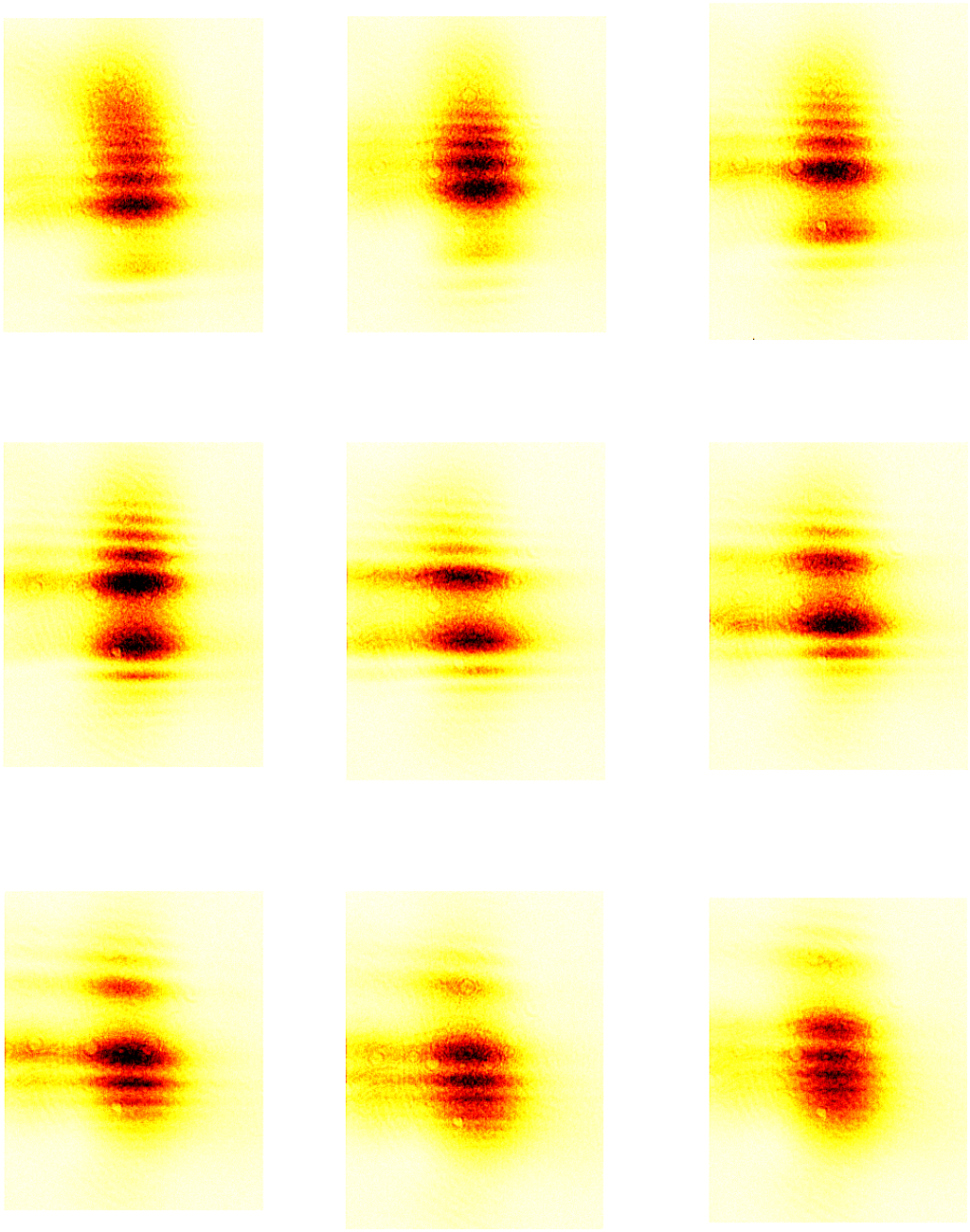

Fig 4. Probe beam intensity images after crossing the filament plasma channel with L = -4.5 cm for different Y_0, from –400 μm to +400 μm with a step of 100 μm. The central image is for $Y_0 = 0$.

References

[1] J. K. Ranka, R. W. Schirmer, and A. L. Gaeta, Phys. Rev. Lett. **77**, 3783 (1996).

[2] S. A. Diddams, H. K. Eaton, A. A. Zozulya, and T. S. Clement, Opt. Lett. **23**, 379 (1998).

[3] H. Nishioka, W. Odajima, K.-I. Ueda, and H. Takuma, Opt. Lett. **20**, 2503 (1995).

[4] J. Kasparian , R. Sauerbrey, D. Mondelain, S. Niedermeier, J. Yu, J.-P. Wolf, Y.-B. André, M. Franco, B. Prade, S. Tzortzakis, A. Mysyrowicz, M. Rodriguez, H. Wille, and L. Wöste, Opt. Lett. **25**, 1397 (2000).

[5] A. Braun, G. Korn, X. Liu, D. Du, J. Squier, and G. Mourou, Opt. Lett. **20**, 73 (1995).

[6] E. T. J. Nibbering, P. F. Curley, G. Grillon, B. Prade, M. Franco, F. Salin, and A. Mysyrowicz, Opt. Lett. **21**, 62 (1996).

[7] A. Brodeur, C. Y. Chien, F. A. Ilkov, S. L. Chin, O. G. Kosareva, and V. P. Kandidov, Opt. Lett. **22**, 304 (1997).

[8] H. Schillinger and R. Sauerbrey, Appl. Phys. B **68**, 753 (1999).

[9] S. Tzortzakis, M. Franco, Y.-B. André, A. Chiron, B. Lamouroux, B. Prade, and A. Mysyrowicz, Phys. Rev. E **60**, R3505-R3507 (1999).

[10] S. Tzortzakis, B. Prade, M. Franco, and A. Mysyrowicz, Opt. Commun. **181**, 123 (2000).

[11] B. La Fontaine, F. Vidal, Z. Jiang, C. Y. Chien, D. Comtois, A. Desparois, T. W. Johnston, J. C. Kieffer, H. Pépin, and H. P. Mercure, Phys. Plasmas **6**, 1615 (1999).

[12] H. D. Ladouceur, A. P. Baronavski, D. Lohrmann, P. W. Grounds, and P. G. Girardi, Opt. Commun. **189**, 107 (2001).

Appendix 1.1

"Formation of a conducting channel in air by self-guided femtosecond laser pulses"

PHYSICAL REVIEW E RAPID COMMUNICATIONS **60**, R3505 (1999)

PHYSICAL REVIEW E VOLUME 60, NUMBER 4 OCTOBER 1999

Formation of a conducting channel in air by self-guided femtosecond laser pulses

S. Tzortzakis, M. A. Franco, Y.-B. André, A. Chiron, B. Lamouroux, B. S. Prade, and A. Mysyrowicz
Laboratoire d'Optique Appliquée, CNRS UMR No. 7639, ENSTA–Ecole Polytechnique, Chemin de la Hunière, F-91761 Palaiseau Cedex, France

(Received 16 February 1999; revised manuscript received 13 July 1999)

We report a drastic reduction of air resistivity following the passage of a self-guided femtosecond pulse from a Ti:sapphire laser system at 800 nm with energies per pulse between 1 and 14 mJ and a pulse duration of 120 fs. Connected plasma filaments with a length that can exceed 150 cm are created by these pulses. The presence of a conducting plasma channel results from multiphoton ionization of air molecules in the filament core. [S1063-651X(99)51210-5]

PACS number(s): 52.40.Nk

A very unusual propagation of light has been observed recently [1–4]. Intense ultrashort laser pulses launched in air self-organize into filaments, which persist over very long distances. This self-guiding effect is interesting in several ways. From a fundamental point of view, long-range self-guided propagation is a beautiful example of strong nonlinear responses conspiring to establish a quasistable dynamic regime. It also suggests interesting applications. For instance, one might use these filaments to trigger and guide an electric discharge. The peak intensity of the pulse inside the filament can reach $10^{14}\,\mathrm{W/cm^2}$ [5], a value sufficient to ionize air molecules by multiphoton transitions. Hence, a channel of weakly ionized plasma should be formed after passage of the pulse that could perhaps act as a precursor for lightning [6]. However, evidence for the existence of such a plasma filament has so far been indirect [1–3,7,8]. In this paper, we present direct evidence that a conducting channel is indeed created by self-guided pulses. Using as little as 14 mJ of laser energy, a plasma column extending over a distance of more than 100 cm is observed. Similar electric conductivity experiments performed in Jena have been published recently [9].

The experiment setup, shown in Fig. 1, is simple in principle. To detect the presence of a conducting column, we measure the change of resistivity of air between two electrodes after passage of a filament. The initial laser pulse is delivered by a Ti:S oscillator followed by a CPA amplifier system. The pulse wavelength is 800 nm, its duration is 120 fs, and its energy can reach 50 mJ. At the output of the compressor stage, the beam profile is nearly Gaussian, with a Gaussian parameter of $w_0 = 12\,\mathrm{mm}$. The beam goes through a diaphragm of variable diameter D and is focused in air with a thin lens of focal distance $F = 1$ or 2 m. This converging beam geometry reduces the distance necessary for the formation of a self-guided pulse, allowing one to perform experiments in a laboratory of restricted dimensions [10].

The filament traverses a first copper electrode through a pinhole drilled in its center. The diameter of the pinhole (1 mm) is a compromise. A smaller diaphragm would destroy most filaments before they reach the second electrode, because of fluctuations in their position from shot to shot. On the other hand, with a larger diaphragm the electric signal diminishes rapidly, due to the high resistivity between the ionized core of the filament and the edge of the electrode. As a first electrode, we have also used a polished stainless steel mirror set at grazing incidence in the vicinity of the filament. The beam then impinges on the second electrode, consisting of a plain copper block or, for short electrode separation $d < 2$ cm, a replica of the first electrode with its pinhole on the axis. A dc voltage of typically 1000 V is applied between both electrodes. One measures the current circulating through the plasma column by recording the voltage induced across a resistance. The electric discharge is non-self-sustained, giving a pulse with a rise time and decay time less than 3 ns across a 100-Ω resistance, limited by the response time of the detection system (see inset of Fig. 3). A more sensitive detection of the presence of free carriers is obtained with an electrometer, which integrates over many laser shots the charges flowing to one electrode.

In Fig. 2, the average charge per laser shot collected by the electrometer is shown as a function of distance L between the geometric focus and the first electrode, keeping the separation between the two electrodes constant at $d = 1.5\,\mathrm{cm}$. Curve (*a*) is for a filament produced by a beam with a diameter limited by the diaphragm to 8 mm. The initial energy of the pulse (before the lens) is about 3 mJ. The lens has a focal distance F of 1 m. Curve (*b*) refers to a diaphragm of 18 mm. The pulse energy is 14 mJ and the lens has a focal distance of 2.24 m. Under these last conditions, shot-to-shot fluctuations were more important, with the filament breaking sometimes in a multifilamentary structure. Careful alignment of the laser reduced the tendency to multifilamentation by improving the transverse mode structure of the laser beam. Nevertheless, fluctuations in position of the filament by a few mrad were still present.

As can be seen in Fig. 2, the self-guided pulse forms an ionized track over a distance of at least 150 cm. In Fig. 3, the peak of the voltage signal, detected across an 8.2-kΩ resis-

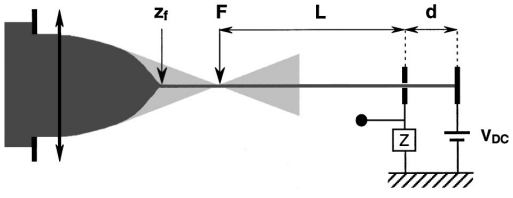

FIG. 1. Experiment setup (see text).

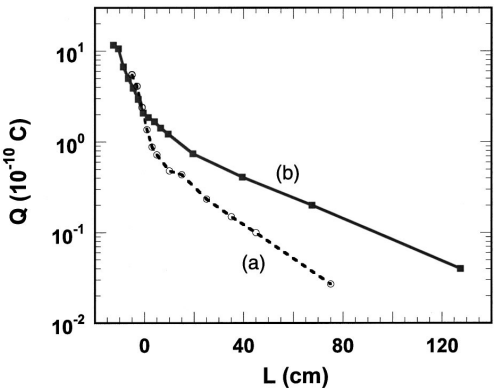

FIG. 2. Integrated electric charge measurements over 100 laser shots, normalized to a single laser shot, made by use of an electrometer connected to the rear electrode. The electrode spacing is 1.5 cm. Curve (*a*) is obtained with 3 mJ energy per pulse and a duration of 120 fs. Curve (*b*) is for 14 mJ energy per pulse. The applied voltage is 1000 V dc.

tance, is plotted as a function of L for the case of a 14-mJ pulse. Single shot detection now allows one to discriminate amplitudes of signals. In the plot of Fig. 3, only those signals of large amplitude corresponding to well connected single filaments are registered. The presence of a plateau of constant conductivity extending beyond the geometric focus to a distance of about 40 cm, which was buried in the averaging procedure of Fig. 2, is now revealed.

The current has also been measured as a function of electrode separation in the plateau region, up to a distance $d = 50$ cm. It reveals a linear dependence of the current with $1/d$, for a fixed applied dc voltage (see Fig. 4), or with ap-

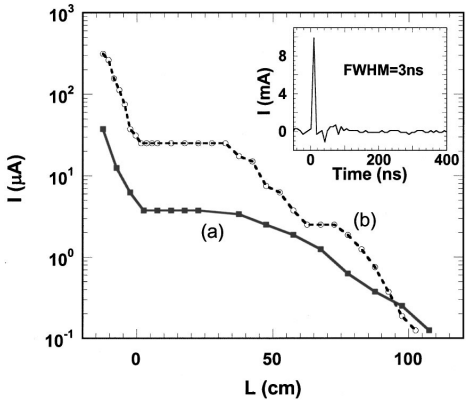

FIG. 3. Single shot electric current measurements as a function of the distance L. The applied voltage is 1000 V dc across the electrodes with spacing (a) $d = 11.5$ cm and (b) $d = 3$ cm. The energy per pulse is 14 mJ and the external resistance is 8.2 kΩ. The origin of L corresponds to the geometric focus of the lens. The inset shows the shape of the transient voltage, measured across a 100-Ω resistance, with an applied voltage of 1500 V. The signal is recorded in a single shot with a numerical oscilloscope (Tektronix TDS 544A) of 500 MHz bandwidth.

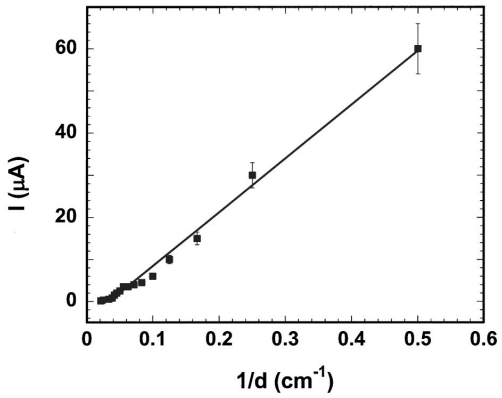

FIG. 4. Electric current measurements as a function of $1/d$, in the plateau region. The first electrode is at $L = 0$. The incident energy per laser pulse is 14 mJ. The applied field is 1000 V. The external resistance is 8.2 kΩ.

plied voltage between 500 and 2500 V for a fixed separation d. This in turn indicates that we are in an Ohmic regime, with the current directly proportional to the applied field. The peak current in the plateau, measured with a 100-Ω resistance, is at least 10 mA.

We now address the question of the origin of the conducting structure. One can reject an interpretation based on the presence of a stream of fast electrons ejected from one electrode and collected by the other from the fact that a second electrode with a pinhole gives essentially the same results as a plain electrode. We have also compared signals obtained by inverting the polarity between the two electrodes. Results are shown in Fig. 5. No significant change of the magnitude of the signal is detected with polarity, except in a small region before the geometric focus of the beam, and for small interelectrode spacing only ($d < 5$ cm).

A more plausible physical origin for the presence of con-

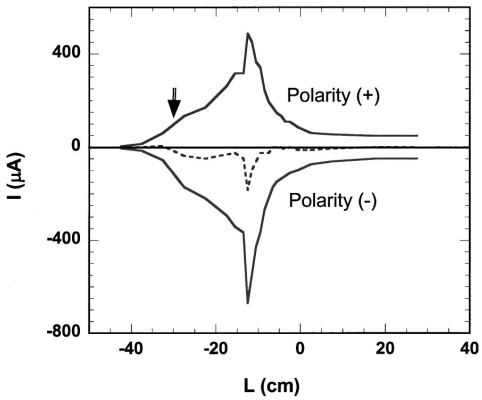

FIG. 5. Electric current measurements as a function of the distance L. The applied voltage is 1000 V for the polarity (+) and −1000 V for the polarity (−). Electrode spacing is $d = 1.5$ cm. The dotted curve is the difference between the signals for each polarity. The pulse energy is 14 mJ. The arrow indicates the calculated position of the beginning of the filament.

ducting charges is multiphoton ionization, a process playing a crucial role in pulse self-guiding [1–3,10]. We have confronted our measurements with the numerical results of a three-dimensional (3D) propagation code with initial conditions close to those of the experiment. According to the simulation, the birth of the filament should occur 30 cm before the geometric focus. This displacement of the onset of filamentation from the geometric focus is understood simply [11]: the focal point of the beam sweeps back from the geometric focus along the propagation axis z during the ascending part of the laser pulse. This sweep forms an ionized track as well, extending from the geometric focus inward up to a distance shown as an arrow in Fig. 5. This position is close to the measured onset of conduction in Fig. 5.

One can also compare the calculated electron density in the conducting core of the filament with values extracted from the measurements. The simulation yields a laser field clamped to a maximum on the order of $10^{14}\,\mathrm{W/cm^2}$ by the rapid surge of ionization [12]. At this field value, the ionization rate is of the order of 10^{-3} and only singly ionized atoms are formed. In the corresponding conducting core with a diameter estimated by the numerical code to lie between 40 and 100 μm (full width at half maximum), an average free-electron density ranging between 3×10^{16} and $2\times10^{17}\,\mathrm{cm^{-3}}$ is expected.

To evaluate the free-electron density from the measurements, we rely on the reported current density per ion, $i=3\times10^{-14}\,\mathrm{A/cm^2}$, quoted in Ref. [13], for air at atmospheric pressure with an applied field of similar magnitude. Taking a filament size of 40 μm diam, we obtain in the plateau region a minimum average peak current flux of 800 $\mathrm{A/cm^2}$ and a plasma resistivity less than 1.2Ω cm. From this, we estimate a free-electron density of $3\times10^{16}\,\mathrm{cm^{-3}}$ [14]. At such densities, the decay of the plasma is expected to be predominantly due to recombination of electrons at the parent ions, following a law $dn/dt=-bn^2$. Assuming a value $b=2.2\times10^{-7}\,\mathrm{cm^3/s}$ from the literature [6], one finds that the majority of carriers disappear within 5 ns, in agreement with the duration of the electric signal $t<3$ ns. More accurate measurements of the decay are now in progress.

In conclusion, using laser pulses of modest energy, we observe the presence of a conducting plasma column over distances exceeding one meter along the track of self-guided filaments. Such a plasma column could be useful for the study of electric lightning, since it may provide an artificial precursor of uniform carrier density, circumventing the complex initial stage of streamer formation preceding electric breakdown of air.

We are thankful to Professor R. Sauerbrey for a private communication of his results on similar measurements before publication.

[1] A. Braun, G. Korn, X. Liu, D. Du, J. Squier, and G. Mourou, Opt. Lett. **20**, 73 (1995).
[2] E. T. J. Nibbering, P. F. Curley, G. Grillon, B. S. Prade, M. A. Franco, F. Salin, and A. Mysyrowicz, Opt. Lett. **21**, 62 (1996).
[3] A. Brodeur, C. Y. Chien, F. A. Ilkov, S. L. Chin, O. G. Kosareva, and V. P. Kandidov, Opt. Lett. **22**, 304 (1997).
[4] L. Wöste *et al.*, Laser Optoelektron. **5**, 29 (1997).
[5] H. R. Lange, A. Chiron, J.-F. Ripoche, A. Mysyrowicz, P. Breger, and P. Agostini, Phys. Rev. Lett. **81**, 1611 (1998).
[6] X. M. Zhao, J.-C. Diels, C. Y. Wang, and J. M. Elizondo, IEEE J. Quantum Electron. **31**, 599 (1995).
[7] M. Mlejnek, E. M. Wright, and J. V. Moloney, Phys. Rev. E **58**, 4903 (1998).
[8] H. Nishioka, W. Odajima, K. Ueda, and H. Takuma, Opt. Lett. **20**, 2505 (1995).
[9] H. Schillinger and R. Sauerbrey, Appl. Phys. B Lasers Opt. **68**, 753 (1999).
[10] H. R. Lange, G. Grillon, J.-F. Ripoche, M. A. Franco, B. Lamouroux, B. S. Prade, and A. Mysyrowicz, E. T. J. Nibbering, and A. A. Chiron, Opt. Lett. **23**, 120 (1998).
[11] J. H. Marburger, Prog. Quantum Electron. **4**, 35 (1975).
[12] This laser field value is in agreement with that extracted from high-order harmonics generated in noble gases by a self-guided pulse; see Ref. [5] above.
[13] L. B. Loeb, *Basic Processes of Gaseous Electronics* (University of California Press, Berkeley, 1960), p. 618.
[14] After submission of this manuscript, a paper was published where initial free-carrier densities exceeding $n=10^{15}\,\mathrm{cm^{-3}}$ have been estimated in a laser-induced filament by interferometry [B. La Fontaine *et al.*, Phys. Plasmas **6**, 1615 (1999)].

Appendix 1.2

"Time-evolution of the plasma channel at the trail of a self-guided IR femtosecond laser pulse in air"

OPTICS COMMUNICATIONS **181**, 123 (2000)

ELSEVIER

1 July 2000

Optics Communications 181 (2000) 123–127

OPTICS COMMUNICATIONS

www.elsevier.com/locate/optcom

Time-evolution of the plasma channel at the trail of a self-guided IR femtosecond laser pulse in air

S. Tzortzakis, B. Prade, M. Franco, A. Mysyrowicz *

Laboratoire d'Optique Appliquée, CNRS UMR 7639, Ecole Nationale Supérieure des Techniques Avancées - Ecole Polytechnique, Chemin de la Hunière, F-91761 Palaiseau Cedex, France

Received 13 March 2000; accepted 3 May 2000

Abstract

The density and decay kinetics of a plasma channel created in air by a self-guided intense ultra-short laser pulse is determined by a new electric cross-conductivity method and by diffraction interferometry. A fast decay is measured, due to the dominant intrinsic recombination process at high plasma density. © 2000 Elsevier Science B.V. All rights reserved.

PACS: 42.65.Jx; 52.40.Nk; 52.25.−b
Keywords: Beam trapping; Laser-plasma interactions; Plasma properties

1. Introduction

In 1996 Braun et al. [1] observed an interesting phenomenon: intense IR femtosecond laser pulses propagating in air self-organize into filaments, which persist over several tens of meters. This effect was confirmed soon after by Nibbering et al. [2] and Brodeur et al. [3]. Wöste et al. [4] reported broad continuum generation by filaments over propagation distances reaching several km. Recently three groups [5–7] demonstrated the existence of a connected plasma channel in the trail of the filaments by measuring an important transient increase of the electric conductivity of air. The average initial electron density for a multifilamentary structure was estimated by Schillinger et al. to be $n > 10^{11}$ cm^{-3}, whereas La Fontaine et al. [6] and Tzortzakis et al. [7] estimated a value $n > 10^{16}$ cm^{-3} for a single filament. The length of a single plasma channel was about 150 cm under the conditions of Ref. [7], where the input pulse energy was 14 mJ. Connected plasma channels with uniform density may be useful to initiate laser-guided discharges [8]. In this respect, it is important to characterize accurately the initial density and the time evolution of these filamentary plasmas. Although the recombination kinetics of air plasmas has been extensively studied both in the

* Corresponding author. Tel.: +33-1-6931-0220; fax: +33-1-6931-0220; e-mail: mysy@enstay.ensta.fr

PII: S0030-4018(00)00734-3

strongly ionized, dense regime and in the low density regime, the intermediate case of a high density, weakly ionized plasma pertaining to a fs laser generated plasma filament is still largely unexplored.

2. Experimental procedure and discussion

We have explored the time evolution of such plasma channels using two complementary methods: time-resolved optical diffractometry, able to explore with high temporal resolution the early decay only, and a new electric cross-conductivity technique [7] with better sensitivity but poorer time-resolution, applicable to later times. The cross-conductivity scheme is illustrated in Fig. 1(a). The filament to be characterized is created by a laser pulse from a Ti:S oscillator followed by a CPA amplifier system. At the output of the compressor stage, the beam profile is nearly Gaussian, with a beam waist of $w_0 = 12$ mm. The beam goes through a diaphragm 17 mm in diameter and is focused in air with a thin lens of focal length $f = 2$ m. The pulse wavelength is 800 nm; its duration is 120 fs and its energy 14 mJ. The self-guided pulse, with energy of about 1 mJ, traverses a copper electrode through a 1.5 mm hole and reaches the center of a second positively charged copper electrode. Both electrodes have lateral dimensions (~ 5 cm) large as compared to the inter-electrode spacing (1–2 cm). Instead of a plain metal plate as it was the case in our previous work [7] the second electrode has a hole drilled in its center, with a diameter (8 mm) much larger than the filament plasma diameter (< 100 μm). Under such conditions, the electric conductivity measured across an external load resistance is poor due to the large resistance between the filament and the edge of the second electrode.

A second plasma channel (switching plasma, see Fig. 1(a)) is independently produced by focusing part of the incident laser pulse with an $f = 1$ m lens. The time of creation of the switching plasma can be adjusted with respect to the filament by introducing an optical delay in the path of the diverted laser pulse. The distance between the electrodes is 16 mm and a 2 kV potential difference is applied. The

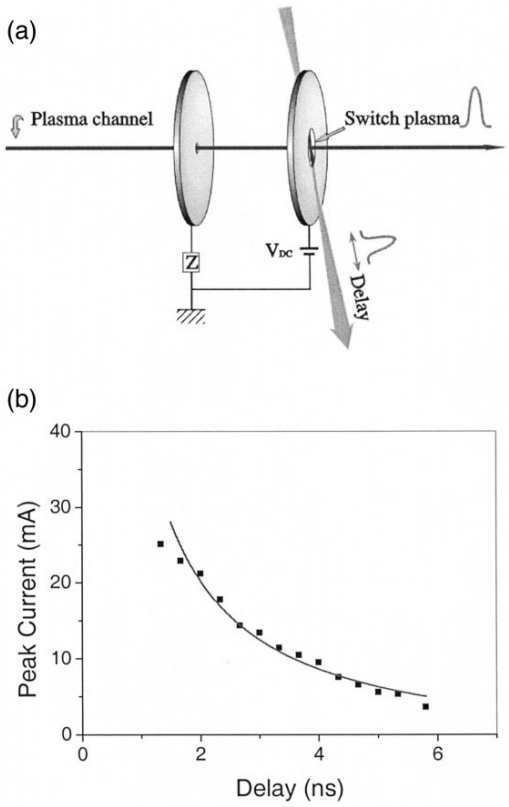

Fig. 1. (a) Experimental scheme for cross-conductivity measurements; and (b) cross-conductivity current recorded as a function of the switching plasma delay. Measurements were performed 6 cm after the origin of the filament plasma channel.

current flowing in the short circuit is measured across an external load resistance of 8.2 kΩ. The signal scales linearly with applied voltage, evidence that no electron avalanche process occurs in the produced filament.

The peak current measured as a function of delay is shown in Fig. 1(b). A positive delay corresponds to a retarded switching plasma at the second electrode. Note that at early times $\tau < 2$ ns, the measurements are not valid, because there is a saturation of the signal due to the current limitation of the power supply and because of the limited response time of the switching gate.

Measurements of the plasma decay at early times ($\tau < 2$ ns) have been made with an all-optical method, with sub-picosecond resolution, shown in Fig. 2. The

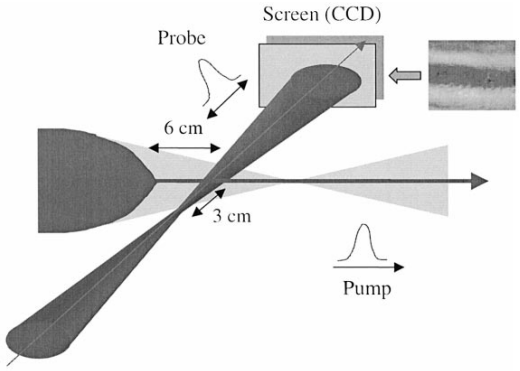

Fig. 2. Experimental scheme for the time-resolved diffractometry. The modified image of a probe beam crossing the filament is recorded at various delays. Also shown is the central dark fringe in the probe far field image for zero time delay.

far field image of a probe beam, modified after passage through the filament, is recorded at various delays with a linear CCD camera. The filament plasma, 40 μm in radius [7], plays the role of a thin diverging lens that refracts the probe beam. The far field probe intensity is expressed as:

$$|F(p,q)|^2 = \int\int_{-\infty}^{+\infty} f(x,y,z)\mathrm{e}^{\mathrm{i}\varphi(x,y)}\mathrm{e}^{\mathrm{i}(px+qy)}\mathrm{d}x\mathrm{d}y$$

where the probe electromagnetic field is written:

$$f(x,y,z) = \frac{1}{1+\mathrm{i}(z/z_\mathrm{r})}\mathrm{e}^{\mathrm{i}(r/w)^2(z/z_\mathrm{r})\times\frac{1}{1+(z/z_\mathrm{r})^2}} \times \mathrm{e}^{-(r/w)^2\times\frac{1}{1+(z/z_\mathrm{r})^2}}$$

where $z_\mathrm{r} = 1$ mm is the Rayleigh length and $w = 20$ μm is the beam waist at the focus of the $f = 0.5$ m focusing lens. The accumulated phase $\varphi(x,y) = \int_{-\infty}^{+\infty} n(x,y,z)\mathrm{d}z$ is related to the plasma density by the relation $n(x,y,z) = 1 - (1/2)(n_\mathrm{e}/n_\mathrm{cr})$, where n_cr is the plasma critical density. For the electronic density time evolution we use the following rate equations, which describe the different relaxation

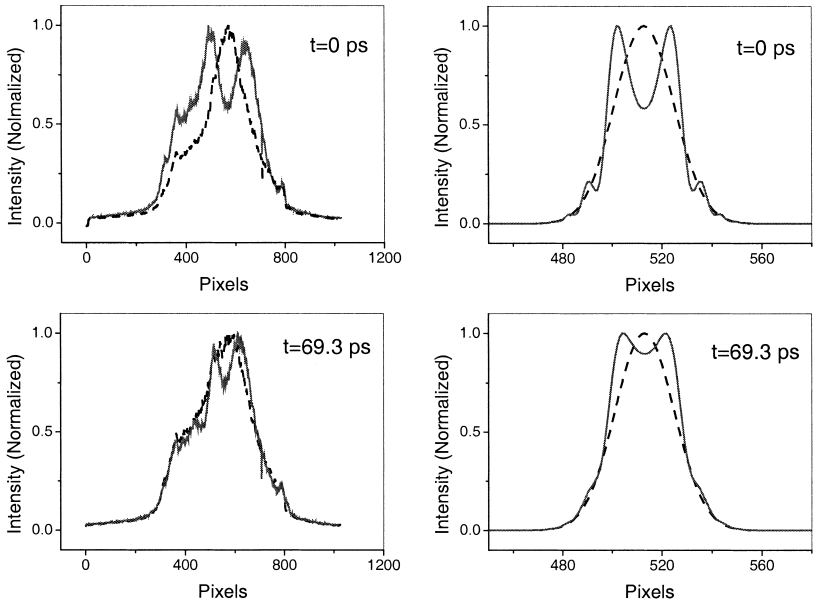

Fig. 3. Characteristic spatial profiles of the probe beam crossing the filament, for two delays. The dashed line is the probe profile without filament. Left: experimental results. Right: simulations.

mechanisms of electrons n_e and positive (negative) ions n_p (n_n) in air as reported in the literature [9]:

$$\frac{\partial n_e}{\partial t} = \gamma n_e - \eta n_e - \beta_{ep} n_e n_p$$

$$\frac{\partial n_p}{\partial t} = \gamma n_e - \beta_{ep} n_e n_p - \beta_{np} n_n n_p$$

$$\frac{\partial n_n}{\partial t} = \eta n_e - \beta_{np} n_n n_p$$

with the following coefficients: $\gamma = 7.4 \times 10^4$ s^{-1} for the impact ionization due to the external electric field, $\eta = 2.5 \times 10^7$ s^{-1} for the attachment of electrons to O_2, $\beta_{ep} = 2.2 \times 10^{-13}$ m^3/s for the electron–ion recombination, and $\beta_{np} = 2.2 \times 10^{-13}$ m^3/s for the ion–ion recombination [9]. As initial conditions we have $n_e(0) = n_p(0) = n_{e0}$ and $n_p(0) = 0$. Air ionization, which occurs in a process involving the simultaneous absorption of 8–10 infrared photons, is instantaneous on the time scale considered here. It produces an initial electronic density n_{e0} that must be determined. For initial densities above 10^{15} cm^{-3} and for times less than 10 ns the main mechanism involved in the plasma relaxation is the recombination process.

Under such conditions, the system of rate equations for electrons simplifies to a recombination term only, of the form $\partial n_e/\partial t = -\beta_{ep} n_e n_p = -\beta_{ep} n_e^2$, which has the analytical solution: $n_e(t) = 1/(\alpha + \beta_{ep} t)$, where $\alpha = 1/n_{e0}$.

Far field images of the probe beam recorded at different delays are displayed in Fig. 3(left). The probe beam crossed the plasma channel 6 cm after its origin under an angle of 3°. The converging probe beam focus was set 3 cm before the plasma channel. For comparison calculated images assuming an initial density of $n_{e0} = 2 \times 10^{17}$ cm^{-3} are shown in Fig. 3(right). The shape of these images is sensitive to the accumulated phase shift, fixing thereby the initial plasma density n_{e0} at $t = 0$ ps. More precisely, we select $\Delta t = 100$ fs to avoid complications due to the nonlinear four-wave mixing effects between the pump and probe beams. The far field images reveal a dark fringe in the center, the contrast of which experiences a rapid fall during the first 100 ps followed by a slower decay during the next 300 ps. This contrast is used for a quantitative analysis of the plasma evolution (Fig. 4). The resolution limit of this technique is reached after about 1 ns, with a corresponding electronic density of about 10^{15} cm^{-3}.

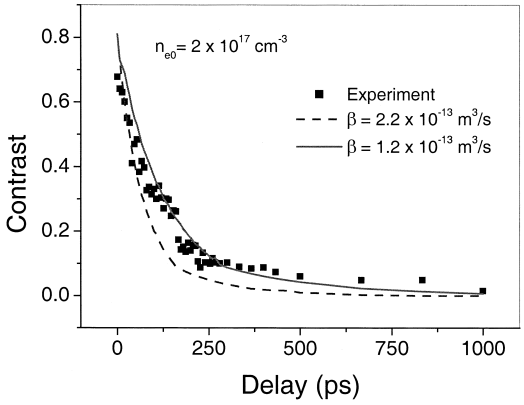

Fig. 4. Optical contrast of the probe wave front central fringe as a function of delay. The dots are experimental results and the lines are simulations.

Using the value of $\beta_{ep} = 2.2 \times 10^{-13}$ m^3/s found in the literature [9] and $n_{e0} = 2 \times 10^{17}$ cm^{-3} one obtains the dashed line shown in Fig. 4. A better fit to the data is obtained, keeping the same initial electron density but adopting a slightly different value of $\beta_{ep} = 1.2 \times 10^{-13}$ m^3/s (solid line in Fig. 4). The value $n_{e0} = 2 \times 10^{17}$ cm^{-3} is in good agreement with ionization rates from 3-D numerical simulations for the nonlinear propagation of intense ultra-short IR laser pulses.

Using the same law $n_e(t) = 1/(\alpha + \beta_{ep} t)$ for the electron density evolution, the same initial value for the electronic density $n_{e0} = 2 \times 10^{17}$ cm^{-3} and $\beta_{ep} = 1.2 \times 10^{-13}$ m^3/s as extracted by fitting the results of the optical measurements we obtain the solid line in Fig. 1(b) that fits also the experimental results of the electric measurements.

3. Conclusion

In conclusion, time-resolved diffractometry and cross-conductivity experiments show that the plasma channel formed in the trail of an intense, self-guided femtosecond laser pulse propagating through atmosphere is short-lived. Its decay is dominated by electron recombination on parent ions. From the

decay kinetics, one extracts an initial plasma density of $n_{e0} \approx 10^{17}$ cm^{-3}.

Acknowledgements

We acknowledge the expert assistance of Y.-B. André and G. Hamoniaux.

References

[1] A. Braun, G. Korn, X. Liu, D. Du, J. Squier, G. Mourou, Opt. Lett. 20 (1995) 73–75.
[2] E.T.J. Nibbering, P.F. Curley, G. Grillon, B.S. Prade, M.A. Franco, F. Salin, A. Mysyrowicz, Opt. Lett. 21 (1996) 62–64.
[3] A. Brodeur, C.Y. Chien, F.A. Ilkov, S.L. Chin, O.G. Kosareva, V.P. Kandidov, Opt. Lett. 22 (1997) 304–306.
[4] L. Wöste, C. Wedekind, H. Wille, P. Rairoux, B. Stein, S. Nikolov, C. Werner, S. Nierdermeier, F. Ronneberger, H. Schillinger, R. Sauerbrey, Laser Optoelektr. 5 (1997) 29–31.
[5] H. Schillinger, R. Sauerbrey, Appl. Phys. B 68 (1999) 753–755.
[6] B. La Fontaine, F. Vidal, Z. Jiang, C.Y. Chien, D. Comtois, A. Desparois, T.W. Johnston, J.-C. Kieffer, H. Pépin, H.P. Mercure, Phys. Plasmas 6 (1999) 1615–1621.
[7] S. Tzortzakis, M.A. Franco, Y.-B. André, A. Chiron, B. Lamouroux, B.S. Prade, A. Mysyrowicz, Phys. Rev. E 60 (1999) R3505–R3507.
[8] X.M. Zhao, et al., Ultrafast Phenomena IX (1994) 233–235.
[9] X.M. Zhao, J.-C. Diels, C.Y. Wang, J.M. Elizondo, IEEE J. Quantum Electron. 31 (1995) 599–612.

Chapter 2

2. Multi-filamentation: break-up and coalescence

2.1. Introduction

When a large laser beam with input power many times above the critical propagate in air it breaks into many filaments. Small irregularities in the initial beam profile (instabilities) are in the origin of this effect. When a nonlinear system exhibits instabilities of this kind then a modulation of the steady state is produced. This phenomenon is known under the name of modulation instability and in our case leads to the multi-filamentation.

In this chapter we present the different stages leading to fs filamentation. We show for the first time clearly, the initial break-up of a fs pulse into two light channels in the Kerr regime. Those two channels farther on coalesce to a single self-guided beam that propagates in the form of a robust filament over many Rayleigh distances. The later coalescence process is of great importance for the long range propagation and the deposition of high intensities at long distances.

The experimental results are confronted to numerical simulations and analytical estimates of the distance required for filament coalescence. The comparison is made step by step along the propagation. The three stages of: break-up during self-focusing, coalescence to a single filament and final beam diffraction are retrieved and are in good qualitative agreement with the experiments.

The detailed analysis is presented in appendix 2.1 and 2.2.

Appendix 2.1

"Break-up and fusion of self-guided femtosecond light pulses in air"

PHYSICAL REVIEW LETTERS **86**, 5470 (2001)

Breakup and Fusion of Self-Guided Femtosecond Light Pulses in Air

S. Tzortzakis,[1] L. Bergé,[2] A. Couairon,[2] M. Franco,[1] B. Prade,[1] and A. Mysyrowicz[1]
[1]*Laboratoire d'Optique Appliquée, ENSTA-École Polytechnique, Chemin de la Hunière, 91761 Palaiseau cedex, France*
[2]*Commissariat à l'Energie Atomique, CEA/DAM–Ile de France, B.P. 12, 91680 Bruyères-le-Châtel, France*
(Received 13 June 2000)

We report experiments showing the breakup and the merging of filaments formed by the modulational instability of femtosecond optical pulses in air. For input powers as high as 25 times the self-focusing threshold, the beams are shown to split into two spots, which coalesce into a self-guided beam. This effect occurs in an optically Kerr regime and plays an important role in the guiding process. Numerical simulations and theoretical estimates both support the comparison with the experimental data.

DOI: 10.1103/PhysRevLett.86.5470 PACS numbers: 42.65.Sf, 42.25.Bs, 42.65.Jx, 42.68.Ay

Nowadays, there is a considerable interest in understanding the propagation of femtosecond optical pulses through the atmosphere, in view of potential LIDAR applications [1]. Laser beams with high peak power are, indeed, known to form robust light guides over very long distances [2–4]. Various attempts in modeling this phenomenon have been proposed, by solving nonlinear Schrödinger-like systems [5–9]. Basically, an input beam having a transverse power, P_{in}, far above the threshold power for self-focusing, P_{cr}, first undergoes a compression in the diffraction plane caused by the Kerr response of air. Next, as its intensity increases by self-focusing, the beam ionizes the medium and creates an electron plasma. For subpicosecond infrared pulses with input intensities less than 10^{14} W/cm^2, optically induced ionization dominates through multiphoton processes [10]. The plasma then counteracts the optical self-focusing by digging a narrow hole in the radial wave profile [5] and by distorting the temporal shape of the beam [6,7,9]. From this dynamical balance between Kerr focusing and plasma defocusing, a self-guided light channel with a characteristic conical emission results [3–5].

However, issues still remain open about the inner dynamics of intense pulses in air. As is well known, a physical beam always exhibits small inhomogeneities that produce short-scale filaments in Kerr media via the modulational instability [11]. It was recently proposed in this respect [8] that under strong perturbations a broad beam with rather large waist ($w_0 \sim 0.7$ cm) and high power ($P_{\text{in}} \sim 35P_{\text{cr}}$) could propagate with a high density of collapsing filaments, regenerated by an accompanying background reservoir of low-amplitude energy. The light beam then forms an optically turbulent guide from multiple, recurrently nucleated filaments, which could maintain a long propagation. Besides, it was shown in [9] that for pulses with powers about $10P_{\text{cr}}$, the beam would produce only a finite number of filaments (mainly two spiky structures), which coalesce around the region of self-focus. On these points, clear observations are missing.

In this Letter, we study the propagation of femtosecond infrared beams exhibiting initially a single hump, with peak powers below 25 times critical. Emphasis is laid on two specific concerns. First, we examine the global features in the propagation and underline its three characteristic stages, namely, (i) the wave self-focusing (SF) in Kerr regime, (ii) the generation of an electron plasma by multiphoton ionization (MPI) and the formation of a self-guided beam, and (iii) the final spreading of the wave. These data, collected experimentally, are compared with results from a numerical code, which involves the main ingredients for describing the dynamics of ultrashort pulses in air. Second, we detail the early propagation of high-power beams. For different input powers, we investigate, both experimentally and theoretically, the breakup of beams with 3 mm waist and display evidence of their ability to merge into a single light guide. The onset of small-scale filamentation preceding the ionization is here thoroughly investigated. For clarity, the beam distortions caused by modulational instability will refer to "Kerr filamentation"; the "filament" resulting from MPI will be termed as light channel.

To start with, we identify the main stages in the dynamics of light self-guiding. From the experimental point of view, the laser source is a kHz, Ti:sapphire oscillator amplifier operating at the wavelength $\lambda_0 = 810$ nm. It delivers horizontally polarized pulses of 50 fs FWHM duration with an energy of up to 8 mJ per pulse. The wave diameter is first reduced by an inverted telescope, then the pulse is launched through the atmosphere in the form of a converging beam with focal distance $f = 2$ m, or as a collimated beam with $f = +\infty$. To record the intensity profiles, we use a pickup plate of BK7 glass at 45° angle. For intensities less than 10^{13} W/cm^2 (i.e., outside the focal region), the plate surface is not optically damaged and, therefore, the reflected part of the beam is not distorted. The reflected beam is imaged with a high aperture ($f/5$) lens onto a CCD camera. The intensity profile of the self-guided pulse and the electron density resulting from air ionization are measured along the propagation axis for different input pulse energies, E_{in}, insured with a relative error of $\pm 10\%$. We also perform far-field measurements of the energy in the resulting light channel after isolating it with a pinhole. Electrons are detected by using the electric-conductivity

 0031-9007/01/86(24)/5470(4)$15.00

technique described in Ref. [12], with synchronous detection adapted to the high repetition rate of our laser system. As in our previous experiments, we measure air resistivity by recording the current flowing between two plane copper electrodes connected by the laser-induced plasma. We calibrate the current as a function of the electron density averaged over the measured beam diameter ~0.5 mm enclosing the light channel, by means of an optical technique probing the plasma decay [13]. The threshold sensitivity of our experimental technique corresponds to an average electron density of $\rho_{\rm th} \sim 10^{15}$ cm^{-3}, represented by the dotted line in Fig. 1.

Numerical simulations are carried out for comparison with these experiments. We employ a three-dimensional code constrained to the axial symmetry, whose basic scheme was detailed in [9]. It resolves the slowly varying envelope of the linearly polarized laser electric field $\mathcal{E}(r,z,t)$, with central wave number $k_0 = k(\omega_0)$ and amplitude expressed in $\sqrt{W}$/cm, which is governed by an extended nonlinear Schrödinger (NLS) equation in the frame moving with the pulse

$$2i\frac{\partial \mathcal{E}}{\partial z} + \frac{1}{k_0}\Delta_\perp \mathcal{E} - k''\frac{\partial^2 \mathcal{E}}{\partial t^2} + k_0 n_2\Big\{|\mathcal{E}|^2 + \frac{1}{\tau_K}\int_{-\infty}^{t} e^{-(t-t')/\tau_K}|\mathcal{E}(t')|^2\,dt'\Big\}\mathcal{E} - k_0\frac{\omega_{pe}^2(\rho)}{\omega_0^2}\mathcal{E} + i\beta^{(K)}|\mathcal{E}|^{2K-2}\mathcal{E} = 0, \quad (1)$$

coupled with the electron density ρ of plasma created by multiphoton transitions. This quantity evolves as

$$\frac{\partial \rho}{\partial t} = \frac{\beta^{(K)}}{K\hbar\omega_0}|\mathcal{E}|^{2K}\Big(1 - \frac{\rho}{\rho_{at}}\Big), \quad (2)$$

where $\rho_{at} = 2.7 \times 10^{19}$ cm^{-3} is the density of neutral atoms satisfying $\rho/\rho_{at} \leq 1\%$. In Eq. (1), z refers to the propagation distance, the two-dimensional Laplacian $\Delta_\perp$ describes the transverse diffraction, and the remaining terms are the group-velocity dispersion (GVD) with coefficient $k'' = 0.2$ fs^2/cm, the Kerr response of air, with both instantaneous and retarded components in ratio $\frac{1}{2}$ fixed by experimental evidence [14], the electron density entering the plasma frequency $\omega_{pe}^2(\rho) = q_e^2\rho/m_e\epsilon_0$ (q_e and m_e are the electron charge and mass), and multiphoton absorption (MPA) with coefficient $\beta^{(K)}$. At atmospheric pressure, the appropriate parameters are $n_2 = 3.2 \times 10^{-19}$ cm^2/W, $K = 10$ for a mean ionization potential $U_i = 14.6$ eV, $\beta^{(10)} \simeq 1.27 \times 10^{-126}$ cm^{17}/W^9 [10,15], $\tau_K = 70$ fs is the characteristic time of molecular motions of air, and the critical power for self-focusing is $P_{\rm cr} = \lambda_0^2/2\pi n_2 \simeq 3.3$ GW. The input beams are modeled by unperturbed Gaussians with power $P_{\rm in}$ [9]. They exhibit a transverse waist $w_0 = 3$ mm ($|\mathcal{E}| \sim e^{-r_\perp^2/w_0^2}$), a temporal FWHM diameter $\Delta T = 50$ fs, and they are either collimated ($f = +\infty$) or focused by a lens with focal length $f = 2$ m [6,9]. We have simulated the evolution of a focused beam with $E_{\rm in} = 5$ mJ and $f = 2$ m, which we compare with experiments performed at the same energy level ($P_{\rm in} \sim 25P_{\rm cr}$). In Fig. 1, we show the radius of the beam and the maximum-in-time electron density, averaged in the radial plane. Apart from discrepancies near the focal point, the numerical results are in good agreement with the experimental measurements. We retrieve the SF stage, followed by an ionization front that remains clamped with the pulse at intensities $\leq 10^{14}$ W/cm^2 and enables light channeling over ten Rayleigh lengths, $z_f = z_0 f^2/(z_0^2 + f^2) \sim 11.4$ cm. Here, $z_0 = \pi w_0^2/\lambda_0 \sim 35$ m is the diffraction length of the collimated beam. Thus, for powers $P_{\rm in}$ around $25P_{\rm cr}$ and narrow waists, the beam self-focuses, creates an electron plasma, and then forms a self-guided light channel with ~100 μm diameter over more than 1 m.

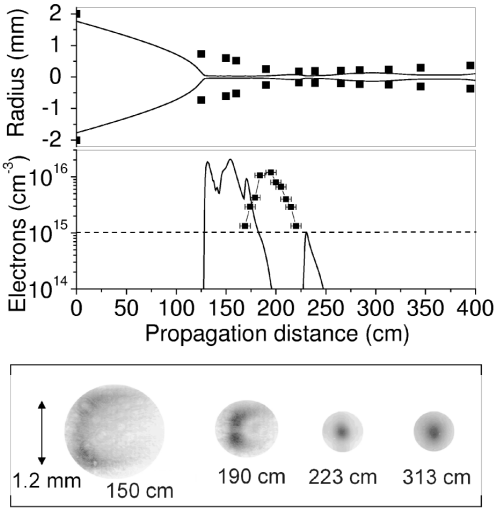

FIG. 1. Experimental results for the mean radius $R(z)$ of a focused beam with energy $E_{\rm in} = 5$ mJ and for the electron density ρ (squares). The numerical counterparts are shown in solid lines [$R(0) = w_0\sqrt{\ln 2/2}$]. The dotted line represents the electron detection threshold. Bottom inset: Dynamics of the 5 mJ beam profile at different propagation distances.

The energy captured in this channel is numerically found to be close to 10% of the input energy, which was confirmed by the experiment. The propagation length covering the early SF range, $z \leq z_c \simeq 1.4 \pm 0.1$ m, is about that attained by a collapsing beam in a purely Kerr medium with an instantaneous response only and an effective critical power $P'_{\rm cr} = 2P_{\rm cr}$. It can readily be determined by employing Marburger's formula [11]: $z_c = z_0/(\chi_M + z_0/f)$ with $\chi_M = (0.367)^{-1}[(\sqrt{P_{\rm in}/P'_{\rm cr}} - 0.852)^2 - 0.0219]^{1/2}$. The number for the maximum electron density is consistent with the simple estimate $\rho \sim \Delta T\beta^{(K)}I^K/K\hbar\omega_0$ that

varies as $(0.25-7.3) \times 10^{16}$ cm^{-3} in the intensity range $I = (5-7) \times 10^{13}$ W/cm^2 attained near focus.

The global features of femtosecond pulse propagation in air are, at least qualitatively, well described by the model equations (1) and (2). However, inspection of the beam profile around the location of the focus reveals a more complex structure. As shown in the inset of Fig. 1, the beam does not evolve as a single-hump Gaussian. Instead, it forms a spatial ring, which breaks up along the vertical axis in two symmetric spots that finally fuse into one central lobe. Ring and two-spot formation mainly results from the Kerr filamentation, which is triggered by small-scale inhomogeneities. In this regard, numerical simulations using the experimentally recorded beam profiles instead of unperturbed Gaussians reproduced the phase of ring formation. Although they did not restore the two-spot pattern because of the constraint imposed by the axial symmetry, these simulations showed amplification and merging of rings *before* the ionization front.

From now on, we examine this early filamentation stage. To make it more visible, we use beams in collimated geometry, which expands the region of interest by suppressing the space compression introduced by the lens. The results are detailed in Fig. 2. This figure shows transverse intensity patterns for input energies varying from 1 mJ ($P_{\rm in} \sim 5P_{\rm cr}$) to 5 mJ ($P_{\rm in} \sim 25P_{\rm cr}$). At low energies (1 mJ, top row), the first sequence illustrates the basic self-focusing, a short guiding, and the final spreading of the beam. At moderate energies (2.5 mJ, middle row), the beam begins to form a ring structure, which breaks up into two distinct spots. Both spots then coalesce in a single lobe that finally disperses at $z = 8.5$ m. At still higher energy (5 mJ, lower row), this scenario becomes clearly apparent. Being modulationally unstable, the beam first decays into an elliptical ring that gives rise to two spots [$z = 2.5$–4.5 m] with typical radial dimensions of the order $\sim$1.5 mm. Those self-focus at their own centroids, before fusing at larger distances [$z = 6.5$–8.5 m]. This evolution is thus generic.

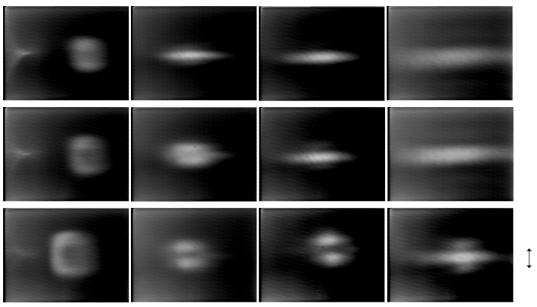

FIG. 2. Propagation patterns of 50 fs unfocused beams in air at different propagation distances = 2.5, 4.5, 6.5, and 8.5 m (for each row, from left to right). Top row: $E_{\rm in} = 1$ mJ; middle row: $E_{\rm in} = 2.5$ mJ; bottom row: $E_{\rm in} = 5$ mJ. The arrow on the right represents a length scale of 2 mm.

To explain this mechanism, we derive analytical estimates from a simplified nonlinear Schrödinger model. At leading order, we consider Eq. (1), in which the electron density is frozen in time and acts as a global saturating nonlinearity. Although strong temporal distortions are known to arise from MPI at high density levels, i.e., after the focus point z_c [6–9], such an approximation holds in the early range $z < z_c$, where the nonlinearities mainly originate from the Kerr term. We verified numerically that the pulse temporal profiles remained unchanged in this early propagation domain. The electron density is thus approximated by $\rho = \Delta T \beta^{(K)} |\mathcal{E}|^{2K}/(K\hbar\omega_0)$. Accordingly, we omit the delayed component in the Kerr response. This amounts to considering an effective critical power for self-focusing being twice $P_{\rm cr}$. We also ignore GVD and MPA, which never significantly affect the beam dynamics in this range, i.e., until far beyond the ionization threshold [8,9]. Therefore, we deal with the NLS equation

$$2ik_0 \frac{\partial \mathcal{E}}{\partial z} + \Delta_\perp \mathcal{E} + k_0^2 (n_2 |\mathcal{E}|^2 - n_{2K} |\mathcal{E}|^{2K}) \mathcal{E} = 0 , \tag{3}$$

where $n_{2K} \simeq 1.3 \times 10^{-143}$ cm^{2K}/W^K. Following the Bespalov-Talanov procedure (see, e.g., [11]), we first determine the incidence of perturbations in the form $\delta\mathcal{E} \sim e^{\gamma z + i\vec{k}_\perp \cdot \vec{r}_\perp}$ with growth rate γ and transverse wave number $k_\perp$, which develop on the beam having the uniform averaged intensity $I_0 = |\mathcal{E}_0|^2$ ($\delta\mathcal{E} \ll \mathcal{E}_0$). The growth rate provides the transverse spacing between filaments, $\Lambda_\perp = [2\pi P_{\rm cr}/I_0(1 - \alpha I_0^{K-1})]^{1/2}$, and their growth length $\Lambda_z \sim \gamma_{\rm max}^{-1} = \Lambda_\perp^2/\pi^2\lambda_0$, where $\alpha \equiv K n_{2K}/n_2$. From these, we infer that MPI efficiently counteracts the Kerr focusing for $I_0 \geq \alpha^{1/(1-K)} \sim 5 \times 10^{13}$ W/cm^2. At moderate intensity levels, $I_0 \leq 10^{13}$ W/cm^2, the dynamics is thus essentially driven by the Kerr response of the medium. For an input intensity of $I_0 = E_{\rm in}/\langle S \rangle \Delta T \simeq (0.7-1) \times 10^{12}$ W/cm^2 with $E_{\rm in} = 5$ mJ distributed on the average surface $\langle S \rangle = \pi w_0^2/2$, we find that filaments form over distances $\Lambda_z \geq 1.2$ m with a transverse size $\Lambda_\perp \simeq 1.8$ mm. These estimates are compatible with the filament growth length and spot sizes detailed in Fig. 3. The first filamentation mode is an annular ring, promoted by almost isotropic perturbations. As this ring is still modulationally unstable with an extension of about 4.5 mm, two cells emerge from it, in agreement with the patterns of Fig. 2. Next, both spots increase in intensity: Using $E_{\rm spot} \simeq 2.5$ mJ and $\langle S \rangle \simeq \pi w_x w_y/2$ computed with the horizontal and vertical spot waists w_x, w_y, I_0 in each spot is found to reach the maximum value $I_0 \simeq 3 \times 10^{12}$ W/cm^2 at $z = 6.5$ m, before the two filaments merge. The wave intensity has thus increased by less than one decade. Because I_0 always remains below 10^{13} W/cm^2, MPI is of negligible influence and, indeed, no significant emission of electrons above $\rho_{\rm th}$ was detected with collimated beams, at least along distances accessible experimentally ($z < 10$ m).

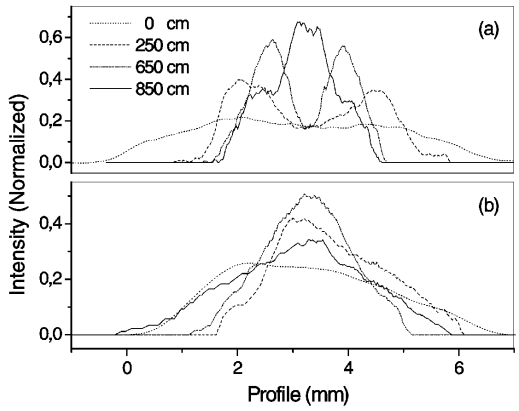

FIG. 3. Measured intensity profiles of a 5 mJ beam with $f = +\infty$ along (a) the y axis (vertical cut) and (b) the x axis (horizontal cut along one spot) at $z = 0$ (dotted line), $z = 2.5$ m (dashed), $z = 6.5$ m (dash-dotted), and $z = 8.5$ m (solid).

In contrast, the mean intensity of the convergent beam shown in Fig. 1 was found to exceed 5×10^{13} W/cm^2 around the linear focus.

As a result, the first propagation stage is actually driven by the Kerr response of air that focuses the beam and breaks it up through modulational instability into two filaments, which is well described by Eq. (3). Note that although each spot might in theory further split with a power $P_{\rm fil} \simeq \pi\Lambda_\perp^2 I_0/4 \approx \pi^2 P_{\rm cr}/2 < 12.5 P_{\rm cr}$ [9,11], only two local intensity maxima are clearly observed here.

Let us now discuss the mutual coalescence of spots, which, for simplicity, we model by two in-phase Gaussians arising at a given $z = z_0$, with waist w_α, individual power P_α, and mutual separation distance δ. We assume that the two spots are identical ($P_1 = P_2$), symmetrically located from the center of coordinates, and they possess equal sizes $\sim w_\alpha$ along the (x, y) directions. They are initially "well separated" with $\delta > \sqrt{2}\, w_\alpha$ [16], which is satisfied by the spots emerging at $z_0 = 6.5$ m in Fig. 3. In SF regime, coalescence results from the vanishing of the total mean-square radius of the beam, denoted by $\langle r_\perp^2 \rangle$, provided that both spots strongly interact. By neglecting MPI for collimated beams, this process can be described from the evolution equation, $d_z^2 \langle r_\perp^2 \rangle = H/k_0^2 P_\alpha$, where H is the Hamiltonian of Eq. (3) expressing at leading order as $H \simeq \int (|\nabla_\perp \mathcal{E}|^2 - \pi |\mathcal{E}|^4/P_{\rm cr})\, d\vec{r}_\perp = H_{\rm free} + H_{\rm int}(\delta)$. Here $H_{\rm free}$ refers to the Hamiltonian contributions of each individual spot and $H_{\rm int}(\delta)$ gathers all interaction terms that exponentially decrease with δ (see [16] for more detail). Self-focusing follows whenever $H < 0$, and the predominance of the interaction terms requires that δ be less than $3w_\alpha$ for P_α above critical. Thus, the two spots can fuse for $\delta < 3w_\alpha$, which definitely applies to the separation distance measured in Fig. 3 at $z = 6.5$ m. It is worth noticing that, in the absence of wave collapse, the fusion is all the more delayed along z as the spots are intense, since at increasing energy they reinforce their own local attractor on their individual centroids. This effect contributes to enlarge the Kerr stage beyond which an electron plasma can be excited, as confirmed by Fig. 2. For a focused beam, $\langle r_\perp^2 \rangle$ vanishes faster (see, e.g., [9]), and the fusion dynamics is accelerated.

In conclusion, we have shown that the early stages preceding the self-guiding in air of femtosecond pulses with peak power lying between 5 and 25 $P_{\rm cr}$ consisted in the breakup of the beam into two spots by modulation instability and their coalescence into one central lobe. This process gives rise to self-channeled light guides. The main stages in the formation of light channels have been confronted with numerical simulations restoring the different propagation regimes inherent to the self-focusing, plasma formation, self-guiding, and ultimate dispersion of the beam. In addition, by means of the NLS model (3), we have justified the filament formation and the fusion process enabling the beam to recombine into one robust lobe. This scenario of breakup and coalescence preceding the self-guiding is *generic, both for focused and for unfocused beams*, in the domain of powers investigated. Note that this does not prevent higher-power pulses to decay into more filaments, as proposed in [8]. To the best of our knowledge, we provided, for the first time, clear evidence of optical coalescence following the filamentation of femtosecond lasers in air, and we obtained good agreements between experimental data, numerical results, and recent theories in this field.

The authors thank Y. B. André and G. Mullot for technical assistance, and A. Chiron, M. Kolesik, and E. Wright for fruitful discussions.

[1] L. Wöste *et al.,* Laser Optoelektron. **29**, 51 (1997).
[2] A. Braun, G. Korn, X. Liu, D. Du, J. Squier, and G. Mourou, Opt. Lett. **20**, 73 (1995).
[3] E. T. J. Nibbering *et al.,* Opt. Lett. **21**, 62 (1996).
[4] B. La Fontaine *et al.,* Phys. Plasmas **6**, 1615 (1999).
[5] V. P. Kandidov, O. G. Kosareva, and S. A. Shlenov, Quantum Electron. **24**, 905 (1994).
[6] M. Mlejnek, E. M. Wright, and J. V. Moloney, Opt. Lett. **23**, 5 (1998); J. Schwarz *et al.,* Opt. Commun. **180**, 383 (2000).
[7] A. Chiron *et al.,* Eur. Phys. J. D **6**, 383 (1999).
[8] M. Mlejnek, M. Kolesik, J. V. Moloney, and E. M. Wright, Phys. Rev. Lett. **83**, 2938 (1999).
[9] A. Couairon and L. Bergé, Phys. Plasmas **7**, 193 (2000); L. Bergé and A. Couairon, Phys. Plasmas **7**, 210 (2000).
[10] L. V. Keldysh, Sov. Phys. JETP **20**, 1307 (1965).
[11] J. H. Marburger, Prog. Quantum Electron. **4**, 35 (1975).
[12] S. Tzortzakis *et al.,* Phys. Rev. E **60**, R3505 (1999).
[13] S. Tzortzakis *et al.,* Opt. Commun. **181**, 123 (2000).
[14] J. F. Ripoche *et al.,* Opt. Commun. **135**, 310 (1997).
[15] A. Talebpour, J. Yang, and S. L. Chin, Opt. Commun. **163**, 29 (1999).
[16] L. Bergé *et al.,* J. Opt. Soc. Am. B **14**, 2550 (1997).

Appendix 2.2

"Infrared femtosecond light filaments in air: simulations and experiments"

Submitted to

JOURNAL OF THE OPTICAL SOCIETY OF AMERICA B (2001)

Infrared femtosecond light filaments in air: simulations and experiments

A. Couairon[1], S. Tzortzakis[2], L. Bergé[1], M. Franco[2], B. Prade[2], A. Mysyrowicz[2]

[1] *Commissariat à l'Énergie Atomique, Département de Physique Théorique et Appliquée, B.P. 12, 91680 Bruyères-le-Châtel, France*

[2] *Laboratoire d'Optique Appliquée, ENSTA-École Polytechnique, Chemin de la Hunière, 91761 Palaiseau Cedex, France*

Recent experiments on the guiding over several meters of infrared ultrashort laser pulses in air are compared to numerical simulations. During a first self-focusing stage affected by the modulational instability, the beam is shown to break up into two light channels, that finally coalesce in a narrow filament able to propagate over several Rayleigh lengths. The filament propagation is first associated with the generation of an electron plasma, the density of which is larger than 10^{16} cm^{-3}, and persists well beyond this region of large electron density. The simulations restore accurately the general dynamics of the pulse and the main propagation stages observed in the experiments.

I. INTRODUCTION

In view of potential applications in lightning protection [1] and LIDAR detection [2], the generation of light filaments in air has become a topic of active experimental and theoretical research during the last decade [3–16].

In the pioneering works by Braun *et al.* [3] and by Nibbering *et al.* [4], laser beams with input power above the critical threshold for self-focusing have been shown experimentally to propagate over several tens of meters by forming robust light guides, or filaments, in the atmosphere. The propagation of these light filaments in the infrared (IR) domain is often associated with generation of white light continuum and conical emission. This effect has been reported to occur at kilometric distances in [2], using large and powerful input beams with initial temporal chirp, pointing out a filament formation in the high atmosphere. From

the numerous attempts in understanding the propagation of IR femtosecond optical pulses through the atmosphere [5–16], the main physical effects sustaining the formation of light filaments have been well identified: apart from differences in the quantitative estimations of their interplay, there is now an agreement on the fact that IR light filaments result from the balance between the Kerr response of air, which overcomes diffraction and focuses the pulse when its input power exceeds the self-focusing threshold, $P_{\rm cr}$, and the defocusing action of self-induced ionization.

This balance does not consist in a local equilibrium valid in some region of space, but in a dynamical equilibrium that may be strongly affected by perturbations. For an input beam having a transverse power, $P_{\rm in}$, above $P_{\rm cr}$, the self-focusing effect compresses the beam in the transverse diffraction plane and the peak intensity increases correspondingly. As is well known from standard analyses, if no stabilizing mechanism were present, the beam would undergo a collapse in the form of a singularity at a finite distance, which may be estimated from the Marburger's formula [17]. This never happens in experiments since higher-order mechanisms saturate the collapse and stabilize the beam. In the case of IR filaments in air, the self-induced ionization acts as such a stabilizing mechanism. As the intensity increases by self-focusing to about 10^{13} W/cm^2, the beam ionizes the medium and creates an electron plasma. The plasma then counteracts the optical self-focusing by digging a narrow hole in the radial wave profile [9] and by distorting the temporal shape of the beam [10–13]. From this balance between Kerr focusing and plasma defocusing, a self-guided light channel results. Although the physical effects entering this balance are well identified, the detailed dynamics of the light channels still remains an open question.

Let us point out here that this dynamics is very sensitive to different parameters such as the pulse duration, the beam size or the homogeneity of the beam. In addition, the equilibrium may be affected by the competition with other mechanisms counteracting the collapse as, e.g., normal group velocity dispersion (GVD). For instance in solid transparent

media such as Sapphire or BK7, white light generation has been interpreted as a result of the pulse splitting phenomenon owing to GVD, the space-time focusing and the self-steepening [18,19], with plasma generation playing a minor role. For IR laser pulses in specific converging beam geometry that propagate in different dispersive media such as silica glasses [20], however, filament formation resulting from a balance between self-focusing and electron generation has been revealed. The formation of a waveguide and the propagation of femtosecond pulses over several Rayleigh lengths in air has also been observed in the UV wavelength domain [21,22]. The role of the dispersive effects is greater than in the IR domain but it is still an open question whether the mechanism stabilizing the Kerr self-focusing is or not the self-induced ionization alone. A competition between self-induced ionization and dispersive effects may take place under certain conditions [23]. Different stabilizing mechanisms relying on other physical effect, such as the saturation of the Kerr effect by quintic nonlinearities [24], have been proposed to model the self-guiding phenomenon. The insight gained from these different approaches is that the dynamics of filaments appears to be extremely rich with a wide variety of possible regimes supporting their long distance propagation.

Different experimental observations on IR light filaments have been explained by several scenarios, namely the "moving focus" model [6] and the "spatial replenishment" model [10], to cite only two of them. According to the "moving-focus" model [6], the pulse is stacked into transverse slices in the time direction; the central slices with power above critical focus along an extended region of the propagation axis, delimited by the collapse points of the two slices with the maximum power and the critical one. Each slice should collapse at a specific point all the farther as the power contained in the slice is close to critical [17]. This model describes the formation of a filament for collimated and for convergent beams, as well as its propagation till the linear focus. Beyond this point, the self-guiding of light persists [7], since self-induced ionization arrests the collapse of the beam by counterbalancing the Kerr

self-focusing, which results in a structure able to sustain propagation. In that connection, it has been shown theoretically that, by taking into account only diffraction, Kerr effect and optically-induced ionization, the propagation of a femtosecond pulse envelope with power close to critical and coupled with an electron plasma created by multiphoton ionization (MPI) evolves to a long-living structure that behaves as a spatial soliton [14]. This structure exhibits a temporal profile having a leading peak that shrinks on the time axis, leading to an optically induced shock regime. The resulting light guide is capable of persisting over considerable distances. This fundamental structure may undergo significant variations in time when, e.g., GVD or other secondary saturating effect are added [14].

From numerical simulations [10], the "spatial replenishment" scenario emphasizes the formation of light guides with a specific dynamics of the beam constituted by successive focusing and defocusing cycles. During a focusing stage, the beam generates a narrow plasma which strongly defocuses the trailing part of the pulse and produces one leading peak in its temporal profile. Due to absorption and different loss mechanisms, the intensity of this peak may decrease sufficiently, so as to turn off plasma generation. The back of the pulse can then focus again, creating thereby a two-spiked structure in the wave temporal profile. This scenario was observed for peak powers above $5P_{\rm cr}$ and most its characteristic stages were confirmed at power levels up to $10P_{\rm cr}$ [13]. The resulting structure is very similar to that obtained in a GVD splitting regime, except that the main effect distorting the wave profile is caused by the coupling with the electron plasma created by MPI, and not by dispersive effects that only contribute to stabilize the spikes. This sequence of events constituting the spatial replenishment scenario were supposed to repeat many times in principle. At higher power levels, a multiple filament regime has been shown numerically to take place [16]. Starting from a broad beam with large waist ($w_0 \sim 0.7$ cm) and high power ($P_{\rm in} \sim 35P_{\rm cr}$), a seemingly disordered optical wave guide is obtained from multiple filaments that are nucleated along propagation. The occurrence of filamentation has been confirmed in several experimental

observations [3,4,7,8,15]. Filamentary structures originate from the small inhomogeneities of the beam that are spatially amplified in Kerr media, via the modulational instability [17]. A striking result in Ref. [15] concerns the coalescence of these filamentary structures, which regenerates a single filament that actually maintains a long propagation of the light beam.

This paper deals with a theoretical and experimental study of IR filaments in air. Examples of coalescence and regeneration of filaments will be described in details: we show both experimentally and theoretically that the propagation of femtosecond IR beams exhibiting initially a single hump, with peak powers below 25 times critical, leads to the break-up of the beam into two small-scale filaments and their merging into a single light guide. To that aim, we compare experimental data with results from the numerical code PULP (Propagation of Ultra-short Laser Pulses), which includes the main ingredients describing the propagation of ultra-short pulses in air. First, we examine the global features in the propagation and underline the three characteristic stages that characterize the propagation, namely: (i) the wave self-focusing and beam break-up in Kerr regime, (ii) the generation of an electron plasma by multiphoton ionization (MPI) and the formation of a self-guided beam, and (iii) the final spreading of the wave. We perform quantitative comparisons between numerical simulations involving a mean ionization rate for MPI in air and a two-specy model involving the separate plasma responses for nitrogen and oxygen. Second, we detail the early propagation stage of high-power beams during which the break-up occurs, and show evidence of their ability to merge into a single light guide at the end of this stage. Third, we study temporal and spatial profiles of the beam. We then discuss the dynamics of the pulse power spectra. The genericity of the propagation scenario is then confirmed by experiments and simulations with collimated beams. Finally, we present some analytical estimates supporting the beam break-up into two spots and their merging into a single filament.

II. PROPAGATION

The evolution of the laser pulse in a gas is described by the vector wave equation

$$-\nabla\times(\nabla\times\mathbf{E})-\frac{1}{c^2}\frac{\partial^2}{\partial t^2}\int_{-\infty}^{t}n^2(\mathbf{r},t-t')\mathbf{E}(t')\,dt'=\mu_0(\frac{\partial\mathbf{J}}{\partial t}+\frac{\partial^2\mathbf{P_{nl}}}{\partial t^2}) \tag{1}$$

where n is the linear refractive index, c and μ_0 are the velocity of light and the permeability in vacuum. The electric field, $\mathbf{E}(r,\phi,z,t)=E\,\mathbf{x}$, depends on the cylindrical coordinates r, ϕ, z and is polarized in the $\mathbf{x}$ direction. In the right hand side (r.h.s.) of Eq. (1), $\mathbf{J}$ denotes the plasma current density associated with the ionized gas and satisfies

$$\frac{\partial\mathbf{J}}{\partial t}=\frac{e^2}{m}\rho\mathbf{E}-\epsilon_0 c\frac{\partial}{\partial t}\left(\frac{\sum_n\rho_n W_n K_n\hbar\omega_0}{|E|^2}\mathbf{E}\right). \tag{2}$$

The first term on the r.h.s. of Eq. (2) leads to plasma defocusing and blueshifting of optical pulses in ionized gases. The quantities e and m denote the electron charge and mass, ϵ_0 is the permittivity in vacuum and ρ is the free electron density. The second term in the r.h.s. of Eq. (2) accounts for absorption due to ionization and will be specified below after describing the coupling of the electric field with the electron plasma density.

The second term in the r.h.s. of Eq. (1) is the nonlinear polarization related to the Kerr cubic term in the series expansion of the polarization field $\mathbf{P}=\epsilon_0(\chi^{(1)}\mathbf{E}+\chi^{(3)}|E|^2\mathbf{E})$. It reads as

$$\mathbf{P_{nl}}=2n_2|E|^2\mathbf{E} \tag{3}$$

where n_2 denotes the nonlinear index of refraction in the Kerr response of air, proportional to the third order component $\chi^{(3)}$ of the susceptibility tensor of the gas. The quantity n_2 is entering $P_{\rm cr}\equiv\lambda_0^2/2\pi n_0 n_2$, where n_0 is the refraction index of air and λ_0 is the laser wavelength in vacuum.

Eqs. (1) to (3) must be supplemented by a system of evolution equations for the electron density ρ and densities of atoms, ρ_n, describing the photo-ionization of air. The electron

density in Eq. (2) is expressed as

$$\rho = \rho_{\rm at} - \rho_{\rm O} - \rho_{\rm N} \tag{4}$$

where $\rho_{\rm O}$ and $\rho_{\rm N}$ denote the densities of oxygen and nitrogen, related to the total atom density ρ_0 by $\rho_0 = 0.2\rho_{\rm O} + 0.8\rho_{\rm N}$. Before the interaction with the pulse, the gas is assumed to be neutral with initial atom density $\rho_0(t \to -\infty) = \rho_{\rm at}$, where $\rho_{\rm at} = 2.7 \times 10^{19}$ cm^{-3}. For the intensities we consider, the electron density will never exceed a few percent of the initial neutral atom density $\rho_{\rm at}$ which in turn is far below the critical plasma density $\rho_c \equiv m\epsilon_0\omega_0^2/e^2 = 1.8 \times 10^{21}$ cm^{-3} at the laser frequency ω_0 associated with the wavelength $\lambda_0 = 810$ nm. During the interaction of the pulse with the gas, ions are created with charge densities governed by

$$\begin{aligned} \frac{\partial \rho_{\rm N}}{\partial t} &= -W_{\rm N}\rho_{\rm N}, \\ \frac{\partial \rho_{\rm O}}{\partial t} &= -W_{\rm O}\rho_{\rm O}. \end{aligned} \tag{5}$$

The ionization rates $W_{\rm N}$ and $W_{\rm O}$ for nitrogen and oxygen are functions of the laser intensity. A general formulation has been given by Keldysh [28] and Perelomov *et al.* [34] for the photo-ionization rates. It covers both the multiphoton regime valid for weak fields, and the tunnel regime valid for strong fields. The Keldysh parameter $\gamma_n \equiv (U_n/2U)^{1/2}$, defined as the ratio between the ionization potential of an atom and the quiver energy of a free electron in the laser field $U = eE^2/4m\omega_0^2$, distinguishes whether ionization occurs in the multiphoton regime ($\gamma_n \gg 1$) or in the tunnel regime ($\gamma_n \ll 1$).

For a laser with central wavelength in vacuum $\lambda_0 = 810$ nm, the multiphoton regime is dominant at moderate intensities, i.e., for peak intensities less than 10^{14} W/cm^2. In this case, Keldysh's general formulation may be simplified into the multiphoton ionization model, according to which the ionization rates are given by $W_n = \sigma_n I^{K_n}$ where $K_n \equiv \mathrm{mod}(U_n/\hbar\omega_0 + 1)$ is the minimum number of photons required to reach ionization of a given

level n with potential U_n and the coefficients σ_n are related to the cross-section for inverse bremsstrahlung (see Appendix A for the expressions of the optical field induced ionization rates and related coefficients σ_n). The tunnel regime is dominant ($\gamma_n \ll 1$) for intensities above 10^{14} W/cm^2. Although this case will not be studied, our model is also valid for such intensities if we adopt the Ammosov *et al.* model proposed in Refs. [29,30] and replace W_n by the tunnel rates.

We now specify the multiphoton absorption current, i.e., the second term in the r.h.s. of Eq. (2): for each free electron, the pulse loses an amount of energy $K_n \hbar\omega_0$ equivalent to the number of photons absorbed to ionize the corresponding atom. The quantities ρ_n, W_n and K_n denote the densities, the ionization rates of atoms and the number of photons necessary to ionize the corresponding species.

The incident beam is linearly polarized and has a cylindrical symmetry around the propagation axis z. We assume that along propagation, the electric field preserves this linear polarization state. Although recent studies [35,36] on vectorial nonlinear Schrödinger (NLS) systems emphasize the possibility of producing filament-like structures from the polarization modes alone, we expect that even in the presence of small noise, an initially linear polarization state will not significantly trigger orthogonal polarization components. Besides, recent experiments showed that the global picture of pulse propagation in air is not changed between linearly and circularly polarized pulses, apart from small differences in the ionization rates [37]. Therefore, we shall consider $\mathbf{E}$ under scalar approximation: it is written as $E = \mathrm{Re}[\mathcal{E} \exp(ik_0 z - i\omega_0 t)]$, where k_0 and ω_0 are the wavenumber and frequency of the carrier wave. The scalar envelope $\mathcal{E}(r, z, t)$ is assumed to be slowly varying in time and along z and evolves according to the propagation equation expressed in the reference

frame moving at the group velocity

$$\frac{\partial \mathcal{E}}{\partial z} = \frac{i}{2k_0} T^{-1} \left(\frac{\partial^2}{\partial r^2} + \frac{1}{r}\frac{\partial}{\partial r} \right) \mathcal{E} - i\frac{k''}{2}\frac{\partial^2 \mathcal{E}}{\partial \tau^2} - i\frac{k_0}{2\rho_c} T^{-1}(\rho \mathcal{E})$$
$$+ ik_0 n_2 T[(1 - x_{dK})|\mathcal{E}|^2 + \frac{x_{dK}}{\tau_{dK}} \int_{-\infty}^{\tau} \mathrm{e}^{-\frac{\tau - \tau'}{\tau_K}} |\mathcal{E}(\tau')|^2 d\tau']\mathcal{E} - \frac{1}{2}\frac{\sum_n \rho_n W_n K_n \hbar \omega_0}{|\mathcal{E}|^2}\mathcal{E} \quad (6)$$

where τ refers to the retarded time variable $t - z/v_g$ with $v_g \equiv \partial\omega/\partial k|_{\omega_0}$. Equation (6) is found by elimination of the carrier wave in Eqs. (1) to (3) and by neglecting the second order derivatives in z. The terms on the r.h.s. of Eq. (6) account for diffraction within the transverse plane, group velocity dispersion with coefficient $k'' \equiv \partial^2 k/\partial\omega^2|_{\omega_0} = 0.2$ fs^2/cm at 810 nm, defocusing due to the plasma with electron density ρ, self-focusing related to the Kerr effect, and multiphoton absorption (MPA). The Kerr response of air possesses both instantaneous and retarded components in ratio $x_{dK} = 1/2$ fixed by experimental evidence [25]. The nonlinear refraction index of air at atmospheric pressure $n_2 = 3.2 \times 10^{-19}$ cm^2/W, and the characteristic time $\tau_K = 70$ fs for the delayed component have been determined in Ref. [25]. With this value for n_2, the critical power for self-focusing is $P_{\rm cr} = \lambda_0^2/2\pi n_0 n_2 \simeq 3.3$ GW. The operator $T \equiv 1 + (i/\omega_0)\partial_\tau$ in front of the cubic nonlinearity gives rise to self-steepening effects and T^{-1} in front of the diffraction term accounts for space-time focusing. By taking this operator into account, we avoid neglecting the cross derivative $\partial^2_{z,\tau}$ which appears in the wave equation expressed in the reference frame of the pulse through the retarded time variable τ. The reader is referred to Refs. [18,19,26,27] for detailed discussions of the effects of the operator T. In the present scope, we verified that the coming results did not significantly differ when the operator T and T^{-1} were turned off in the numerics. At the laser wavelength $\lambda_0 = 810$ nm, the orders of multiphoton ionization are $K_{\rm N} = 11$ for nitrogen and $K_{\rm O} = 8$ for oxygen, with ionization potentials $U_{\rm N} = 15.6$ eV and $U_{\rm O} = 12.1$ eV. The ionization rates computed at 810 nm from the Keldysh theory in the multiphoton limit are $W_{\rm N} = \sigma_{\rm N} I^{K_{\rm N}}$ with $\sigma_{\rm N} = 5.08 \times 10^{-144}$ s^{-1} cm^{22}/W^{11} and $W_{\rm O} = \sigma_{\rm O} I^{K_{\rm O}}$ with $\sigma_{\rm O} = 2.88 \times 10^{-99}$ s^{-1} cm^{16}/W^8. As will be seen below, we have checked that the results are

nearly the same when Eqs. (5) are replaced by a single equation as

$$\frac{\partial \rho}{\partial t} = \sigma_{\rm air} I^{K_{\rm air}} (\rho_{\rm at} - \rho), \tag{7}$$

describing the ionization of air with a mean ionization potential $U_i = 14.6$ eV, for which we obtain $K_{\rm air} = 10$ and $\sigma_{\rm air} \simeq 1.38 \times 10^{-128}$ s^{-1}cm^{20}/W^{10}.

Avalanche and recombination processes may be included in the r.h.s. of Eq. (7) as $(\sigma/n_0^2 U_i)\rho I - a\rho^2$, with $\sigma = 5.1 \times 10^{-18}$ cm^2 and $a = 5 \times 10^{-7}$ cm^3/s [31]. We have checked numerically that these effects are of secondary importance for femtosecond pulses, since they only slightly modify the wave amplitude and density whose levels remain of the order of those induced by MPI alone (see [12,13] for details). In the following, we will therefore consider that MPI constitutes the main ionization sources and we neglect other processes.

The input beams are modeled by unperturbed Gaussians with peak input power $P_{\rm in}$,

$$\mathcal{E}(r,t,0) = \sqrt{\frac{2P_{\rm in}}{\pi w_0^2}} {\rm e}^{-r^2/w_0^2 - t^2/t_p^2 - ikr^2/2f}. \tag{8}$$

They exhibit a transverse waist $w_0 = 3$ mm, a temporal FWHM diameter $\Delta T = \sqrt{2\log 2}\, t_p = 50$ fs (temporal half width $t_p = 42$ fs), and they are either collimated ($f = +\infty$) or focused by a lens with focal length $f = 2$ m. The Rayleigh length obtained with a focal length of 2 m is $z_f = z_0 f^2/(z_0^2 + f^2) \sim 11.4$ cm, where $z_0 = \pi w_0^2/\lambda_0 \sim 35$ m is the diffraction length of the collimated beam. The energy of a Gaussian input beam given by Eq. (8) reads as $E_{\rm in} = P_{\rm in} t_p \sqrt{\pi/2}$ and the input peak power is expressed as a function of the peak intensity as $P_{\rm in} = \pi w_0^2 I_0/2$. The peak power and intensity are deduced from these formulas by using the value of the input beam energy $E_{\rm in}$ measured experimentally. The incident beam may also be introduced as a data table obtained from experimental measurements. In order to preserve the revolution symmetry, the experimentally measured input beam is then averaged over the azimuthal coordinate and the resulting beam profile $g(u)$, with $u = r/w_0$, is introduced in the code. From our experiments, it has been checked that this profile is very close to a super-Gaussian $\mathcal{E}(r) \simeq {\rm e}^{-r^3/w_0^3}$, [$g(u) \simeq {\rm e}^{-u^3}$], with small inhomogeneities.

In this case a shape factor enters the relation between input peak power and intensity as $P_{\rm in} = (\pi w_0^2 I_0/2) \times 4 \int_0^{+\infty} g^2(u) u\, du$. Similarly, the pulse temporal profile may be introduced as a table $h(v)$, with $v = t/t_p$, different from a Gaussian, and a shape factor enters the relation between input peak power and energy $E_{\rm in} = P_{\rm in} t_p \int_{-\infty}^{+\infty} h^2(v) dv$. In all cases, peak power and intensity are deduced from the experimental measurement of the energy and beam/pulse shapes.

III. RESULTS FROM EXPERIMENTS AND SIMULATIONS

A. Experimental procedure

In the present experiments, the IR laser pulses were obtained from a kHz, chirped pulse amplification (CPA), Ti:Sapphire laser system. The laser peak emission wavelength was $\lambda_0 =$ 810 nm, the pulse duration (FWHM) about 50 fs, and the output energy could reach 8 mJ. Attenuation of the laser beam energy was possible by adjusting the angle of a $\lambda/2$ waveplate placed in front of the grating pair of the laser pulse compressor. The temporal profile of the input pulse was measured, using a non-collinear second-harmonic autocorrelator employing a Barium Borate (BBO) crystal that served as nonlinear medium. Its autocorrelation trace is shown in Fig. 1 (solid line), which can be fitted with a sech^2 function (dotted line) with duration of about 50 fs. The laser beam diameter was first reduced using an inverted telescope (0.2x), as shown in Fig. 2. The beam profile is shown in Fig. 3. Averaged over the azimuthal angle, it has shape very close to a super-Gaussian with waist $w_0 = 3$ mm. The laser beam is then launched in air either as a collimated beam or in a slightly converging geometry using a lens with focal length $f = 2$ m.

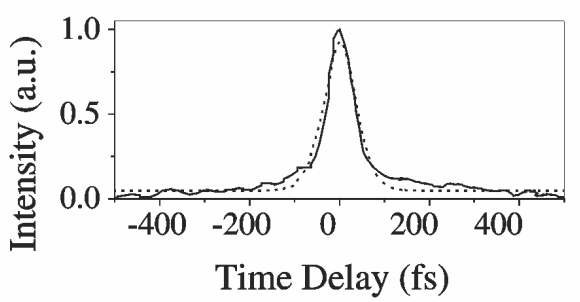

FIG. 1. Autocorrelation of the initial laser pulse (solid line). Fit by the autocorrelation function of a sech^2 profile with 50 fs duration.

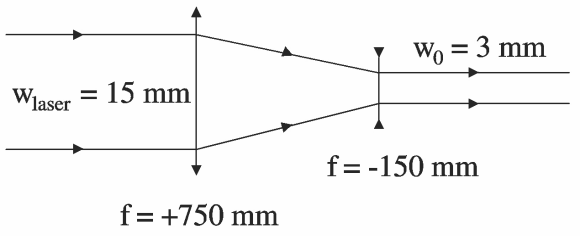

FIG. 2. Inverted telescope.

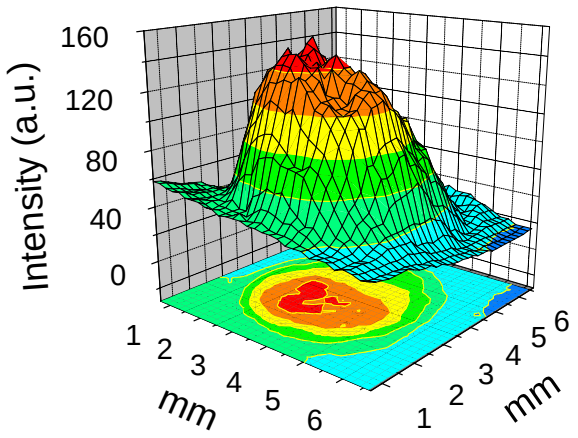

FIG. 3. Initial laser beam profile.

Beam intensity profiles have been recorded using a simple imaging technique. A thick glass plate (BK7) is placed on the beam propagation axis at 45° angle. A weak reflection is obtained, which is imaged with a high aperture ($f/5$) lens onto a linear CCD camera. All spatial measurements concern beam structures detected out of the region of the nonlinear focus. The intensities there were always below 10^{13} W/cm^2 leaving the plate surface, i.e., the entrance window of the glass plate, undamaged. Thus the reflected beam was not distorted. Filamentation with concomitant plasma channel formation was verified by measuring the electric conductance of air as a function of the propagation distance. To detect the presence of a conducting channel, we measured the change in resistivity of air between two electrodes after passage of the filament. All details relative to this electric technique can be found in Ref. [32]. The electron detector was calibrated by means of an optical diffractometry technique described in Ref. [33]. The far field image of a probe beam, modified after the passage through the filament is recorded at different delays. The diffraction patterns obtained in this way are sensitive to the accumulated phase shift, fixing thereby the electron plasma density. This yields a peak electron density, in the filament, slightly above 10^{16} electrons cm^{-3}. The threshold sensitivity of the electric conductivity technique corresponds to electron densities around $\rho_{\rm th} \sim 10^{15}$ cm^{-3}, represented below by the dotted line in Fig. 7. Spectral measurements were performed taking a weak reflection of the laser beam using the pick-up BK7 glass plate as described above. The reflected beam is directed in a $f = 25$ cm spectrometer equipped with a 600 grooves/mm diffraction grating and a linear 16-bit CCD camera as detector. Spectra were recorded as a function of the propagation distance for different input pulse energies. Autocorrelation traces inside the filament could not be recorded because of shot to shot intensity fluctuations.

B. Numerical scheme

Numerical simulations are carried out for comparison with these experiments. We employ the three-dimensional code PULP constrained to the axial symmetry, whose basic scheme was detailed in [12]. (i) This consisted in an alternating-direction implicit method on a two-dimensional grid (coordinates r and t) with steps number and size suited to the beam size and pulse duration. The code PULP can also use other numerical schemes to solve Eq. (6): (ii) a Crank-Nicholson method applied to each time slice that are not explicitly coupled, when GVD is not taken into account; (iii) a Fourier spectral decomposition in the time direction and a Crank-Nicholson scheme for the spatial part (z, r coordinates) applied to each spectral component, allowing us to take into account all the effects of the model coupling space (r) and time (t); (iv) a pseudo-spectral method using Chebishev collocation points in the transverse and time directions, avoiding the use of periodic boundary conditions or absorbing boundary layers at the edges of the numerical box. In the latter method, a mapping between physical space and computational space must be tuned very carefully in order to obtain a good accuracy. Evolution of the electron density is computed for each position r, z by a variable step Runge-Kutta method where only the steps coinciding with the grid points used to integrate Eq. (6) are retained in the coupling. All methods cannot be used for every set of physical parameters because the resolution required to solve Eqs. (5) and (6), in particular at high pulse energy, cannot be achieved by the three methods simultaneously. However, we have checked that the three methods converge to the same results for problems which can be solved by all of them on our computers. Most of the results in the present paper have been obtained with the numerical method (iii). Some of them have been verified with method (i).

C. General propagation scenario

We have simulated the evolution of a focused Gaussian beam given by Eq. (8) with $f = 2$ m for three different input energies $E_{\rm in} = 1$ mJ, 2.5 mJ, 5 mJ. In Fig. 4, we show the radius of the beam, defined as the width at half-maximum of the fluence $F(r,z) = \int |\mathcal{E}|^2 dt$, the peak electron density and the intensity as a function of the propagation distance. The general scenario predicted numerically for the propagation of fs pulses consists of three distinct stages: (i) a self-focusing stage during which the pulse shrinks in the transverse diffraction plane. (ii) an ionization stage that promotes the formation and the propagation of a filament over several Rayleigh lengths. Its diameter is about 100 μm. (iii) a diffraction stage. The threshold for the formation of the filament is predicted to be around 2.5 mJ and the length over which the filament propagates increases with the energy of the input beam. The curves in Fig. 4 show that when the input energy exceeds a certain threshold around 2.5 mJ, we retrieve the self-focusing stage, followed by an ionization front that remains clamped with the pulse at intensities smaller than 10^{14} W/cm^2 [Fig. 4(a)] and electron densities, mainly given by oxygen ionization, exceeding 10^{16} cm^{-3} [Fig. 4(b)]. The electron density clamped below 10^{15} cm^{-3} [bold line in Fig. 4(b)] is obtained from nitrogen ionization for the largest energy (5 mJ) and could be neglected in front of oxygen ionization, as expected. This enables light channeling over more than ten Rayleigh lengths for the highest energy [Fig. 4(c)]. Thus, for powers $P_{\rm in} < 25 P_{\rm cr}$ and narrow waists, the beam self-focuses, creates an electron plasma and then forms a self-guided light channel over more than one meter. The energy captured in this channel varies between 5% and 10% of the input energy [Fig. 4(d)]. The propagation length of the filament increases with the energy of the input beam. The propagation range, $0 \leq z \leq z_c \sim 1.4$ m for $E_{\rm in} = 5$ mJ, covering the early self-focusing stage is about that attained by a collapsing beam in a purely Kerr medium with an instantaneous response (effective critical power: $P_{\rm cr}^{\rm eff} = 2P_{\rm cr}$), and it can readily be determined by

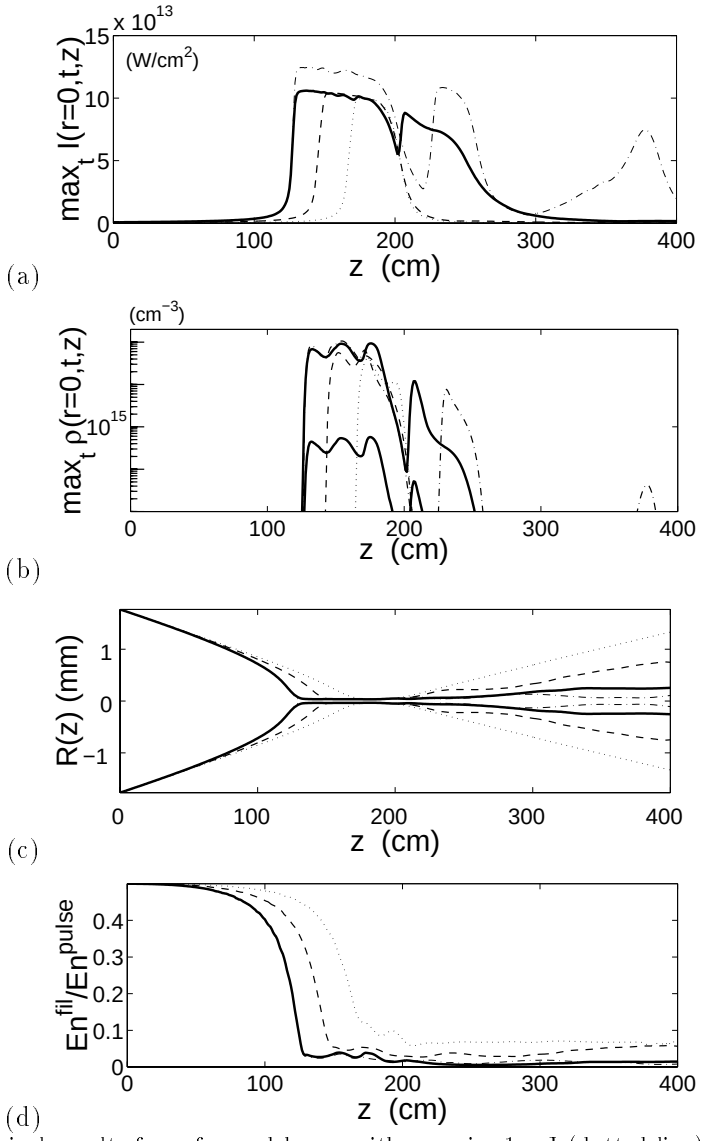

FIG. 4. Numerical results for a focused beam with energies 1 mJ (dotted line), 2.5 mJ (dashed line) and 5 mJ (solid line) for the two-specy model and for the single-specy model at 5 mJ (dash-dotted line). (a) Peak intensity on axis $r = 0$ as a function of the propagation distance z. (b) Electron density as a function of the propagation distance. The bold curve at level $\sim 10^{14}$ cm^{-3} corresponds to the electron density due to nitrogen ionization by a 5 mJ pulse. Electrons produced by oxygen ionization dominates in the total electron density. (c) Mean radius $R(z)$. (d) Energy fraction in the filament with radius plotted in (a).

employing Marburger's formula [17]: $z_c = z_0/(\chi_M + z_0/f)$ with $\chi_M = (0.367)^{-1}[(\sqrt{P_{\rm in}/P_{\rm cr}^{\rm eff}} - 0.852)^2 - 0.0219]^{1/2}$.

All simulations have been done with a two-specy model. For comparison with earlier simulations [15], Figs. 4(a,b,c) show in dash-dotted line the mean radius, electron density and peak intensity obtained with a one-specy model and a mean ionization potential of 14.6 eV for an input beam with 5 mJ energy. The global propagation scenario and the order of magnitude of the radius and length of the filament, electron density and peak intensity are comparable in both simulations performed at 5 mJ. The result might seem surprising since the mean ionization potential of 14.6 eV in the single-specy model is closer to the nitrogen potential than to the oxygen potential, whereas the latter is the prevailing ionized specy when the two-specy model is used. In fact, when the wave intensity is much larger than the intensity threshold above which ionization is triggered, saturation of the self-focusing effect by the defocusing plasma generated by MPI prevails to determine the maximum density level. This level depends only slightly on the ionization potential. This is confirmed by a rough evaluation as $\rho_{\rm max}/2\rho_c \sim n_2 I$ with $\rho_{\rm max} \sim \sigma_K I^K \rho_{at} \Delta T$. For a mean ionization potential of 14.6 eV and $\Delta T = 50$ fs, we find $\rho_{\rm max} \simeq 8.4 \times 10^{16}$ cm^{-3} with $I_{\rm max} \simeq 7.3 \times 10^{13}$ W/cm^2. For oxygen with $\rho_{\rm O} = 0.2\rho_{\rm at}$, we find $\rho_{\rm max} \simeq 6.3 \times 10^{16}$ cm^{-3} with $I_{\rm max} \simeq 5.5 \times 10^{13}$ W/cm^2. These crude evaluations are in agreement with the numerical results in Fig. 4 and are compatible with the fact that the maximum density level is determined by saturation of the Kerr effect whatever the ionization potential of the gas may be. Even if the values of σ_K as a function of the ionization potential differ from each other, the maximum density level depending on $\sigma_K I^K$ remains of comparable magnitude.

D. Filamentation instability during the self-focusing stage

The scenario obtained from numerical results is in good agreement with the experimental measurements. The self-focusing stage is, however, affected by the modulational instability

which may amplify the inhomogeneities of the input beam and break the beam into a ring in the transverse diffraction plane. Because of the revolution symmetry imposed in the simulations, rings constitute the patterns obtained under the action of the modulational instability. In experiments, the break-up of the beam into smaller fully 3D spots does not preserve the revolution symmetry and may therefore create patterns differents from rings. Fig. 5 shows the transverse beam profile obtained experimentally at different distances along propagation, for the set of three energies 1, 2.5, and 5 mJ in focused geometry ($f = 2$ m).

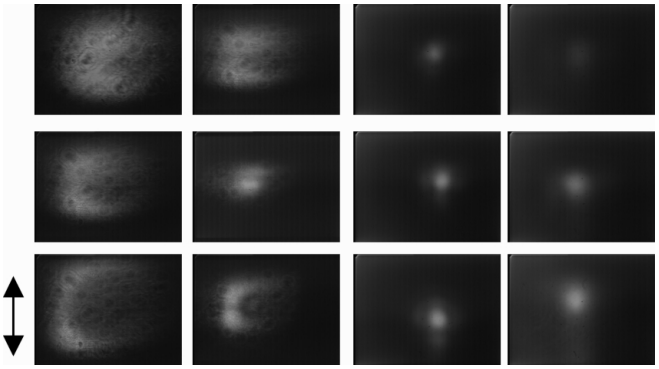

FIG. 5. Transverse beam profiles. First row: $E_{\rm in} = 1$ mJ; $z = 125$ cm; $z = 150$ cm; $z = 197$ cm; $z = 232$ cm. Second row: $E_{\rm in} = 2.5$ mJ; $z = 150$ cm; $z = 190$ cm; $z = 199$ cm; $z = 237$ cm. Third row: $E_{\rm in} = 5$ mJ; $z = 150$ cm; $z = 190$ cm; $z = 223$ cm; $z = 313$ cm. The arrow indicates the length scale of 1.2 mm.

At 1 mJ (first row), the small inhomogeneities of the input beam are not amplified during the self-focusing stage and the diffraction stage follows the linear focus of the lens. At 2.5 mJ (second row), the formation of a ring during the self-focusing stage can be seen on the first close-up ($z = 150$ cm). This ring results from the modulational instability. It finally coalesces into a short filament around the linear focus ($190 < z < 230$ cm). At 5 mJ, the ring now clearly appears ($z = 150$ cm) during the self-focusing stage and then even splits into two spots ($z = 190$ cm). This is still an effect of the modulational instability with a symmetry breaking. The two spots then coalesce into a single filament ($z > 223$ cm) able

to propagate by self-guiding over more than 10 Rayleigh lengths ($z_f \simeq 11$ cm).

Using a Gaussian input beam in the simulations, the Gaussian shape is found to be robust in the initial self-focusing stage. When holes are dipped in the fluence distribution, they always appear near the nonlinear focus, as the electron plasma density increases abruptly. They only result from the defocusing effect of the plasma. In order to get an insight on the influence of the modulational instability during the self-focusing stage, the input beam has been measured experimentally and introduced in the code after averaging the fluence distribution over the azimuthal direction to preserve the revolution symmetry. The resulting beam is rather close to a slightly perturbed third-order super-Gaussian, as defined above. Figure 6 displays the fluence distributions obtained numerically for the different input energies used in the experiments. The main result obtained from these simulations is that the general scenario is preserved, but the first self-focusing stage is now significantly affected by the modulational instability and exhibits the formation of a ring pattern well before the excitation of an electron plasma is triggered.

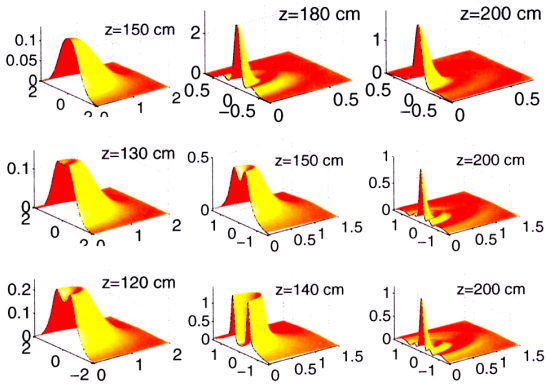

FIG. 6. Fluence distributions in J/cm^2, obtained numerically along propagation from incident beams shaped on the experimental beam. The scale lengths on the x and y-axis are in mm. First row: $E_{\text{in}} = 1$ mJ; $z = 150$ cm; $z = 180$ cm; $z = 200$ cm. Second row: $E_{\text{in}} = 2.5$ mJ; $z = 130$ cm; $z = 150$ cm; $z = 200$ cm. Third row: $E_{\text{in}} = 5$ mJ; $z = 120$ cm; $z = 140$ cm; $z = 200$ cm.

At 1 mJ, no ring appears during the self-focusing stage. The plasma defocusing occurring beyond the nonlinear focus does not even dip any hole in the fluence distribution [Fig. 6(b,c)]. At 2.5 mJ in contrast, inhomogeneities of the input beam are amplified during the self-focusing stage and clearly create a ring ($z > 120$ cm) due to the modulational instability, since the plasma density is not significant till $z \sim 150$ cm. This tendency is even more enhanced at 5 mJ where a deeper ring structure appears during the self-focusing stage [Fig. 6(h)] and finally coalesces into a single filament [Fig. 6(i)]. As the beam refocuses at center, the density increases and the second stage starts. By mutual coupling with the electron plasma, the filament is able to propagate over several Rayleigh lengths before ultimately diffracting. The rings obtained in the numerical simulations display a good agreement with the patterns observed in the experimentally-measured beam profiles, except for the location of the nonlinear focus along the propagation axis.

Measurements of the transverse beam waist and electron density are reported in figure 7 for a 5 mJ input beam and display good agreement with the numerics (solid line). The threshold for the formation of a filament is around 2.5 mJ. The nonlinear focus, i.e., the distance at which the filament is created is larger in the experiments than in the numerics, and slightly larger with the measured input beam than with a Gaussian beam. The symmetry breaking associated with the spot formation is responsible for these differences. Because of these spots, the diameter of the filament is slightly larger than that obtained in the simulation. The width at half maximum of the fluence distribution is indeed smaller for a ring distribution than for a two-spots pattern with the same energy, for which this width includes the distance between the spots. The order of magnitude of 100 μm still holds. The peak intensity reaches 10^{14} W/cm^2 beyond the nonlinear focus. Averaging over a 1 mm radius, however, the mean intensity does not exceed 3×10^{12} W/cm^2. Even if the beam self-focusing leads to a narrower filament in the simulations than in the experiments, the peak intensity attaining 10^{14} W/cm^2 is reached only locally along the propagation axis. As

shown in Fig. 7(c), the computed mean intensity remains below the damage threshold of the glass used in our imaging technique.

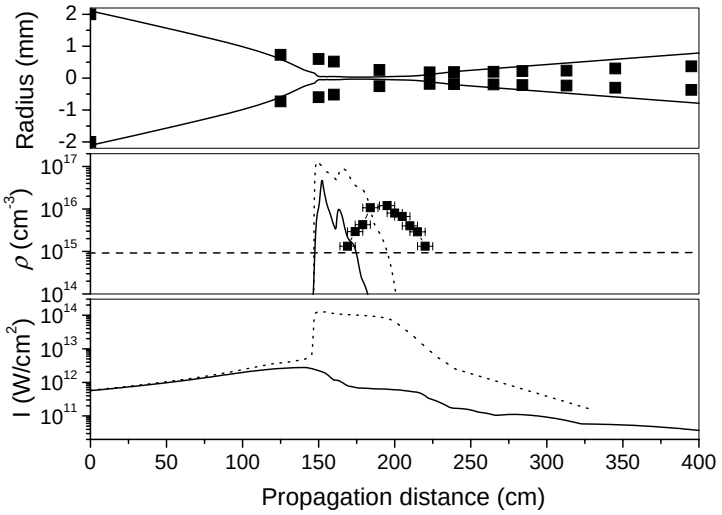

FIG. 7. Experimental (squares) and numerical results (lines) for a focused beam with energies 5 mJ. (a) Mean radius $R(z)$. (b) peak (dashed line) and averaged (solid line) electron density and (c) peak (dashed line) and averaged (solid line) intensity as a function of the propagation distance.

E. Pulse power spectra and temporal profiles

The cubic nonlinear term in Eq. (6) is responsible for the Kerr effect, i.e., the spatial compression of the beam in the transverse diffraction plane. This term also induces self-phase modulation in the spectral domain, the effect of which on the temporal profiles is the counterpart of the Kerr effect on the beam profiles. In order to test the importance of self-phase modulation, we have recorded beam power spectra step by step along the propagation axis at different energies from 1 to 5 mJ. Fig 8(a) shows the beam power spectra at $z = 225$ cm for the set of three energies 1, 2.5 and 5 mJ. A spectral broadening is visible at high energy while the spectrum at 1 mJ is close to that measured for the input beam. These spectra seem to indicate that broadening occurs above the threshold for creating a filament.

At 5 mJ, i.e., when the input beam energy is increased above this threshold, the redshifted component does not significantly change.

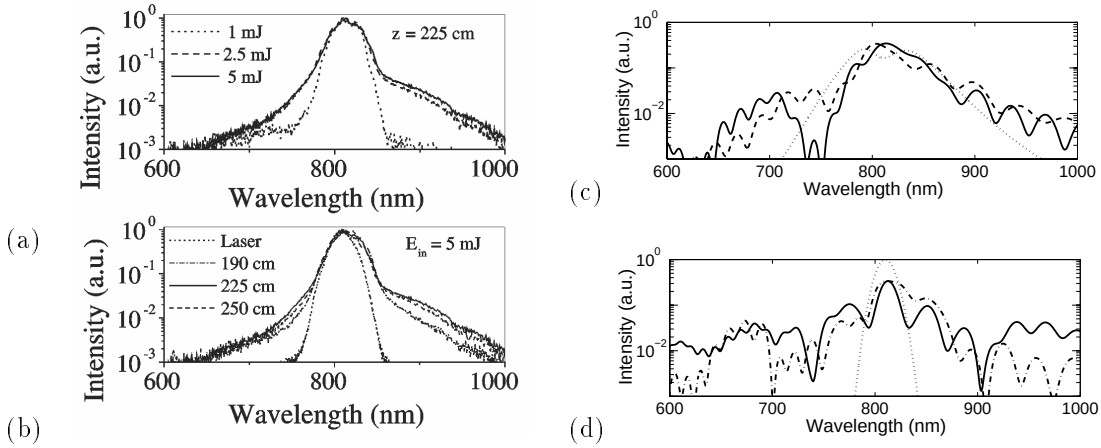

FIG. 8. (a) Pulse power spectra (integrated over 500 shots) measured at $z = 225$ cm, for a focused beam with energies 1 mJ (dotted line), 2.5 mJ (dashed line) and 5 mJ (solid line). (b) Pulse power spectra for $E_{\rm in} = 5$ mJ recorded at different propagation distances: $z = 0$ (dotted line), $z = 190$ cm (dash-dotted line), $z = 225$ cm (solid line) and $z = 250$ cm (dashed line). Their numerical counterparts are shown in (c) at $z = 170$ cm for the same energies as in (a) and in (d) at 5 mJ for the same distances as in (b).

Fig. 8(b) shows spectra recorded at different propagation distances for an input beam with 5 mJ energy. The largest spectral broadening is measured at $z = 225$ cm. Far beyond the linear focus, the blueshifted and redshifted pedestals of the spectra no longer evolve. The spectra obtained numerically at the propagation distance $z = 170$ cm, i.e., roughly 25 cm beyond the nonlinear focus, are reported in Fig. 8(c) for the same energies as in Fig. 8(a). Although the spectral broadening is larger than that measured experimentally, the spectra exhibit similar evolution as a function of the pulse energy: at 2.5 and 5 mJ, they only show small differences. Fig. 8(d) shows the numerical spectra at the same distances as in Fig. 8(b) for a 5 mJ pulse. Again the broadening is larger than that obtained experimentally. Another difference concerns the evolution of the blueshifted and redshifted pedestals still occurring at large distances.

Spectral broadening indicate that the temporal profiles in the numerical simulations are likely to contain short spiky structures. Figure 9 indeed shows the pulse temporal profiles for an input energy of 5 mJ and different propagation distances. During the self focusing stage, the pulse temporal profile evolves as a single hump [Fig. 9(a)]. When the electron plasma is excited, it defocuses the trailing part of the pulse (where the plasma density attains a ionization degree of a few percent) and a spiky structure is created in the leading part of the temporal profile [Fig. 9(b)]. This spike may keep exciting a sufficiently high plasma density that prevents a second hump from refocusing at the back of the pulse. At high energy however, from the ever present self-focusing effect acting on the transverse slices with power exceeding $P_{\rm cr}$, a second spike that overcomes plasma defocusing emerges along propagation of the filament [Fig. 9(c,d)].

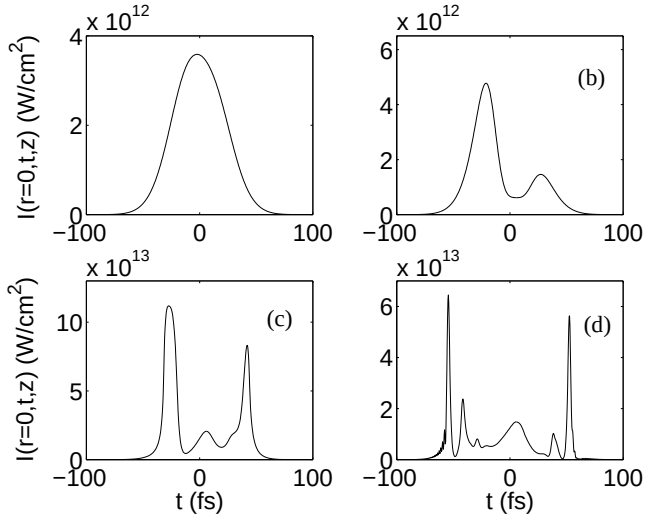

FIG. 9. Pulse temporal profiles from numerical simulations with a 5 mJ input beam. (a) $z = 120$ cm, (b) $z = 140$ cm, (c) $z = 160$ cm, (d) $z = 200$ cm.

These spiky structures thus explains the spectral broadening, while the modulations in the spectra are due to interferences between differents peaks in the temporal profile. In the experiments, the dynamical equilibrium between Kerr self-focusing and MPI is likely

to prevail in the early formation of the light channel only. The resulting filament propagates, but neither the electron density is excited above the detection threshold, nor the blueshifted pedestal in the spectra evolves. In fact, the equilibrium between Kerr effect and MPI in this range creates fine structures restored by the numerics which show their interaction during several Rayleigh lengths. These are, however, inaccessible through experimental measurements. Although the blueshifted and redshifted parts of the experimentally measured spectra are one decade below that obtained by numerical simulations [Figs. 8(b,d)], we have observed that these differences were reduced by averaging the numerical results over the radius of the optical fiber of the spectrometer (1 mm). Thus, numerical simulations may overemphasize the formation of short spiky structures, for which the envelope approximation may break down. On the other hand, the absence of fringes in the measured spectra is probably due to the same shot to shot fluctuations which previously prevented precise measurement of autocorrelation traces.

F. Self-guided propagation of collimated beams

In order to test the genericity of the scenario obtained numerically and experimentally for the formation of a filament, we have suppressed the focusing geometry introduced by the lens. The theoretical nonlinear focus is proportional to the Rayleigh length (35 m with a 3 mm beam waist in collimated geometry) and is equal to $z_c = 4.8$ m for an input beam with $25P_{cr}$. As will be shown below, the experimental nonlinear focus is larger and the total propagation distance is increased well beyond our experimental room (9 m). Thus, only the early filamentation and self-focusing stage has been observable in this geometry. The transverse intensity patterns for input energies varying from 1 mJ to 5 mJ are presented in Fig. 10. At 1 mJ (top row), the input beam self focuses into a short light channel which propagates over more than 2 meters and finally spreads out. At 2.5 mJ, the beam forms a ring pattern ($z = 2.5$ m) during the self-focusing stage. Two spots are then formed ($z = 4.5$

m) from the break-up of this ring before recoalescence ($z = 6.5$ m) into a single light channel and final dispersion at $z = 8.5$ m. With a 5 mJ input beam, the ring ($z = 2.5$ m) and the two spots (4.5 m $< z <$ 6.5 m) are now clearly apparent. A mutual interaction between the two spots occurs over more than two meters. During this stage, each spot seems to self-focus at its own centre. This process delays their fusion into a single filament, which appears at $z = 8.5$ m only, and is likely to increase the total propagation distance beyond the wall of the experimental room.

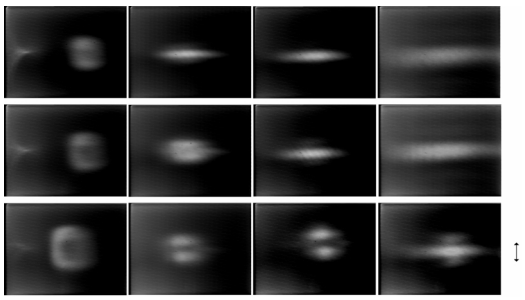

FIG. 10. Propagation patterns of 50 fs unfocused beams in air at different propagation distances $z = 2.5$ m, 4.5 m, 6.5 m and 8.5 m. Top row: $E_{\rm in} = 1$ mJ; middle row: $E_{\rm in} = 2.5$ mJ; bottom row: $E_{\rm in} = 5$ mJ. The arrow indicates the length scale of 2 mm.

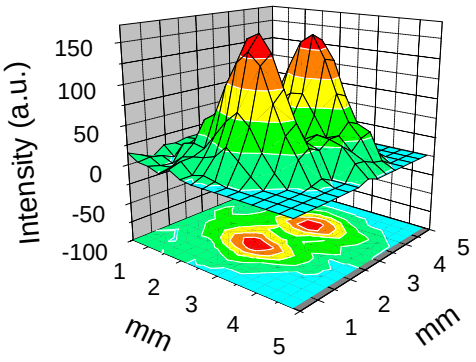

FIG. 11. Three-dimensional plot of the intensity distribution at $z = 4.5$ m for an initially collimated beam with 5 mJ energy.

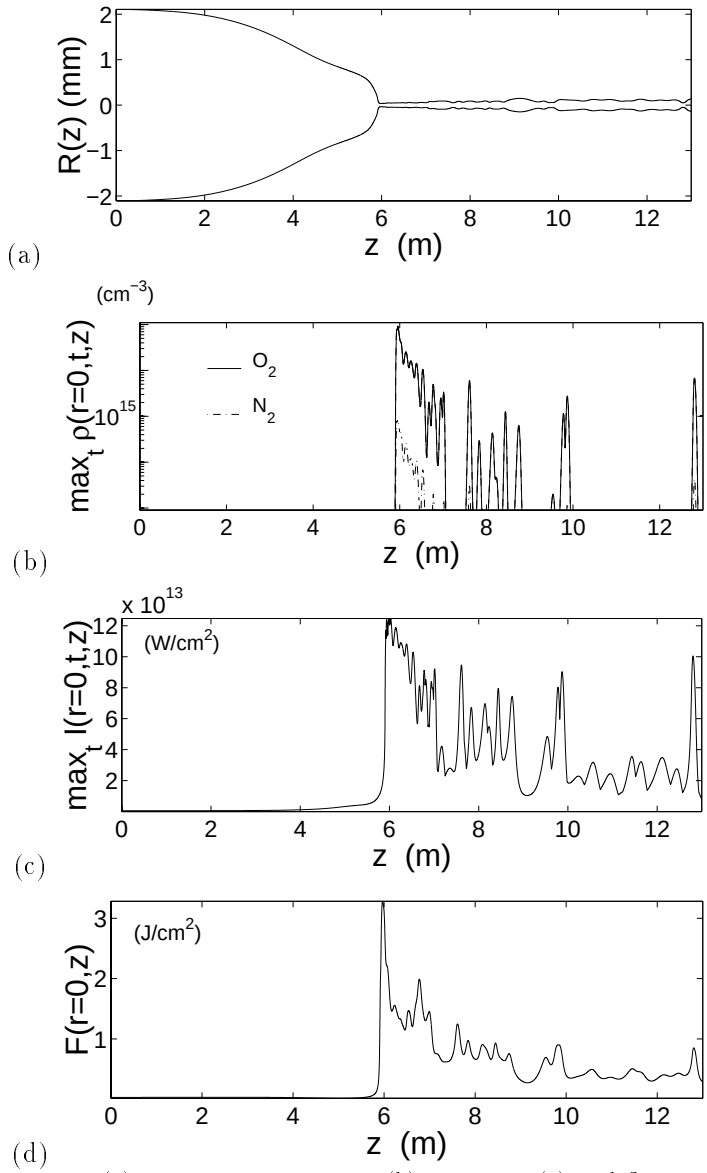

FIG. 12. Mean radius (a) peak electron density (b), intensity (c) and fluence (d) as a function of the propagation distance for a collimated input beam with 5 mJ energy

Figure 11 shows the beam intensity measured experimentally at $z = 4.5$ m and clearly exhibits the two spots resulting from modulational instability. Numerical simulations showing the propagation of a collimated input beam modeled around the experimental laser beam with 5mJ energy, are reported in Figs. 12 and 13. Fig. 12 shows that the general scenario

observed in focusing geometry is preserved. In self-focusing regime, the modulational instability forms a ring pattern which exists over 3 m, while the intensity stays below the threshold for exciting an electron plasma. A single filament reforms at $z \sim 6$ m from the coalescence of the ring pattern on its center. Figs. 12(b) and (c) give a detailed picture of the dynamical equilibrium between self-focusing and MPI which occurs during the propagation of the output filament. The intensity reaches locally 10^{14} W/cm^2 as the electron density attains 10^{16} cm^{-3}. In the main part of the propagation range, however, the plasma remains below 10^{15} cm^{-3}.

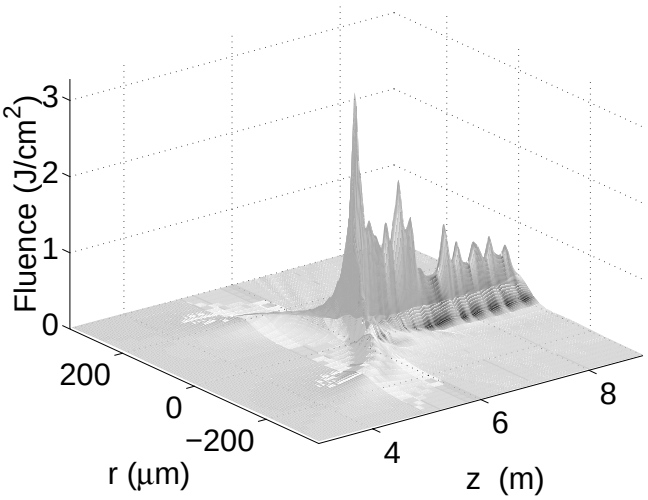

FIG. 13. Fluence distribution $F(r, z)$ for a collimated input beam with 5 mJ energy

Fig. 13 clearly shows the coalescence process and the subsequent propagation of the filament clamped with the electron plasma over several meters. Comparison of these results with experimental measurements show that the experimental nonlinear focus lays beyond the numerical one. Again, we emphasize that the revolution symmetry in our code allows us to find a ring pattern only, whereas the experiments display two well separated spots during the self-focusing stage. In spite of these discrepancies, the general trends in the filament

formation (accessible experimentally) are, however, qualitatively well restored.

IV. ANALYTICAL ESTIMATES FOR THE EARLY FILAMENTATION STAGE

This section is devoted to analyze the mechanisms of break-up and fusion of the spots created by modulational instability. For technical convenience, we derive analytical estimates from a simplified nonlinear Schrödinger model. At leading order, we consider Eq. (6), in which the electron density is frozen in time and acts as a global saturating nonlinearity. Although strong temporal distortions are expected to arise from MPI at high density levels, i.e., after the focus point z_c [10–12,16], such an approximation holds in the early range $z < z_c$, where the nonlinearities mainly originate from the Kerr term. This assumption has been verified numerically: as shown in the previous section (Fig. 9), the pulse temporal profiles do not significantly vary in the propagation domain preceding the emergence of the ionization front. The electron density in this domain is thus approached by $\rho = \Delta T \sigma \rho_{\rm at} |\mathcal{E}|^{2K}$. Accordingly, as the delayed component in the Kerr response is only relevant in a narrow time window, we simply omit it. This amounts to considering an effective critical power for self-focusing being twice $P_{\rm cr}$. We also ignore GVD, space-time focusing, self steepening and MPA contributions, which never significantly affect the beam dynamics in this range [12]. Therefore, we deal with the nonlinear Schrödinger (NLS) equation

$$2ik_0 \frac{\partial \mathcal{E}}{\partial z} + \Delta_\perp \mathcal{E} + k_0^2 (n_2 |\mathcal{E}|^2 - n_{2K} |\mathcal{E}|^{2K}) \mathcal{E} = 0, \tag{9}$$

with $n_{2K} \simeq 1.3 \times 10^{-143}$ cm^{2K}/W^K and $K = 10$ in the framework of the single-specy model. In the sequel the analysis is divided into two parts. First, in the framework of Eq. (9), we study the development of perturbations affecting the beam shape, by performing a modulational instability theory similar to that originally derived by Bespalov and Talanov in the sixties [38] (see also [17] for a review). Second, we characterize the process of nonlinear coalescence allowing for the recombination of the beam from filamentary structures.

A. Modulational instability in Kerr regime

Let us first look for a perturbed solution of Eq. (9) in the form $\mathcal{E} = \mathcal{E}_0 + \delta\mathcal{E}$. We assume that $\mathcal{E}_0$ can be approximated by a plane-wave background with uniform averaged intensity $I_0 = |\mathcal{E}_0|^2$ and the perturbation $\delta\mathcal{E}$ behaves as $\delta\mathcal{E} \sim \mathrm{e}^{\gamma z + i\mathbf{k}_\perp \cdot \mathbf{r}}$ with growth rate γ and transverse wavenumber $k_\perp$. Following Bespalov-Talanov procedure, this growth rate provides the transverse spacing between filaments, $\Lambda_\perp$, and their growth length, $\Lambda_z \sim \gamma_{\max}^{-1}$, which are respectively given by

$$\Lambda_\perp = [\frac{2\pi P_{\mathrm{cr}}}{I_0(1-\alpha I_0^{K-1})}]^{1/2},\ \Lambda_z = \frac{\Lambda_\perp^2}{\pi^2 \lambda_0}, \tag{10}$$

where $\alpha \equiv K n_{2K}/n_2$. From these quantities, we infer that MPI efficiently counteracts the modulational instability for $I_0 \geq \alpha^{1/(1-K)} \sim 5 \times 10^{13}$ W/cm^2. So, at moderate intensity levels $I_0 \leq 10^{13}$ W/cm^2, the plasma response is negligible and the dynamics is essentially driven by the Kerr response of the medium. To apply Eq. (10) to the experimental beams, we first define an averaged surface $S \simeq \pi w_0^2/2$ along which the laser intensity is distributed. With a pulse time duration $\Delta T \simeq 50$ fs that remains unchanged during the early propagation stage, we estimate the averaged intensity in the input beam having the energy $E_{\mathrm{in}} = 5$ mJ as $I_0 \simeq 0.7 - 1 \times 10^{12}$ W/cm^2. From the above modulation lengths, we then find that filaments form over distances $\Lambda_z \geq 1.2$ m with a transverse size $\Lambda_\perp \simeq 1.8$ mm. These estimates are compatible with the filament growth length and spot sizes revealed in Fig. 14. The first filamentation mode is an annular ring, promoted by almost isotropic perturbations. As this ring has a typical dimension exceeding $2\Lambda_\perp$ and is still modulationally unstable, two cells emerge from it, in agreement with the patterns previously shown.

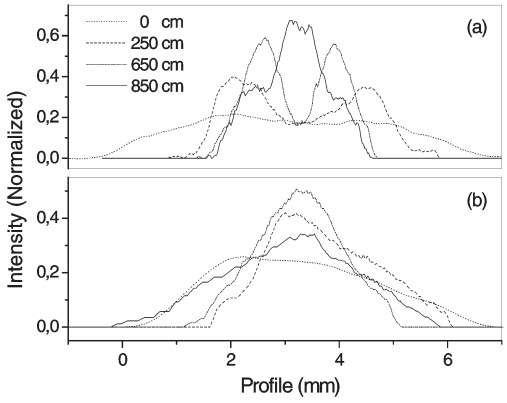

FIG. 14. Intensity profiles of the filaments along the y-axis (a), along the x-axis (b) and for a collimated input beam with $E_{\rm in} = 5$ mJ. Dotted line: $z = 0$ cm; dashed line: $z = 250$ cm; Dash-dotted line: $z = 650$ cm; solid line: $z = 850$ cm.

We can then compute the increase in the mean intensity of the beam along the early propagation. From Fig. 14, we repeat the previous arguments: we estimate the horizontal and vertical scale lengths w_x, w_y of the beam patterns, yielding the average surface $\langle S \rangle \simeq \pi w_x w_y/2$, and straightforwardly calculate the corresponding beam intensity. Knowing that energy losses are small in the Kerr stage, each spot contains an energy close to $E_{\rm spot} \simeq 2.5$ mJ, while the preceding ring pattern and the central lobe following the merging of spots are assumed to contain the energy $E_{\rm in} \simeq 5$ mJ. For a collimated beam, the averaged intensity in the ring is then found to approach the value $I_0^{\rm ring} \simeq 2.7 \times 10^{12}$ W/cm^2 at $z = 2.5$ m. At later $z = 6.5$ m, the mean intensity in each spot reaches $I_0^{\rm spot} \simeq 3 \times 10^{12}$ W/cm^2. These two spots finally coalesce at $z = 8.5$ m, where the total intensity does not exceed $I_0 \simeq 5 \times 10^{12}$ W/cm^2. The wave intensity has thus increased by less than one decade. Because I_0 always remains below 10^{13} W/cm^2, MPI is of negligible influence. As recalled previously, no significant emission of electrons above $\rho_{\rm th}$ was detected with collimated beams, at least along distances accessible experimentally, i.e., for $z < 10$ m.

For comparison, we here mention some intensity estimations found for a focused beam

with $f = 2$ m. Applying the same procedure, we obtain $I_0^{\rm ring} \simeq 8 \times 10^{12}$ W/cm^2 at $z = 150$ m, $I_0^{\rm spot} \simeq 10^{13}$ W/cm^2 in each spot at $z = 190$ cm, and the mean total intensity reaches 7×10^{13} W/cm^2 at $z = 223$ cm. At this distance close to the linear focus, MPI significantly acts against self-focusing and promotes the guiding of the resultant central lobe.

In summary, the first propagation stage preceding the nonlinear focus z_c is actually driven by the Kerr response of air, which focuses the beam and breaks it up through the modulational instability. It promotes the formation of two filaments, which is well described by Eq. (11). Although each spot captures a power nearby $12.5P_{\rm cr}$ and might in theory further break up into secondary filaments containing $P_{\rm fil} \simeq \pi\Lambda_\perp^2 I_0/4 \approx \pi^2 P_{\rm cr}/2$ [12,17], only two local intensity maxima are clearly observed here.

B. Nonlinear coalescence of spots

Let us now discuss the mutual coalescence of spots, which, for simplicity, we model by two in-phase Gaussians:

$$\mathcal{E}(r,0) = \sum_{j=1,2} \sqrt{\frac{2P_j}{\pi w_j^2}} \exp\left(-\frac{(\mathbf{r} - \langle \mathbf{r}_j \rangle)^2}{w_j^2}\right), \tag{11}$$

arising at a given $z = z_0$, with waist w_j, individual power P_j and mutual separation distance $\delta = |\langle \mathbf{r_1} \rangle - \langle \mathbf{r_2} \rangle|$. We assume that the two spots are identical ($P_1 = P_2$), symmetrically located from the center of coordinates ($\delta = 2|\langle \mathbf{r_1} \rangle|$), and they possess equal sizes $\sim w_j$ along the (x, y) directions. On this basis, we then apply the procedure developed in [39] for describing the amalgamation of Gaussian filaments from the cubic NLS equation. The criterion conditioning the amalgamation of Gaussian filaments applies to "well separated" structures having a total transverse power,

$$P = \int |\mathcal{E}|^2 d\mathbf{r} = 2P_j(1 + {\rm e}^{-\delta^2/2w_j^2}), \tag{12}$$

close to $2P_j$, which imposes $\delta > \sqrt{2} w_j$. This preliminary condition is particularly fulfilled by the spots arising at $z_0 = 6.5$ m for 5 mJ collimated beams. Here, the spots are separated

by the distance $\delta \simeq 1.2$ mm, which indeed remains above $\sqrt{2}w_{0y} \sim 1.1$ mm.

In self-focusing regime, coalescence then results from the vanishing of the total mean-square radius of the beam defined by $\langle r^2 \rangle = \int r^2 |\mathcal{E}|^2 d\mathbf{r}/P$. This quantity satisfies

$$d_z^2 \langle r^2 \rangle = 2H/k_0^2 P, \tag{13}$$

where H denotes the total Hamiltonian

$$H = \int \{|\nabla_\perp \mathcal{E}|^2 - \frac{k_0^2 n_2}{2}|\mathcal{E}|^4 + \frac{k_0^2 n_{2K}}{K+1}|\mathcal{E}|^{2(K+1)}\} d\mathbf{r}, \tag{14}$$

which is invariant for Eq. (9). From the initial condition (11), and by considering MPI as perturbative, H can be expanded as

$$H \simeq \frac{4P_j}{w_j^2}[1 + (1 - \frac{\delta^2}{2w_j^2})\mathrm{e}^{-\frac{\delta^2}{2w_j^2}} - \frac{P_j}{2P_{\rm cr}}(1 + 3\mathrm{e}^{-\frac{\delta^2}{w_j^2}} + 4\mathrm{e}^{-\frac{3\delta^2}{4w_j^2}}) + \varepsilon\{1 + 2(K+1)\mathrm{e}^{-\frac{2K+1}{K+1}\frac{\delta^2}{2w_j^2}}\}], \tag{15}$$

where $\varepsilon = w_j^2 k_0^2 n_{2K} (2P_j/\pi w_j^2)^K/4(K+1)^2 \ll 1$ in the ranges of powers and spot waists investigated. In Eq. (15), all contributions in δ compose the interaction part of H; the others terms enter the free Hamiltonian contributions related to each individual spot, such as $H = H_{\rm free} + H_{\rm int}(\delta)$. Basically, the coalescence process follows in self-focusing regime, as the squared radius $\langle r^2 \rangle$, which also includes the separation distance between spots, tends to zero. In this regime, the Kerr nonlinearity dominates over wave diffraction and localizes the total beam. For making the spots merge to center, $H_{\rm int}$ must dominate over $H_{\rm free}$. This amounts to defining a critical distance δ_c, function of P_j, below which the two spots amalgamate at center and beyond which they freely self-focus at their own centroids. This critical distance is determined by plotting H as a function of δ and, for $P_j = 12.5 P_{\rm cr}$, it is found to be attained around $\delta_c \simeq 3w_j$. Thus, the two spots can fuse for $\delta < 3w_j$, which definitely applies to the separation distance measured in Fig. 10 at $z = 6.5$ m. It is worth noticing that, in the absence of wave collapse, the fusion is all the more delayed along z as the spots are intense, since at increasing energy they reinforce their own local attractor on

their individual centroids. This effect contributes to enlarge the Kerr stage beyond which an electron plasma can be excited, as it can be seen in Fig. 12. For a focused beam, $\langle r^2 \rangle$ vanishes faster with $f < +\infty$ (see, e.g., [12]), and the fusion dynamics is accelerated compared with that for a collimated beam.

APPENDIX A: OPTICAL FIELD IONIZATION RATES

The optical field ionization rates of singly ionized atoms and solids have been obtained by Keldysh [28], for an electromagnetic wave of frequency lower than the ionization potential. In the limiting case of low frequencies, these rates change into the probability of tunnel ionization. At high frequencies, they describe the multiphoton process in which several photons are absorbed simultaneously by an atom. For an atom with ionization potential U_0 in a linearly polarized laser field with frequency ω_0 and peak electric field F, the adiabadicity parameter

$$\gamma = \frac{\omega_0}{eF}\sqrt{2mU_0} \tag{A1}$$

is defined as the square root of the ratio of the ionization potential U_0 by the ponderomotive energy of the electron and it distinguishes whether the optical field induced ionization occurs in the tunnel regime $\gamma \ll 1$ or in the multiphoton regime $\gamma \gg 1$. Optical field ionization rates have been the subject of subsequent developments by Perelomov *et al.* [34], leading to a general formula valid for any atom or ion with quantum numbers l and m and charge state Z:

$$w(\omega_0, F) = \omega_{\text{a.u.}}\sqrt{\frac{3}{2\pi}}\,|C_{n^*,l^*}|^2 f(l,m)\frac{U_0}{U_H} \times \left(\frac{2F_0}{F\sqrt{1+\gamma^2}}\right)^{2n-|m|-3/2} A_m(\omega_0,\gamma)\exp\left(-\frac{2F_0}{3F}g(\gamma)\right) \tag{A2}$$

where $n = Z(2U_0/U_H)^{-1/2}$, U_H is the ionization potential of hydrogen, $\omega_{\text{a.u.}} = eF_0/\sqrt{2mU_H} \simeq 4.1\times10^{16}$ s^{-1} and $F_0 = e^5m^2/\hbar^4(4\pi\epsilon_0)^3 \simeq 514$ GV/m. For a given atom, the

dimensionless constant C_{n^*,l^*} is adapted from the formula known for the hydrogen atom [34] by replacing the principal n and orbital l quantum numbers by their effective counterparts $n^* = n - \delta_l$ and $l^* = l - \delta_l$, respectively, and $\delta_l = n - (2U_0)^{-1/2}$ is the quantum defect:

$$|C_{n^*,l^*}|^2 = \frac{2^{2n^*}}{n^*\Gamma(n^* + l^* + 1)\Gamma(n^* - l^*)} \tag{A3}$$

where Γ is the gamma function [40]. The constant $f(l,m)$ reads

$$f(l,m) = \frac{(2l+1)(l+|m|)!}{2^{|m|}(|m|)!(l-|m|)!}, \qquad f(0,0) = 1. \tag{A4}$$

The other functions entering formula (A2) read as

$$A_m(\omega_0,\gamma) = \frac{4}{\sqrt{3\pi}}\frac{1}{|m|!}\frac{\gamma^2}{1+\gamma^2} \times \sum_{\kappa\geq\nu}^{+\infty} \exp[-\alpha(\kappa-\nu)]\Phi_m\left(\sqrt{\beta(\kappa-\nu)}\right), \tag{A5}$$

$$\Phi_m(x) = \mathrm{e}^{-x^2}\int_0^x (x^2-y^2)^{|m|}\mathrm{e}^{y^2}dy, \tag{A6}$$

$$\beta(\gamma) = \frac{2\gamma}{\sqrt{1+\gamma^2}}, \tag{A7}$$

$$\alpha(\gamma) = 2\left[\sinh^{-1}\gamma - \frac{\gamma}{\sqrt{1+\gamma^2}}\right] = \begin{cases} 2\gamma^3/3 & \gamma \ll 1 \\ 2(\log 2\gamma - 1) & \gamma \gg 1 \end{cases} \tag{A8}$$

$$g(\gamma) = \frac{3}{2\gamma}\left[(1+\frac{1}{2\gamma^2})\sinh^{-1}\gamma - \frac{\sqrt{1+\gamma^2}}{2\gamma}\right] = \begin{cases} 1 - \dfrac{\gamma^2}{10} + \dfrac{9\gamma^4}{280} & \gamma \ll 1 \\ \dfrac{3}{2\gamma}(\log 2\gamma - \dfrac{1}{2}) & \gamma \gg 1 \end{cases} \tag{A9}$$

$$\nu = \frac{U_0}{\hbar\omega_0}\left(1 + \frac{1}{2\gamma^2}\right), \qquad \kappa_0 = \mathrm{mod}(\nu+1) \tag{A10}$$

Let us comment the tunnel and multiphoton limits separately:

Tunnel limit: the optical field induced ionization rates in the tunnel regime are obtained when $\gamma \ll 1$. In this case, $A_0(\gamma) \to 1$ and

$$w(\omega_0,F) = \omega_{\mathrm{a.u.}}\sqrt{\frac{3}{2\pi}}|C_{n^*,l^*}|^2 f(l,m)\frac{U_0}{U_H} \times \left(\frac{2F_0}{F}\right)^{2n-|m|-3/2}\exp\left(-\frac{2F_0}{3F}\right) \tag{A11}$$

In Fig. 15, the tunnel ionization rates (A11) are plotted in dashed line and coincide with the general formula (A2) when $I > 10^{15}$ W/cm^2.

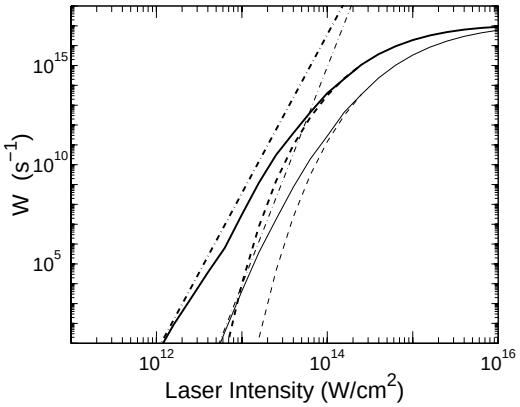

FIG. 15. Comparison of the general ionization rates (A2) (solid lines) with tunnel rates (A11) (dashed lines) and their counterpart in the multiphoton limit (A13) (dash-dotted lines), for oxygen (bold lines) and nitrogen (fine lines), as a function of the laser intensity.

Multiphoton limit: a multiphoton expression of the optical field induced ionization rates is obtained when $\gamma \gg 1$ by taking into account only the term $\kappa = \kappa_0$ in the series for $A_m(\omega_0, \gamma)$ [Eq. (A5)] and by using the relation $F_0/F\gamma = 2U_0/\hbar\omega_0$,

$$w(\omega_0, F) = \omega_{\text{a.u.}} \frac{2\sqrt{2}}{\pi} |C_{n^*,l^*}|^2 \frac{U_0}{U_H} \frac{f(l,m)}{|m|!} (4\nu_0)^{2n-|m|-3/2} \times \frac{1}{(4\gamma^2)^{\kappa_0}} \exp[2\kappa_0 - \nu_0(1 + 1/\gamma^2)] \Phi_m \left(\sqrt{2(\kappa_0 - \nu)}\right) \quad \text{(A12)}$$

where $\nu_0 = E_0/\hbar\omega_0$. When $\gamma \to +\infty$, the ionization rates become proportional to a power of the laser intensity $I \equiv F^2$:

$$w(\omega_0, F) = \sigma I^K \quad \text{(A13)}$$

with $K = \text{mod}(\nu_0 + 1)$ and

$$\sigma = \omega_{\text{a.u.}} \frac{4^{2n-|m|}}{2\pi\sqrt{2}} |C_{n^*,l^*}|^2 \frac{f(l,m)}{|m|!} \frac{U_0}{U_H} (\nu_0)^{2(n+K)-|m|-3/2} \times \exp(2K - \nu_0) \Phi_0 \left(\sqrt{2(K - \nu_0)}\right) \frac{1}{F_0^{2\kappa_0}} \quad \text{(A14)}$$

For oxygen and nitrogen with ionization potentials $U_O = 12.1$ eV and $U_N = 15.6$ eV, the coefficients σ in the multiphoton ionization rates (A13) are equal to $\sigma_O = 2.88 \times 10^{-99}$ s^{-1} cm^{16}/W^8 and $\sigma_N = 5.08 \times 10^{-144}$ s^{-1} cm^{22}/W^{11}. The MPI rates (A13) are plotted in dash-dotted line in Fig. 15 and asymptote the general formula (A2) at low intensity.

Acknowledgements: The authors thank Y.B. André and G. Mullot for technical assistance.

---

[1] F. Vidal *et al.*, "Modeling the triggering of streamers in air by ultrashort laser pulses," *IEEE Trans. Plasma Science*, **28**, 418 (2000).

[2] L. Wöste *et al.*, "Femtosecond atmospheric lamp," *Laser und Optoelectronics* **29**, 51 (1997).

[3] A. Braun, G. Korn, X. Liu, D. Du, J. Squier and G. Mourou, "Self channeling of high-peak-power femtosecond laser pulses in air," *Opt. Lett.* **20**, 73 (1995).

[4] E. T. J. Nibbering, P. F. Curley, G. Grillon, B. S. Prade, M. A. Franco, F. Salin and A. Mysyrowicz, "Conical emission from self-guided femtosecond pulses in air," *Opt. Lett.* **21**, 62 (1996).

[5] S. Henz and J. Herrmann, "Two-dimensional spatial optical solitons in bulk Kerr media stabilized by self-induced multiphoton ionization: variational approach" *Phys. Rev. E* **53**, 4092 (1996).

[6] A. Brodeur, C. Y. Chien, F. A. Ilkov, S. L. Chin, O. G. Kosareva, and V. P. Kandidov, "Moving focus in the propagation of ultrashort laser pulses in air," *Opt. Lett.* **22**, 304 (1997); O. G. Kosareva, V. P. Kandidov, A. Brodeur, C. Y. Chien, and S. L. Chin, "Conical emission from laser-plasma interactions in the filamentation of powerful ultrashort laser pulses in air," *Opt. Lett.* **22**, 1332 (1997).

[7] H. R. Lange, G. Grillon, J.-F. Ripoche, M. A. Franco, B. Lamouroux, B. S. Prade, A. Mysyrowicz, E. T. J. Nibbering and A. Chiron, "Anomalous long-range propagation of femtosecond laser pulses through air: moving focus or pulse self-guiding ?" *Opt. Lett.* **23**, 120 (1998).

[8] B. La Fontaine, F. Vidal, Z. Jiang, C. Y. Chien, D. Comtois, A. Desparois, T. W. Johnston,

J.-C. Kieffer and H. Pépin, "Filamentation of ultrashort pulse laser beams resulting from their propagation over long distances in air," *Phys. Plasmas* **6**, 1615 (1999).

[9] V. P. Kandidov, O. G. Kosareva, and S. A. Shlenov, "Influence of transient self-defocusing on the propagation of high-power femtosecond laser pulses in gases under ionization conditions," *Quant. Electron.* **24**, 905 (1994).

[10] M. Mlejnek, E. M. Wright and J. V. Moloney, "Dynamic spatial replenishment of femtosecond pulses propagating in air," *Opt. Lett.* **23**, 382 (1998).

[11] A. Chiron, B. Lamouroux, H. R. Lange, J.-F. Ripoche, M. A. Franco, B. S. Prade, G. Bonnaud, G. Riazuelo and A. Mysyrowicz, "Numerical simulations of the nonlinear propagation of femtosecond optical pulses in gases," *Eur. Phys. J. D* **6**, 383 (1999).

[12] A. Couairon and L. Bergé, "Modeling the filamentation of ultra-short pulses in ionizing media," *Phys. Plasmas* **7**, 193 (2000).

[13] L. Bergé and A. Couairon, "Nonlinear propagation of self-guided ultra-short pulses in ionized gases," *Phys. Plasmas* **7**, 210 (2000).

[14] L. Bergé and A. Couairon, "Gas-induced solitons," *Phys. Rev. Lett.* **86**, 1003 (2001).

[15] S. Tzortzakis, L. Bergé, A. Couairon, M. A. Franco, B. S. Prade and A. Mysyrowicz, "Break-up and fusion of self-guided femtosecond light pulses in air," to appear in *Phys. Rev. Lett.* (2001).

[16] M. Mlejnek, M. Kolesik, J. V. Moloney, and E. M. Wright, "Optically turbulent femtosecond light guide in air," *Phys. Rev. Lett.* **83**, 2938 (1999).

[17] J. H. Marburger, "Self-focusing: theory," *Prog. Quant. Electr.* **4**, 35 (1975).

[18] A. L. Gaeta, "Catastrophic collapse of ultrashort pulses," *Phys. Rev. Lett.*, **84**, 3582 (2000).

[19] A. A. Zozulya, S. A. Diddams, A. G. Van Engen and T. S. Clement, "Propagation dynamics of intense femtosecond pulses: Multiple splittings, coalescence, and continuum generation," *Phys. Rev. Lett.*, **82**, 1430 (1999).

[20] S. Tzortzakis, L. Sudrie, M. Franco, B. Prade, A. Mysyrowicz, A. Couairon and L. Bergé, *Phys. Rev. Lett.*, submitted (2001).

[21] S. Tzortzakis, B. Lamouroux, A. Chiron, M. A. Franco, B. S. Prade, A. Mysyrowicz and S. D. Moustaizis, "Nonlinear propagation of subpicosecond ultraviolet laser pulses in air," *Opt. Lett.* **25**, 1270 (2000).

[22] J. Schwarz, P. Rambo, J.-C. Diels, M. Kolesik, E. M. Wright and J. V. Moloney, "Ultraviolet filamentation in air", *Opt. Commun.* **180**, 383 (2000).

[23] J. Schwarz *et al.*, in Quantum Electronics and Laser Science Conference, 2000 OSA Technical Digest Series (Optical Society of America, San Francisco CA, 2000).

[24] N. Aközbek, C. M. Bowden, A. Talebpour and S. L. Chin, "Femtosecond pulse propagation in air: variational analysis," *Phys. Rev. E* **61**, 4540 (2000).

[25] J. F. Ripoche, G. Grillon, B. S. Prade, M. A. Franco, E. Nibbering, H. R. Lange and A. Mysyrowicz, "Determination of the time dependence of n_2 in air," *Opt. Commun.* **135**, 310 (1997).

[26] P. Mora and T. M. Antonsen jr, "Kinetic modeling of intense, short laser pulses propagating in tenuous plasmas," *Phys. Plasmas* **4**, 217 (1997).

[27] T. Brabec and F. Krausz, "Nonlinear optical pulse propagation in the single-cycle regime," *Phys. Rev. Lett.* **78**, 3282 (1997).

[28] L. V. Keldysh, "Ionization in the field of a strong electromagnetic wave," *ZhETF*, 47:1945, 1964. [*Sov. Phys. JETP*, 20:1307, 1965].

[29] M. V. Ammosov, N. B. Delone and V. P. Krainov, "Tunnel ionization of complex atoms and of atomic ions in an alternating electromagnetic field," *Sov. Phys. JETP*, **64** 1191 (1986).

[30] F. A. Ilkov, J. E. Decker and S. L. Chin, "Ionization of atoms in the tunneling regime with experimental evidence using Hg atoms," *J. Phys. B: At. Mol. Opt. Phys.* **25**, 4005 (1992).

[31] M. D. Feit and J. A. Fleck, "Effect of refraction on spot-size dependence of laser-induced breakdown," *Appl. Phys. Lett.* **24**, 169 (1974).

[32] S. Tzortzakis, M. A. Franco, Y. B. André, A. Chiron, B. Lamouroux, B. S. Prade and A. Mysyrowicz, "Formation of a conducting channel in air by self-guided femtosecond laser pulses," *Phys. Rev. E* **60**, R3505 (1999).

[33] S. Tzortzakis, M. A. Franco, B. S. Prade and A. Mysyrowicz, "Time evolution of the plasma

channel at the trail of a self-guided IR femtosecond laser pulse in air," *Opt. Commun.* **181**, 123 (2000).

[34] A. M. Perelomov, V. S. Popov and M. V. Terent'ev, "Ionization of atoms in an alternating electric field," *Sov. Phys. JETP*, **23**, 924 (1966). [*ZhETF*, **50** 1393–1409 (1966)].

[35] C. S. Milsted and C. D. Cantrell, "Vector effects in self-focusing," *Phys. Rev. A* **53**, 3536 (1996).

[36] J. Schjødt-Eriksen, J. V. Moloney, E. M. Wright and P. L. Christiansen, "Pulse splitting of modulationally unstable femtosecond pulse", submitted to Optics Express.

[37] S. Petit, A. Talebpour, A. Proulx and S. L. Chin, "Polarization dependence of the propagation of intense laser pulses in air," *Opt. Commun.* **175**, 323 (2000).

[38] V. I. Bespalov and V. I. Talanov, *ZhETF Pis'ma* **3**, 471 (1966) [*JETP Lett.* **3**, 307 (1966)].

[39] L. Bergé, M. R. Schmidt, J. J. Rasmussen, P. L. Christiansen, and K.Ø. Rasmussen, *J. Opt. Soc. Am. B* **14**, 2550 (1997).

[40] M. Abramowitz and I. A. Stegun, *Handbook of mathematical functions*, Dover, New York, 1972.

Chapter 3

3. Ultraviolet laser pulse filamentation in air

3.1. Introduction

Infrared femtosecond pulse filamentation was already studied to some extent at the beginning of my thesis. However very few information was available on the nonlinear propagation of ultraviolet intense short pulses. In the absence of experimental observations, even the existence of UV filaments was questioned. The much higher ionization cross sections when using ultraviolet pulses compared to infrared made people believe that the plasma generated would have such high densities that it would prohibit the formation of filaments.

The absence of experiments was mainly due to the fact that there were not so many powerful laser systems working in the ultraviolet range as compared to the usual case of IR terawatt laser systems. Even in our days such laser systems are rare. We had the opportunity to use a powerful UV laser system via access to a European large scale facility (TMR program) at the FORTH institute in Greece. Using this great installation we performed a series of experiments using powerful short pulses at 248 nm.

In this chapter we present the first detailed experimental study on the nonlinear propagation of ultraviolet laser pulses in air. Self-guiding of UV pulses is demonstrated with robust filaments propagating over several meters, putting thus an end to the questions as for the existence of UV filaments. The experimental study including beam intensity profiles, ionization measurements, pulse temporal profiles and power spectra are complemented and compared to numerical simulations. The simulations reproduce most experimental observations, allowing for a better understanding of the phenomena involved in the filamentation process. A comparison with IR filaments is also made.

The detailed analysis of all the experimental and numerical results is presented in appendixes 3.1 and 3.2.

Appendix 3.1

"Non-linear propagation of sub-picosecond UV laser pulses in air"

OPTICS LETTERS **25**, 1270 (2000)

Nonlinear propagation of subpicosecond ultraviolet laser pulses in air

S. Tzortzakis, B. Lamouroux, A. Chiron, M. Franco, B. Prade, and A. Mysyrowicz

Laboratoire d'Optique Appliquée, Centre Nationale de la Recherche Scientifique Unité Mixte de Recherche 7639, École Nationale Supérieure des Techniques Avancées–Ecole Polytechnique, Chemin de la Hunière, 91761 Palaiseau Cedex, France

S. D. Moustaizis

Foundation for Research and Technology Hellas, Institute of Electronic Structure and Laser, P.O. Box 1527, Heraklion 711 10, Greece

Received May 8, 2000

We report filamentation of subpicosecond UV laser pulses with only millijoule energy in atmosphere. The results are in good agreement with a numerical simulation using a quasi-three-dimensional propagation code.

OCIS codes: 190,5530, 350.5400.

Intense ultrashort IR pulses launched in air undergo important changes in their propagation pattern. If the peak pulse power exceeds a critical value of $P_{cr} \sim 10^{11}$ W, narrow filaments with radii of $\sim 100\ \mu$m and peak intensities reaching $\sim 10^{13}$ to 10^{14} W/cm^2 are formed. These filaments remain stable over tens of meters or more, much longer than the beam's Rayleigh distance.[1–3] This self-guiding effect has been attributed to a dynamic balance between beam self-focusing (owing to the optical Kerr effect) and beam defocusing (owing to multiphoton ionization of air molecules). A signature of filamentation is the formation of a thin plasma column in the track of the self-guided pulse, owing to multiphoton ionization of air molecules. The presence of such a weakly ionized column was recently detected by electric-conductivity measurements of air.[4–6]

In this Letter we report nonlinear propagation of intense ultrashort UV pulses in air and their evolution into filaments. With the exception of an oral presentation at a conference,[7] to our knowledge filamentation with ultrashort UV pulses has not been reported, and no details on properties of such self-guided pulses are available. We have characterized the properties of these filaments by recording the beam profile and the pulse-power spectrum as a function of propagation distance. We have also verified that an ensuing plasma column is formed in the track of the self-guided pulse over a distance of several meters. These experimental results were compared with a three-dimensional numerical simulation with realistic parameters.

We obtained a UV laser pulse by doubling the output of a femtosecond dye laser and amplifying it with an excimer laser amplifier. The laser's peak emission wavelength was at 248 nm. The laser beam had a rectangular profile of 8 mm $\times$ 26 mm and a full divergence angle of ~ 0.15 mrad. Its energy distribution was flat along the longer dimension of the rectangular area and Gaussian along the shorter dimension. The laser-pulse duration (FWHM) before propagation was measured by autocorrelation with NO molecules in a cell as a nonlinear medium.[8] The laser could operate either in the femtosecond mode (pulse duration, 450 fs; pulse energy, <10 mJ) or in the picosecond mode (5-ps pulse duration; energy per pulse of up to 15 mJ). Measurements were obtained with 450-fs-long pulses. The laser beam was directed through a circular diaphragm of radius 3.5 mm and then focused with a lens of focal distance $f = 9.5$ m. It was first verified that attenuated, low-intensity pulses propagated according to the laws of geometric optics.

At high intensities, strong modification of the beam propagation was observed. For incident pulse energy of ~ 2 mJ and pulse duration of 450 fs, the focal spot was displaced by 2.5 m toward the lens. Half of the beam energy was lost in this new focal region. Approximately 10% of the initial beam energy propagated beyond the focus in the form of a central filament, and 40% was contained in a diverging conical beam surrounding the filament. The filament extended over a distance of approximately 4 m, with a nearly constant radius of 150 μm (see Fig. 1, top).

The pulse-power spectrum was measured at different distances z along the propagation axis, by extraction of a weak part of the beam with an adjustable pinhole and recording of the spectrum in the far field. In the region before the focus, a small broadening can be observed. This spectral broadening becomes more pronounced once the filament is formed. The conical beam also shows spectral broadening, albeit less pronounced.

Filamentation with concomitant plasma-channel formation was verified by measurement of the electric conductance of air as a function of propagation distance by use of the conductivity technique described in Ref. 6. We measured air resistivity behind the femtosecond laser pulse by recording the current flowing between two plane metal electrodes with 4-mm holes bored in their centers to allow passage of the filament. A typical voltage of 2 kV was applied between the electrodes, which were separated by 1.5 cm. As shown in Fig. 1 (bottom), a connected plasma column extending over 6 m could be readily observed by use of this method. A rough estimate

0146-9592/00/171270-03$15.00/0

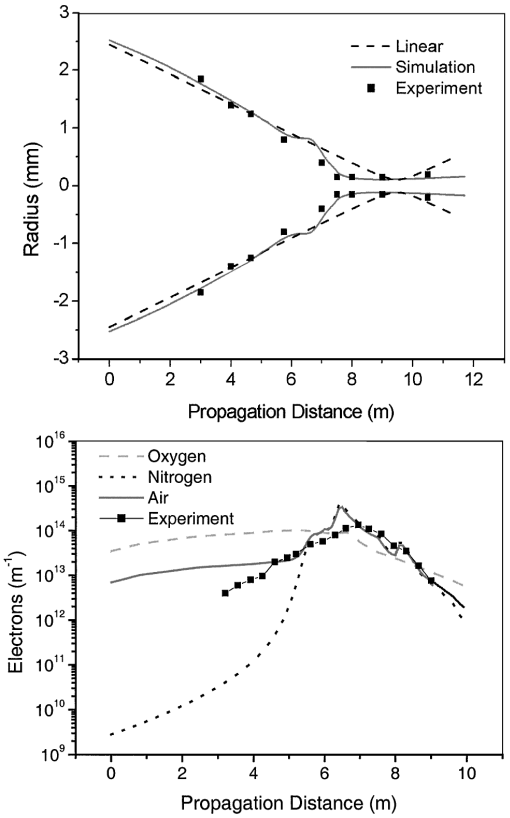

Fig. 1. Top, spatial profile of the laser beam with distance. The dashed curves correspond to beam propagation in the linear regime. Bottom, electrons per unit length measured along the propagation path, together with the numerical simulation including ionization of oxygen, nitrogen, and a gas mixture of 80% N_2 and 20% O_2.

of the filament diameter was obtained from the size of a spot burned on exposed photographic film. From the measured peak current and the filament radius of 150 μm, we extract a mean free-electron density of 10^{16} cm^{-3} in the region from 6.5 to 8.5 m (see Fig. 1, bottom).

These experimental results were compared with numerical simulations by use of a three-dimensional propagation code with axial symmetry. This code has been successfully applied to the propagation of IR femtosecond laser pulses.[9] The code treats nonlinear beam self-focusing that is due to the optical Kerr effect, beam defocusing that is due to multiphoton ionization of molecules with associated radiation losses, and normal beam diffraction. We adopted as the initial condition a super-Gaussian transverse beam profile to take into account the effect of the diaphragm. Beam convergence was simulated with a quadratic spatial phase factor. The initial time pulse profile was assumed to be of the form of a sech^2 pulse with t_0 = 450 fs. The initial power spectrum was taken as a Gaussian, approximating the measured spectrum, with a flat spectral phase. Calculations were performed with different initial pulse energies corresponding to the experimental values. The value of the instantaneous nonlinear Kerr index, $n_2 = 8 \times 10^{-19}$ cm^2/W, was obtained from Ref. 7. We did not include the retarded Kerr effect because the laser spectrum did not exhibit a significant spectral shift to lower energies in the ionization-free region before the focus. The absence of a redshift in the first spectral moment indicates that the noninstantaneous Kerr response is small and can be neglected.[10] The formation of the plasma was modeled by single ionization of oxygen and nitrogen molecules, with corresponding ionization potentials of 12 and 15.5 eV, involving simultaneous absorption of three and four UV photons, respectively. Calculated free electrons produced per unit length for pure nitrogen and oxygen and for an 80% N_2–20% O_2 gas mixture are shown in the bottom part of Fig. 1.

The simulation reproduces a large part of the experimental results surprisingly well. The calculated beam waist is plotted in Fig. 1 (top), together with the recorded beam diameters. Spatial repartition of the fluence at different locations, before and after filament initiation, is shown in Fig. 2. In the initial Kerr region, in which ionization does not significantly alter the propagation ($z < 7000$ mm), one can observe the formation of rings merging inward to the beam center. The appearance of ring patterns can be seen in the burning spots of the laser beam on UV photographic paper recorded at the same distance (see the insets of Fig. 2). Once a filament is formed, the trend is reversed, and light energy is radiated in the form of outward-traveling rings, in agreement with the observed conical emission. The code predicts ~8% of the total initial pulse energy channeled into the filamentary core.

A striking feature emerging from the simulations is the occurrence of stable situations in which the pulse in the filamentary core stays unchanged over more than 4 m for an input energy of 2 mJ. This stability is in contrast with the results for IR filaments, which in our simulations show pulse shortening and breaking.[9] In this stable region the peak intensity is ~10^{11} W/cm^2, 3 orders of magnitude less than in IR filaments. Yet ~25 times more free electrons are produced; note, however, that the corresponding free-electron density is smaller by a factor of 10, since it is distributed over a larger column.

Simulations of filamentation with IR or UV pulses reveal other basic differences between the two types of filament. For UV filaments, propagation losses that are due to multiphoton ionization are significantly higher, because the number of photons involved in one ionization step is reduced from 8–10 to 3–4. Consequently, the formation of a plasma column is more pronounced than with IR pulses. For instance, we find a tenfold increase in the measured length of a connected conducting column, compared with the case of IR pulses, for similar pulse energy.

It may be worth commenting on the large differences between UV and IR filamentation. In filamentation,

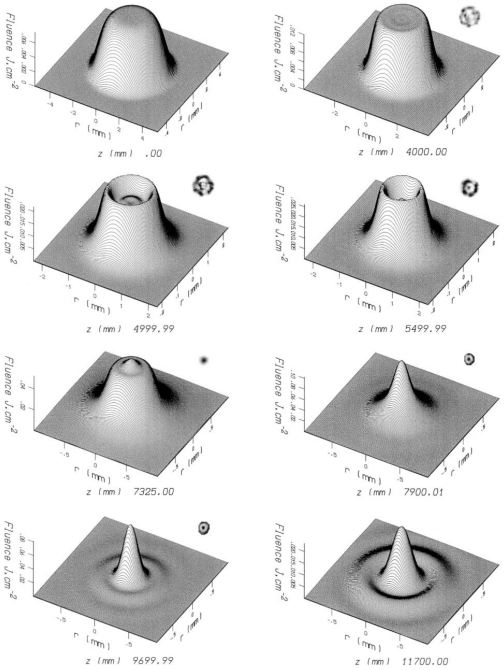

Fig. 2. Three-dimensional fluence simulated profiles for different distances. Insets, experimental burning spots of the laser on photographic paper at the same distances. The sizes of the burning spots are not to scale.

the optical Kerr effect and multiphoton absorption play crucial antagonistic roles, the first by acting as an intensity amplifier by means of beam self-focusing and the second by acting as an intensity limiter. If it is allowed to proceed sufficiently, beam self-focusing is accompanied by pulse shortening[11,12] and eventually pulse breakup.[13] Therefore the complexity of the situation depends sensitively on the value of the multiphoton cross section. With UV pulses, in which the ionization cross section is much higher, since it requires 3–4 photons instead of 8–10, beam self-focusing is hindered much earlier. The resulting situation is much simpler and closer to a true dynamic equilibrium.

We acknowledge the assistance of A. Egklezis, D. Anglos, G. Zacharakis, and C. Fotakis. This study was made possible through access to the Foundation for Research and Technology Hellas Institute provided by the European Training and Mobility of Researchers program "Access to Large Facilities." A. Mysyrowicz's e-mail address is mysy@enstay.ensta.fr.

References

1. A. Braun, G. Korn, X. Liu, D. Du, J. Squier, and G. Mourou, Opt. Lett. **20,** 73 (1995).
2. E. T. J. Nibbering, P. F. Curley, G. Grillon, B. S. Prade, M. A. Franco, F. Salin, and A. Mysyrowicz, Opt. Lett. **21,** 62 (1996).
3. A. Brodeur, C. Y. Chien, F. A. Ilkov, S. L. Chin, O. G. Kosareva, and V. P. Kandidov, Opt. Lett. **22,** 304 (1997).
4. H. Schillinger and R. Sauerbrey, Appl. Phys. B **68,** 753 (1999).
5. B. La Fontaine, F. Vidal, Z. Jiang, C. Y. Chien, D. Comtois, A. Desparois, T. W. Johnston, J.-C. Kieffer, H. Pépin, and H. P. Mercure, Phys. Plasmas **6,** 1615 (1999).
6. S. Tzortzakis, M. A. Franco, Y.-B. André, A. Chiron, B. Lamouroux, B. S. Prade, and A. Mysyrowicz, Phys. Rev. E **60,** R3505 (1999).
7. X. M. Zhao, P. Rambo, and J.-C. Diels, in *Quantum Electronics and Laser Science Conference,* Vol. 16 of 1995 OSA Technical Digest Series (Optical Society of America, Washington, D.C., 1995), p. 178.
8. S. Szatmari and F. P. Schäfer, Opt. Commun. **68,** 196 (1988).
9. A. Chiron, B. Lamouroux, R. Lange, J.-F. Ripoche, M. Franco, B. Prade, G. Bonnaud, G. Riazuelo, and A. Mysyrowicz, Eur. Phys. J. D **6,** 383 (1999).
10. J.-F. Ripoche, G. Grillon, B. Prade, M. Franco, E. T. J. Nibbering, R. Lange, and A. Mysyrowicz, Opt. Commun. **135,** 310 (1997).
11. R. Lange, J.-F. Ripoche, A. Chiron, B. Lamouroux, M. Franco, B. Prade, E. T. J. Nibbering, and A. Mysyrowicz, in *Proceedings of the XI International Conference on Ultrafast Phenomena, 1998* (Springer-Verlag, Berlin, 1998), p. 115.
12. I. G. Koprinkov, A. Suda, P. Wang, and K. Midorikawa, Phys. Rev. Lett. **84,** 3847 (2000).
13. J. K. Ranka, R. W. Schirmer, and A. L. Gaeta, Phys. Rev. Lett. **77,** 3783 (1996).

Appendix 3.2

"Femtosecond and picosecond ultraviolet laser filaments in air: experiments and simulations"

To appear in

OPTICS COMMUNICATIONS (2001)

Femtosecond and picosecond ultraviolet laser filaments in air: experiments and simulations

S. Tzortzakis[1*], B. Lamouroux[1], A. Chiron[1], S. D. Moustaizis[2], D. Anglos[2], M. Franco[1], B. Prade[1], and A. Mysyrowicz[1]

[1]*Laboratoire d'Optique Appliquée, CNRS UMR 7639, ENSTA – Ecole Polytechnique, Chemin de la Hunière, 91761 Palaiseau Cedex, France*

[2]*Foundation for Research and Technology Hellas, Institute of Electronic Structure and Laser, P.O. Box 1527, Heraklion 711 10, Greece*

Abstract

We report a study of the long-range self-guided propagation of intense femtosecond and picosecond UV laser pulses in air. Measurements of the laser beam profile along the propagation axis together with the ionization rate, the pulse temporal profile and power spectrum provide a comprehensive image of the UV filamentation process and its characteristics. Self-guiding is shown to subsist in both fs and ps cases, with a robust filament propagating over several meters in air. Stable filamentation is accompanied by an important restructuring of the pulse temporal profile. Complementary numerical simulations, using a 3-dimension propagation code, are compared to the experimental results. The simulations reproduce most experimental observations, allowing for a better understanding of the phenomena involved in this unique propagation mode.

PACS: 42.65.Tg, 42.65.Jx

Keywords: Nonlinear guided waves, Beam trapping.

[*]E-mail address: stzortz@enstay.ensta.fr

I. Introduction

Propagation of electromagnetic pulses is of fundamental importance in pure and applied science, and the recent development of sources of intense ultra-short laser pulses has added many interesting twists to this long standing problem. The broad spectral bandwidths, high peak powers, and (3+1)-dimensional nature of these fields give rise to complex linear and nonlinear effects that have posed significant challenges to researchers.

In the last years an important effort has been devoted to the study of the propagation of powerful laser beams in atmosphere as well as in other transparent media, i.e. glasses. A particular interest has focused on femtosecond laser systems, able to deliver very high peak powers with a modest energy output. Due to the high power the nonlinear response of the medium plays a key role in the propagation. Complementary to the experiments, the nonlinear propagation is simulated numerically by solving a complex extended nonlinear Schrödinger equations (NLS) including: linear diffraction, the optical Kerr effect, plasma generation from multiphoton absorptions (MPI), normal group velocity dispersion (GVD) or even other higher order terms of temporal dispersion.

Beam self-guiding and filamentation using IR femtosecond powerful lasers has been observed and reported by several groups [1-3]. The key role of multiphoton ionization has been well identified. Schillinger and Sauerbrey [4] and Tzortzakis *et al*. [5,6] have measured the electric conductivity of air in the trail of those filaments and provided estimates of the electron density in the filament, with Schillinger giving a lower limit of 10^{12} cm^{-3} and Tzortzakis a mean density between 10^{16} and 10^{17} cm^{-3}. La Fontaine *et al*. [7] have reported long-range filamentation in excess of 200 m using a laser system providing pulses at 795 nm and duration of 60 fs. They have measured the electron density in the

filament, using longitudinal spectral interferometry, and found it to be a few times 10^{16} cm^{-3}. The same group has performed experiments of laser-triggered discharges using a powerful femtosecond IR laser. They have observed long discharges of more than 2.5 m and an important enhancement of the leader propagation speed by a factor of 10 [8].

Talebpour *et al*. [9] have reported measurements of the photoemission spectrum of N_2 molecules and N_2^+ molecular ions in the filament. By measuring the intensity of the photoemission signal at different distances they were able to trace the laser beam intensity along the propagation axis. In this way they reported on the observation of refocusing, a feature that has been predicted by several numerical simulations [10-12].

Mlejnek *et al*. [10] presented numerical simulations of nonlinear pulse propagation in air whereby an initial pulse is formed, absorbed by plasma generation, and subsequently replenished by power from the trailing edge of the pulse. The evolution of the pulse is dynamic, involving the development of a leading-edge pulse that subsequently decays and is replaced by a new pulse. Spatial ring formation around the filament was also reported. The same research group reported recently [13] a real 3-dimension (3D) numerical simulation where the introduction of a large laser beam (7 mm) with power more than $35P_{cr}$ leads to multi-break-up and multi-filamentation. Aközbek et al. [14] provided an alternative analytical method for describing the properties of the femtosecond pulse propagation in air. They approach the plasma generation as an effective higher-order $\chi^{(n)}$ like effect. This method reproduced part of the more complex numerical simulations and was in good qualitative agreement with several experimental results.

Koprinkov *et al*. [15] have recently reported on the existence of spatio-temporal solitons when intense femtosecond laser pulses propagate in gases under high pressure or even

transparent solids such as fused silica. Bergé and Couairon have obtained recently a numerical confirmation of a spatio-temporal soliton propagating in atmosphere over a distance of about 60 m [16].

Recently Schwarz *et al*. [17] and Tzortzakis *et al*. [18] reported on the filamentation of ultrashort UV laser pulses. In this paper we present a detailed experimental and numeric study on the nonlinear propagation of ultraviolet femtosecond and picosecond laser pulses in air. The comparison between experimental results and the simulations is in most cases very good. We begin in section II with a description of the UV laser system and the experimental techniques used. Then in section III a description of the physical model used in our simulations is given and the numerical procedure followed is described. We provide the reader with all the details relative to the model and the numerical values used. A special effort was made to select the physical parameters known from the current literature and to use initial conditions close to the experimental ones. In section IV a detailed presentation of the most important and significant results is given, both experimental and numerical. Laser beam intensity profiles, electron densities, pulse temporal profiles and power spectra at different distances along the laser propagation axis are shown. We report on experimental and numerical evidence of femtosecond and picosecond UV pulse filamentation with long plasma channels and pulse splitting promoted by MPI.

II. Experimental procedure

The UV laser pulses were obtained by doubling the output of a femtosecond dye laser and amplifying it with an Excimer laser amplifier, the whole system operating at a few Hz repetition rate. The laser peak emission wavelength was at 248 nm. The laser could operate either in the fs mode, (pulse duration 450 fs and energy per pulse up to 10 mJ) or in the ps mode (5 ps pulse duration and energy per pulse up to 15 mJ). Measurements described here

were obtained with both 450 fs and 5 ps long pulses for several input laser energies. The laser beam was directed through a circular diaphragm 7 mm in diameter, and then focused with a lens of focal distance $f = 9.5$ m.

Laser beam profiles were recorded at different propagation distances on UV photographic paper. Filamentation with concomitant plasma channel formation was verified by measuring the electric conductance of air as a function of propagation distance. To detect the presence of a conducting channel, we measure the change of resistivity of air between two electrodes after passage of the filament. All details relative to the electric technique can be found in Ref. [5]. The electron detector was calibrated by means of an optical diffractometry technique described in Ref. [6]. The far field image of a probe beam, modified after the passage through the filament is recorded at different delays. The diffraction patterns obtained in this way are sensitive to the accumulated phase shift, fixing thereby the electron plasma density.

Measurements of the temporal pulse shape were performed using an autocorrelation technique based on the 2-photon ionization of NO molecules. A collinear Michelson type interferometer coupled with a cell filled with pure NO molecules at low pressure (typically about 100 mbar) was used [19]. A small part of the laser beam is introduced in the Michelson interferometer from a glass (BK7) plate reflection placed on the laser propagation axis at 45° angle. Measurements were performed only at distances for which the entrance window of the glass plate was not damaged by the laser beam intensity (i.e., outside the focal region) and therefore the reflected beam was not distorted. The free electrons produced from the laser - NO molecules interaction are captured using a system of two electrodes placed in the cell where a moderate potential difference is applied. The signal measured in this way is directly proportional to the number of free electrons

produced by the 2-photon ionization process of the 248 nm laser radiation used here. The signal measured in this case is proportional to $S(\tau)$ with:

$$S(\tau) = 1 + 2\int I(t)\, I(t+\tau)\, dt \,/\, \int I^2(t)\, dt \qquad (1)$$

where I is the laser intensity. From the above formula, for $\tau \to \infty$ one has $S(\tau) = 1$, while for $\tau = 0$, $S(\tau) = 3$. Thus the expected ratio of the peak signal to the baseline in the autocorrelation traces is 3. This ratio was an experimental criterion for the validity of the experimental autocorrelation measurements. Fig. 1 (squares and solid line) shows the autocorrelation trace of the initial pulse for the case of fs pulses before propagation, which could be fitted with a sech^2 function (dashed line) with duration of 450 fs, in agreement with the laser specifications.

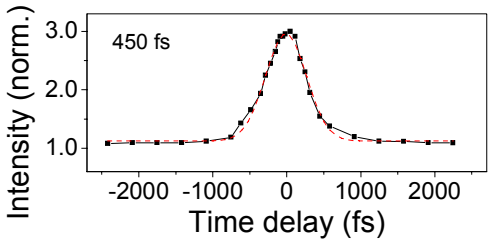

Fig 1: Measured autocorrelation trace of the initial UV fs pulse before propagation. The dashed line is the fit using a sech^2 function with duration 450 fs.

Spectral measurements of the laser pulse before and after propagation were performed, taking a small reflection of the beam into an f = 1 m spectrometer equipped with a 1200 grooves/mm diffraction grating. In some cases another system was used with an f = 25 cm spectrometer with a 1200 grooves/mm diffraction grating and a 16 bit linear CCD camera.

Beam profiles and ionization measurements, together with temporal autocorrelations and pulse power spectra were recorded at different propagation distances for both fs and ps pulses for several input laser pulse energies.

III. Numerical approach

The propagation of an intense femtosecond laser pulse in a gas involves linear diffraction, linear and nonlinear refraction as well as ionization of air molecules. Much numerical simulation effort has been devoted during the last years to reproduce the experimental observations of the filamentation of intense ultrashort IR laser pulses as well as to provide some predictions, see e.g. Ref. [10-12,20,21]. For a numerical code to be reliable for predictions, it has to be able, at least, to reproduce most experimental observations by employing realistic physical parameters and initial conditions close to the experimental ones.

Here the experimental results are compared to numerical simulations, using a 3D propagation code with axial symmetry. This code has been successfully applied before to the nonlinear propagation of IR [11] and UV [18] fs laser pulses. This code solves numerically the nonlinear Schrödinger equation, coupled with the density of electrons produced by multiphoton ionization. We assume that the beam is linearly polarized with the central frequency ω_0 (λ_0 = 248 nm) and wavenumber $k_0 = \omega_0/c$. The pulse has the radial symmetry and its complex envelope $\mathcal{E}(r,t,z)$ evolves according to

$$2i\frac{\partial \mathcal{E}}{\partial z} + \frac{1}{k_0}\Delta_\perp \mathcal{E} + k_0 n_2 \left|\mathcal{E}\right|^2 \mathcal{E} - k_0 \frac{\omega_{pe}^2(\rho)}{\omega_0^2}\mathcal{E} + i\sum_m \beta^{K_m} \left|\mathcal{E}\right|^{2K_m-2} \mathcal{E} = 0, \qquad (2)$$

$$\frac{\partial \rho}{\partial t} = \sum_m \frac{\beta^{K_m}}{K_m \hbar \omega_0} \left|\mathcal{E}\right|^{2K_m} \left(1 - \frac{\rho_m}{\rho_{at}}\right). \qquad (3)$$

This is a multi-species code and here, in the case of air, it treats O_2 and N_2 molecules in the

density proportion 20% and 80% respectively. In equations (2) and (3) m represents the two species and K is the respective number of photons needed in the multi-photon ionization processes that is 3 for O_2 (U_i = 12.06 eV) and 4 for N_2 (U_i = 15.58 eV). $\rho = \rho_{O_2} + \rho_{N_2}$ is the plasma electron density, while $\rho_{at} = 2.7\times10^{19}$ cm^{-3} is the background atom density satisfying the relation $\rho / \rho_{at} \le 1\%$. The second term of Eq. (2) describes diffraction in the transverse plane, followed by the Kerr self-focusing with nonlinear refraction index $n_2 = 8\times10^{-19}$ cm^2/W, plasma defocusing that involves the electron density entering in the plasma frequency $\omega_{pe}^2(\rho) = q_e^2\rho / m_e\varepsilon_0$, with q_e and m_e being the charge and mass of the electron and ε_0 the dielectric constant in vacuum, excited by multiphoton ionization (MPI) and the related multiphoton absorption (MPA) with coefficients β^{K_m}.

Depending on the laser intensity the creation of free electrons is described by one of the following models: the multiphoton ionization model or the tunnel ionization model. The separation between these regimes is given by the Keldysh constant Γ defined by [22]: $\Gamma_k = \left[U_k / 2\mathcal{V}\right]^{1/2}$, where U_k is the ionization potential of one atom and $\mathcal{V}$ the quiver energy of the free electron in the laser field; $\mathcal{V} = eE^2 / 4m_e\omega_0^2$. The multiphoton regime dominates when U_k is much larger than the quiver energy, which corresponds to $\Gamma > 1$. For the intensities considered in this study, < 10^{12} W/cm^2, we are placed in the multiphoton regime. The MPA coefficients read as $\beta^3 \simeq 2.14\times10^{-32}$ m^3/W^2 and $\beta^4 \simeq 1.13\times10^{-50}$ m^5/W^3 for oxygen and nitrogen molecules respectively. These coefficients are calculated based on the Keldysh formulation [22] as analyzed in Ref. [11].

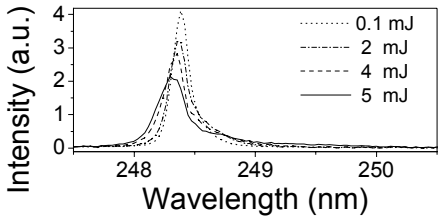

Fig. 2: Measured pulse power spectra of fs UV pulses recorded after 30 m of free propagation in air. In this figure spectra are shown for different input laser pulse energies. They show a small broadening but no global shift of the center of gravity.

Equation (2) is solved numerically using a Crank-Nicholson scheme which is an implicit finite-difference method recognized as condition less stable. The continuous field $\mathcal{E}(r,t,z)$ is represented on a regular grid with mesh size Δz and Δr along the axial and transverse directions, respectively. The time evolution t is segmented into k elements t_k. The Crank-Nicholson scheme is applied to each time element. As initial conditions, we consider input beams having a spatial super-Gaussian shape (simulating the diaphragm used in the experiments) with a transverse waist of $w_0 = 3$ mm. The temporal profile was assumed of the form of a sech^2 pulse with $\tau_0 = 450$ fs. The beam convergence corresponds to the experimental situation, where a lens with focal length $f = 9.5$ m was used. We did not include in our calculations the retarded Kerr effect. This approximation is justified by the fact that the laser spectrum did not exhibit significant spectral shift to lower energies in the ionization-free region before the focus. This is demonstrated in Fig. 2 where the power spectra of the laser pulse (fs case) are recorded for different input energies after free propagation (collimated beam) over 30 m in air. The absence of a red shift in the first spectral moment indicates that the non-instantaneous Kerr response is small and can be neglected [23]. We also neglect the effect of the group velocity dispersion (GVD) as we

deal with pulses, which have rather long duration and relatively short distances of propagation in air for the considered pulse durations (typically several meters).

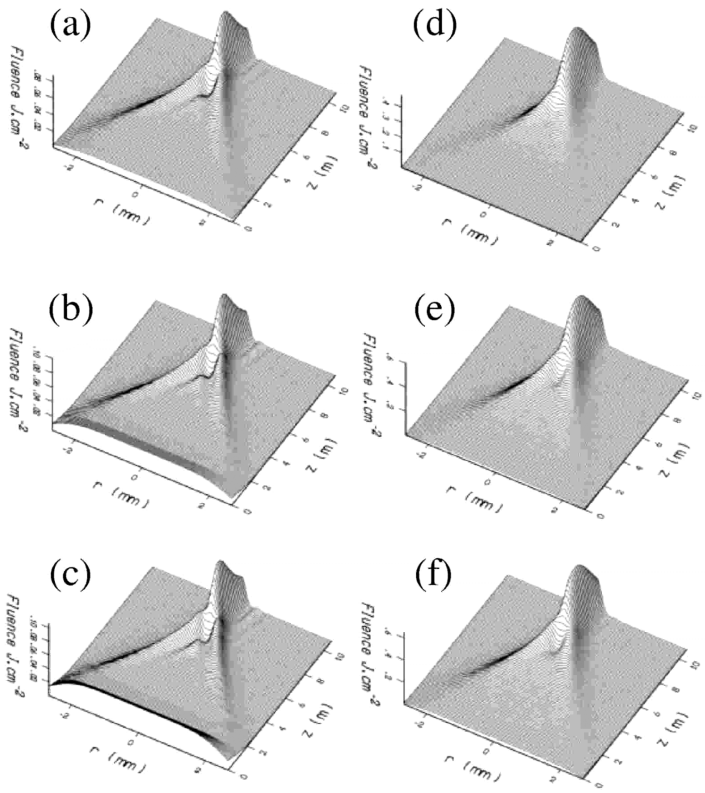

Fig. 3: Calculated fluence distributions along the propagation axis for fs pulses (first column) and ps pulses (second column). The first row is for input energy of 2 mJ, the second for 5 mJ and the third for 7.5 mJ.

IV. Propagation of Ultraviolet short pulses in air

A. Spatial characteristics

Fluence diagrams of the spatial evolution of the laser beam as results from the simulations are shown in Fig. 3. The column on the left presents results on 450 fs long pulses while the column on the right presents results for 5 ps long pulses, the first row is for input pulse energy of 2 mJ the second row for 5 mJ and the third for 7.5 mJ. From those figures the main stages in the propagation can be clearly recognized, showing in all cases the existence of a filament. First the beam self focuses because of the nonlinear Kerr effect with the

nonlinear focus being at about 7.25 m. In this first stage one observes the formation of rings merging inwards to the beam center. Those rings are less pronounced in the case of ps pulses than in the case of fs pulses. As the input energy increases the rings become more perceptible. Another characteristic especially noticeable in the case of fs pulses is the rapid reduction of the fluence in the first meter of propagation. This is due to losses from multiphoton absorptions as we will see later. The filament emerges from the nonlinear focus and propagates on for about 4 m subject to radiation losses. Rings merging outwards surround the filament. The number of rings is larger for higher initial pulse energy and is more visible in the fs case.

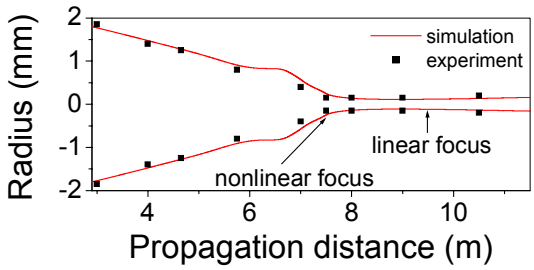

Fig. 4: Comparison between the measured (squares) and calculated (solid line) beam profile in the case of 450 fs, 2 mJ pulses.

In Fig. 4 is shown for comparison the calculated and measured radius of the laser beam along the propagation axis for input pulses of 450 fs, 2 mJ. The agreement is very clear showing well the existence of a filament propagating over about 4 m in air, having an almost constant diameter of about 150 μm. The nonlinear focus is shifted in front of the linear one by about 2.5 m.

Spatial repartitions of the fluence at two different distances along the propagation axis are presented in Fig. 5 for the case of 450 fs, 2 mJ pulses. In the first meters in front of the

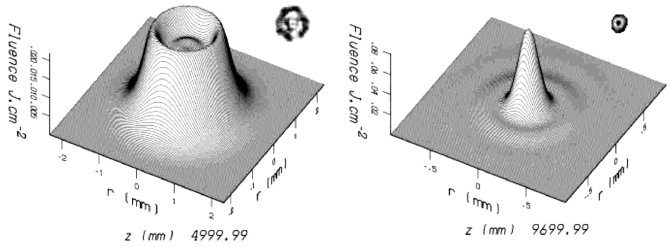

Fig. 5: Calculated spatial fluence distributions at two distances along the propagation axis. For comparison are also shown (small insets) measurements as recorded on UV photographic paper at the same distances. Observe the excellent agreement between the measurements and the simulations.

nonlinear focus one can observe rings merging inward to the beam center, as we have also seen in Fig. 3. The appearance of ring patterns can be seen on the burning spot of the laser beam on UV photographic paper recorded at the same distance (see inset in Fig. 5). On the experimental profile one can see that the rings are not really uniform but due to the modulational instability they break in many small filaments that later on coalesce to a single filament. The role of the modulational instability has been addressed recently by Tzortzakis *et al*. [24] in the case of fs IR filaments in air. Once the filament is formed, the trend is reversed, and light rings merge outwards in agreement with the experimental measurements.

B. Ionization

Comparative simulation results of 450 fs long pulses at different input energies are presented in Fig. 6. The dotted lines represent the 2 mJ, the dashed lines the 5 mJ, and the solid lines the 7.5 mJ. In Fig. 6 are shown results on the laser beam radius at FWHM, the maximum on axis (r = 0) fluence, and peak electron density from 7 to 11 m. For all the input energies considered here the results are very close, a filament is formed that propagates over many meters with a constant diameter of about 150 μm. The maximum fluence reaches 0.1 J/cm^2

and the maximum electron density reaches 10^{15} e^-/cm^3. This electron density is lower than the corresponding of IR fs filaments, which is about 10^{16} e^-/cm^3.

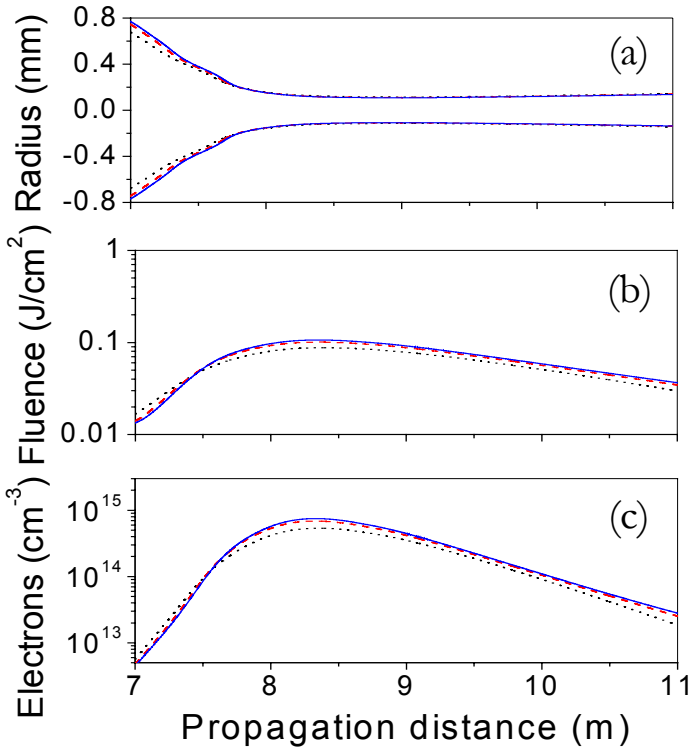

Fig. 6: Calculated beam radius (a), maximum on axis fluence (b), and peak electron density (c), along the propagation axis from 7 to 11 m. On those graphs results are shown for fs pulses with input energies of 2 mJ (dotted line), 5 mJ (dashed line) and 7.5 mJ (solid line).

The same comparison as above is shown in Fig. 7 for 5 ps long pulses and for the same input pulse energies as in Fig. 6. For the set of energies shown here the results are nearly the same, showing the existence of filaments propagating over many meters in air with constant diameter of about 200 μm, slightly larger than for fs filaments. The maximum fluence reaches almost 1 J/cm^2 and the maximum electron density exceeds 10^{15} e^-/cm^3. The factor 10 found when comparing the values of fluence in the case of 450 fs and 5 ps long pulses is

directly related to the factor 10 difference in pulse duration, resulting in the same intensity in both cases in the filaments.

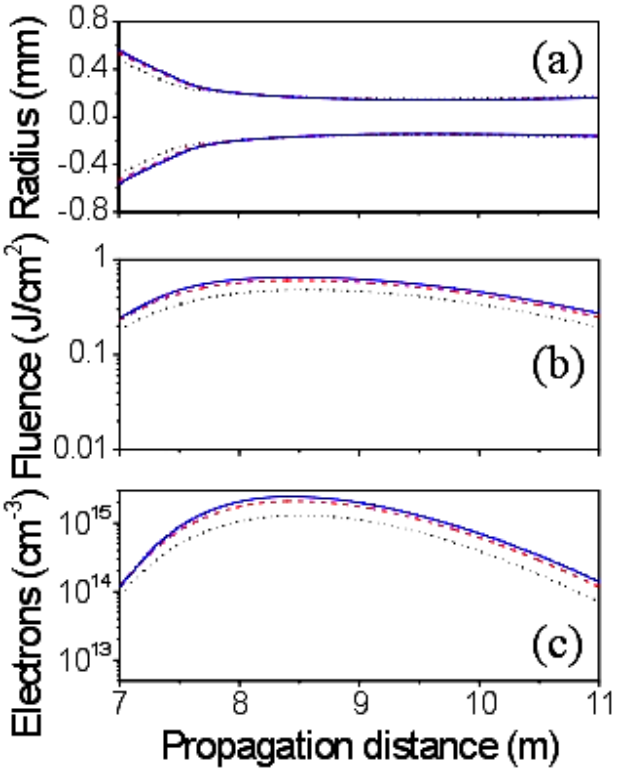

Fig. 7: Calculated beam radius (a), maximum on axis fluence (b), and peak electron density (c), along the propagation axis from 7 to 11 m. On those graphs results are shown for ps pulses with input energies of 2 mJ (dotted line), 5 mJ (dashed line) and 7.5 mJ (solid line).

A comparison between the ionization in the fs filament and the ps filament is presented in Fig. 8. In dashed line is the calculated electron density for 450 fs, 2 mJ pulses, which is to be compared with the measurements represented by the triangles. The solid line is the calculated electron density for 5 ps, 2 mJ pulses, which is to be compared to the measurements represented by the circles. Both calculations and measurements show clearly that in the case of ps UV filaments the electron density is higher than for fs UV filaments.

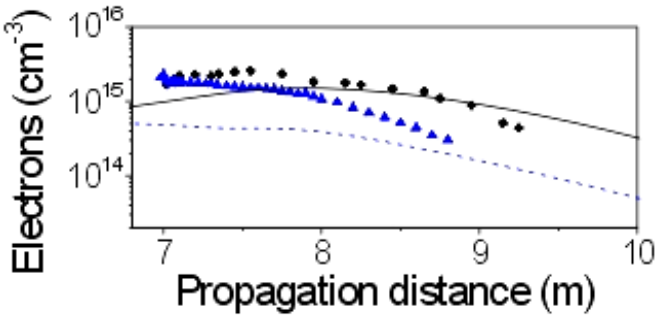

Fig. 8: Calculated and measured electron densities for 450 fs, 2 mJ pulses (dashed line and triangles respectively), and for 5 ps, 2 mJ pulses (solid line and circles respectively).

In Fig. 9 the role of the different species of the air (O_2 and N_2) is demonstrated for both fs (Fig. 9a) and ps pulses (Fig. 9b), for input laser pulse energy of 5 mJ. The dotted lines represent the N_2 contribution, the dashed lines represent the O_2 contribution, and the solid

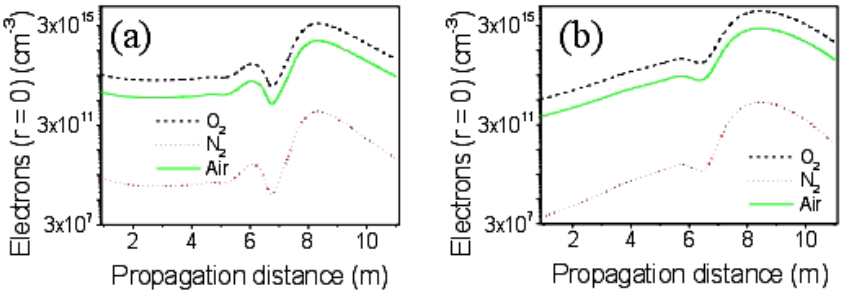

Fig. 9: Calculated electron densities for fs (a) and ps pulses (b) at input energy of 5 mJ. The respective contribution of N_2 (dotted line) and O_2 (dashed line), in the mixed air composition (solid line) is shown.

lines represent air with the mixed contribution of oxygen and nitrogen. A first observation is the clear predominance of O_2 molecules ionization in the total electron density. Even if the N_2 molecules are in much higher proportion in air (80% compared to 20% for oxygen) this is an expected result because of the much lower ionization threshold of oxygen compared to

nitrogen. The electron density is slightly larger in the ps filaments than in the fs ones. Nevertheless the on axis electron density along the whole propagation distance from 0 to 11 m is much more uniform in the fs case, ranging over two orders of magnitude, than in the ps where the range is extended to four orders of magnitude.

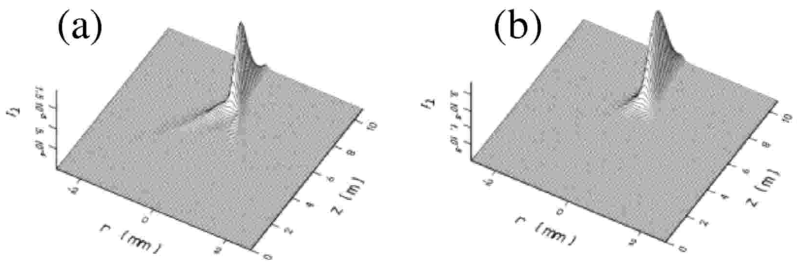

Fig. 10: Calculated spatial image of the ionization contribution (degree of ionization) along the propagation in the fs (a) and ps case (b), for input pulse energy of 2 mJ.

Fig. 10 presents the degree of ionization as a function of *r* and *z* for fs pulses (Fig. 10a) and the ps pulses (Fig. 10b), for input laser energy of 2 mJ. Observing those two figures one can see the important contribution to the ionization of the initial spatial rings in the case of fs pulses. By contrast, in the case of ps pulses this contribution is negligible.

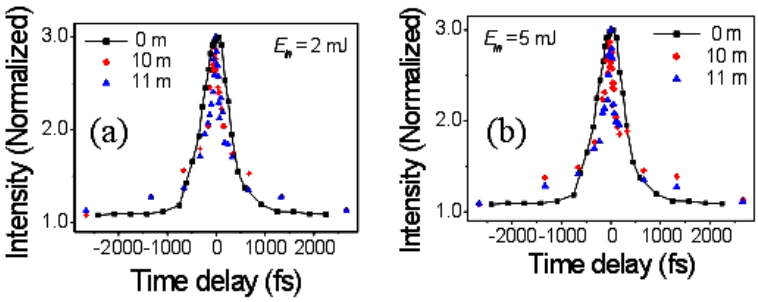

Fig. 11: Measured autocorrelation traces in fs filaments for two input energies of 2 mJ (a) and 5 mJ (b). Measurements at two different distances of 10 m (circles) and 11 m (triangles) are shown together with the initial pulse autocorrelation trace (squares with solid line).

C. Pulse temporal and spectral evolution

Temporal autocorrelation measurements at different distances along the propagation of the laser beam are presented in Fig. 11 for fs pulses at two input laser pulse energies of 2 mJ (Fig. 11a) and 5 mJ (Fig. 11b). For comparison the initial pulse autocorrelation is also shown. For both energies the results are very close: the shortening of the central autocorrelation peak and the pedestal at the wings suggest a break-up of the initial pulse. The central peak is about a factor two shorter than that of the initial pulse autocorrelation. This in turn suggests a corresponding compression of the pulse duration in the filament of the order of two. The stability of this structure over many meters of propagation is also remarkable, supporting the existence of a particular propagation mode.

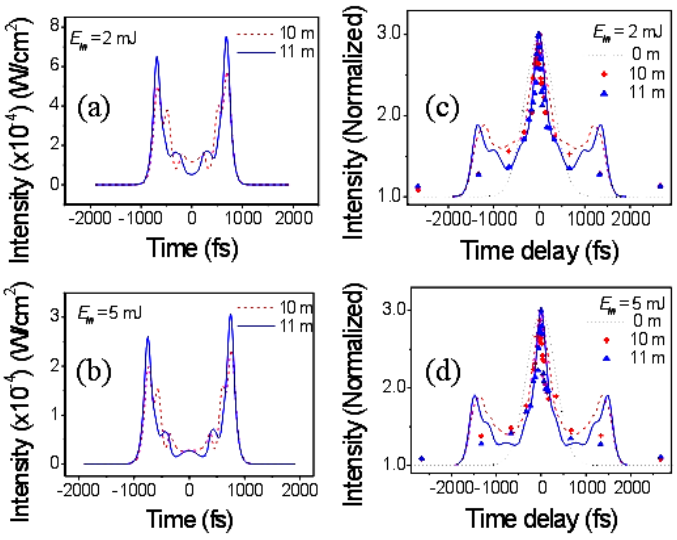

Fig. 12: Calculated pulse temporal profiles (a, b) and corresponding autocorrelations (c, d) in the fs filaments for input energies of 2 mJ (a, c) and 5 mJ (b, d). Results are shown for two distances of 10 m (dashed lines) and 11 m (solid lines). In (c, d) is also shown the autocorrelation trace of the initial pulse (dotted line) and the measured autocorrelations at 10 m (circles) and 11 m (triangles).

In Fig. 12a,b the calculated pulse temporal profile in the filament is shown at two distances of the propagation. The initial pulse splits into two shorter sub-pulses, which propagate almost unchanged over about 4 m. In Fig. 12c,d autocorrelation traces resulting from the simulations are directly compared to the experimental measurements. The numerically calculated autocorrelation curves result from application of the formula (1). Results at two different distances in the filament are shown together with the initial pulse autocorrelation for both initial pulse energies. The simulations reproduce in a very good way the central peak of the experimentally obtained autocorrelations, while a small discrepancy is observed at the wings. The difference is located in the amplitude of the pedestal and the secondary peaks of the autocorrelations. In the simulations the two peaks of the pulse structure have almost the same amplitude, which translates to high amplitude secondary peaks in the autocorrelation. On the other hand the experimental autocorrelations show less pronounced secondary peaks, which probably indicates that the two peaks in the double pulse do not have the same amplitude.

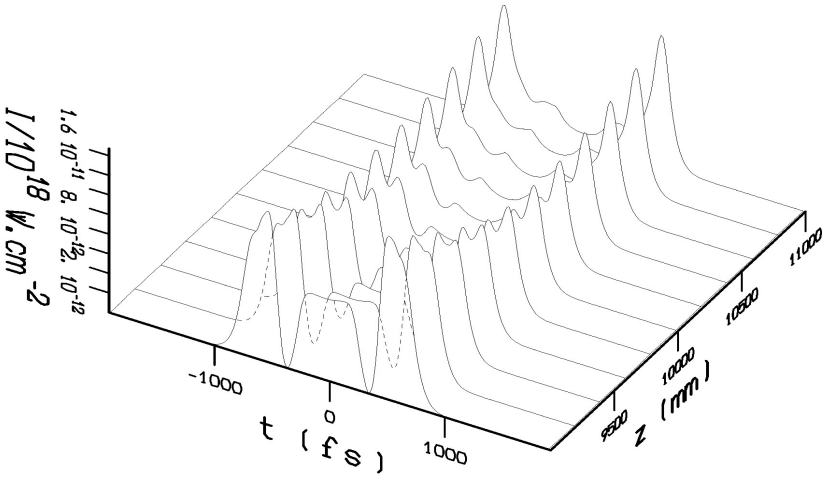

Fig. 13: Calculated pulse temporal profile evolution along the propagation axis from 9 to 11 m, for 5 mJ pulses with 450 fs initial duration.

In Fig. 13 the pulse evolution along the propagation axis of the fs filament is shown, for input laser energy of 5 mJ. This figure clearly indicates that energy from the central part of the pulse nourish the filament and the two surrounding peaks. Once this energy-reservoir is empty, after 11 m, the filament starts diffracting, as seen from the inspection of the spatial profile measurements and calculations shown, i.e. in Fig. 5.

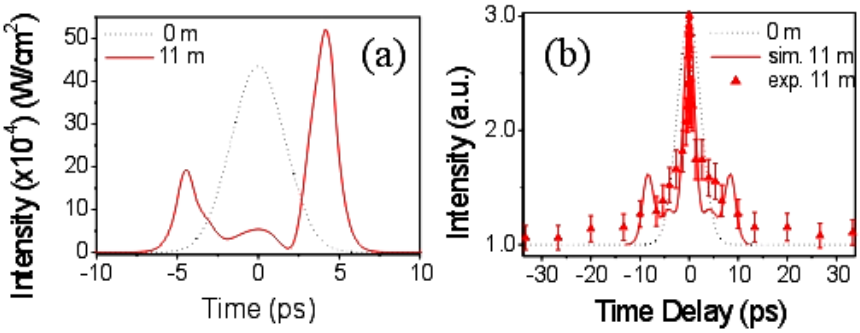

Fig. 14: Calculated pulse temporal profiles (a) and corresponding autocorrelations (b) in the ps filaments for input energy of 7.5 mJ. Results are shown at 11 m (solid lines) together with the initial pulse (dotted lines). In (b) is also shown the measured autocorrelation at 11 m (triangles).

In Fig. 14a the calculated pulse temporal profile in the ps filament is shown at 11 m together with the initial pulse (dotted line). The initial pulse splits into two shorter sub-pulses, which in this case do not have the same amplitude, as was the case with the fs filaments described above. In Fig. 14b the autocorrelation trace resulting from the simulation at 11 m is directly compared to the experimental measurement (triangles). The initial pulse autocorrelation is also shown in the same figure represented by the dotted line.

In Fig. 15 the pulse evolution along the propagation axis of the ps filament is shown, for input laser energy of 7.5 mJ. This figure clearly indicates that energy from the central part of the pulse nourish the filament and the two surrounding peaks. Moreover it shows that

contrary to the fs case here the intensity distribution in the two peaks is not symmetric. Here it is the rear peak (positive times) that gains more energy from the center. As was the case with fs pulses, once this energy-reservoir is empty, after 11 m, the filament starts diffracting.

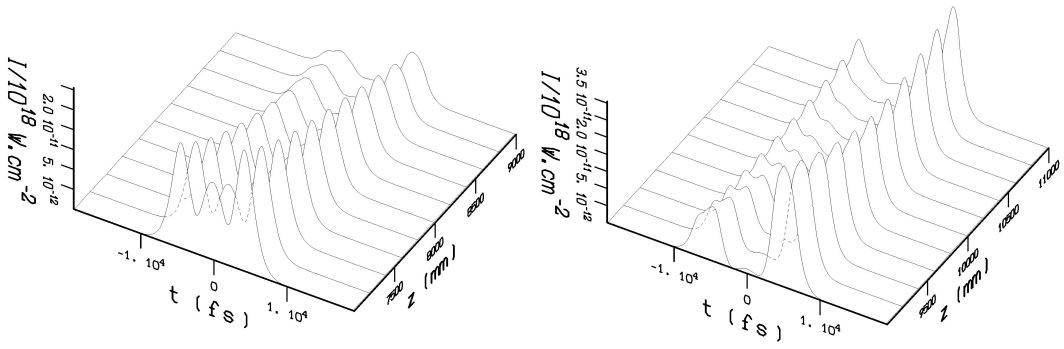

Fig. 15: Calculated pulse temporal profile evolution along the propagation axis from 7 to 11 m, for 7.5 mJ pulses with 5 ps initial duration.

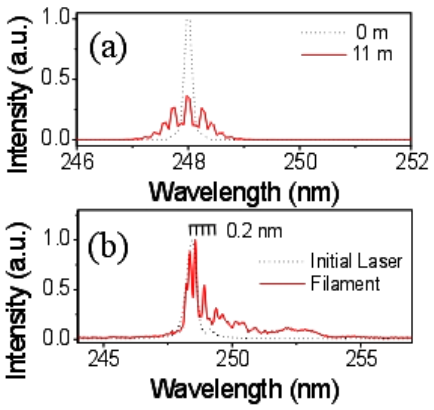

Fig. 16: Calculated (a) and measured spectra (b) for 450 fs, 5 mJ pulses. The initial pulse is in dotted line and the filament at 11 m is in solid. Both calculated and measured spectra in the filament have a fringe structure with an inter-fringe space of 0.2 nm.

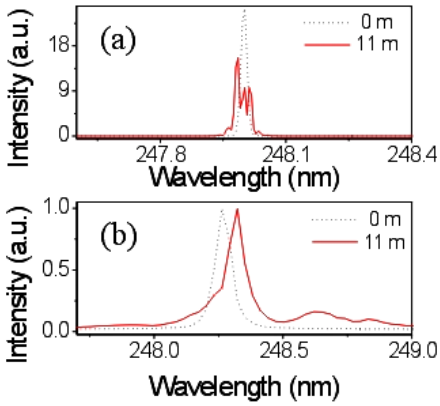

Fig. 17: Calculated (a) and measured spectra (b) for 5 ps, 7.5 mJ pulses.
In dotted line in the initial pulse and in solid the filament at 11 m.

Another way to verify the presence of a double peak structure is to compare the measured and simulated power spectra. The numerically produced double pulse structure in the fs filament has a power spectrum (Fig. 16a) with a characteristic fringe pattern with an inter-fringe space of about 0.2 nm. This is in good agreement with the measurement presented in Fig. 16b. The same comparison in the case of ps pulses, shown in Fig. 17, does not clearly indicate the existence of fringes in the spectrum, which is also in agreement with the measurements and the nonsymmetrical pulse structure in the ps filament.

In Fig. 18 more spectra are shown for the case of fs pulses at two input energies of 2 mJ (Fig. 18a) and 5 mJ (Fig. 18b). The spectra are plotted on a logarithmic scale and show measurements at different distances of the propagation. One can observe that the spectral broadening exists only in the filament. Moreover the shape of the spectra in the filament stays quite stable being another proof of the stability and the existence of a special propagation mode. Similar are the conclusions as it concerns ps filaments the spectra of which are shown in Fig. 19.

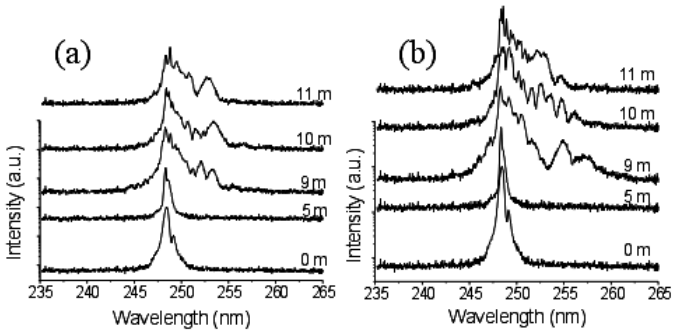

Fig. 18: Measured power spectra at different distances along the propagation axis for 450 fs initial pulses with input energy of 2 mJ (a) and 5 mJ (b). The y-axis is in logarithmic scale. Notice the stable spectral structure in the filaments (9, 10, 11 m).

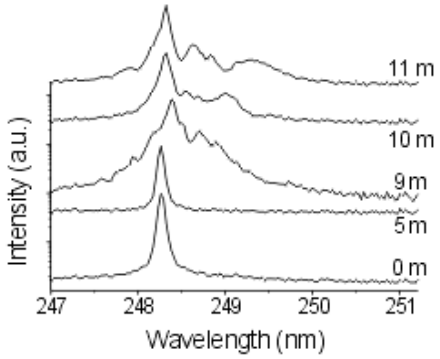

Fig. 19: Measured power spectra at different distances along the propagation axis for 5 ps initial pulses with input energy of 7.5 mJ. The y-axis is in logarithmic scale. Notice the stable spectral structure in the filaments (9, 10, 11 m).

Two general remarks can be made about the reported measured spectra. First, the observed spectral broadening is significantly smaller than for IR filaments. This is due to the almost two orders of magnitude lower intensity in the UV filaments as compared to the IR ones. This is the result of the much higher ionization cross sections of the ultraviolet radiation as compared to the infrared one. Thus the laser intensity needed to obtain a certain threshold value of the electronic density is lower. The second remark is that the spectrum's center of gravity shifts slightly towards lower energies. This is opposite to what is observed in the IR

filamentation. A possible explanation to this could be the relatively long pulse durations used in this study (450 fs and 5 ps) as compared to the IR filamentation. Gaeta [20] has attributed the spectral shift, towards higher energies, in the IR fs (~100 fs) filamentation to important pulse steepening effects giving rise to very sharp and spiky structures. In the present case such pulse steepening effects are not observed due to the initially longer pulses and the lower intensities in the filament.

V. Conclusion

In conclusion, we have presented a detailed experimental and numerical study on the nonlinear propagation of short (femtosecond and picosecond) UV pulses in air. Long-range beam filamentation has been observed both with fs and ps pulses. The filament characteristics are similar in both regimes; a slightly larger diameter and more electrons are produced for the ps as compared to the fs filament. In both cases the initial pulse breaks down to two sub-pulses with shorter duration. In the fs case the two sub-pulses seem to be symmetric while in the ps case the rear sub-pulse dominates over the leading one. The pulse splitting is promoted mainly by MPI. This break-up is of great importance in the formation and propagation of the filament, as it seems to play the role of a spatio-temporal waveguide.

We kindly acknowledge the assistance of A. Eglezis in the experimental procedure. We also thank A. Couairon for fruitful discussions. This study was made possible through the access to the Ultraviolet Laser Facility operating at FORTH-IESL under the “Improving Human Potential-Access to Research Infrastructures” Programme (Contract No: HPRI-CT 1999-00074) of the EU.

References

[1] A. Braun, G. Korn, X. Liu, D. Du, J. Squier, G. Mourou, Opt. Lett. 20 (1995) 73-75.

[2] E.T.J. Nibbering *et al.*, Opt. Lett. 21 (1996) 62-64.

[3] A. Brodeur, C.Y. Chien, F.A. Ilkov, S.L. Chin, O.G. Kosareva, V.P. Kandidov, Opt. Lett. 22 (1997) 304-306.

[4] H. Schillinger, R. Sauerbrey, Appl. Phys. B 68 (1999) 753-756.

[5] S. Tzortzakis *et al.*, Phys. Rev. E 60 (1999) R3505-R3507.

[6] S. Tzortzakis, B. Prade, M. Franco, A. Mysyrowicz, Opt. Commun. 181 (2000) 123-127.

[7] B. La Fontaine *et al.*, Phys. Plasmas 6 (1999) 1615-1621.

[8] D. Comtois *et al.*, Appl. Phys. Lett. 76 (2000) 819-821.

[9] A. Talebpour, S. Petit, S.L. Chin, Opt. Commun. 171 (1999) 285-290.

[10] M. Mlejnek, E.M. Wright, J.V. Moloney, Opt. Lett. 23 (1998) 382-384.

[11] A. Chiron *et al.*, Eur. Phys. J. D 6 (1999) 383-396.

[12] A. Couairon, L. Bergé, Phys. Plasmas 7 (2000) 193-209.

[13] M. Mlejnek, M. Kolesik, J.V. Moloney, E.M. Wright, Phys. Rev. Lett. 83 (1999) 2938-2941.

[14] N. Akôzbek, C.M. Bowden, A. Talebpour, S.L. Chin, Phys. Rev. E 61 (2000) 4540-4549.

[15] I.G. Koprinkov, A. Suda, P. Wang, K. Midorikawa, Phys. Rev. Lett. 84 (2000) 3847-

3850.

[16] L. Bergé , A. Couairon, Phys. Rev. Lett. 86 (2001) 1003-1006.

[17] J. Schwarz, P. Rambo, J.-C. Diels, M. Kolesik, E.M. Wright, J.V. Moloney, Opt. Commun. 180 (2000) 383-390.

[18] S. Tzortzakis *et al.*, Opt. Lett. 25 (2000) 1270-1272.

[19] S. Szatmari, F.P. Schäfer, Opt. Commun. 68 (1988) 196-202.

[20] A.L. Gaeta, Phys. Rev. Lett. 84 (2000) 3582-3585.

[21] A. Zozulya, S.A. Diddams, A.G. Van Engen, T.S. Clement, Phys. Rev. Lett. 82 (1999) 1430-1433.

[22] L.V. Keldysh, Sov. Phys. JETP 20 (1965) 1307-1314.

[23] J.-F. Ripoche *et al.*, Opt. Commun. 135 (1997) 310-314.

[24] S. Tzortzakis, L. Bergé, A. Couairon, M. Franco, B. Prade, A. Mysyrowicz, Phys. Rev. Lett. 86 (2001) 5470-5473.

Chapter 4

4. Femtosecond filament-guided electric discharges

4.1. Introduction

Since ancestry humans were astonished and terrified observing lightning. Numerous myths have been plotted around this impressive physical phenomenon. During the last few centuries scientists are trying to control it. A result of this effort is the development of the lightning-rod that protects today all high buildings. However the dream of scientists was always to have the complete control; to be able to decide the place and the time or in other words to trigger and guide lightning. Much effort has been devoted to this objective using always state of the art technological tools. A commonly used method to trigger lightning is to fire small rockets pulling up wires towards the thundercloud. Generally, the success rate of this technique is about 60%.

The idea of using lasers to trigger lightning crossed the mind of numerous investigators in the 70's. Since powerful CO_2 lasers could produce plasma in air, it seemed logical that such an ionized column could provide a preferential path for lightning. However the application of this technique was not without problems. The high density plasma formed by such laser systems is opaque to the laser radiation, resulting to a dotted conducting path rather than a continuous one. After many laboratory and on field experiments scientists have now concluded that such a method is inadequate for discharge and lightning control.

For a detailed presentation of the physics of lightning the reader can look in several specialized books, see e.g. Yu P. Raizer "Gas discharge Physics". Also a nice analysis is given in the dissertation of X. M. Zhao (University of New Mexico).

In this chapter we report the first experimental demonstration of a (short-scale) guided electric discharge triggered by a femtosecond laser filament. We analyze and give a concrete physical explanation of the mechanisms involved in this special kind of electric discharge.

The novelty here is in the use of a uniform, partially ionized air channel that covers the whole space between two electrodes (connects the two electrodes). With our experimental measurements and numerical simulations we show, in a lucid way, the physical evolution of such a system. The electric discharge is the result of a local on-axis air density reduction explaining on

the same time the initiation and the guiding. This depression is the result of the Joule heating of the initial low electron density plasma channel. The detailed presentation of the experimental procedure and the numerical analysis is given in appendix 4.1. The possibility to use this method to trigger lightning is, however, a question that needs much more study as the present work of short electric discharge cannot scale directly over long paths.

Appendix 4.1

"Femtosecond Laser-guided Electric Discharge in Air"

Submitted to

PHYSICAL REVIEW E RAPID COMMUNICATIONS (2001)

Femtosecond Laser-guided Electric Discharge in Air

S. Tzortzakis[*], B. Prade, M. Franco, A. Mysyrowicz[**]

Laboratoire d'Optique Appliquée, CNRS UMR 7639, ENSTA – Ecole Polytechnique, Chemin de la Hunière, F-91761 Palaiseau Cedex, France

S. Hüller, and P. Mora

Centre de Physique Théorique, CNRS UMR 7644, Ecole Polytechnique, F-91128 Palaiseau Cedex, France

Abstract

The filament due to the self-guided propagation of an infrared femtosecond laser pulse in atmospheric-pressure air is used to trigger and guide an electric discharge. The long low density plasma channel due to the filament is first heated by the Joule effect during an initial transient plasma stage. The heated channel of recombined gas then hydrodynamically expands radially. The onset of a discharge starts when the density depression on axis reaches the threshold discharge value. This model is supported by detailed experimental and numerical analysis.

PACS: 52.80.Tn, 52.38.Hb

[*]*E-mail address: stzortz@enstay.ensta.fr*

[**]*E-mail address: mysy@enstay.ensta.fr*

The initiation of an electric discharge through charged atmosphere, although complex, is basically understood. A crucial feature is the displacement of charges. Free carriers present in air gather around a point of high local field to screen it, leading to an increased local field. Eventually, the enhanced field reaches the value required to start a local avalanche process, with electrons multiplying and streaming outwards. Streamers coalesce into a self-sustained conducting path called leader. The leader moves in the direction of the opposite electrode, preceded by streamers. When contact is established, a large return current occurs. This streamer-leader interplay explains why a discharge can develop if the applied field is less than the critical field for dielectric rupture of air (E = 27 kV/cm at atmospheric pressure). It also explains the long and erratic incubation time between application of the voltage and onset of discharge.

Several experiments have shown that laser beams can trigger electric discharges in air [1-11]. Free electrons are generated by the laser field, usually at a focal point. The same scenario as above then develops, but with a reduced incubation time for leader formation. More recently, it has been shown that the speed of leader progression can be increased considerably by focusing an intense subpicosecond laser pulse between two charged electrodes [11]. In this letter we report on the first experimental demonstration of femtosecond filament triggered and guided electric discharge, suggesting a new mechanism of laser-induced electric discharge in air. One main characteristic of this kind of discharge is that it is uniform along its axis. The basic scenario is as follows. The self-guided femtosecond IR laser pulse produces in its wake a weakly ionized plasma filament with uniform longitudinal free electron density of a few times 10^{16} e^-/cm^3 and of a length that can exceed 50 cm [12]. This low temperature plasma filament cannot trigger by itself a self-sustained discharge between

two charged electrodes during its short (ns) lifetime. On the other hand, the current circulating during the brief conducting plasma phase produces significant Joule heating of a thin air column. This rapid heating is followed by a radial hydrodynamic expansion of the heated channel. Eventually a central air depression meets the conditions to provide a linear path for a self-discharge. Since this scenario does not involve the displacement of charged carrier gradients, it is reproducible in time but occurs with a characteristic delay. We model it by taking into account the hydrodynamic expansion of the heated air into the surrounding cold air.

Fig. 1 illustrates the difference between a usual (Fig. 1a) laser-triggered discharge and the scheme of the present experiment using a laser filament (Fig. 1b). The electric circuit consists of two metallic plates (electrodes), 1.5 cm apart, with an applied voltage of 28 kV. This voltage is well below the critical field for spontaneous discharge, which is close to 40 kV [13]. Fig. 1a shows an example of an ordinary laser-triggered discharge using a laser. Charges are deposited only at the middle point between the two electrodes by a focused femtosecond laser pulse with energy of 10 mJ. Following carrier injection by the laser, a discharge occurs with more than 90% probability. The delay between the creation of free carriers and the initiation of the discharge is long and erratic, varying typically between 1-5 μs. On the other hand Fig. 1b, which illustrates the present experiment, shows a discharge initiated and guided by a femtosecond laser-induced filament. The filament traverses and connects both electrodes through two pinholes with 3 mm diameters. It creates a uniform, partially ionized air channel that covers the whole space between the two electrodes. The onset of the discharge shown in Fig. 1b is now reduced to 80 ns. It occurs with 100 %

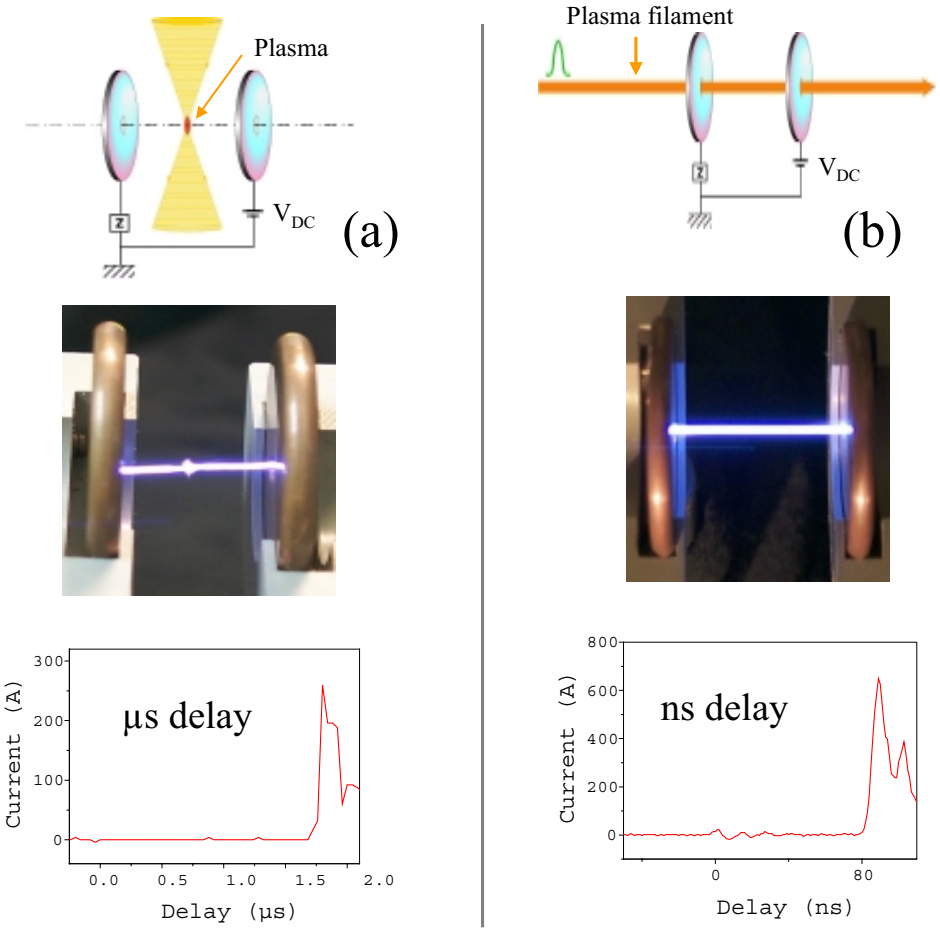

Fig. 1: Experimental configuration of the discharge circuit, (a) when the laser beam is focused between the two electrodes and (b) when a self-guided filament produced plasma channel is used to connect the two electrodes. On the top of the figure is a schematic representation of the set-up while in the middle is a photo of a real experiment. At the bottom part we show characteristic curves of the current flowing in the circuit. Notice the important difference on the time delay in the two configurations.

probability with a jitter less than 5%. The electric discharge is the result of a local on-axis air density reduction explaining on the same time the initiation and the guiding.

In order to quantify the scenario sketched above, we have performed a series of measurements to characterize the air channel at different times between the passage of the self-guided laser pulse and the onset of the discharge. These experimental results were confronted to a numerical simulation. The experimental method is time-resolved diffractometry [14]. This technique allows to time-resolve small local changes (gradients) of the refractive index in a gas. In a previous paper, we used this technique to characterize the initial short-lived plasma channel, its electronic density and radial dimensions [14]. Here we measure the local changes of the refractive index of air at later times owing to the gas expansion.

The experimental set-up is shown in Fig. 2. The probe beam crosses the filament path under an angle of θ = 4°. The probe beam was focused 3.5 cm in front of the plasma channel. A long optical delay line (from 0 to 25 m) was necessary in order to cover the whole time-window between 0 and 80 ns. The spatial profile of the probe beam was cleaned after the delay line with a spatial filter in order to obtain a Gaussian profile. The far field image of the probe beam, after crossing the heated air channel, was recorded with a linear CCD camera for different delays. Two examples of the far field pattern observed in the presence of a DC field of 28 kV at 12 ns and 60 ns delay are shown in Fig. 2. Beam intensity profiles scanned through the fringes at different delays are shown in Fig. 3, represented by the upper curves. At early times, just after the passage of the laser pulse (Fig. 3 (0 ns)) a dark fringe appears in the center. This is characteristic for the presence of the plasma caused by the laser pulse. It vanishes within the first nanosecond, translating the

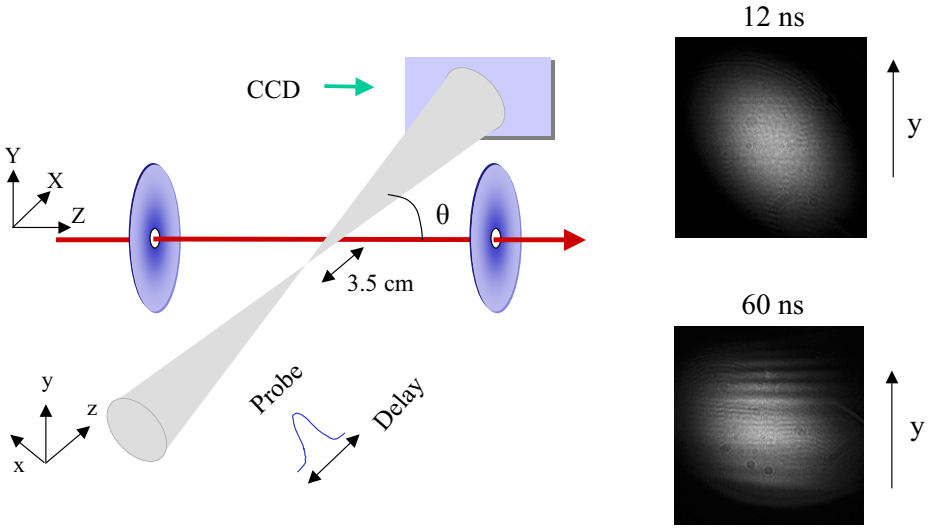

Fig. 2:Experimental configuration of the time-resolved diffractometry. The far-field images of the probe beam after crossing the heated channel are recorded for different delays. On the right two characteristic diffraction patterns at 12 ns and 60 ns are presented. The arrows next to the images indicate the axis along which we acquire the intensity profile that we use in our analysis (see Fig. 3).

fast recombination lifetime of the electrons in the filament-generated plasma. Details on the characterization of this initial plasma and its recombination lifetime can be found in Ref. [14].

A second diffraction pattern appears after an incubation time of 30 ns (Fig. 3 (30 ns)). This second diffraction pattern increases with time (Fig. 3 (45 ns, 60 ns, 80 ns)) until the arrival of the discharge, after 80 ns. This second diffraction pattern occurs only in the presence of the external electric field, being a direct demonstration of its role in the Joule heating of the air channel. In the following we show that these observations are consistent with the hydrodynamic evolution of the heated air channel, creating a density depression along its axis.

The expansion of the heated gas channel was computed with the hydrodynamic code MULTI [15,16]. This code has been modified appropriately for the particular conditions here. We consider cylindrical geometry to describe the radial motion around the laser axis. We also consider an ideal gas equation of state. As initial temperature perturbation we impose the radial profile:

$$T(r) = T_{room} + \delta T \exp\left(-r^2 / w_0^2\right) \tag{1}$$

where δT is the temperature elevation owing to the small electric current flowing in the circuit during the first few nanoseconds, w_0 is the plasma channel waist. The following set of equations for continuity, motion and energy are solved numerically:

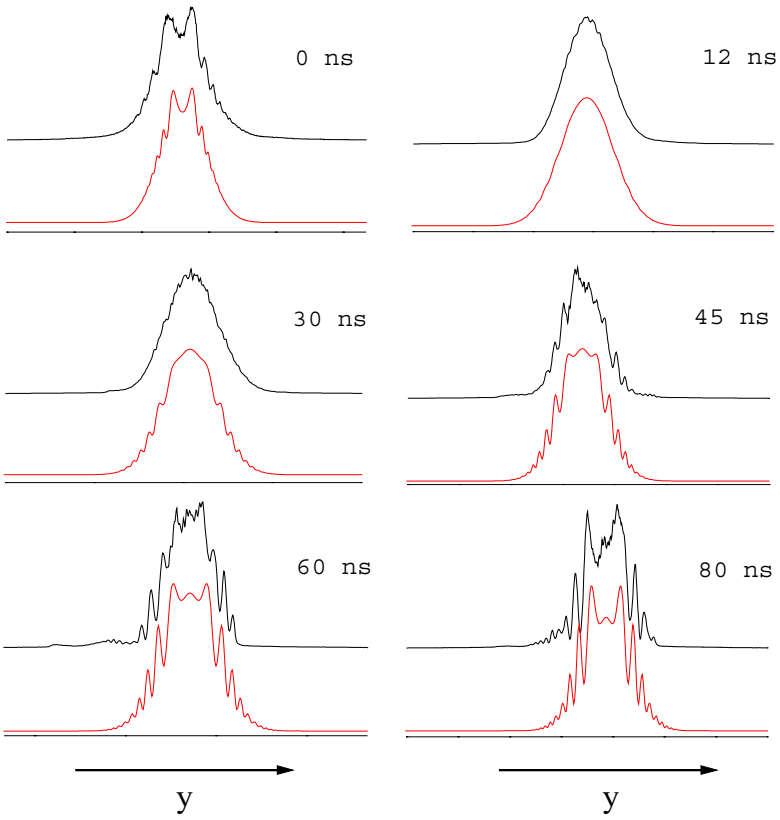

Fig. 3: Experimental results from the time-resolved diffractometry and comparison with the numerical simulations for different delays. The experimental results are represented by the upper curves while the lower ones are the simulations.

$$\frac{d\rho}{dt} = -\rho \, \nabla \cdot \vec{u} \tag{2}$$

$$\rho \, \frac{du_r}{dt} = -\frac{1}{m}\frac{\partial}{\partial r}\left(\rho k_B T\right) \tag{3}$$

$$\frac{5}{2}\frac{dT}{dt} = -T \, \nabla \cdot \vec{u} \tag{4}$$

where ρ is the gas density, $\vec{u}$ is the velocity (retaining only the radial term of $\nabla \cdot \vec{u}$), m stands for the mass of air molecules, and k_B is the constant of Boltzmann. Other loss terms due to collisions and radiation can be neglected.

We adopt the value of w_0 = 40 μm. This is not an adjustable parameter, but was extracted from diffraction analysis of the filament plasma channel as was reported in Ref. [14]. Thus the only adjustable parameter in our model and simulations is the initial gas temperature perturbation, which we adjust for a best fit to the experimental results. The numerical results shown in Fig. 4 correspond to an ambient temperature T_{room} = 300 K with an initial temperature increase of δT = 100 K. An outgoing pressure wave is observed, with a central depression eventually reaching 30% of the initial value after 80 ns. This value in turn is in agreement with the threshold pressure expected for the onset of a discharge as calculated according to the Paschen law and represented by the dashed line in Fig. 4.

From the density profiles obtained from the hydro-simulations one can calculate the diffraction patterns of the probe beam owing to the changes of the refractive index induced by the expansion of the channel. We express the far field probe beam intensity as:

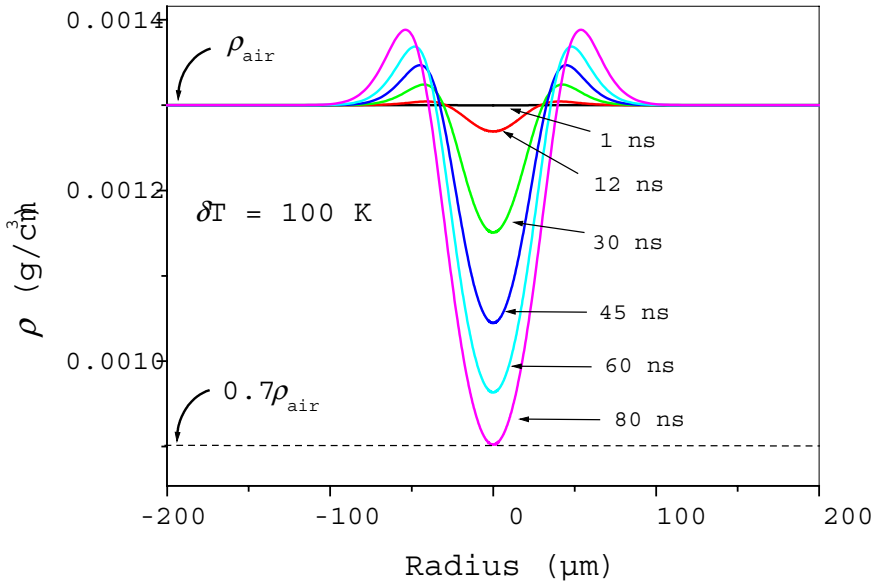

Fig. 4: Results of the hydrodynamic code MULTI for the depression of a heated channel with initial temperature elevation of 100 K and waist of 40 μm. The depression reaches the 70% limit imposed by the Paschen law (represented by the dashed line) after 80 ns in agreement with the experiment.

$$\left| F(\vec{q}) \right|^2 = \left| \int_{-\infty}^{+\infty} \int f(\vec{r}, z)\, e^{i\varphi(\vec{r})}\, e^{i\vec{q}\cdot\vec{r}}\, dxdy \right|^2 \tag{5}$$

with the probe beam electromagnetic field written as:

$$f(\vec{r}, z) = \frac{1}{1 + i\,(z / z_r)} \exp\left(-\frac{r^2 / w^2}{1 + i(z / z_r)} \right) \tag{6}$$

where $\vec{r} = x\vec{e}_x + y\vec{e}_y$, z_r = 1 mm is the Rayleigh length and w = 20 μm is the beam waist at the focus of the f = 0.5 m focusing lens. The accumulated phase is $\varphi(y) = (2\pi / \lambda \sin\theta) \int_{-\infty}^{+\infty} \left[n\left(\sqrt{\mu^2 + y^2}\right) - n_\infty \right] d\mu$, where we have introduced a change of coordinates $\mu = x\cos\theta + z\sin\theta$ (for the different systems of coordinates see Fig. 2). This phase is related to the gas density $\rho(r)$ by: $n(r) = 1 + C\rho(r)$. The constant C is estimated as follows. For $r \to \infty$ and for λ = 800 nm the index of refraction of the air is $n_\infty = n_{air}$ = 1.000275 and its density is $\rho_\infty = \rho_{air}$ = 1.3 x 10^{-3} g/cm^3, from which $C = (n_{air} - 1) / \rho_{air}$ = 0.21 cm^3/g.

The evolution of the fringe pattern was calculated for different temperatures of the heated channel. An excellent agreement was found for δT = 100 K. The corresponding set of measured (upper curves) and calculated fringe patterns (lower curves) can be seen in Fig. 3. The value of δT = 100 K is also consistent with the time delay of 80 ns shown in Fig. 4.

In conclusion we have observed a new type of reproducible laser-guided electric discharge in air. It is triggered by the expansion of a thin hot air wire produced by a self-guided IR femtosecond laser pulse. From time-resolved diffraction measurements coupled with a

hydrodynamic model for the wire expansion, quantitative information on the evolution of the air wire density and temperature as well as on the discharge initiation have been extracted. This type of electric discharge may find applications when on axis uniformity is crucial.

We kindly acknowdlege the expert assistance of Y.-B. André and G. Hamoniaux.

References

[1] J. R. Greig, D. W. Koopman, R. F. Fernsler, R. E. Pechacek, I. M. Vitkovitsky, and A. W. Ali, Phys, Rev. Lett. **41**, 174 (1978).

[2] G. N. Aleksandrov, V. L. Ivanov, G. D. Kadzov, V. A. Parfenov, L. N. Pakhomov, V. Yu. Petrun'kin, V. A. Podlevskii, and Yu. G. Seleznev, Sov. Phys. Tech. Phys. **22**, 1233 (1978).

[3] A. A. Antipov, A. Z. Grasyuk, A. K. Zhigalkyn, L. L. Losev, and V. I. Soskov, Sov. Phys. Tech. Phys. **36**, 490 (1991).

[4] M. Hijikawa, H. Tamura, H. Arishima, K. Horioka, and K. Kasuya, Appl. Phys. Lett. **45**, 234 (1984).

[5] C. Honda, K. Muraoka, T. Takuma, M. Akazaki, F. Kinoshita, and O. Katahira, Electr. Eng. Jap. **114**, 32 (1993).

[6] E. I. Asinovskii, L. M. Vasilyak, and S. Yu. Unkovskii, Sov. Phys. Tech. Phys. **37**, 335 (1992).

[7] A. A. Antipov, A. Z. Grasyuk, A. K. Zhigalkyn, L. L. Losev, and V. I. Soskov, Sov. Phys. Tech. Phys. **36**, 490 (1991).

[8] X. M. Zhao, J.-C. Diels, C. Y. Wang, and J. M. Elizondo, IEEE J. Quantum Electron. **31**, 599 (1995).

[9] M. Miki, and A. Wada, J. Appl. Phys. **80**, 3208 (1996).

[10] B. La Fontaine, F. Vidal, D. Comtois, C. Y. Chien, A. Desparois, T. W. Johnston, J.-C. Kieffer, H. P. Mercure, H. Pépin, and F. A. M. Rizk, IEEE Trans. Plasma Sci. **27**, 688 (1999); F. Vidal *et al.*, IEEE Trans. Plasma Sci. **28**, 418 (2000).

[11] D. Comtois, C. Y. Chien, A. Desparois, F. Génin, G. Jarry, T. W. Johnston, J.-C. Kieffer, B. La Fontaine, F. Martin, R. Mawassi, H. Pépin, F. A. M. Rizk, F. Vidal, P. Couture, H. P. Mercure, C. Potvin, A. Bondiou-Clergerie, and I. Gallimberti, Appl. Phys. Lett. **76**, 819 (2000).

[12] S. Tzortzakis, M. A. Franco, Y.-B. André, A. Chiron, B. Lamouroux, B. S. Prade, and A. Mysyrowicz, Phys. Rev. E **60**, R3505 (1999).

[13] Due to local field effects, a spontaneous discharge can occur occasionally between the edges of the electrodes, already from an applied voltage of 30 kV.

[14] S. Tzortzakis, B. Prade, M. Franco, and A. Mysyrowicz, Opt. Commun. **181**, 123 (2000).

[15] R. Ramis, R. Schmalz, and J. Meyer-ter-Vehn, Comput. Phys. Commun. **49**, 475 (1988).

[16] K. Eidmann, J. Meyer-ter-Vehn, T. Schlegel, S. Hüller, Phys. Rev. E **62**, 1202 (2000).

Chapter 5

5. Filamentation in transparent solids

5.1. Introduction

In the present chapter we present experimental evidence of a self-guided ultrashort pulse propagating over many Rayleigh distances in fused silica. The experimental measurements of the filament characteristics are directly confronted to numerical simulations using a 3D numerical code. This comparison reveals the mechanisms that lead to the beam filamentation and clarify questions relative to the temporal evolution of those self-guided structures. Basically the same scenario as in air is found where GVD, although much more important in fused silica, plays a secondary role. The detailed presentation of the experimental and numerical results are presented in appendix 5.1. The present work was performed in collaboration with Lionel Sudrie in the frame of his thesis work, which is on the study of optical damages produced in glasses by intense femtosecond pulses.

Appendix 5.1

"Self-guided propagation of ultrashort IR laser pulses in fused silica"

Submitted to

PHYSICAL REVIEW LETTERS (2001)

Self-guided propagation of ultrashort IR laser pulses in fused silica

S. Tzortzakis[*], L. Sudrie, M. Franco, B. Prade, A. Mysyrowicz[**]

Laboratoire d'Optique Appliquée, CNRS UMR 7639, Ecole Nationale Supérieure de Techniques Avancées – Ecole Polytechnique, Chemin de la Hunière, F-91761 Palaiseau Cedex, France

A. Couairon, L. Bergé

CEA/DAM-Ile de France Bruyères-le-châtel, France

Abstract

We report self-guided propagation of ultra-short IR laser pulses in fused silica over several Rayleigh lengths. Self-guiding is accompanied by pulse splitting and time compression. Numerical simulations involving pulse self-focusing, temporal dispersion and multi-photon ionization are found to be in good agreement with the experimental results. They show that a quasi-dynamic equilibrium between multi-photon ionization and self-focusing drives the filamentation process, while temporal dispersion plays a negligible role.

PACS: 42.25.Bs, 42.65.Jx, 42.65.Re, 42.65.Sf

[*]*E-mail address: stzortz@enstay.ensta.fr*

[**]*E-mail address: mysy@enstay.ensta.fr*

Recently, considerable attention has been paid to the propagation of femtosecond optical pulses in gases. For instance, intense ultrashort infrared (IR) laser pulses propagating through the atmosphere have been shown to self-organize in narrow filaments with high peak intensity close to 10^{13} W/cm^2, which persist over exceptionally long distances [1-7]. This effect results from the dynamical competition between two effects. Due to the nonlinear Kerr response of air, a light beam with input power higher than the self-focusing threshold, focuses over a finite distance. The on-axis beam intensity increases through this process, until multiphoton-ionization occurs [8]. The ensuing electron plasma defocuses the beam. At powers around critical, the equilibrium between multiphoton ionization (MPI) and Kerr self-focusing (SF) may result in the formation of a long-living solitonlike waveguide [9]. At higher power levels, a dynamic interplay between both processes can sustain the propagation over very long distances [5]. However, besides MPI, other processes have been proposed as potential candidates for limiting the collapse of SF ultra-short pulses. Among them, normal group-velocity dispersion (GVD) is known as promoting pulse splitting, that leads to the sharing of the temporal beam profile into mainly two symmetric sub-pulses [10,11]. In addition, the self-steepening and space-time focusing effects described from deviations to the usual slowly-varying envelope approximation [12] may act to shift the beam energy into one of the two pulse edges formed by GVD [13,14]. This mechanism also occur in transparent materials other than gases. For example, 90-fs pulses with powers moderately above critical were experimentally observed to split into sub-pulses in BK7 samples. This splitting process was mainly attributed to GVD [15-17], although in [18] the measured continuum generation and blue-shifted spectra suggested a non negligible role of MPI. On the other hand, a recent numerical simulation [19] predicts formation of self-guided filaments in fused silica, with no significant influence from GVD,

similar to the case of air. On the experimental side, there is no report on self-guiding of femtosecond pulses in bulk transparent media, except for a short report of fs filamentation in Ti:sapphire [20] and a brief mention for fused silica [21].

This letter shows the first detailed observation of a long-lived light channel (filament) in fused silica. Measurements include the recording of the beam intensity profile along its propagation axis as well as modifications in the pulse power spectrum, and evolution of the pulse temporal profile using an autocorrelation technique. The experimental results are confronted with direct numerical simulations that account for SF, MPI, GVD, self-steepening and space-time focusing effects, using realistic parameters and initial conditions close to the experiment.

The experimental conditions to obtain the filament are stringent. Formation of the filament occurs when the incident laser power P exceeds about $3P_{cr}$, where in silica glass $P_{cr} = \lambda_0^2 / 2\pi n_0 n_2 \simeq 2.3$ MW is the critical threshold power for self-focusing, where n_0 = 1.453 is the linear refraction index and n_2 = 3.2 10^{-16} cm^2/W is the nonlinear refraction index for fused silica. The input pulse duration is 160 fs, and its peak emission wavelength is $\lambda_0 = 800$ nm. Forming this filament also requires an adapted incident laser beam geometry. We use a focusing lens with f = 80 mm and we situate the entrance face of the silica plate close to the waist of the beam. This positioning is delicate, since a deviation by more than 20% leads to the disappearance of the filament. The high repetition rate of our laser system (200 kHz) presents also a difficulty for observing filamentation: absorption of even a small amount of energy from every laser shot results in a substantial heating of the sample. This heating, in turn, changes the intrinsic physical properties of the medium and destroys the self-guided mode within a few seconds. To overcome this problem we moved

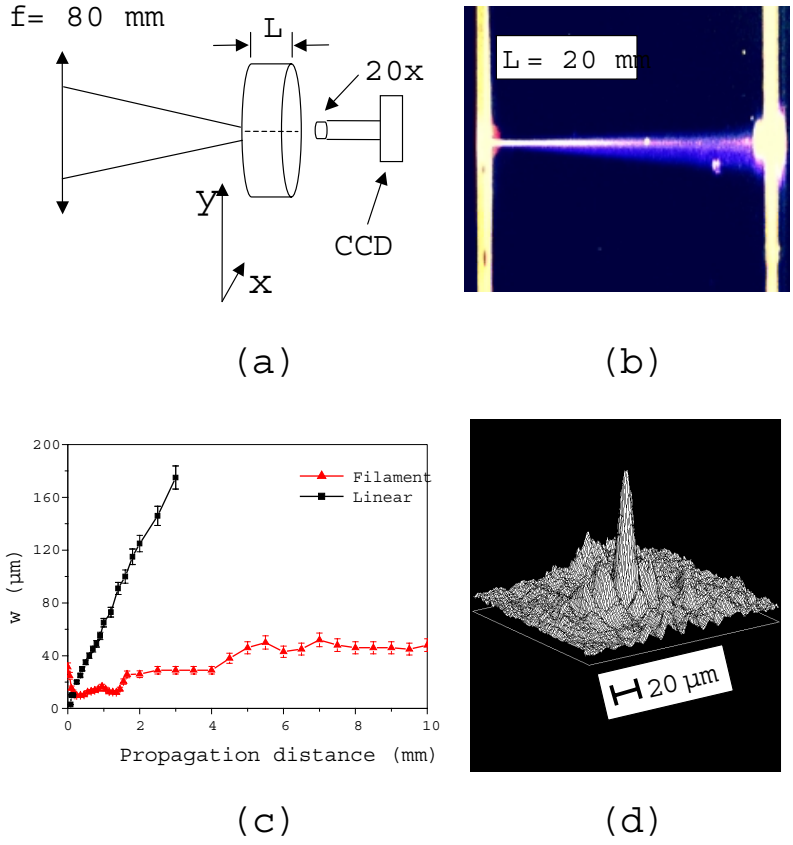

Fig. 1: (a) Experimental procedure for the detection of self-guided filaments in fused silica. $L = 2, 5, 10$ mm is the thickness of the silica plate. The plate has a continuous planar motion by means of an xy motorized-stage. (b) A transverse photograph of the self-guided filament in fused silica at input energy $E_{in} = 2$ µJ. (c) Measured diameter of the filament along its propagation. For comparison the measured linear diffraction regime at low input energy (50 nJ) is shown. (The 0 of the x-axis corresponds to the entrance face of the fused silica plate.) (d) A 3D fluence plot of the filament at 2.8 mm from the entrance window of the silica glass sample.

continuously the fused silica plate by means of an xy motorized-stage as shown in figure 1a. A self-guided light channel is then produced over a distance exceeding several mm, as shown in Fig. 1b and 1c. The filament size ranges between 10 and 40 μm, which corresponds to maximum intensities of the order of 10^{13} W/cm^2, leading to the production of free electrons by multi-photon absorption [22].

The self-guided pulses were characterized as follows. A microscope objective (magnification of 20x) coupled to a linear CCD camera recorded the beam intensity profile at different distances along the beam propagation axis (see fig. 1a). The corresponding laser beam diameters for input energy $E_{in} = 2$ μJ are shown in figure 1c. On the same figure is also shown for comparison the linear regime with much lower input energy $E_{in} \simeq 50$ nJ, for which the laser beam diffracts according to the law of Gaussian optics. In figure 1d we present a 3D fluence plot of the filament at the distance of z = 2.8 mm inside the silica glass. A narrow filament can clearly be observed, surrounded by light rings.

We have also performed measurements of the pulse temporal profile in the filament. For this purpose we used a second harmonic non-collinear autocorrelator with a thin Barium Borate (BBO) crystal as a nonlinear medium. The time resolution of this autocorrelator is of the order of 30 fs. The dotted line in Fig. 2a shows the autocorrelation trace of the input laser pulse with duration of about 160 fs. After exiting the fused silica plate, the filament propagates in air and diffracts over a distance of 50 cm. The central part of the diffracted beam at the exit plane of the sample is introduced in the autocorrelator. In Fig. 2a the autocorrelation traces of the self-guided pulse at 2 and 5 mm are shown. These autocorrelation traces have a three peak shape, which indicates a pulse splitting of the input

laser pulse to mainly two sub-pulses. This temporal structure stays relatively stable along the filament propagation.

Fig. 2b shows the power spectrum of the initial laser pulse, as well as a representative spectrum of the self-guided beam, integrated over about 100 shots. The laser beam leaving the 10 mm-thick sample of fused silica is collected and directed to a $f = 25$ cm spectrometer equipped with a 600 grooves/mm diffraction grating and a linear 16 bit CCD camera. The entrance slit is set at 10 μm. The power spectrum of the nonlinearly propagating pulse exhibits a broadening which extends over the entire visible spectrum. Less than 1% of the incident energy is contained in the visible part of the white continuum. As can be seen from Fig. 2b, there is a fringe structure on the self-guided pulse spectrum with an inter-fringe space of about 16 nm. This spectral interval corresponds to the fringe pattern of two ultrashort (~ 60 fs) pulses separated by 120 fs and is thus compatible with the double-peak pulse structure implied from the autocorrelation traces shown in Fig. 2a.

We have used a three-dimensional code to simulate the propagation of ultra-short laser pulses in fused silica. The code resolves an extended nonlinear Schrödinger equation, coupled with the density of electrons produced by multiphoton band-to-band transitions. We assume that the beam is linearly polarized with the central frequency ω_0 ($\lambda_0 = 800$ nm) and wavenumber $k = n_0 k_0$ ($k_0 = \omega_0/c$). The pulse has the radial symmetry and its complex envelope $\mathcal{E}(r,t,z)$ evolves according to

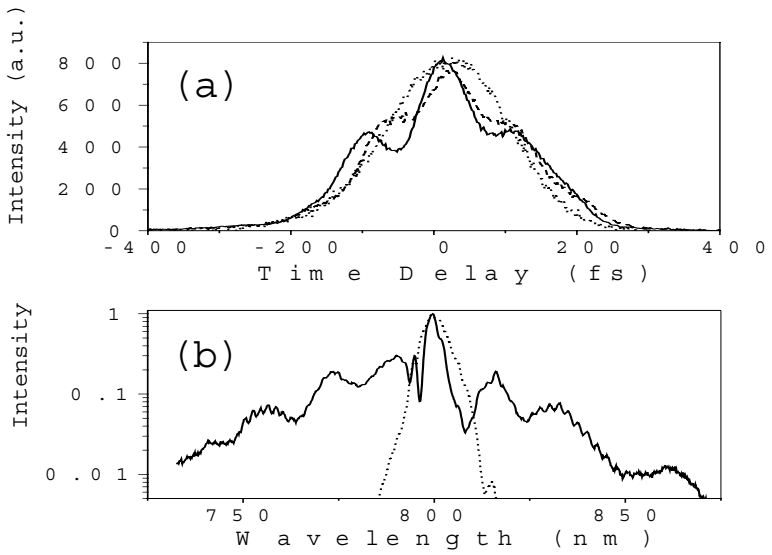

Fig. 2: (a) Measured autocorrelation of the filament at 2 mm (solid) and 5 mm (dashed), together with that of the initial laser pulse (dotted). (b) Power spectrum of the input pulse (dotted) and that of the filament at 10 mm (solid).

$$\frac{\partial \mathcal{E}}{\partial z} = \frac{i}{2k} T^{-1} \left(\frac{\partial^2}{\partial r^2} + \frac{1}{r} \frac{\partial}{\partial r} \right) \mathcal{E} - \frac{ik''}{2} \frac{\partial^2 \mathcal{E}}{\partial \tau^2} + ik_0 n_2 T \left(|\mathcal{E}|^2 \mathcal{E} \right)$$
$$- \left(\frac{n_0^2 U_i \alpha}{2} + \frac{ik_0}{2\rho_c} \right) T^{-1} (\rho \mathcal{E}) - \frac{K \hbar \omega_0 \sigma_K \rho_{at}}{2} |\mathcal{E}|^{2K-2} \mathcal{E}, \quad (1)$$

$$\partial \rho / \partial \tau = \sigma_K |\mathcal{E}|^{2K} (\rho_{at} - \rho) + \alpha \rho |\mathcal{E}|^2 - \rho / \tau_r, \quad (2)$$

where τ is the retarded time variable $t - z/v_g$ with group velocity v_g. The right-hand side of Eq. (1) describes diffraction in the transverse plane, normal group-velocity dispersion (GVD) with coefficient $k'' \equiv \partial^2 k / \partial \omega^2 \big|_{\omega_0} = 361$ fs^2/cm, Kerr self-focusing, plasma absorption ($\sim n_0^2 U_i \alpha$) and defocusing that involve the electron density ρ excited by multiphoton ionization (MPI), and related multiphoton absorption (MPA). Connected with these last two quantities, ρ_c denotes the critical plasma density and ρ_{at} is the background atom density ($\rho_{at} / \rho_c \simeq 12$ where ρ_{at} = 2.1 10^{22} atoms/cm^3). Band-to-band transitions are induced in silica from the gap potential U_i = 7.6 eV [23], yielding the number of photons K = 5 required for ionization. The MPI coefficient then reads as σ_K = 1.3 10^{-55} s^{-1}cm^{2K}/W^K. The first term on the right-hand side of Eq. (2) describes the MPI contribution to free electron generation, while the second term accounts for avalanche ionization with $\alpha = \sigma / n_0^2 U_i$ where σ is the inverse bremsstrahlung cross-section [5]. The third term represents electron recombination with a characteristic time $\tau_r \simeq 150$ fs in fused silica [22]. In addition, we included, through the operator $T \equiv 1 + (i/\omega_0) \partial / \partial \tau$, self-steepening effects with the operator T in front of the cubic nonlinearity, and space-time focusing with T^{-1} in front of the transverse Laplacian (see, e.g., Refs. [12, 14] for more details)

Fig. 3(a)

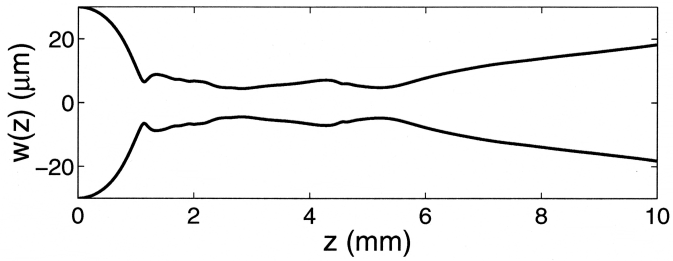

Fig. 3(b)

Fig. 3(c)

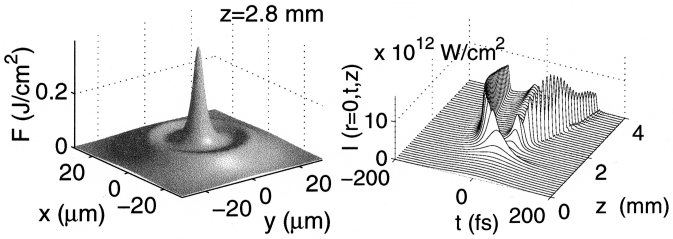

Fig. 3: (a) Calculated diameter of the filament along its propagation. (b) Calculated 3D fluence profile of the filament at 2.8 mm. (c) Temporal profile of the filament along the first 4 mm of propagation.

.

Equation (1) is solved by means of a Fourier spectral decomposition in time and a standard Crank-Nicholson scheme in space, applied to each spectral component. As initial conditions, we consider input beams lying at the entrance face of the glass sample similarly to the experiment. Those have the standard Gaussian shape with input power P_{in}, and a waist w_0 = 30 μm (measured experimentally). The temporal FWHM diameter is 160 fs. The results for initial energy E_{in} = 2 μJ and power $P_{in} \simeq 5P_{cr}$ are shown in Fig. 3. Fig. 3(a) displays evidence of the emergence of a light channel, having a diameter close to that measured experimentally. Fig. 3(b) shows a 3D fluence profile of the filament at a distance of z = 2.8 mm. Note the ring structure that surrounds the filament, in agreement with the experiment (Fig. 1d). Fig. 3(c) shows the distortions in the temporal intensity profile of the beam. Two main peaks are formed, which both undergo a sharp steepening. They keep an almost similar distribution over a distance of about 4 mm, while afterwards a more complex multi-peaked structure develops.

For completeness, we also numerically computed the intensity spectra in wavelength and the temporal autocorrelations of the transmitted beam. The latter, detailed in Fig. 4(a), form a three-peaked structure. Keeping in mind that the number of peaks $\mathcal{N}$= 2N - 1 yields the number of split pulses, N, one easily infers that two main spikes characterize the temporal profile of the beam. By comparing the experimental (Fig. 2a) and numerical autocorrelations, we can observe their similar aspects at different propagation distances. Fig. 4(b) show the input laser pulse power spectrum, together with the filament spectrum at

Fig. 4(a)

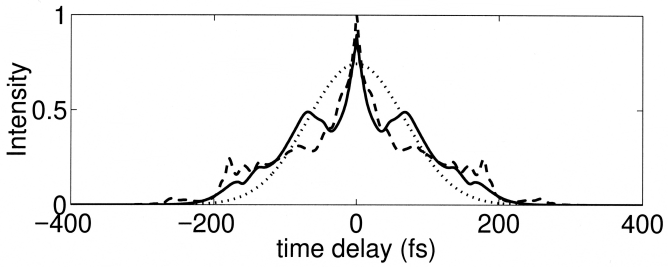

Fig. 4(b)

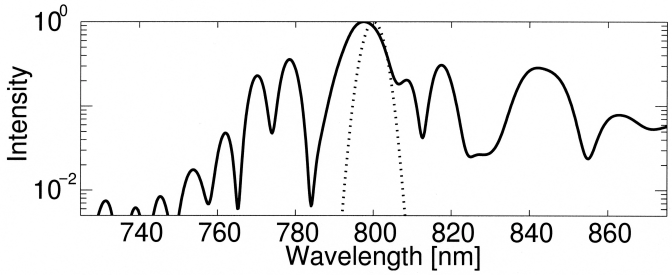

Fig. 4: (a) Calculated autocorrelations: of the initial pulse (dotted), of the filament at 2 mm (solid) and 5 mm (dashed). (b) Power spectra: initial pulse (dotted) and filament (solid) at 10 mm.

10 mm. Again, we can notice the good agreement between the experimental data (Fig. 2b) and the numerical results, even on the satellite spectral components of the filament.

Inspection of the simulations brings to light that filament robustness is mainly due to a dynamic balance between MPI and optical Kerr effect. Although they may promote a resembling two-spike temporal profile, group-velocity dispersion, self-steepening and space-time focusing play a secondary role in the present case. To check this point, we performed several simulations, with and without temporal dispersive effects (GVD and/or the operators T, T^{-1}). We observed that the action of these terms had no significant influence on the stabilization of the light channel, which is actually promoted by the plasma density alone. This property agrees with the prediction by Henz and Herrmann [19]. However, the numerical simulations of Ref [19] does not show the formation of two pulses.

It is interesting to compare our results to the cases previously explored in Ref. [15-17]. Using different initial conditions (i.e., beam geometry), these authors found a propagation regime in fused silica without long-range channeling, but where pulse splitting occurred. From their model equation eluding MPI, GVD, together with self-steepening and space-time focusing, was concluded to provide the main mechanism in limiting the self-focusing of ultra-short pulses through the splitting process. Similar regimes led by the interplay between GVD and self-focusing, with plasma generation playing a minor role, were revealed in our simulations but for much larger values of the GVD coefficient (such as the one used in Ref. [14]) or larger initial beams (as those used in Ref. [15-17]).

In conclusion we have presented, for the first time, a long range filamentation in fused silica using femtosecond IR laser pulses. The self-guided pulse is accompanied by an

important spectral broadening (super-continuum generation) and pulse breaking with two or more shorter sub-pulses. Our numerical simulations reproduce most of the experimental observations. They show that the self-guided filament actually results from the balance between self-focusing and MPI.

We kindly acknowdlege the expert assistance of Y.-B. André and G. Hamoniaux.

References

[1] A. Braun, G. Korn, X. Liu, D. Du, J. Squier, and G. Mourou, Opt. Lett. **20**, 73 (1995).

[2] E. T. J. Nibbering *et al.,* Opt. Lett. **21**, 62 (1996).

[3] L. Wöste *et al*., Laser und Optoelektronik **29**, 51 (1997).

[4] B. La Fontaine *et al*., Phys. Plasmas **6**, 1615 (1999).

[5] M. Mlejnek, E. M. Wright, and J. V. Moloney, Opt. Lett. **23**, 382 (1998).

[6] H. R. Lange *et al.*, Opt. Lett. **23**, 120 (1998); A. Chiron *et al*., Eur. Phys. J. D **6**, 383 (1999).

[7] L. Bergé and A. Couairon, Phys. Plasmas **7**, 210 (2000).

[8] L.V. Keldysh, Sov. Phys. JETP **20**, 1307 (1965).

[9] L. Bergé and A. Couairon, Phys. Rev. Lett. **86**, 1003 (2001).

[10] P. Chernev and V. Petrov, Opt. Lett. **17**, 172 (1994); J. E. Rothenberg, *ibidem*, 583 (1992).

[11] V. Tikhonenko, J. Christou, and B. Luther-Davies, Phys. Rev. Lett. **76**, 2698 (1996).

[12] T. Brabec and F. Krausz, Phys. Rev. Lett. **78**, 3282 (1997); *ibidem*, Rev. Mod. Phys. 72, 545 (2000).

[13] J. K. Ranka and A. L. Gaeta, Opt. Lett. **23**, 534 (1998).

[14] A. L. Gaeta, Phys. Rev. Lett. **84**, 3582 (2000).

[15] J. K. Ranka, R. W. Schirmer, and A. L. Gaeta, Phys. Rev. Lett. **77**, 3783 (1996).

[16] S. A. Diddams, H.K. Eaton, A.A. Zozulya, and T.S. Clement, Opt. Lett. **23**, 379 (1998).

[17] A. A. Zozulya, S. A. Diddams, A. G. Van Engen, and T. S. Clement, Phys. Rev. Lett. **82**, 1430 (1999).

[18] A. Brodeur and S. L. Chin, J. Opt. Soc. Am. B **16**, 637 (1999).

[19] S. Henz and J. Herrmann, Phys. Rev. A **59**, 2528 (1999).

[20] E. Baubeau, C. Le Blanc, F. Salin, CLEO'97, 407 (1997).

[21] I. G. Koprinkov, A. Suda, P. Wang, K. Midorikawa, Phys. Rev. Lett. **84**, 3847 (2000).

[22] P. Audebert et al., Phys. Rev. Lett. **73**, 1990 (1994).

[23] R. Tohmon, H. Mizuno, Y. Ohki, K. Sasagane, K. Nagasawa, Y. Hama, Phys. Rev. B **39**, 1337 (1989).

6. Continuum generation: "Teramobile"

6.1. Introduction

In the present chapter we focus are interest to the spectral characteristics of the femtosecond laser filaments discussed in the previous chapters of this thesis. In the view of potential LIDAR application white light continuum generation in the femtosecond filaments has attracted much interest the last years. A French-German collaboration between four research groups from four different universities (Ecole Polytechnique, University of Jena , University of Lyon, and University of Berlin) are involved in a common project to study long range propagation of terrawatt femtosecond laser pulses in atmosphere using a prototype mobile laser system ("Teramobile" project). Here we present the first measurement of the infrared extension (from the visible to above 4 μm) in the filament continuum spectrum, done within this collaboration project. The details of the experiment are presented in appendix 6.1.

6.2. Continuum generation

The strong self-phase modulation, four-photon coupling, induced modulation, and cross-phase modulation by an ultrashort pulse make a visible laser spectrum white. A large spectral coverage radiation has been developed as a useful light source for pump-probe time-resolved spectroscopy. UV Excimer lasers and frequency-upconverted solid-state lasers have been introduced as a pumping laser source to extend the white spectrum to shorter-wavelength regions. The continuum's spectral intensity, however, drastically decreases with detuning frequency. This limitation is caused mainly by the nonuniform intensity distribution in the beam cross section through a focal point because the modulation depth changes as a function of light intensity. Efficient modulations are produced only in the central part of the focusing spot with a limited interaction length. The maximum possible laser intensity is also limited by an excessive amount of nonlinear absorption or plasma formation in a self-phase-modulation medium. Spatial uniformity and an extremely large intensity interaction-length product are required for a wideband and flat-topped spectral shape to be realized. For this reason femtosecond filaments are ideal candidates for maximum spectral conversion.

Appendix 6.1

"Infrared extension of the supercontinuum generated by femtosecond terawatt laser pulses propagating in the atmosphere"

OPTICS LETTERS **25**, 1397 (2000)

Infrared extension of the supercontinuum generated by femtosecond terawatt laser pulses propagating in the atmosphere

J. Kasparian and R. Sauerbrey

Institut für Optik und Quantenelektronik, Max-Wien-Platz 1, 07743 Jena, Germany

D. Mondelain, S. Niedermeier, J. Yu, and J.-P. Wolf

Laboratoire de Spectrometrie Ionique et Moléculaire, Université Claude Bernard Lyon 1, Unité Mixte de Recherche 5579, Centre National de la Recherche Scientifique, F-69622 Villeurbanne Cedex, Lyon, France

Y.-B. André, M. Franco, B. Prade, S. Tzortzakis, and A. Mysyrowicz

Laboratoire d'Optique Appliquée, Unité Mixte de Recherche 7639, Centre National de la Recherche Scientifique Ecole Nationale Supérieure des Techniques Avancées—Ecole Polytechnique, Centre de l'Yvette, F-91761 Palaiseau Cedex, France

M. Rodriguez, H. Wille, and L. Wöste

Institut für Experimentalphysik, Freie Universität Berlin, Arnimallee 14, D-14195 Berlin, Germany

Received July 5, 2000

We investigated the spectral behavior of a white-light continuum generated in air by 2-TW femtosecond laser pulses at 800 nm. The spectrum extends at least from 300 nm to 4.5 μm. From 1 to 1.6 μm the continuum's intensity increases strongly with the laser energy and depends on the initial chirp. © 2000 Optical Society of America

OCIS codes: 190.1900, 190.7110, 280.3640, 300.6340.

The propagation of high-peak-power laser pulses in transparent matter gives rise to strong nonlinear effects such as four-wave mixing,[1] stimulated Raman processes,[2] self-focusing,[3] and self-phase modulation (SPM),[4–6] which lead to strong modifications of the pulse characteristics. Self-focusing occurs because of the radial intensity variation in the laser beam, whereas SPM is due to the temporal variation of the laser intensity. Although both effects may be observed in conventional laser pulse propagation experiments, they dominate the behavior of ultrashort terawatt laser pulses. One of the most spectacular features observed is the formation of white-light filaments in air, so-called self-guided channels.[7,8] Self-focusing produces a large increase in rise of intensity in the filaments and permits multiphoton ionization of air and thus the formation of a low-density plasma, as demonstrated by electrical conductivity measurements.[9,10] Therefore self-focusing is balanced by diffraction as well as by refraction from the plasma, and thus the focused laser intensity is limited. The propagation is dynamically guided over distances much longer than the Rayleigh length, as much as several tens of meters,[8,11] with a diameter reported to be $\sim$100 μm.[7]

The spectral content of the white-light supercontinuum generated by high-power lasers has been a subject of interest since 1970.[1,12,13] However, because of limited peak power, experiments then were restricted to condensed media. Recently improvements in ultrashort lasers have permitted the results to be extended to gases. The spectral content of the supercontinuum generated by a 2-TW laser propagating in atmospheric-pressure rare gases has been measured in the visible and the UV, from 150 to 900 nm.[14] Until now, however, to our knowledge no experiment in the IR part of the supercontinuum generated in atmospheric-pressure gases has been performed.

In this Letter we report the measurement of the spectrum of the white-light continuum, particularly in the IR, up to 4.5 μm. The influence of the laser's initial power and chirp is also investigated. Besides the fundamental interest, that in measuring the IR part of the supercontinuum is stimulated by the potential application of the laser-induced continuum to lidar remote-sensing measurements.[15,16] The laser-induced continuum, as opposed to the traditional lidar technique,[17] allows simultaneous multispectral measurements to be made. This is especially interesting in the 3–3.5-μm IR band, where high-energy tunable laser pulses are difficult to produce and where a number of pollutant gases, in particular, volatile organic compounds have strong overlapping absorption bands.

In our experiments we used two state-of-the-art Ti:sapphire chirped-pulse amplification laser systems that had the following parameters. For system A (located at the École National Supérieure de Techniques Avancées): 60-mJ energy; 35-fs minimal pulse duration after the compressor (corresponding to 86-fs minimal pulse duration after the focusing lens); and beam diameter, 25 mm FWHM. The duration of the

0146-9592/00/181397-03$15.00/0

laser pulse was elongated by use of the grating compressor, thus producing chirped pulses. For system B (located at the Institut für Optkik und Quantenelektronic): 200-mJ energy; 100-fs minimal pulse duration after the compressor; and beam diameter, 35 mm FWHM. The energy was varied continuously. Both systems provided a peak power of ~2 TW at 800 nm (i.e., $\sim 10^{16}$ W/cm^2 if it was focused into a single filament), but, because the pulse durations were different, the intensity rise and fall times of the two systems were different.

We used several detection systems to cover the wavelength domain under investigation. For the visible spectral region an optical multichannel analyzer (Chromex 500 IS; $f/8$; spectral range, 400–1000 nm; grating, 150 lines/mm; resolution, 1.28 cm^{-1}; cooled; Si-ICCD-576, Princeton Instruments; 576 × 394 pixels) was used. In the IR, a prism spectrometer (Zeiss; 400 nm–2.7 μm; resolution, <5 nm) and a Perkin-Elmer double-pass prism spectrometer (focal length, 27 cm; LiF prism; transmission, up to 10 μm) were equipped with a germanium detector and a liquid-nitrogen-cooled InSb detector (1.5–5.6 μm, Hamamatsu). Additionally, IR interference filters (Corion) suppressed the fundamental wavelength of the laser beam.

In the experiment, the output of the laser was slightly focused with thin fused-silica lenses with 8- and 10-m focal lengths. We verified experimentally that, because of the lenses' large diameter (25 mm FWHM) and small thickness (3 mm), no continuum was generated in the lenses. Generation of the continuum occurred in the focal region, with the broadband continuum propagating farther with nearly the same divergence as the laser beam itself (see below). Power measurements before and after the focus showed that the continuum generation process caused no significant energy loss in the focus.

The spectral measurements took place at a total distance of ~30 m from the lens and hence after ~20 m of filament propagation. At this position the laser beam had a diameter of 20–25 cm. The angular pattern of white-light generation is beyond the scope of this Letter and is currently under investigation.[18] However, the white light is emitted mainly in the forward direction. Therefore all the spectral measurements were made in the forward direction, with an aluminum-coated mirror reflecting a small portion of the light to the entrance slit of the spectrometer used. The detection setup and the detectors were identical for both laser systems.

Figure 1 shows the spectral distribution of the white-light continuum generated in air by laser system A for a pulse duration of 115 fs after the focusing lens without chirp at the end of the compressor and for an 86-fs pulse duration. The spectrum was assembled from four single spectra (300–900 and 700–1800 nm and 1.5–2.7 and 1.5–4.5 μm) taken with four distinct detection systems with overlapping sensibility domains. The continuum band is very broad, extending at least to 4.5 μm.

In the IR, a region in which we know of no previous experiments in air, an almost exponential decay over 4 orders of magnitude up to 2.5 μm is observed. From 2.5 to 4.5 μm a slower decay is recorded, of 1 order of magnitude only. Above 4.5 μm, the spectral intensity was too low permit us to discriminate detector noise. Water absorption bands superimposed over a flat continuum spectrum are observed at 1.8 and 2.5 μm, suggesting that the use of a white-light continuum as a light source for spectroscopic remote sensing of the atmosphere[16] can be extended to the IR.

The dependence of the signal on the incident laser pulse energy was investigated with laser system B. As shown in the inset of Fig. 1, an initial factor-of-2 variation in intensity leads not to a variation in spectral shape in the 1–1.6-μm region to only to an overall decrease in efficiency by almost a factor of 1. Note that the conversion efficiency with laser system B, which provides shorter pulses, is 1 order of magnitude lower than with system A (Fig. 1), although both systems provide the same peak power of 2 TW.

The signal's dependence on the chirp (and thus the pulse duration) was investigated with laser system A. Figure 2 shows the continuum conversion efficiency at two wavelengths (1.7 and 3 μm, with 5-nm resolution) as a function of laser chirp. The optimal chirp setting depends on the emission wavelength to be optimized. Moreover, as shown in Fig. 1, the overall conversion efficiency in the near IR changes significantly when the chirp setting is changed.

SPM is generally believed to be the dominant process involved in continuum emission.[4–6,14,19] A simple calculation, with parameters that are typical of our experiments, and with a constant Gaussian beam, showed that SPM alone is in semiquantitative agreement with our experiments: (i) the calculated

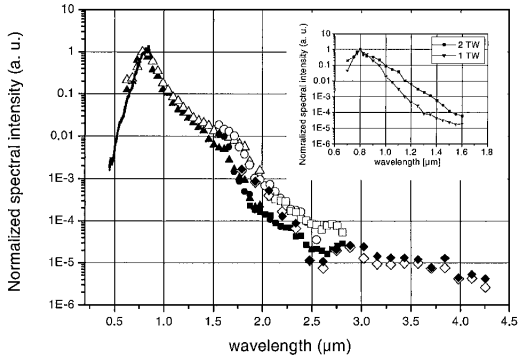

Fig. 1. Measured spectrum of the white-light continuum generated in the center of the beam by 2-TW laser pulses (laser system A). The results are shown for two different chirp settings that correspond to (i) an initial pulse duration of 35 fs without chirp after the compressor (filled symbols) and (ii) a 55-fs initial pulse duration with negative chirp after the compressor (open symbols). These curves are composed of 5 (4) distinct spectra from 5 (4) detection units, respectively, that correspond to the different symbol shapes for each curve. Inset, spectrum of the white-light continuum generated in the center of the beam by 100 fs pulses (laser system B) as a function of pulse power value (200 and 100 mJ for 2 and 1 TW, respectively). The two curves have the same normalization factor.

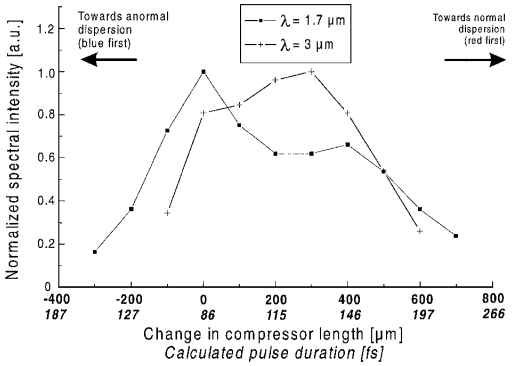

Fig. 2. Initial chirp dependence of the white-light continuum generated by laser system A at two distinct wavelengths (1.7 and 3 μm, with 5 nm resolution). The two curves have the same normalization. The chirp scale is shown as the change in the compressor length, with 0 set arbitrarily, to the chirp value of the curve with open symbols in Fig. 1. Numbers in italics are the corresponding calculated pulse lengths after the exit window and the lens.

spectral content of white light after 20-m propagation in a filament extends from a few hundred nanometers to at least 5 μm; (ii) laser system A, with shorter pulses, has a larger white-light generation efficiency than system B. This result supports the assumption that SPM is the main process in white-light continuum generation in air. However, a quantitative understanding of the continuum is still a subject for research and needs much more-complex discussion,[19,20] which is beyond the scope of this Letter. Understanding the influence of chirp will require more-detailed calculations.

For atmospheric applications the initial pulse chirp is also critical for the behavior of laser propagation. In particular, because of group-velocity dispersion in air, a negatively chirped pulse will recombine as an ultrashort pulse at a given distance away from the laser,[16,21] giving rise to localized white-light generation. The white-light pulse will also undergo group-velocity dispersion. However, because of tiny changes in the refractive index of air, the pulse broadening will be only 12 ps/km, as calculated with the Rank formula for a pulse ranging from 300 nm to 4.5 μm.

In conclusion, we have measured the wavelength dependence of the white-light continuum emitted from filaments generated in air by high-power femtosecond laser pulses up to 4.5 μm and down to 300 nm. The results show that the shape and the rate of rise in power of the excitation laser pulses have critical effects on conversion efficiency. As far as applications are concerned, a white-light continuum provides broadband pulses with a smooth spectrum up to at least 4.5 μm. It could therefore be used as an *in situ*–produced white lamp, permitting multispectral lidar measurements of atmospheric constituents to be expanded from the visible region[15,16] to the IR.

The authors acknowledge the help of the laser teams at the institutions at Palaiseau and Jena; of A. Reichmann, who provided the prism spectrometer; and of T. Töpfer, who provided valuable calibrations, tools, and some detectors. This study was done in the framework of the Teramobile project, a joint French–German project funded by the Centre National de la Recherche Scientifique and the Deutsche Forschungsgemeinschaft. R. Sauerbrey's e-mail address is sauerbrey@qe.physik.uni-jena.de.

References

1. R. R. Alfano and S. L. Shapiro, Phys. Rev. Lett. **24,** 584 (1970).
2. L. Smith, P. Liu, and M. Bloembergen, Phys. Rev. A **15,** 2396 (1977).
3. D. Strickland and P. B. Corkum, J. Opt. Soc. Am. B **11,** 492 (1994).
4. R. Alfano and S. L. Shapiro, Phys. Rev. Lett. **24,** 592 (1970).
5. R. R. Alfano and S. L. Shapiro, Phys. Rev. Lett. **24,** 1217 (1970).
6. A. Brodeur and S. L. Chin, J. Opt. Soc. Am. B **16,** 637 (1999).
7. A. Braun, G. Korn, X. Liu, D. Du, J. Squier, and G. Mourou, Opt. Lett. **20,** 73 (1995).
8. E. T. J. Nibbering, P. F. Curley, G. Grillon, B. S. Prade, M. A. Franco, F. Salin, and A. Mysyrowicz, Opt. Lett. **21,** 62 (1996).
9. H. Schillinger and R. Sauerbrey, Appl. Phys. B **68,** 753 (1999).
10. S. Tzortzakis, M. Franco, Y.-B. Andre, A. Chiron, B. Lamouroux, B. Prade, and A. Mysyrowicz, Phys. Rev. E **60,** R3505 (1999).
11. M. Mlejnek, M. Kolesik, J. V. Moloney, and E. M. Wright, Opt. Lett. **23,** 2938 (1999).
12. W. Yu, R. R. Alfano, C. L. Sam, and R. J. Seymour, Opt. Commun. **14,** 344 (1975).
13. P. B. Corkum, P. P. Ho, R. R. Alfano, and J. T. Manassah, Opt. Lett. **10,** 624 (1985).
14. H. Nishioka, W. Odajima, K. Ueda, and H. Takuma, Opt. Lett. **20,** 2505 (1995).
15. L. Wöste, C. Wedekind, H. Wille, P. Rairoux, B. Stein, S. Nikolov, Chr. Werner, S. Niedermeier, H. Schillinger, and R. Sauerbrey, Laser Optoelektron. **29,** 51 (1997).
16. P. Rairoux, H. Schillinger, S. Niedermeier, M. Rodriguez, F. Ronneberger, R. Sauerbrey, B. Stein, D. Waite, C. Wedekind, H. Wille, and L. Wöste, "Remote sensing of the atmosphere using ultrashort laser pulses," Phys. B (to be published).
17. R. M. Measures, *Laser Remote Sensing—Fundamentals and Applications* (Wiley/Interscience, New York, 1984).
18. D. Mondelain, G. Ange, R. Volk, S. Niedermeier, J. Kasparian, J. Yu, R. Sauerbrey, and J. P. Wolf, Laboratoire Spectrométrie Ionique et Moléculaire, Université Claude Bernard Lyon 1, Unité Mixte de Recherche 5579, Centre National de la Recherche Scientifique, F-69622 Villeurbanne Cedex, Lyon, France, are preparing a manuscript to be called "Self-reflection-enhanced back scattering from white light filaments induced by high intensity femtosecond laser pulses propagating in air."
19. A. Gaeta, Phys. Rev. Lett. **84,** 3582 (2000).
20. I. Golub, Opt. Lett. **16,** 305 (1990).
21. J. Kasparian and J.-P. Wolf, Opt. Commun. **152,** 355 (1998).

Final Remarks

Femtosecond pulse filamentation has been studied for more than 6 years now and we have a quite broad view of its characteristics and physical mechanisms involved. In this thesis we have described the results of our experimental and numerical studies on the subject during the last three years. We have presented new observations and calculations on femtosecond pulse filamentation in different transparent nonlinear media at different initial conditions. The information included in the current study complements our knowledge on fs filamentation and helps to the better understanding of the physics involved. General, common characteristics are revealed for all type of fs filaments. Spatial confinement, electron plasma channel formation, spectral broadening as well as pulse breaking with a double pulse formation are some of the attributes that seems to identify fs filaments.

The novelties present in this thesis can be summarized as follows. In chapter 1 we presented experimental evidence of ionization in the filament with precise estimation of the electron density that was possible employing two techniques especially conceived for this purpose. Multi-filamentation and the first clear experimental evidence of femtosecond beam break-up and coalescence were described in chapter 2. The first detailed study of femtosecond ultraviolet pulse filamentation was analyzed in chapter 3. One of the most interesting applications of fs laser filaments that of triggering and guiding electric discharges was addressed in chapter 4. There we presented the first experimental demonstration of filament-guided electric discharges using only the fs filament plasma channel, not the hot plasma produced at the focal region of a lens. Our analysis provided a concrete physical explanation of the mechanisms involved in this special kind of electric discharge. In chapter 5 we reported the first observation of fs filamentation in fused silica. Finally in chapter 6 we discussed the continuum generation in fs filamentation.

Although this is an extensive study, research on fs filamentation is far from being saturated. Numerous questions remain open both on fundamental aspects as well as on experimental observations. To cite only a few examples: polarization dependence of filamentation, control of multi-filamentation, kilometric distance propagation, continuum optimization, long scale discharge control, LIDAR etc.

Résumé en Français

Introduction

La propagation d'impulsions électromagnétiques est d'importance fondamentale en science pure et appliquée, et le développement récent des sources d'impulsions laser ultra-courtes intenses a ajouté beaucoup de visions intéressantes à ce problème. Les larges bandes spectrales, les puissances très élevées, et la nature (3+1) dimensionnelle de ces champs (3 dimensions spatiales plus le temps) provoquent des effets linéaires et non-linéaires complexes qui ont posé des défis significatifs aux chercheurs.

Ces dernières années un effort important a été consacré à l'étude de la propagation des faisceaux laser puissants en atmosphère aussi bien que dans d'autres matériaux transparents, comme par exemple des verres. Un intérêt particulier s'est concentré sur des systèmes laser femtoseconde (fs), capables de fournir des puissances très élevées avec peu d'énergie. En raison de la puissance élevée, la réponse nonlinéaire du milieu joue un rôle prépondérant dans la propagation. Quand des impulsions laser ultracourtes et intenses sont lancées dans l'air il s'auto-organisent en filaments, qui se propagent sur des distances très longues. En parallèle aux expériences, de simulations numériques de propagation nonlinéaire ont été développées qui résolvent une équation de Schrödinger nonlinéaire (NLS) incluant: la diffraction linéaire, l'effet Kerr optique, la génération de plasma par des absorptions multiphotoniques (MPI), la dispersion normale de vitesse de groupe (GVD) ou même d'autres termes d'ordre plus élevé de dispersion temporelle.

Cette thèse présente les études d'autoguidage des impulsions femtoseconde (appeler aussi dans la suite filamentation) que j'ai réalisées pendant les trois dernières années. La filamentation des faisceaux employant des impulsions laser IR femtoseconde puissantes avaient déjà été observé et rapporté par plusieurs groupes [1-3]. De ces premiers travaux on a généralement accepté que l'ionisation joue le rôle le plus important après l'auto-focalisation (SF) pour la filamentation d'impulsions fs dans l'air. Cependant aucune évidence expérimentale d'ionisation n'était disponible au début de mon travail de thèse. Nous avons développé et appliqué deux techniques expérimentales originales, qui ont permis de donner des évaluations précises de la densité

électronique dans les filaments. Les résultats de ces expériences avec une analyse complète sont présentés dans le *chapitre 1 (section 1 de ce résumé)*.

Mlejnek *et al.* ont rapporté récemment [4] une vraie simulation numérique tri-dimensionnelle (3d) où l'introduction d'un faisceau laser étendu (diamètre de 7 millimètres) avec une puissance supérieure à 35 fois la puissance critique (P_{cr}) mène à une multi-filamentation. Dans le *chapitre 2 (section 2 de ce résumé)* nous présentons les différentes étapes menant à la filamentation fs. Nous montrons pour la première fois clairement, la rupture initiale d'une impulsion fs en deux canaux de lumière dans le régime Kerr. Ces deux canaux fusionnent plus loin en un seul faisceau auto-guidé qui se propage sous forme d'un filament robuste sur un grande nombre de distances de Rayleigh.

La plupart des recherches sur les filaments fs ont été faites avec des impulsions laser infrarouges et très peu d'information était disponible, au début de ma thèse, sur la propagation nonlinéaire d'impulsions fs ultraviolettes. Dans le *chapitre 3 (section 3 de ce résumé)* nous présentons la première étude expérimentale détaillée sur la propagation nonlinéaire d'impulsions ultraviolettes ultracourtes dans l'air. L'autoguidage d'impulsions UV est démontré avec des filaments robustes se propageant sur plusieurs mètres.

Les décharges déclenchées à l'aide de lasers IR fs puissants est un domaine actif de recherche. Dans le *chapitre 4 (section 4 de ce résumé)* nous rapportons la première démonstration expérimentale d'une décharge électrique déclenchée et guidée par un filament créé par une impulsion fs. Nous analysons et donnons une explication physique concrète des mécanismes impliqués dans ce genre spécial de décharge électrique.

Ranka *et al.* [5] Zozulya *et al.* [6] et Diddams *et al.* [7] ont présenté la fragmentation d'impulsions fs en de multiples sous-impulsions après propagation dans des verres transparents (BK7). Henz et Herrmann [8] ont présenté une simulation numérique qui montre l'existence d'un quasi-soliton se propageant dans la silice fondue. Ce filament est le résultat de l'équilibre entre l'auto-focalisation et l'ionisation multiphotonique, la dispersion de vitesse de groupe jouant un rôle mineur négligeable. Dans le *chapitre 5 (section 5 de ce résumé)* nous présentons la première évidence expérimentale d'un filament fs auto-guidé se propageant sur un grande nombre de distances de Rayleigh dans la silice fondue. Nous montrons que les impulsions se cassent et se raccourcissent au cour de leur propagation.

Brodeur et Chin [9] ont présenté les mécanismes de la génération de continuum de lumière blanche quand des impulsions intenses ultracourtes traversent des solides transparents. Ils ont aussi démontré que la lumière blanche est un rayonnement cohérent (laser de lumière blanche) [10,11]. Nishioka *et al.* [12] ont montré que le spectre des filaments fs dans l'UV et le visible s'étendait de 150 nm à 900 nm. Dans le *chapitre 6 (section 6 de ce résumé)* nous présentons la première mesure de l'extension infrarouge du spectre des filaments fs, jusqu'à 4.5 μm, et nous discutons sur des applications LIDAR.

Ce sommaire en français présente brièvement, seulement les résultats les plus importants. Le lecteur est invité à consulter les chapitres précédents pour plus de détails.

1. Ionisation

L'importance de l'ionisation comme limiteur d'intensité et son rôle comme stabilisateur dans l'auto-guidage d'impulsions ultracourtes est généralement acceptée. Les simulations prévoient une densité moyenne d'électrons dans le filament d'environ 10^{16} cm^{-3}. Ces niveaux de densité sont très bas et rendent leur observation expérimentale très difficile, particulièrement à la pression atmosphérique. En conséquence au début de mon travail de thèse aucune mesure expérimentale de densité électronique n'avait été rapportée dans la littérature. Dans ce qui suit nous décrivons deux techniques expérimentales employées pour détecter de telles densités électroniques. La première est une technique électrique et la seconde une technique purement optique. La combinaison des deux peut nous fournir des mesures sensibles et précises.

1.1 Technique de conductivité électrique

Dans cette section, nous présentons l'évidence directe qu'un canal conducteur est en effet créé par des impulsions auto-guidées. En utilisant 14 mJ d'énergie laser, on observe une colonne de plasma se prolongeant au-delà d'une distance de 100 centimètres.

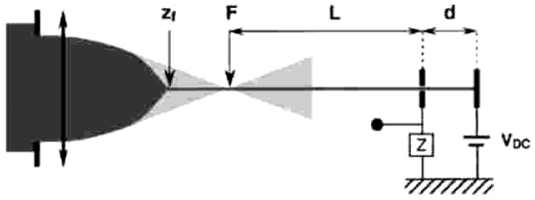

Fig. 1: Système expérimental. (voir texte)

Le montage expérimental, montré dans la Fig. 1, est simple dans son principe. Pour détecter la présence d'une colonne conductrice, nous mesurons le changement de la résistivité de l'air entre deux électrodes après passage d'un filament. L'impulsion laser initiale est fournie par un oscillateur Ti:S suivi d'un système d'amplification CPA. La longueur d'onde centrale est 800 nm, sa durée est 120 fs et son énergie peut atteindre 50 mJ. A la sortie du compresseur, le profil du faisceau est presque gaussien, avec un paramètre gaussien de w_0=12 mm. Le faisceau passe par un diaphragme de diamètre variable D et est focalisé dans l'air avec une lentille mince d'une distance focale F = 1 ou 2 m. Cette géométrie convergente réduit la distance nécessaire pour la formation d'une impulsion auto-guidée, permettant la réalisation d'expériences dans un laboratoire des dimensions restreintes.

Le filament traverse une première électrode en cuivre par un trou foré en son centre. Le diamètre du trou (1 millimètre) est un compromis. Un plus petit diaphragme détruirait la plupart des filaments avant qu'ils atteignent la deuxième électrode, en raison des fluctuations de leur position d'un tir à l'autre. D'autre part, avec un plus grand diaphragme le signal électrique diminue rapidement, en raison de la résistivité élevée entre le noyau ionisé du filament et le bord de l'électrode. Comme première électrode, nous avons également utilisé un miroir poli en acier inoxydable mis à incidence rasante à proximité du filament. Le faisceau empiète alors sur la deuxième électrode, se composant d'un bloc de cuivre massif ou, pour une séparation courte d'électrodes $d < 2$cm, d'une réplique de la première électrode avec son trou sur l'axe. Une tension DC typiquement de 1000 V est appliquée entre les deux électrodes. On mesure la circulation du courant par la colonne de plasma en enregistrant la tension induite à travers une résistance. La décharge électrique est non entretenue, donnant une impulsion avec un temps de montée et de descente de moins de 3 ns à travers une résistance de 100 Ω, limitée par le temps de réponse du système de détection (voir l'encart de fig. 2).

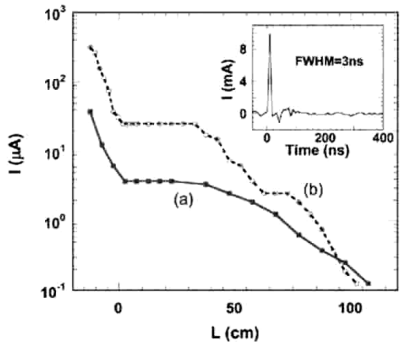

Fig. 2: Mesure du courant électrique en fonction de la distance L. La tension appliquée est de 1000 V DC avec un espacement d'électrodes de a) d = 11.5cm et b) d = 3 cm. L'énergie par impulsion est de 14 mJ et la résistance externe est de 8.2 k**Ω**. L = 0 est le foyer géométrique de la lentille. L'encart montre la forme de la tension, mesurée à travers une résistance de 100 **Ω**, avec une tension appliquée de 1500 V. Le signal est enregistré avec un oscilloscope numérique (Tektronix TDS 544A) d'une bande passante de 500 MHz.

Dans la fig. 2, le signal de tension crête, détecté à travers une résistance de 8.2 kΩ, est tracé en fonction de L pour le cas d'une impulsion de 14 mJ. La présence d'un plateau de conductivité

constante se prolongeant au delà du foyer géométrique à une distance d'environ 40 centimètres, est visible dans la fig. 2.

Le courant a été également mesuré en fonction de la séparation de deux électrodes dans la région de plateau, jusqu'à une distance d = 50 centimètres. Il indique une dépendance linéaire du courant avec $1/d$, pour une tension continue fixée (voir la fig. 3), ou avec la tension appliquée entre 500 et 2500 V pour une séparation fixée d. Ceci indique que nous sommes dans un régime ohmique, avec le courant directement proportionnel au champ appliqué. Le courant crête dans le plateau, mesuré avec une résistance de 100 Ω, est au moins 10 mA.

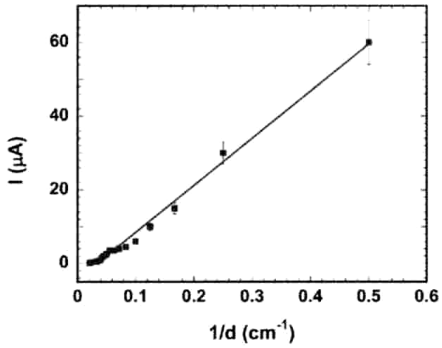

Fig. 3: Mesures du courant électrique en fonction de $1/d$, dans la région du plateau. La première électrode est à $L = 0$. L'énergie par impulsion laser est 14 mJ. La tension appliquée est 1000 V. La résistance externe est 8.2 kΩ.

Nous discutons maintenant la question de l'origine de la conductivité. On peut rejeter une interprétation basée sur la présence d'un jet d'électrons rapides éjectés d'une électrode et rassemblés par l'autre du fait qu'une deuxième électrode avec un trou donne essentiellement les mêmes résultats que l'électrode massive. Nous avons également comparé les signaux obtenus en inversant la polarité entre les deux électrodes. Les résultats sont montrés dans la fig. 4. Aucun changement crucial du signal n'est détecté avec la polarité, sauf dans une petite région avant le foyer géométrique du faisceau, et seulement pour un petit espacement entre les électrodes (d < 5 centimètres).

Une origine physique plus plausible pour la présence des charges de conduction est l'ionisation multiphotonique, un processus jouant un rôle crucial dans l'auto-guidage d'une impulsion. Nous avons confronté nos mesures avec les résultats numériques d'un code de propagation 3d avec

des conditions initiales proches de celles de l'expérience. Selon la simulation, la naissance du filament devrait se produire 30 centimètres avant le foyer géométrique. Ce déplacement du début de la filamentation avant le foyer géométrique peut s'expliquer simplement [13]: le point focal se déplace en arrière du foyer géométrique le long de l'axe z de propagation pendant la partie croissante de l'impulsion laser. Ce champ forme un canal ionisé s'étendant du foyer géométrique jusqu'à une distance montrée par la flèche dans la fig. 4. Cette position est proche du début de la zone de conduction mesurée (fig. 4).

On peut également comparer la densité calculée d'électrons dans le noyau de conduction du filament aux valeurs extraites à partir des mesures. La simulation rapporte une intensité de l'ordre de $10^{14} W/cm^2$ par la montée subite de l'ionisation. À cette valeur d'intensité, le taux d'ionisation est de l'ordre de 10^{-3} et seulement des atomes une fois ionisés sont formés. Dans le noyau de conduction correspondant à un diamètre estimé par le code numérique devant se trouver entre 40 et 100 μm (FWHM), une densité libre moyenne d'électrons s'étendant entre 3×10^{16} et $2\times10^{17} cm^{-3}$ est prévue.

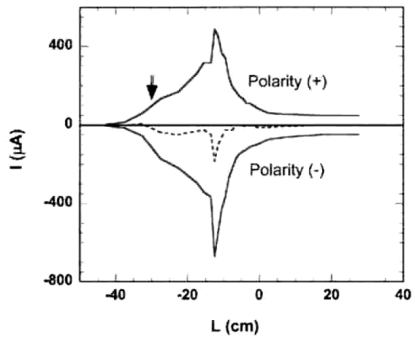

Fig. 4: Mesures du courant électrique en fonction de la distance *L*. La tension appliquée est 1000 V pour la polarité (+), et -1000V pour la polarité (-). L'espacement d'électrodes est *d* = 1.5 cm. La courbe pointillée est la différence entre les signaux pour chaque polarité. L'énergie par impulsion est 14mJ. La flèche indique la position calculée du début du filament.

Pour évaluer la densité libre d'électrons mesurée, nous utilisons la densité de courant par ion, $i = 3\times10^{-14} A/cm^2$, citée en réf. [14], pour l'air à la pression atmosphérique soumis à un champ appliqué de même ordre de grandeur. Prenant une taille de filament de 40 μm de diamètre, nous obtenons dans la région de plateau un flux moyen minimum de courant crête de 800 A/cm^2 et une résistivité de plasma inférieure à 1.2 Ω.cm. À partir de ceci, nous estimons une densité libre

d'électrons de $3\times10^{16}\,cm^{-3}$. À de telles densités, on s'attend à ce que l'affaiblissement du plasma soit principalement dû à la recombinaison des électrons aux ions parents, suivant une loi $dn/dt = -bn^2$. En utilisant la valeur $b = 2.2\times10^{-7}\,cm^3/s$ trouvée dans la littérature [15], on constate que la majorité des porteurs disparaissent en moins de 5 ns, en accord avec la durée du signal électrique mesuré qui est inférieure à 3 ns.

En conclusion, en utilisant des impulsions laser d'énergie modeste, nous observons la présence d'une colonne conductrice de plasma à des distances supérieures à un mètre le long des filaments auto-guidés. Une telle colonne de plasma pourrait être utile pour l'étude de la foudre électrique, puisqu'elle peut fournir un précurseur artificiel de densité uniforme de porteurs, évitant l'étape initiale complexe de formation d'un streamer qui précède la décharge.

1.2 Diffractometrie Résolue dans le Temps

Nous avons exploré l'évolution temporelle du canal de plasma en utilisant la diffractometrie optique résolue dans le temps, une méthode complémentaire à la technique de conductivité décrite ci-dessus.

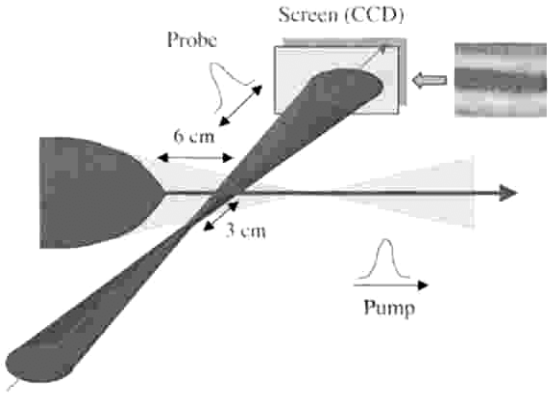

Fig. 1: Arrangement expérimental pour la diffractometrie résolue dans le temps. L'image modifiée d'un faisceau sonde croisant le filament est enregistrée à divers retards. On montre la frange centrale sombre dans l'image du champ lointain de la sonde pour un retard nul.

Le montage expérimental est montré dans la fig. 1. L'image en champ lointain du faisceau sonde, modifiée après passage par le filament, est enregistrée à divers retards avec une camera CCD linéaire. Le plasma du filament, de rayon 40 μm, joue le rôle d'une lentille mince divergente qui réfracte le faisceau sonde. L'intensité de la sonde en champ lointain s'écrit:

$$\left| F(p,q) \right|^2 = \left| \int_{-\infty}^{+\infty}\int f(x,y,z)\, e^{i\varphi(x,y)}\, e^{i(px+qy)} dxdy \right|^2$$

où $f(x, y, z)$ représente le champ électromagnétique de la sonde:

$$f(x,y,z) = \frac{1}{1+i\,(z/z_r)}\, e^{\,i(r/w)^2(z/z_r)\times\frac{1}{1+(z/z_r)^2}}\, e^{\,-(r/w)^2\times\frac{1}{1+(z/z_r)^2}}$$

où z_r, w et f sont respectivement la distance de Rayleigh, le rayon du col du faisceau et la focale de la lentille (z_r = 1 mm, w = 20 μm, f = 0.5 m). La phase accumulée $\varphi(x,y) = [2\pi/\lambda \sin\theta] \int_{-\infty}^{+\infty} [n(x,y,z) - n_\infty] dz$ est reliée à la densité du plasma par la relation $n(x,y,z) = 1 - \frac{1}{2}\frac{n_e}{n_{cr}}$ où n_{cr} est la densité critique du plasma. Pour l'évolution temporelle de la densité électronique nous utilisons les équations ci-dessous, qui décrivent les différents mécanismes de relaxation des électrons (n_e) des ions positifs (n_p) et des ions négatifs (n_n) dans l'air:

Error! Objects cannot be created from editing field codes.

avec les coefficients: $\gamma = 7.4\times10^4 s^{-1}$ pour l'ionisation par le champ électrique externe, $\eta = 2.5\times10^7 s^{-1}$ pour l'attachement des électrons à l'O_2, $\beta_{ep} = 2.2\times10^{-13} m^3/s$ pour la recombinaison électron-ion, et $\beta_{np} = 2.2\times10^{-13} m^3/s$ pour la recombinaison ion-ion [15]. Comme conditions initiales nous avons $n_e(0) = n_p(0) = n_{e0}$ et $n_n(0) = 0$. L'ionisation de l'air, qui est un processus multiphotonique d'absorption simultanée de 8-10 photons infrarouges, est instantanée dans l'échelle de temps considérée ici. Elle produit une densité électronique initiale n_{e0} qui doit être déterminée. Pour des densités initiales supérieures à $10^{15} cm^{-3}$ et pour des temps inférieurs à 10 ns le mécanisme principal qui conduit à la relaxation du plasma est le processus de recombinaison.

Dans de telles conditions, le système d'équations pour des électrons peut être simplifié à la limite de recombinaison sous la forme $\partial n_e/\partial t = -\beta_{ep}\, n_e n_p = -\beta_{ep} n_e^2$, et donne la solution analytique: $n_e(t) = 1/(\alpha + \beta_{ep}\, t)$ où $\alpha = 1/n_{e0}$.

Des images du champ lointain du faisceau sonde enregistré à différents retards sont montrées dans la fig. 2 (gauche). Le faisceau sonde a croisé le canal de plasma 6 centimètres après son origine sous un angle de 3°. Le foyer convergent du faisceau de la sonde a été placé 3 centimètres avant le canal de plasma. Pour comparaison des images calculées en adoptant une densité de $n_{e0} = 2\times10^{17} cm^{-3}$ sont montrées en fig. 2 (droite). La forme de ces images est sensible au déphasage accumulé, ce qui fixe la densité initiale n_{e0} de plasma à t = 0 ps. Pour plus

de précision, nous choisissons Δt = 100 fs pour éviter des complications dues aux effets nonlinéaires du mélange à quatre-ondes entre la pompe et la sonde. Les images du champ lointain indiquent une frange foncée au centre dont le contraste subit une chute rapide pendant les 100 premières ps suivi d'un affaiblissement plus lent pendant les 300 ps suivantes. Ce contraste est employé pour une analyse quantitative de l'évolution du plasma (fig. 3). La limite de résolution de cette technique est atteinte après environ 1 ns, avec une densité électronique correspondante d'environ $10^{15} cm^{-3}$.

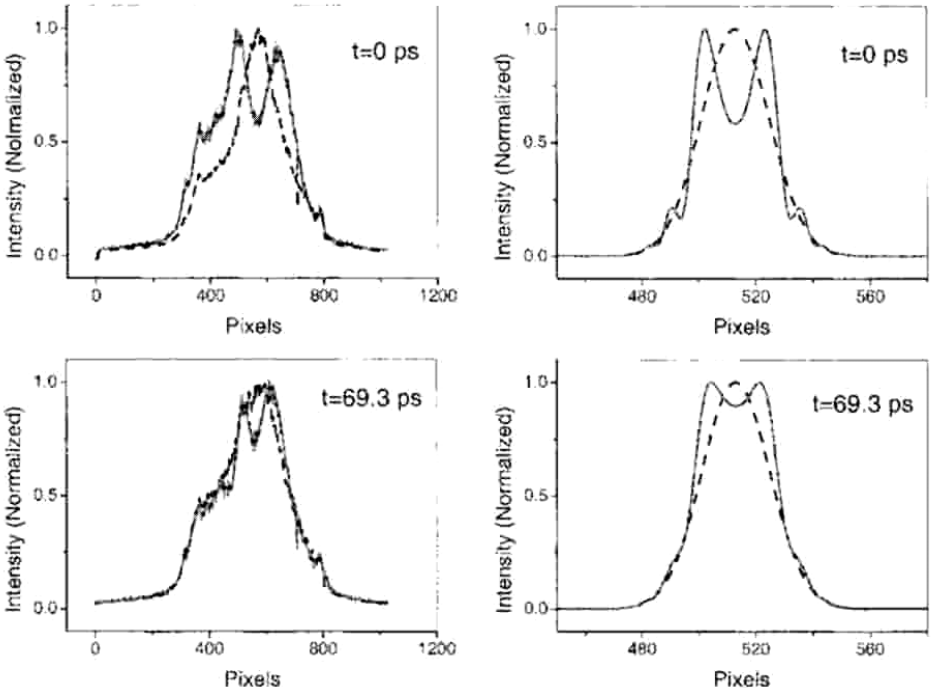

Fig. 2: Des profils spatiaux caractéristiques de la sonde après croisement avec le filament, pour deux retards. La ligne en tirets est le profil de sonde sans filament. Gauche: résultats expérimentaux. Droite: simulations.

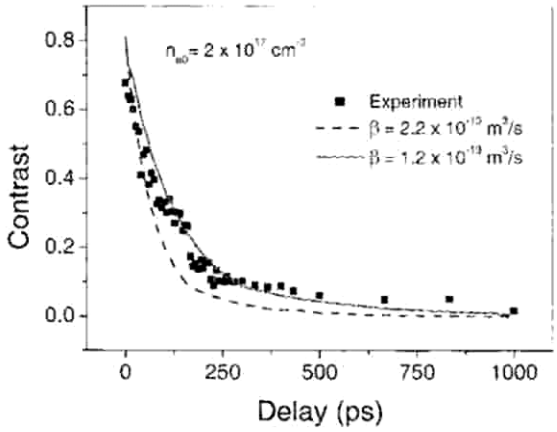

Fig. 3: Contraste optique de la frange centrale en fonction du retard. Les points sont des résultats expérimentaux et les lignes sont des simulations.

En utilisant les valeurs $\beta_{ep} = 2.2 \times 10^{-13} m^3 / s$ [15] et $n_{e0} = 2 \times 10^{17} cm^{-3}$ nous obtenons la ligne en tirets montrée dans la fig. 3. Un meilleur ajustement aux données est obtenu en gardant la même densité initiale d'électrons mais en adoptant une valeur légèrement différente de $\beta_{ep} = 1.2 \times 10^{-13} m^3 / s$ (en trait plein dans la fig. 3). La valeur $n_{e0} = 2 \times 10^{17} cm^{-3}$ est en bon accord avec les taux d'ionisation des simulations numériques de la propagation nonlinéaire d'impulsions laser IR ultracourtes intenses.

2. Division et coalescence d'impulsions auto-guidées

Dans cette section nous présentons les différentes étapes menant à la filamentation fs. Nous montrons pour la première fois clairement, la cassure initiale d'une impulsion fs en deux canaux de lumière dans le régime Kerr. Ces deux canaux fusionnent plus loin en un seul faisceau auto-guidé qui se propage sous forme d'un filament robuste au-delà d'un grand nombre de distances de Rayleigh. Les résultats expérimentaux sont confrontés aux simulations numériques et aux évaluations analytiques. La comparaison est faite étape par étape le long de la propagation. Les trois étapes successives de cassure pendant l'auto-focalisation, de coalescence en un seul filament et de diffraction finale du faisceau sont étudiées numériquement et sont en bon accord qualitatif avec les expériences. Pour une description complète des techniques expérimentales et numériques ainsi que pour tous les résultats le lecteur peut se rapporter aux annexes 2.1 et 2.2. Ici nous mentionnons brièvement seulement les résultats principaux.

Le scénario général de propagation prévu numériquement pour la propagation des impulsions fs se compose de trois étapes: (i) une étape d'auto-focalisation pendant laquelle le faisceau se rétrécit dans le plan transversal de diffraction, (ii) la formation et la propagation d'un filament au-dessus de plusieurs longueurs de Rayleigh (avec un diamètre d'environ 100 μm), (iii) une étape de diffraction. Ce scénario a été validé par les mesures expérimentales. La première étape d'auto-focalisation est cependant affectée par l'instabilité modulationnelle, qui amplifie les inhomogénéités du faisceau d'entrée et crée un anneau spatial qui se casse plus loin en deux taches. La fig. 1 montre les profils transverses du faisceau obtenus expérimentalement à différentes distances le long de la propagation d'un faisceau focalisé (f = 2 m) pour l'ensemble de trois énergies 1, 2.5 et 5 mJ.

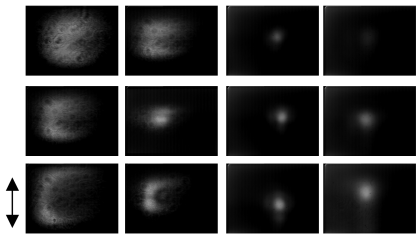

Fig. 1. Profils du faisceau. Première ligne: E_{in} = 1 mJ; (de gauche à droite) (a) z = 125 cm; (b) z = 150 cm; (c) z= 197 cm; (d) z = 232 cm. Deuxième ligne: E_{in} = 2.5 mJ; (a) z = 150 cm; (b) z = 190 cm; (c) z= 199 cm; (d) z = 237 cm. Troisième ligne: E_{in} = 5 mJ; (a) z = 150 cm; (b) z = 190 cm; (c) z= 223 cm; (d) z = 313 cm. La flèche représente l'échelle de 1.2 mm.

Des mesures de la taille du faisceau et de la densité électronique dans le cas de 5 mJ sont rapportées dans la fig. 2 et montrent une bonne concordance avec les calculs (lignes solides). Le foyer nonlinéaire, c'est-à-dire, la distance à laquelle le filament est formé est plus grand dans les expériences que dans les simulations. La rupture de symétrie associée à la formation des deux taches peut être responsable de ces différences.

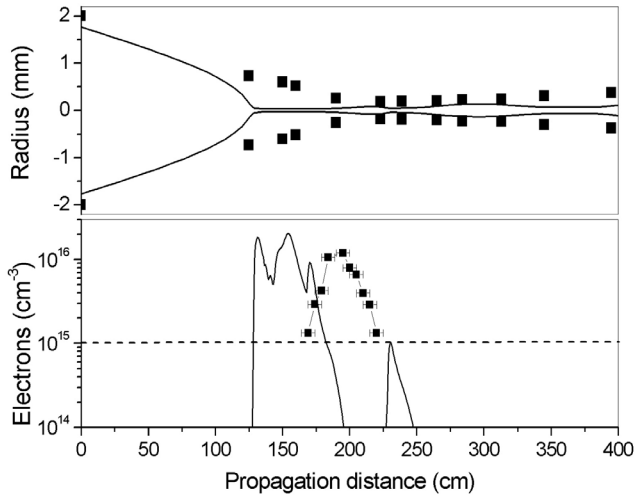

Fig. 2. Résultats expérimentaux pour le rayon du faisceau focalisé (E_{in} = 5 mJ) et pour la densité d'électron. Les résultats numériques sont représentés par les lignes solides. La ligne pointillée représente le seuil expérimental de détection électronique.

Afin d'examiner la généralité du scénario obtenu numériquement et expérimentalement pour la formation des filaments, nous avons supprimé la géométrie convergente présentée par l'objectif. Les structures transverses d'intensité des faisceaux collimatés pour des énergies de 1 à 5 mJ sont présentées dans la fig. 3. À 1 mJ, le faisceau s'auto-focalise dans un canal de lumière court qui se propage au-delà de 2 m et finalement diffracte. À 2.5 mJ, le faisceau forme un anneau pendant l'étape d'auto-focalisation. Deux taches sont alors formées (4.5 m) de cet anneau avant la coalescence en un seul canal, et une diffraction finale à 8.5 m. Avec un faisceau de 5 mJ, l'anneau et les deux canaux sont maintenant clairement évidents. Une interaction mutuelle entre les deux canaux de lumière se produit au-delà de 2 m. Pendant cette étape, chaque canal semble s'auto-focaliser en son propre centre. Ce processus retarde la fusion des deux canaux en un seul filament, qui apparaît à 8.5 m seulement.

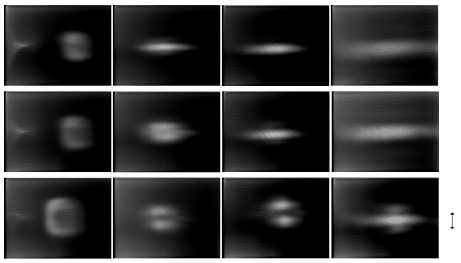

Fig. 3. Images en intensité de faisceaux laser (50 fs) pour la propagation libre dans l'air à différentes distances de propagation (de gauche à droite) z = 2.5 m, 4.5 m, 6.5 m et 8.5 m. Première ligne: E_{in} = 1 mJ, deuxième 2.5 mJ et troisième 5 mJ. La flèche représente l'échelle de 2 millimètres.

En résumé, nous avons montré que les premières étapes précédant l'auto-guidage dans l'air d'impulsions fs pour des puissances situées entre 5 et 25P_{cr} ont consisté en une division du faisceau en deux canaux en raison de l'instabilité modulationnelle suivi de leur coalescence en un seul canal, le filament. Les étapes principales de la formation de ces canaux de lumière ont été confrontées avec des simulations numériques reconstituant les différents régimes de propagation: l'auto-focalisation, la formation de plasma, l'auto-guidage et la diffraction finale du faisceau. En outre, au moyen d'un modèle NLS (voir l'annexe 2.1 et 2.2), nous avons justifié la formation de filaments et le processus de fusion permettant au faisceau de se recombiner en un seul filament robuste. Ce scénario de la division et de la coalescence précédant l'auto-guidage est générique, pour des faisceaux focalisés et non-focalisés, dans le domaine des puissances étudiées. Notons que ceci n'empêche pas des impulsions de plus haute puissance d'éclater en plus de filaments, comme proposé dans la réf. [4].

3. Filamentation d'impulsions ultraviolettes

Dans cette section nous présentons une étude expérimentale et numérique détaillée sur la propagation nonlinéaire d'impulsions laser ultraviolettes femtosecondes et picosecondes dans l'air. La comparaison entre les résultats expérimentaux et les simulations est dans la plupart des cas très bonne.

Procédure expérimentale

Les impulsions laser UV ont été obtenues en doublant la fréquence d'un laser à colorant femtoseconde et en l'amplifiant avec un amplificateur excimère, le système entier fonctionnant au taux de répétition de quelques hertz. La longueur d'onde centrale du laser était à 248 nm. Le laser pouvait fonctionner en mode fs, (durée 450 fs et énergie par impulsion jusqu'à 10 mJ) ou en mode ps (durée 5 ps et énergie par impulsion jusqu'à 15 mJ). Les mesures décrites ici ont été obtenues avec des impulsions de 450 fs et 5 ps de durée pour plusieurs énergies d'entrée. Le faisceau laser a été limité par un diaphragme circulaire de 7 mm de diamètre et focalisé avec un objectif de $f = 9.5$ m.

Des profils d'intensité du faisceau laser ont été enregistrés à différentes distances de propagation sur du papier photographique UV. La filamentation avec la formation concomitante d'un canal de plasma a été vérifiée en mesurant la conductivité électrique de l'air en fonction de la distance de propagation. Pour détecter la présence d'un canal de conduction, nous mesurons le changement de résistivité de l'air entre deux électrodes après passage du filament. Tous les détails relatives à la technique électrique peuvent être trouvés dans la réf. [16]. Le détecteur électronique a été calibré au moyen d'une technique de diffractometrie optique décrite dans la réf. [17]. L'image du champ lointain d'un faisceau sonde, modifiée après le passage par le filament est enregistrée à différents retards. Les profils de diffraction obtenus de cette façon sont sensibles au déphasage accumulé, donnant la densité de plasma d'électrons.

Des mesures de la forme de l'impulsion ont été effectuées en utilisant une technique d'autocorrélation basée sur l'ionisation à 2-photons des molécules de NO. Un interféromètre de type Michelson couplé à une cellule remplie de molécules de NO à basse pression (en général environ 100 mbar) a été utilisé [18]. Une petite partie du faisceau laser est introduite dans l'interféromètre par une réflexion sur une plaque de verre (BK7) placée à 45° sur l'axe de propagation du laser. Ces mesures n'ont été effectuées qu'aux distances pour lesquelles la fenêtre

d'entrée du verre n'est pas endommagée par l'intensité de faisceau laser (c'est-à-dire, en dehors de la région focale) et dont le faisceau réfléchi n'a pas été modifié. Les électrons libres produits sont capturés en utilisant un système de deux électrodes placées dans la cellule où une différence de potentiel modérée est appliquée. Le signal mesuré de cette façon est directement proportionnel au nombre d'électrons libres produits par le procédé de l'ionisation à 2-photons du laser à 248 nm utilisé ici. Le signal mesuré dans ce cas-ci est proportionnel à $S(\tau)$ avec:

$$S(\tau) = 1 + 2\int I(t)\, I(t+\tau)\, dt \,/\, \int I^2(t)\, dt \qquad (1)$$

où I est l'intensité du laser. De la formule ci-dessus, $S(\tau) = 1$ pour $\tau \to \infty$, tandis que $S(\tau) = 3$ pour $\tau = 0$. Ainsi le rapport prévu du signal maximal à la ligne de base dans les traces d'autocorrélation est 3. Ce rapport était un critère expérimental pour la validité des mesures expérimentales d'autocorrélation.

Des mesures spectrales avant et après la propagation du laser ont été effectuées en prenant une petite réflexion du faisceau dans un spectromètre de focale 1 m équipé d'un réseau de diffraction de 1200 l/mm. Dans certains cas un autre système a été employé avec un spectromètre f = 25 cm muni d'un réseau de diffraction de 1200 l/mm et une camera CCD linéaire possédant 16 bits de dynamique.

Des profils du faisceau laser et des mesures d'ionisation, ainsi que des autocorrélations et des spectres de puissance d'impulsion ont été enregistrés à différentes distances de propagation pour des impulsions fs et ps pour plusieurs énergies d'entrée.

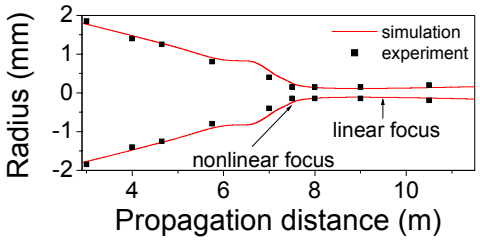

Fig. 1: Comparaison entre le profil mesuré (carreaux) et calculé (ligne solide) du faisceau dans le cas 450 fs, 2 mJ.

Approche Numérique

Ici les résultats expérimentaux sont comparés aux simulations numériques, en utilisant un code de propagation 3d à symétrie axiale. Ce code a été appliqué avec succès auparavant à la propagation nonlinéaire des impulsions IR [19] et UV fs [20]. Ce code résout numériquement l'équation nonlinéaire de Schrödinger, couplée à la densité des électrons produits par ionisation multiphotonique. Tous les détails relatif au code peuvent être trouvés dans l'annexe 3.3.

A. Caractéristiques Spatiales

La fig. 1 montre, pour comparaison, le rayon calculé et mesuré du faisceau laser le long de l'axe de propagation pour des impulsions d'entrée de 450 fs, 2 mJ. L'accord est très bon, montrant l'existence d'un filament qui se propageant sur plus de 4 m dans l'air, ayant un diamètre presque constant d'environ 150 μm. On peut observer que le foyer nonlinéaire se situe à environ 2.5 m, avant le foyer géometrique.

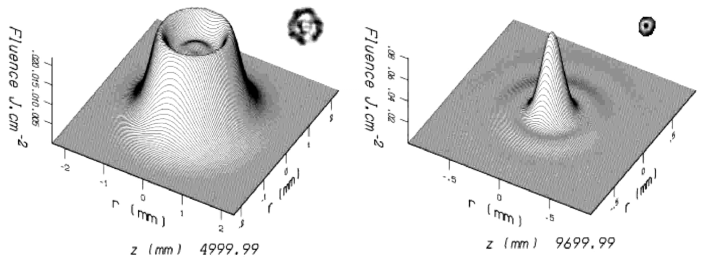

Fig. 2: Distributions spatiales calculées de fluence à deux distances le long de l'axe de propagation. Pour la comparaison sont également montrées des mesures (petits encarts) enregistrées sur du papier photographique UV aux mêmes distances. Observez l'excellent accord entre les mesures et les simulations.

Des répartitions spatiales de fluence à deux distances différentes le long de l'axe de propagation sont présentées dans la fig. 2 pour des impulsions de 450 fs, 2 mJ. Dans les premiers mètres avant le foyer nonlinéaire on peut observer des anneaux qui fusionnent vers le centre du faisceau. L'aspect des anneaux peut être vu sur la tache experimentale enregistrée à la même distance sur du papier photographique UV (voir l'encart dans la fig. 2). Sur le profil expérimental on peut voir que les anneaux ne sont pas vraiment uniformes, et en raison de l'instabilité modulationnelle de nombreux petits filaments coexistent qui fusionneont plus tard en un seul. Le rôle de l'instabilité modulationnelle a été relevé récemment par Tzortzakis *et al.* [21] dans le cas des filaments IR fs dans l'air (voir le chapitre 2). Une fois que le filament est formé, la

tendance est renversée, et les anneaux de lumière diffractent en accord avec les mesures expérimentales.

B. Ionisation

Une comparaison entre l'ionisation dans le filament fs et le filament ps est présentée dans la fig. 3. La densité électronique calculée pour les impulsions de 450 fs, 2 mJ (ligne en tirets), peut être comparée aux mesures représentées par les triangles. La ligne solide est la densité électronique calculée pour les impulsions de 5 ps, 2 mJ, à comparer aux mesures représentées par les cercles. Les calculs et les mesures prouvent clairement que dans le cas des filaments UV ps la densité d'électrons est plus élevée que pour les filaments UV fs.

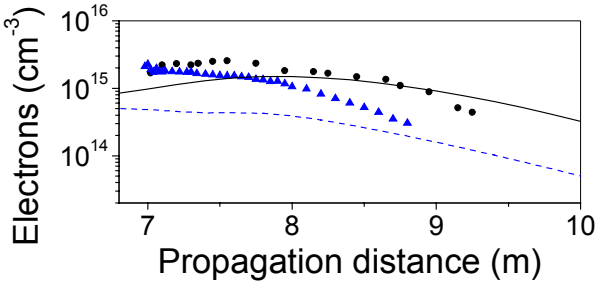

Fig. 3: Densités calculées et mesurées d'électrons pour 450 fs, 2 mJ (ligne en tirets et triangles respectivement), et pour 5 ps, 2 mJ (ligne solide et cercles respectivement).

Le taux d'ionisation en fonction de r et z est présenté dans la fig. 4 pour le cas fs (fig. 4a) et le cas ps (fig. 4b), pour une énergie d'entrée de 2 mJ. Une observation de ces deux figures nous montre la contribution importante dans l'ionisation des anneaux spatiaux dans le cas des impulsions fs. En revanche, dans le cas d'impulsions ps cette contribution est négligeable.

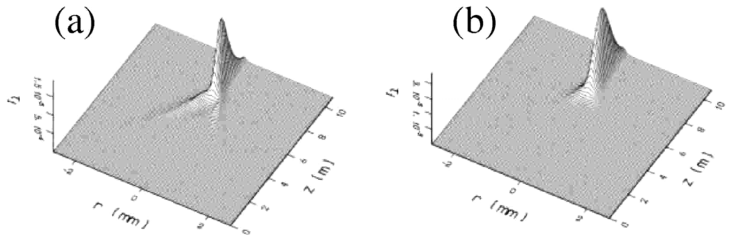

Fig. 4: Image spatiale calculée du taux d'ionisation le long de la propagation dans le cas fs (a) et ps (b), pour une énergie d'impulsion d'entrée de 2 mJ.

C. Evolution temporelle et spectrale

Dans la fig. 5 le profil temporel calculé d'impulsion dans le filament est montré à deux distances de propagation. L'impulsion initiale est divisée en deux impulsions plus courtes, qui se propagent presque sans changement sur plus que 4 m. Dans la même figure les traces d'autocorrélation résultant des simulations sont directement comparées aux mesures expérimentales. Des résultats à deux distances différentes dans le filament sont montrés ainsi que l'autocorrélation initiale de l'impulsion. Les simulations reproduisent d'une manière très bonne la partie centrale des autocorrélations expérimentales, alors qu'on observe un petit désaccord aux ailes. La différence est située dans l'amplitude du piédestal et des bosses secondaires d'autocorrélations. Dans les simulations les deux sous-impulsions dans la structure de l'impulsion ont presque la même amplitude, donnant lieu aux satellites d'amplitude élevée dans l'autocorrélation. D'autre part les autocorrélations expérimentales montrent des bosses secondaires moins prononcées, qui indiquent probablement que les deux impulsions de la double impulsion n'ont pas la même amplitude.

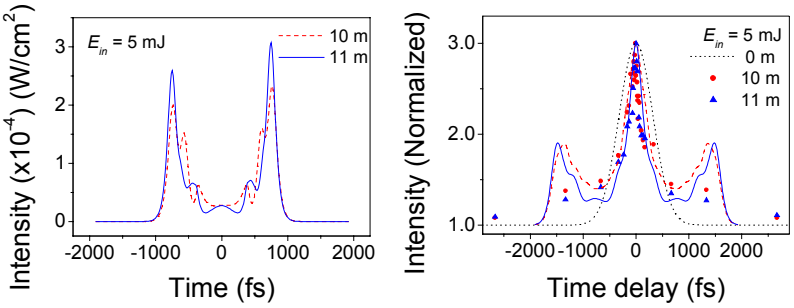

Fig. 5: Profils temporels calculés de l'impulsion et autocorrélations correspondantes dans les filaments fs pour l'énergie d'entrée de 5 mJ pour deux distances: 10 m (lignes en tirets) et 11 m (lignes solides). La trace d'autocorrélation de l'impulsion initiale (ligne pointillée) et les autocorrélations mesurés à 10 m (cercles) et à 11 m (triangles) sont également montrées.

Dans la fig. 6 le profil temporel calculé de l'impulsion dans le filament ps est montré à 11 m ainsi que celui de l'impulsion initiale (ligne pointillée). L'impulsion initiale est divisée en deux impulsions secondaires plus courtes, qui dans ce cas-ci n'ont pas la même amplitude, comme c'était le cas avec les filaments fs décrits ci-dessus. Dans la même figure la trace d'autocorrélation résultant de la simulation à 11 m est directement comparée à la mesure expérimentale (triangles).

L'autocorrélation de l'impulsion initiale est également montrée dans la même figure représentée par la ligne pointillée. La simulation et la mesure sont en bon accord.

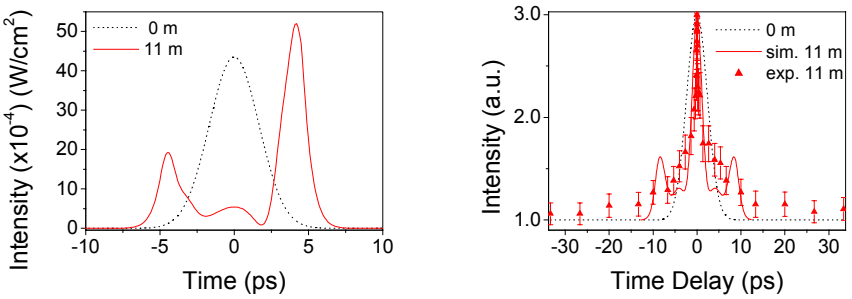

Fig. 6: Profils temporels calculés de l'impulsion (a) et autocorrélations correspondantes (b) dans les filaments ps pour l'énergie d'entrée de 7.5 mJ à 11 m (lignes solides) ainsi que l'impulsion initiale (lignes pointillées). En (b) est également tracée l'autocorrélation mesurée à 11 m (triangles).

Une autre manière de vérifier la présence d'une double impulsion est de comparer les spectres de puissance mesurés et simulés. L'impulsion calculée au niveau du filament dans le cas femtoseconde possède un spectre modulé avec un inter-frange d'environ 0.2 nm. Ceci est en bon accord avec la mesure présentée dans la fig. 7. La même comparaison dans le cas de la picoseconde n'indique pas clairement l'existence des franges dans le spectre, ce qui est également en accord avec les mesures et la structure asymétrique de l'impulsion.

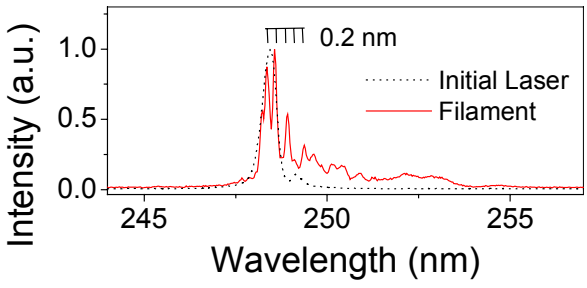

Fig. 7: Spectres mesurés pour 450 fs, 5 mJ. L'impulsion initiale est montrée en pointillé et le filament à 11 m est en ligne continue. Une structure de franges avec un inter-frange de 0.2 nm est présent dans le spectre du filament.

Conclusion

En conclusion, nous avons présenté une étude expérimentale et numérique sur la propagation nonlinéaire (femtoseconde et picoseconde) d'impulsions UV dans l'air. On a observé la filamentation à longue portée des faisceaux fs et ps. Les caractéristiques du filament sont semblables dans les deux régimes; un diamètre légèrement plus grand et plus d'électrons sont produits dans le filament ps par rapport au filament fs. Dans les deux cas l'impulsion initiale est divisée en deux sous-impulsions de plus courte durée. Dans le cas fs les deux impulsions secondaires semblent être symétriques tandis que dans le cas ps la deuxième impulsion domine la première. Le dédoublement d'impulsion est favorisé principalement par l'ionisation multiphotonique. Cette dissociation est de grande importance dans la formation et la propagation du filament, car elle semble jouer le rôle d'un guide d'ondes spatio-temporel. Plus de détails et de résultats peuvent être trouvés dans les annexes 3.1 et 3.2.

4. Décharges initiées et guidées par des filaments femtoseconde

Le déclenchement d'une décharge électrique dans l'atmosphère chargée, bien que complexe, est fondamentalement compris. Un phénomène crucial est le déplacement des charges. Les porteurs libres dans l'air se rassemblent autour d'un point de champ local élevé, menant à un champ local accru. Par suite de l'accroissement du champ un processus local d'avalanche se produit avec des électrons se multipliant et s'écoulant à l'extérieur. Les "streamers" fusionnent dans un canal de conduction auto-entretenu appelé "leader". Le leader se déplace vers la direction opposée de l'électrode, précédé par des streamers. Quand le contact est établi, un grand courant de retour se produit. Cet effet de streamer-leader explique pourquoi une décharge peut se développer si le champ appliqué est inférieur au champ critique pour la rupture diélectrique de l'air (E = 27 kV/cm dans l'air sec à la pression atmosphérique). Il explique également le long et erratique temps d'incubation entre l'application de la tension et le début de la décharge.

Plusieurs expériences ont prouvé que les faisceaux laser peuvent déclencher des décharges électriques dans l'air, voir par exemple [15,22]. Des électrons libres sont produits par le laser, habituellement en un point focal. Le même scénario comme ci-dessus se développe alors, mais avec un temps réduit d'incubation pour la formation du leader. Plus récemment, une étude a montré que la vitesse de progression du leader peut être augmentée considérablement en focalisant une impulsion laser intense sub-picoseconde entre deux électrodes chargées [23]. Dans cette section nous décrirons la première démonstration expérimentale d'une décharge électrique déclenchée et guidée par un filament femtoseconde, suggérant un nouveau mécanisme de décharge électrique induite par laser dans l'air. Un point caractéristique de ce genre de décharge est qu'elle est uniforme le long de son axe. Le scénario de base est comme suit. L'impulsion laser IR auto-guidée fs produit dans son sillage un filament faiblement ionisé de plasma avec une densité libre longitudinale uniforme d'électrons de quelques fois 10^{16} e^-/cm^3 et d'une longueur qui peut excéder 50 centimètres [16]. Ce filament de plasma de basse température ne peut pas déclencher par lui-même une décharge auto-entretenue entre deux électrodes chargées pendant sa courte durée de vie (ns). D'autre part, la circulation d'un courant pendant la brève phase de conduite de plasma produit un chauffage Joule significatif d'une colonne mince d'air. Ce chauffage rapide est suivi d'une expansion hydrodynamique radiale du canal chauffé. Par la suite une dépression centrale d'air rencontre les conditions pour fournir un chemin linéaire pour une décharge spontanée. Puisque ce scénario n'implique pas le déplacement des charges, il est reproductible en temps mais se produit avec un retard caractéristique. Nous le modélisons en

tenant compte de l'expansion hydrodynamique d'une colonne d'air chauffé dans l'air froid environnant.

La fig. 1 illustre la différence entre une décharge déclenchée par laser selon la configuration habituelle de la fig. 1a et l'arrangement de l'expérience actuelle en utilisant un filament fs (fig. 1b). Le circuit électrique se compose de deux plaques métalliques (électrodes), écartées de 1.5 cm et soumises à une tension de 28 kV. Cette tension est bien au-dessous du champ critique pour l'amorçage d'une décharge spontanée, qui est de près de 40 kV. La fig. 1a montre un exemple d'une décharge ordinaire déclenchée à l'aide d'un laser. Des charges sont déposées seulement en un point entre les deux électrodes par une impulsion laser fs focalisée avec une énergie de 10 mJ.

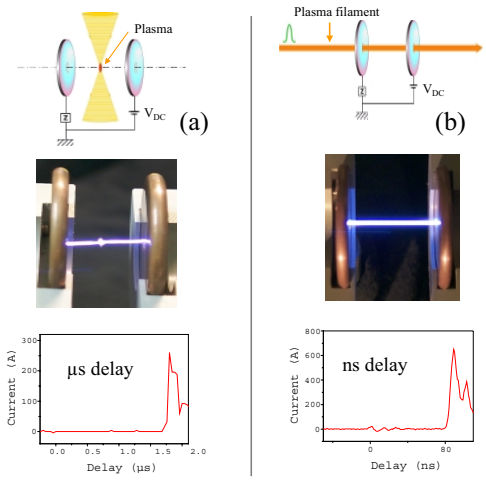

Fig. 1: Configuration expérimentale du circuit de décharge, (a) quand le faisceau laser est focalisé entre les deux électrodes et (b) quand un canal auto-guidé de plasma produit par filament est utilisé pour relier les deux électrodes. Sur le dessus de la figure est une représentation schématique de l'installation tandis qu'au milieu est une photo d'une vraie expérience. À la partie inférieure nous montrons les courbes caractéristiques du courant dans le circuit. Noter la différence importante sur le délai dans les deux configurations.

Après injection de porteurs par le laser, une décharge se produit avec plus que 90% de probabilité. Le retard entre la création des porteurs libres et du déclenchement de la décharge est long et erratique, typiquement entre 1-5 µs. D'autre part la fig. 1b illustre l'expérience actuelle et montre une décharge déclenchée et guidée par un filament laser. Le filament traverse et relie les

deux électrodes par deux trous de diamètre 3 mm. Il crée un canal uniforme d'air partiellement ionisé qui couvre l'espace entier entre les deux électrodes. Le début de la décharge montrée dans la fig. 1b est maintenant réduit à 80 ns. Il se produit avec 100 % de probabilité avec une fluctuation inférieure à 5%. La décharge électrique est le résultat d'une réduction locale de densité de l'air sur l'axe expliquant en même temps le déclenchement et le guidage.

Afin de valider le scénario esquissé ci-dessus, nous avons effectué une série de mesures pour caractériser le canal d'air à différents temps entre le passage de l'impulsion laser auto-guidée et le début de la décharge. Ces résultats expérimentaux ont été confrontés à une simulation numérique. La méthode expérimentale est la diffractometrie résolue dans le temps [17]. Cette technique résout dans le temps de petits changements locaux (gradients) de l'indice de réfraction dans un gaz. Dans le chapitre 1, nous avions utilisé cette technique pour caractériser le canal de plasma d'un filament, sa densité électronique, sa durée de vie et ses dimensions radiales [17]. Ici nous mesurons les changements locaux de l'indice de réfraction de l'air aux temps postérieurs dus à l'expansion de gaz.

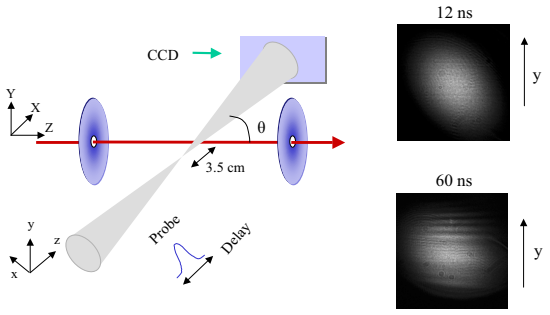

Fig. 2: Configuration expérimentale de la diffractometrie résolue dans le temps. Les images du champ lointain du faisceau sonde après qu'il ait croisé le canal chauffé sont enregistrées pour différents retards. Deux images de diffraction caractéristiques à 12 ns et 60 ns sont aussi présentés. Les flèches à côté des images indiquent l'axe le long duquel nous acquérons le profil d'intensité que nous employons dans notre analyse (voir la fig. 3).

Le montage expérimental est montré dans la fig. 2. Le faisceau sonde croise le chemin de filament sous un angle de $\theta = 4°$. Le faisceau sonde a été focalisé 3.5 cm avant le canal de

plasma. Une longue ligne à retard optique (de 0 à 25 m) était nécessaire afin de couvrir la fenêtre temporelle entre 0 et 80 ns. Le profil spatial du faisceau sonde a été nettoyé après la ligne à retard à l'aide d'un filtre spatial afin d'obtenir un profil gaussien. L'image du champ lointain du faisceau sonde, après avoir croisé le canal chauffé, a été enregistrée avec une camera CCD linéaire pour différents retards. Deux exemples du champ lointain observé en présence d'une tension continue de 28 kV pour des retards de 12 ns et de 60 ns sont montrés sur la fig. 2. Des profils d'intensité de faisceau à différents retards sont montrés sur la fig. 3, représentée par les courbes supérieures. Juste après le passage de l'impulsion laser (fig. 3 (0 ns)) une frange sombre apparaît au centre. Ceci est caractéristique de la présence du plasma provoqué par l'impulsion laser. Elle disparaît dans la première ns, traduisant la recombinaison rapide des électrons dans le plasma. Des détails sur la caractérisation de ce premier plasma et de son temps de vie peuvent être trouvés dans la réf. [17].

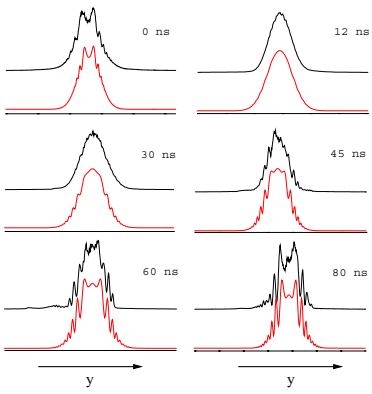

Fig. 3: Résultats expérimentaux de la diffractometrie résolue dans le temps et comparaison avec les simulations numériques pour différents retards. Les résultats expérimentaux sont représentés par les courbes supérieures tandis que les courbes inférieures sont les simulations.

Une deuxième image de diffraction apparaît après un temps d'incubation de 30 ns (fig. 3 (30 ns)). Le contraste des franges de cette deuxième image de diffraction augmente avec le retard (fig. 3 (45 ns, 60 ns, 80 ns)) jusqu'à l'arrivée de la décharge, après 80 ns. Cette deuxième image de diffraction se produisant seulement en présence du champ électrique externe est une démonstration directe de son rôle dans le chauffage Joule du canal d'air. Dans ce qui suit nous prouvons que ces observations sont conformes à l'évolution hydrodynamique du canal d'air chauffé, menant à une dépression de densité le long de son axe.

L'expansion du canal de gaz chauffé a été calculée avec le code hydrodynamique MULTI [24]. Ce code a été modifié convenablement pour nos conditions particulières et nous nous plaçons dans un cas de géométrie cylindrique, nous considérons également une équation d'état de gaz idéale. Comme perturbation initiale de la température nous imposons le profil radial:

$$T(r) = T_{room} + \delta T \exp\left(-r^2 / w_0^2\right) \tag{1}$$

où δT est l'élévation de la température dû au petit courant électrique dans le circuit pendant les quelques premières ns, w_0 est la taille du canal de plasma. L'ensemble d'équations pour la continuité, le mouvement et l'énergie sont résolus numériquement:

$$\frac{d\rho}{dt} = -\rho \, \nabla \cdot \vec{u} \tag{2}$$

$$\rho \, \frac{du_r}{dt} = -\frac{1}{m} \frac{\partial}{\partial r} \left(\rho k_B T\right) \tag{3}$$

$$\frac{5}{2} \frac{dT}{dt} = -T \, \nabla \cdot \vec{u} \tag{4}$$

où ϱ est la densité de gaz, $\vec{u}$ est la vitesse (en maintenant seulement le terme radial $\nabla \cdot \vec{u}$), m représente la masse des molécules d'air, et k_B est la constante de Boltzmann. D'autres termes de perte dues aux collisions et au rayonnement peuvent être négligées.

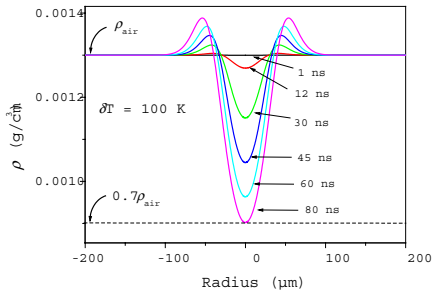

Fig. 4: Résultats du code hydrodynamique MULTI pour la dépression d'un canal chauffé avec une élévation initiale de la température de 100 K et taille de 40 μm. La dépression atteint la limite de 70% imposée par la loi de Paschen (représentée par la ligne en tirets) après 80 ns en accord avec l'expérience.

Nous adoptons la valeur de w_0 = 40 μm qui n'est pas un paramètre ajustable, mais a été extrait à partir de l'analyse de diffraction du canal de plasma du filament. Ainsi le seul paramètre réglable dans notre modèle et nos simulations est la perturbation initiale de la température du gaz, que nous ajustons à un meilleur accord sur les résultats expérimentaux. Les résultats numériques montrés dans la fig. 4 correspondent à une température ambiante T_{room} = 300 K et à une première augmentation de la température de δT = 100 K. On observe une dépression centrale atteignant 30% de la valeur initiale après 80 ns. Cette valeur est en accord avec la pression de seuil prévue par la loi de Paschen représentée par la ligne en tirets dans la fig. 4.

À partir des profils de densité obtenus à partir des simulations hydrodynamiques on peut calculer les profils de diffraction du faisceau sonde dus aux changements de l'indice de réfraction induits par l'expansion du canal. Nous exprimons l'intensité du champ lointain du faisceau sonde par:

$$\left| F(\vec{q}) \right|^2 = \left| \int_{-\infty}^{+\infty}\int f(\vec{r},z)\; e^{i\varphi(\vec{r})}\; e^{i\vec{q}\cdot\vec{r}}\, dxdy \right|^2 \tag{5}$$

où $f(r, z)$ représente le champ électromagnétique du faisceau sonde:

$$f(\vec{r},z) = \frac{1}{1+i\,\left(z/z_r\right)} \exp\left(-\frac{r^2/w^2}{1+i\left(z/z_r\right)} \right) \tag{6}$$

où $\vec{r} = x\vec{e}_x + y\vec{e}_y$, z_r = 1 mm est la distance de Rayleigh et w = 20 μm est le rayon du col du faisceau au foyer de la lentille de f = 0.5 m. La phase accumulée est:

$$\varphi(y) = \left(2\pi/\lambda \sin\theta\right) \int_{-\infty}^{+\infty} \left[n\left(\sqrt{\mu^2+y^2}\right) - n_\infty \right] d\mu\,,$$

où nous avons introduit le changement de coordonnées $\mu = x\cos\theta + z\sin\theta$ (voir Fig. 2 pour les différents systèmes de coordonnées). Cette phase est reliée à la densité du gaz $\rho(r)$ par: $n(r) = 1 + C\rho\left(r\right)$. La constante C est estimée de la façon suivante. Pour $r \to \infty$ et pour λ = 800 nm l'indice de réfraction de l'air est $n_\infty = n_{air}$ = 1.000275 et sa densité est $\rho_\infty = \rho_{air}$ = 1.3 x 10^{-3} g/cm^3, d'ou $C = \left(n_{air} - 1\right)/\rho_{air}$ = 0.21 cm^3/g.

L'évolution du profil de franges a été calculée pour différentes températures du canal chauffé. Un excellent accord a été trouvé pour δT = 100 K, comme il peut être constaté dans la fig. 3. La valeur de δT = 100 K est également conforme au délai de 80 ns comme le montre la courbe de la fig. 4.

En conclusion nous avons observé un nouveau type de décharge électrique guidée par laser. Il est déclenché par l'expansion d'un fil mince d'air chaud produit par une impulsion laser IR auto-guidée. À partir des mesures de diffraction résolues dans le temps couplées à un modèle hydrodynamique pour l'expansion du fil, l'information quantitative sur l'évolution de la densité du fil d'air et la température aussi bien que sur le déclenchement de la décharge ont été extraites. Ce type de décharge électrique peut trouver des applications quand l'uniformité sur l'axe est cruciale.

5. Filamentation femtoseconde dans les solides

Dans cette section nous montrons la première observation détaillée d'un canal auto-guidé dans la silice fondue. Les mesures incluent l'enregistrement du profil d'intensité de faisceau le long de son axe de propagation, le spectre de puissance de l'impulsion ainsi que l'évolution de l'autocorrelation de l'impulsion. Les résultats expérimentaux sont confrontés avec les simulations numériques directes qui incluent des effets de SF, de MPI, de GVD, et d'auto-raidissement, en utilisant des paramètres réalistes et des conditions initiales proches de l'expérience.

Les conditions expérimentales pour obtenir le filament sont rigoureuses. La formation du filament se produit quand la puissance P du laser excède $3P_{cr}$, où $P_{cr} = \lambda_0^2 / 2\pi n_0 n_2 \simeq 2.3$ MW est la puissance critique de seuil pour l'auto-focalisation, n_0 = 1,453 est l'indice de réfraction linéaire et n_2 = 3.2 10^{-16} cm^2/W l'indice nonlinéaire de la silice fondue. La durée de l'impulsion d'entrée est 160 fs, et sa longueur d'onde centrale est $\lambda_0 = 800$ nm. La formation de ce filament exige également une géométrie adaptée du faisceau laser incident. Nous utilisons un objectif de focalisation de f = 80 mm et nous situons l'entrée de la plaque de silice près du col du faisceau. Le taux élevé de répétition de notre système laser (200 kHz) présente également une difficulté pour observer le filamentation: l'absorption, même faible, provoque à cette cadence un chauffage substantiel de l'échantillon. Ce chauffage, à son tour, change les propriétés physiques intrinsèques du milieu et détruit le mode auto-guidé en quelques secondes. Pour surmonter ce problème nous avons déplacé sans interruption la plaque de silice au moyen d'un moteur xy comme représenté sur la figure 1a. Un canal de lumière auto-guidé est alors produit au-dessus d'une distance excédant plusieurs millimètres, comme on le voit sur les figures 1b et 1c. La taille du filament s'étend entre 10 et 40 μm, qui correspond aux intensités maximales de l'ordre de 10^{13} W/cm^2, menant à la production d'électrons libres par des absorptions multiphotoniques [25].

Les impulsions auto-guidées ont été caractérisées comme suit. Un objectif de microscope (grandissement 20x) couplé à une camera CCD linéaire a enregistré le profil d'intensité du faisceau à différentes distances le long de l'axe de propagation du faisceau (voir la fig. 1a). Les diamètres correspondants du faisceau laser pour l'énergie d'entrée $E_{in} = 2$ μJ sont montrés sur la figure 1c. Sur la même figure est également montré pour comparaison le régime linéaire avec une énergie d'entrée $E_{in} \simeq 50$ nJ, pour laquelle le rayon laser se diffracte selon les lois des faisceaux gaussiens. Dans la figure 1d nous présentons une image de fluence en 3 dimensions du

filament à une distance z = 2.8 mm du dioptre d'entrée de l'échantillon à l'intérieur du verre de silice. On peut clairement observer un filament étroit, entouré par des anneaux de lumière.

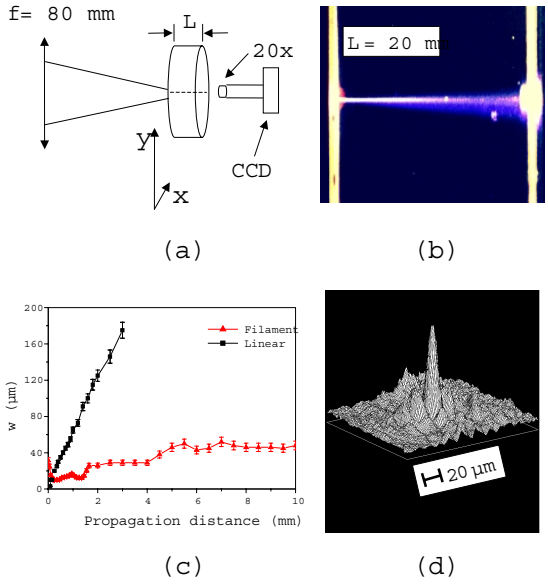

Fig. 1: (a) Procédé expérimental pour la détection des filaments auto-guidés dans la silice fondue. *L* est l'épaisseur de la plaque de silice. La plaque a un mouvement planaire continu au moyen d'une moteur xy. (b) Une photographie transversale du filament auto-guidé dans la silice fondue avec énergie d'entrée E_{in} = 2 μJ. (c) Diamètre mesuré du filament le long de sa propagation. Pour comparaison le régime linéaire de diffraction mesuré à basse énergie d'entrée (50 nJ) est montré aussi. (le 0 de l'axe des abscisses correspond à la face d'entrée de la plaque de silice.) (d) Une image mesurée de fluence 3d du filament à 2.8 mm de la fenêtre d'entrée de l'échantillon de silice.

Nous avons également effectué des mesures d'autocorrélation de l'impulsion dans le filament. À cette fin nous avons employé un autocorrélateur équipé d'un cristal mince de borate de baryum (BBO) comme milieu nonlinéaire. La ligne pointillée dans la fig. 2a montre la trace d'autocorrélation de l'impulsion de laser d'entrée avec une durée d'environ 160 fs. Après être sorti de l'échantillon de silice, le filament se propage dans l'air et se diffracte au-delà d'une distance de 50 cm. La partie centrale du faisceau diffracté à la sortie de l'échantillon est introduite dans l'autocorrélateur. Dans la fig. 2a les traces d'autocorrélation de l'impulsion auto-guidée à 2 et 5 mm de l'entrée de l'échantillon sont montrées. Ces traces d'autocorrélation ont une forme

avec trois bosses, qui indique la division de l'impulsion laser d'entrée principalement en deux secondaires impulsions. Cette structure temporelle reste relativement stable le long de la propagation du filament.

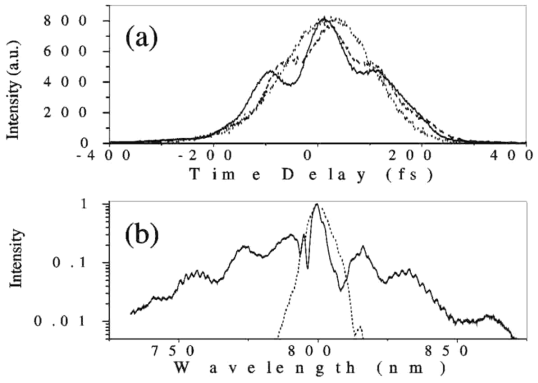

Fig. 2: (a) Autocorrélation mesuré du filament à 2 mm (pleine) et à 5 mm (tiret), ainsi que cela de l'impulsion laser initiale (pointillée). (b) Spectre de puissance de l'impulsion d'entrée (pointillée) et de celle du filament à 10 mm (pleine).

La fig. 2b montre le spectre de puissance de l'impulsion laser initiale, aussi bien qu'un spectre représentatif du faisceau auto-guidé, intégré sur environ 100 balayages de l'oscilloscope. Le faisceau laser sortant de l'échantillon de 10 mm de silice fondue est dirigé vers un spectromètre de focale f = 25 cm équipé d'un réseau de diffraction de 600 l/mm et d'une camera CCD linéaire de 16 bits. La fente d'entrée est fermée à 10 μm. Le spectre de puissance de l'impulsion après la propagation nonlinéaire montre un élargissement qui se prolonge sur tout le spectre visible. Moins que 1% de l'énergie incidente est contenue dans la partie visible du continuum blanc. Comme on le voit sur la fig. 2b, il y a une structure de franges sur le spectre de l'impulsion auto-guidée avec un inter-frange d'environ 16 nm.

Nous avons employé un code tridimensionnel pour simuler la propagation des impulsions laser ultra-courtes dans la silice fondue. Le code résout une équation nonlinéaire de Schrödinger, couplée à la densité d'électrons produits par des transitions inter-bandes multiphotoniques. Pour des détails sur le code le lecteur peut regarder dans l'annexe 5.1.

Les résultats numériques pour l'énergie initiale E_{in} = 2 μJ et puissance $P_{in} \simeq 5P_{cr}$ sont montrés dans la fig. 3. La fig. 3(a) montre l'évidence de l'apparition d'un canal de lumière, ayant un diamètre proche de celui mesuré expérimentalement. La fig. 3(b) montre un profil de fluence 3d

du filament à une distance z = 2.8 mm. Notez la structure d'anneau qui entoure le filament, en accord avec le résultat expérimental de la fig. 1d. La fig. 3(c) montre les déformations dans le profil temporel d'intensité du faisceau. Deux sous-impulsions principales sont formées, et toutes les deux subissent un rétrécissement temporel. Elles gardent une distribution presque semblable au-dessus d'une distance d'environ 4 millimètres, alors qu'ensuite une structure plus complexe se développe.

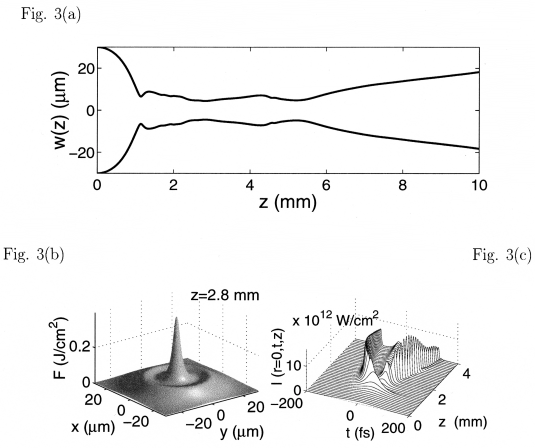

Fig. 3: (a) Diamètre calculé du filament le long de sa propagation. (b) Profil calculé de fluence 3d du filament à 2.8 mm. (c) Profil temporel du filament le long des 4 premiers millimètres de propagation.

Nous avons également calculé numériquement les spectres d'intensité et les autocorrélations temporelles du faisceau transmis. Ces dernières, détaillées dans la fig. 4(a), forment une structure à trois bosses. En comparant les autocorrélations expérimentales (fig. 2a) et numériques, nous pouvons observer leurs aspects semblables à différentes distances de propagation. Dans la Fig.4(b) nous montrons le spectre de puissance de l'impulsion laser d'entrée, ainsi que le spectre du filament à 10 mm. Nous pouvons noter également la bonne concordance entre les données

expérimentales (fig. 2b) et les résultats numériques, ainsi que sur les composantes spectrales satellites du filament.

L'inspection des simulations met en évidence que la robustesse de filament est principalement due à un équilibre dynamique entre ionisation multiphotonique (MPI) et effet Kerr optique. Bien qu'ils puissent favoriser un profil temporel à deux bosses, la dispersion de vitesse de groupe, l'auto-raidissement et la focalisation spatio-temporelle jouent un rôle secondaire dans le cas actuel. Pour vérifier ce point, nous avons effectué plusieurs simulations, avec et sans effets dispersifs temporels (GVD et/ou les opérateurs T, T^{-1}). Nous avons observé que l'action de ces termes n'a eu aucune influence significative sur la stabilisation du canal auto-guidé, qui est favorisée réellement par la densité de plasma. Cette propriété est conforme à la prévision de Henz et Herrmann [26]. Cependant, les simulations numériques de cette référence ne montrent pas la formation de deux impulsions.

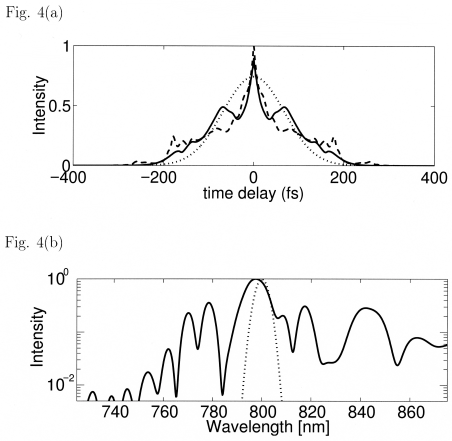

Fig. 4: (a) Autocorrélations calculées: de l'impulsion initiale (pointillée), du filament à 2 mm (pleine) et à 5 mm (tiret). (b) Spectres de puissance: impulsion initiale (pointillée) et filament (pleine) à 10 mm.

En conclusion nous avons présenté, pour la première fois, une filamentation de longue portée dans la silice fondue en utilisant des impulsions laser IR femtoseconde. L'impulsion auto-guidée

est accompagnée d'un élargissement spectral important (génération de continuum spectral), l'impulsion se cassant en deux impulsions secondaires plus courtes. Nos simulations numériques reproduisent la plupart des observations expérimentales. Elles prouvent que le filament auto-guidé résulte réellement de l'équilibre entre auto-focalisation et MPI.

6. Génération de continuum – "Teramobile"

Dans cette section nous focalisons notre intérêt sur les caractéristiques spectrales des filaments laser femtoseconde. En vue des applications potentielles pour le LIDAR [27,28] la génération du continuum de lumière blanche dans les filaments a suscité beaucoup d'intérêt ces dernières années. Quatre groupes de recherche de différentes universités (Ecole Polytechnique, Université d'Iéna, Université de Lyon, et Université de Berlin) sont impliqués dans un projet franco-allemand commun pour étudier la propagation à longue porte des impulsions laser terawatt dans l'atmosphère en utilisant un système laser terawatt mobile (projet "Teramobile").

Ici nous présentons la première mesure de l'extension infrarouge (jusqu'à 4.5 μm) dans le spectre du continuum du filament qui a été effectuée dans le cadre du projet Teramobile. L'influence de la puissance initiale et du chirp temporel du laser sont également étudiés. Le continuum induit par laser permet des mesures multispectrales simultanées, contrairement à la technique linéaire traditionnelle de LIDAR. C'est particulièrement intéressant dans la bande infrarouge de 3-3.5 μm où il est difficile de produire des impulsions laser réglables en longueur d'onde et d'énergie élevée et où un certain nombre de gaz de polluant (particulièrement de composés organiques volatils (VOCs)) ont de fortes bandes d'absorption.

Deux systèmes laser CPA Ti:Sapphire ont été employés avec les paramètres suivants: (a) 60 mJ d'énergie, durée d'impulsion de 35 fs (Ecole Polytechnique, LOA) et (b) 200 mJ d'énergie, durée d'impulsion de 100 fs (Université d'Iéna). Plusieurs systèmes de détection ont été employés pour couvrir les domaines de longueur d'onde étudiés. Pour la région spectrale dans le visible (VIS) un analyseur multi-canaux optique (Chromex 500 IS, *f*/8; gamme spectrale: 400 nm - 1000 nm; 150 l/mm, résolution 1.28 cm^{-1}, Si-ICD-576 Princeton Instruments, Pixel 576x394 refroidis) ont été employés. Dans l'IR, un spectromètre à prisme (Zeiss; 400 nm – 2.7 μm, résolution < 5 nm) et un spectromètre à prisme à double passage Perkin-Elmer (longueur focale 27 cm, prisme en fluorure de lithium (LiF), transmission jusqu'à 10 μm) ont été équipés d'un détecteur Ge-(600 nm – 1800 nm) et d'un détecteur InSb refroidi (1.5 μm - 5.6 μm, Hamamatsu). De plus, des filtres d'interférence (Corion) suppriment la longueur d'onde fondamentale du faisceau laser.

Dans l'expérience, le laser a été légèrement focalisé avec des lentilles minces en silice fondue de longueur focale 8 et 10 m. Nous avons vérifié expérimentalement qu'en raison du grand diamètre du faisceau (25 millimètres FWHM) et la petite épaisseur de la lentille (3 millimètres),

aucun continuum n'a été produit dans la lentille. La génération du continuum s'est produite dans la région focale, avec le continuum se propageant plus loin avec la même divergence que le faisceau laser lui-même. Les mesures de puissance avant et après le foyer ont prouvé qu'aucune perte d'énergie significative ne s'est produite au foyer dû au procédé de génération de continuum. Les mesures spectrales ont eu lieu à environ 30 m de la lentille, par conséquent après approximativement 20 m de propagation de filament. À cette position le faisceau laser a un diamètre de 20 à 25 centimètres. Toutes les mesures spectrales ont été faites en transmission directe, avec un miroir en aluminium réfléchissant une petite partie de la lumière vers la fente d'entrée du spectromètre utilisé. Le montage de détection et les détecteurs étaient identiques pour les deux systèmes de laser.

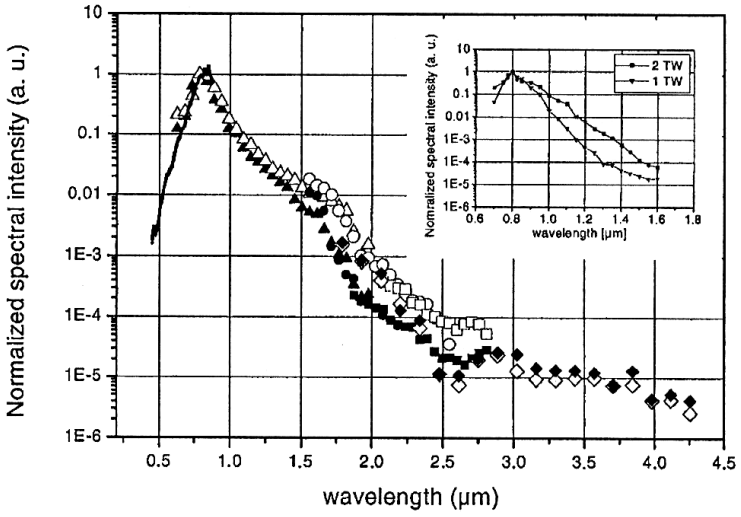

Fig. 1 Spectre mesuré du continuum produit au centre du faisceau par des impulsions de 2 TW (laser (a)). les résultats sont montrés pour deux chirp différents, correspondant (i) durée d'impulsion 35 fs après le compresseur sans chirp (symboles remplis), et (ii) 55 fs après le compresseur à chirp négatif (symboles ouverts). Chaque courbe se compose de respectivement 5 et 4 spectres distincts à partir de 5 (4) unités de détection, correspondant à la forme différente de symbole pour chaque courbe. Encart: Spectre du continuum produit au centre du faisceau par des impulsions de 100 fs (laser (b)) en fonction de la puissance (200mJ et 100mJ, c.-à-d. 2 TW et 1 TW, respectivement). Les deux courbes ont le même facteur de normalisation.

La fig. 1 montre la distribution spectrale du continuum blanc produit dans l'air par le système laser (a) pour (i) une durée d'impulsion de 115 fs et (ii) 86 fs. Le spectre a été assemblé à partir de quatre spectres (300-900 nm; 700-1800 nm; 1.5-2.7 μm; 1.5-4.5 μm) pris avec quatre systèmes distincts de détection avec des domaines de recouvrement de sensibilité. La bande de continuum est très large, se prolongeant au moins jusqu'à 4.5 μm. Dans l'infrarouge, où aucune expérience

n'avait été précédemment réalisée dans l'air, on observe un affaiblissement presque exponentiel de plus de quatre ordres de grandeur jusqu'au 2.5 μm. De 2.5 μm à 4.5 μm un affaiblissement plus lent est enregistré, d'un ordre de grandeur seulement. Au-dessus du 4.5 μm, l'intensité du signal était trop faible pour la distinguer du bruit du détecteur. On observe les bandes d'absorption de l'eau à 1.8 μm et à 2.5 μm dans le spectre du continuum. Ceci suggère que l'utilisation d'un continuum étendu comme source lumineuse pour la télédétection spectroscopique de l'atmosphère puisse être prolongée à l'infrarouge.

La dépendance du signal avec l'énergie de l'impulsion laser incidente a été étudiée avec le système laser (b). Comme on le voit dans l'encart de la fig. 1, une première variation d'intensité par un facteur de deux ne mène pas à une variation de la forme spectrale dans la région de 1 – 1.6 μm, mais seulement à une diminution globale d'efficacité par un facteur de presque un ordre de grandeur. On doit également noter que l'efficacité de conversion avec le laser (b) fournissant des impulsions plus courtes est un ordre de grandeur plus bas qu'avec le laser (a) (fig. 1, graphique principal), bien que les deux systèmes fournissent la même puissance maximale de 2 TW.

La dépendance au chirp temporel (dérive temporelle de fréquence) a été étudiée avec le système de laser (a). Les résultats sont montrés dans la fig. 2 où l'on a mesuré l'efficacité de conversion du continuum à deux longueurs d'onde (1.7 μm et 3 μm avec 5 nm de résolution), en fonction du chirp du laser. Le réglage optimal du chirp dépend de la longueur d'onde d'émission à optimiser. D'ailleurs comme on le voit sur la fig. 1, l'efficacité globale de conversion dans l'infrarouge proche change de manière significative quand on modifie le chirp.

On pense que généralement la SPM est le processus dominant impliqué dans l'émission de continuum (voir par exemple Brodeur et Chin [9]). Un calcul simple effectué avec la SPM seule et les paramètres typiques de nos expériences est en accord qualitatif avec nos observations: (i) la teneur spectrale calculée de la lumière blanche après la propagation de 20 m dans un filament s'étend de quelques centaines de nanomètres jusqu'au moins 5 μm; (ii) le système laser (a) avec des impulsions plus courtes a une plus grande efficacité de génération de lumière blanche que le système (b). Ceci nous amène à penser que la SPM constitue le processus principal de génération du continuum de lumière blanche dans l'air. Cependant une compréhension quantitative du continuum est toujours un sujet actif de recherche et a besoin d'une discussion beaucoup plus complexe, voir par exemple Gaeta [29].

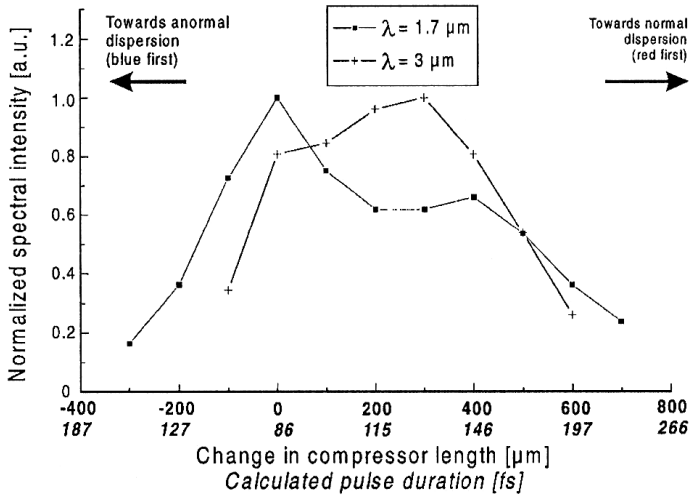

Fig. 2 Dépendance avec le chirp du continuum blanc produit par le système laser (a) à deux longueurs d'onde distinctes (1.7 µm et 3 µm, avec une résolution de 5 nm). Les deux courbes ont la même normalisation. L'échelle du chirp est indiquée ainsi que la variation de longueur du compresseur, avec le 0 choisi arbitrairement, à la valeur du chirp de la courbe (ii) sur la fig. 1. Les nombres en italiques sont les durées d'impulsion calculées correspondantes après la fenêtre de sortie et la lentille.

Comme conclusion, nous avons mesuré la dépendance en longueur d'onde du continuum blanc émis par des filaments produits dans l'air par des impulsions laser femtoseconde de puissance élevée, entre 300 nm et 4.5 µm. Les résultats prouvent que la puissance et la forme temporelle des impulsions du laser d'excitation ont un impact critique sur l'efficacité de conversion. En ce qui concerne les applications, le continuum blanc fourni par les filaments pourrait être employé comme "lampe blanche" produite in-situ, permettant des mesures multispectrales de Lidar des constituants atmosphériques de la région visible à l'infrarouge.

Conclusion

La filamentation d'impulsions femtoseconde a été étudiée depuis plus de 6 ans maintenant et nous avons une vue tout à fait générale de ses caractéristiques et mécanismes physiques impliqués. Dans cette thèse nous avons décrit les résultats de nos études expérimentales et numériques sur le sujet pendant les trois dernières années. Nous avons présenté de nouvelles observations et calculs sur la filamentation d'impulsions femtoseconde dans différents milieux non-linéaires transparents à différentes conditions initiales. L'information incluse dans l'étude courante complète notre connaissance sur le filamentation et aide à la meilleure compréhension des mécanismes physiques impliqués. Des caractéristiques générales et communes sont indiquées pour tous types de filaments. Le confinement spatial, la formation d'un canal de plasma d'électrons, l'élargissement spectral comme le fait que l'impulsion se casse avec la formation d'une double impulsion sont certains des attributs qui semblent identifier les filaments femtoseconde.

Les nouveautés dans cette thèse peuvent être récapitulées comme suit. Au chapitre 1 nous avons présenté l'évidence expérimentale de l'ionisation dans le filament avec l'évaluation précise de la densité électronique obtenue en utilisant deux techniques particulièrement conçues à cette fin. La multi-filamentation et la première évidence expérimentale claire de la division et de la coalescence d'un faisceau ont été décrites au chapitre 2. La première étude détaillée de la filamentation ultraviolette d'impulsion fs et ps a été analysée au chapitre 3. Une des applications les plus intéressantes des filaments laser fs, celle de déclencher et de guider des décharges électriques a été étudiée au chapitre 4. Nous y avons présenté la première démonstration expérimentale des décharges électriques guidées par des filaments par formation d'un canal de plasma. Notre analyse a fourni une explication physique concrète des mécanismes impliqués dans ce type de décharge électrique. Au chapitre 5 nous avons rapporté la première observation de la filamentation fs dans la silice fondue. Et enfin au chapitre 6 nous avons discuté de la génération du continuum dans la filamentation femtoseconde.

Bien que ce soit une étude étendue, la recherche sur la filamentation fs est loin d'être achevée. Des questions nombreuses demeurent ouvertes sur des aspects fondamentaux aussi bien que sur des observations expérimentales. Pour citer seulement quelques exemples: la dépendance en polarisation de la filamentation, le contrôle de la multi-filamentation, la propagation sur des

distances très longues (plusieurs km), l'optimisation du continuum, le contrôle de longues décharges électriques, le LIDAR etc …

References

[1] A. Braun, G. Korn, X. Liu, D. Du, J. Squier, and G. Mourou, Opt. Lett. **20**, 73 (1995).

[2] E. T. J. Nibbering, P. F. Curley, G. Grillon, B. Prade, M. Franco, F. Salin, and A. Mysyrowicz, Opt. Lett. 21, **62** (1996).

[3] A. Brodeur, C. Y. Chien, F. A. Ilkov, S. L. Chin, O. G. Kosareva, and V. P. Kandidov, Opt. Lett. **22**, 304 (1997).

[4] M. Mlejnek, M. Kolesik, J. V. Moloney, and E. M. Wright, Phys. Rev. Lett. **83**, 2938 (1999).

[5] J. K. Ranka, R. W. Schirmer, and A. L. Gaeta, Phys. Rev. Lett. **77**, 3783 (1996).

[6] A. Zozulya, S. A. Diddams, A. G. Van Engen, and T. S. Clement, Phys. Rev. Lett. **82**, 1430 (1999).

[7] S. A. Diddams, H. K. Eaton, A. A. Zozulya, and T. S. Clement, Opt. Lett. **23**, 379 (1998).

[8] S. Henz and J. Herrmann, Phys. Rev. A **59**, 2528 (1999).

[9] A. Brodeur and S. L. Chin, J. Opt. Soc. Am. B **16**, 637 (1999).

[10] S. L. Chin, A. Brodeur, S. Petit, O. G. Kosareva, and V. P. Kandidov, J. Nonlinear Opt. Phys. & Materials **8**, 121 (1999).

[11] S. L. Chin, S. Petit, F. Borne, and K. Miyazaki, Jpn. J. Appl. Phys. **38**, L126-L128 (1999).

[12] H. Nishioka , W. Odajima, K.-I. Ueda, and H. Takuma, Opt. Lett. **20**, 2503 (1995).

[13] J. Marburger, Prog. Quantum Electron. **4**, 35 (1975).

[14] L. B. Loeb, *Basic Processes of Gaseous Electronics* (University of California Press, Berkley, 1960).

[15] X. M. Zhao, J. C. Diels, C. Y. Wang, and J. M. Elizondo, IEEE J. Quantum Electron. **31**, 599 (1995).

[16] S. Tzortzakis, M. Franco, Y.-B. André, A. Chiron, B. Lamouroux, B. Prade, and A. Mysyrowicz, Phys. Rev. E **60**, R3505-R3507 (1999).

[17] S. Tzortzakis, B. Prade, M. Franco, and A. Mysyrowicz, Opt. Commun. **181**, 123 (2000).

[18] S. Szatmari and F. P. Schäfer, Opt. Commun. **68**, 196 (1988).

[19] A. Chiron, H. R. Lange, J.-F. Ripoche, B. Lamouroux, M. Franco, B. Prade, and A. Mysyrowicz, Eur. Phys. J. D **6**, 383 (1999).

[20] S. Tzortzakis, B. Lamouroux, A. Chiron, M. Franco, B. Prade, A. Mysyrowicz, and S. D. Moustaizis, Opt. Lett. **25**, 1270 (2000).

[21] S. Tzortzakis, L. Bergé, A. Couairon, M. Franco, B. Prade, and A. Mysyrowicz, Phys. Rev. Lett. **86**, 5470 (2001).

[22] B. La Fontaine, F. Vidal, D. Comtois, C. Y. Chien, A. Desparois, T. W. Johnston, J. C. Kieffer, H. P. Mercure, H. Pépin, and F. A. M. Rizk, IEEE Trans. Plasma Sci. **27**, 688 (2000).

[23] D. Comtois, C. Y. Chien, A. Desparois, F. Génin, G. Jarry, T. W. Johnston, J.-C. Kieffer, B. La Fontaine, F. Martin, R. Mawassi, H. Pépin, F. A. M. Rizk, F. Vidal, P. Couture, H. P. Mercure, C. Potvin, A. Bondiou-Clergerie, and I. Gallimberti, Appl. Phys. Lett. **76**, 819 (2000).

[24] K. Eidmann, J. Meyer-ter-Vehn, T. Schleger, and S. Hüller, Phys. Rev. E **62**, 1202 (2000).

[25] P. Audebert, Ph. Daguzan, A. Dos Santos, J. C. Gauthier, J. P. Geindre, S. Guizard, G. Hamoniaux, K. Krastev, P. Martin, G. Petite, and A. Antonetti, Phys. Rev. Lett. **73**, 1990 (1994).

[26] S. Henz and J. Herrmann, Phys. Rev. E 53, 4092 (1996).

[27] L. Wöste *et al.*, Laser Und Optoelectronik **29**, 51 (1997).

[28] P. Rairoux, H. Schillinger, S. Niedermeier, M. Rodriguez, F. Ronneberger, R. Sauerbrey, B. Stein, D. Waite, C. Wedekind, H. Wille, L. Wöste, and C. Ziener, Appl. Phys. B **71**, 573 (2000).

[29] A. L. Gaeta, Phys. Rev. Lett. **84**, 3582 (2000).

Bibliography

1. **Agrawal, G. P.**, Nonlinear fiber optics. Academic Press (1989).

2. **Akhmanov, S. A., A. P. Sukhorukov, and R. V. Khokhlov**, Self-focusing and self-trapping of intense light beams in a nonlinear medium, Sov. Phys. JETP **23**, 1025-1033 (1966).

3. **Akhmediev, N. N., V. I. Korneev, and R. F. Nadiev**, Modulation instability of the ground state of the nonlinear wave equation: optical machine gun, Opt. Lett. **17**, 393-395 (1992).

4. **Aközbek, N., C. M. Bowden, A. Talebpour, and S. L. Chin**, Femtosecond pulse propagation in air: variational analysis, Phys. Rev. E **61**, 4540-4549 (2000).

5. **Aközbek, N., C. M. Bowden, A. Talebpour, and S. L. Chin**, Laser pulse propagation in ionizing air: a semianalytical approach, Laser Phys. **10**, 101-106 (2000).

6. **Aleksandrov, G. N., V. L. Ivanov, G. D. Kadzov, V. A. Parfenov, L. N. Pakhomov, V. Yu. Petrun'kin, V. A. Podlevskii, and Yu. G. Seleznev**, Effect of a laser-produced ionization channel on a long discharge in air, Sov. Phys. Tech. Phys. **22**, 1233-1234 (1977).

7. **Ammosov, M. V., N. B. Delone, and V. P. Krainov**, Tunel ionization of complex atoms and of atomic ions in an alternating electromagnetic field, Sov. Phys. JETP **64**, 1191 (1986).

8. **Antipov, A. A., A. Z. Grasyuk, A. K. Zhigalkyn, L. L. Losev, and V. I. Soskov**, Propagation of ionization (streamer) waves in air along a channel induced by ultraviolet laser radiation, Sov. Phys. Tech. Phys. **36**, 490-492 (1991).

9. **Asinovskii, E. I., L. M. Vasilyak, and S. Yu. Unkovskii**, The space-time evolution of an electrical discharge directed by a laser spark, Sov. Phys. Tech. Phys. **37**, 335-337 (1992).

10. **Audebert, P., Ph. Daguzan, A. Dos Santos, J. C. Gauthier, J. P. Geindre, S. Guizard, G. Hamoniaux, K. Krastev, P. Martin, G. Petite, and A. Antonetti**, Space-time observation of an electron gas in SiO_2, Phys. Rev. Lett. **73**, 1990-1993 (1994).

11. **Augst, S., D. D. Meyerhofer, D. Strickland, and S. L. Chin**, Laser ionization of noble gases by coulomb-barrier suppression, J. Opt. Soc. Am. B **8**, 858-867 (1991).

12. **Ball, L.** , The laser lightning rod system: thunderstorm domestication, Appl. Opt. **13**, 2292-2296 (1974).

13. **Bendib, A., A. Tahraoui, K. Kalache, P. Chessa, and P. Mora**, Spectral modifications in ultra-short pulses induced by ionization fronts and relativistic plasma waves, Opt. Commun. **142**, 146-152 (1997).

14. **Bergé, L. and A. Couairon**, Nonlinear propagation of self-guided ultra-short pulses in ionized gases, Phys. Plasmas **7**, 210-230 (2000).

15. **Bergé, L. and A. Couairon**, Gas-Induced Solitons, Phys. Rev. Lett. **86**, 1003-1006 (2001).

16. **Blagoeva, A. B., S. G. Dinev, A. A. Dreischuh, and Naidenov**, Light bullets formation in a bulk media, IEEE J. Quantum Electron. **27**, 2060-2065 (1991).

17. **Boyd, R. W.**, Nonlinear optics. Academic Press (1992).

18. **Boyd, R. W. and G. S. Agarwal**, Preventing laser beam filamentation through use of the squeezed vacuum, Phys. Rev. A **59**, R2587-R2589 (1999).

19. **Brabec, T. and F. Krausz**, Nonlinear Optical Pulse Propagation in the Single-Cycle Regime, Phys. Rev. Lett. **78**, 3282-3285 (1997).

20. **Braun, A., G. Korn, X. Liu, D. Du, J. Squier, and G. Mourou**, Self-channeling of high-peak-power femtosecond laser pulses in air, Opt. Lett. **20**, 73-75 (1995).

21. **Brodeur, A., C. Y. Chien, F. A. Ilkov, S. L. Chin, O. G. Kosareva, and V. P. Kandidov**, Moving focus in the propagation of ultrashort laser pulses in air, Opt. Lett. **22**, 304-306 (1997).

22. **Brodeur, A. and S. L. Chin**, Band-gap dependence of the ultrafast white-light continuum, Phys. Rev. Lett. **80**, 4406-4409 (1998).

23. **Brodeur, A. and S. L. Chin**, Ultrafast white-light continuum generation and self-focusing in trasparent condenced media, J. Opt. Soc. Am. B **16**, 637-650 (1999).

24. **Brodeur, A., F. A. Ilkov, and S. L. Chin**, Beam filamentation and the white light continuum divergence, Opt. Commun. **129**, 193-198 (1996).

25. **Cao, X. D., G. P. Agrawal, and C. J. McKinstrie**, Self-focusing of chirped optical pulses in nonlinear dispersive media, Phys. Rev. A **49**, 4085-4092 (1994).

26. **Cerullo, G., A. Dienes, and V. Magni**, Space-time coupling and collapse threshold for femtosecond pulses in dispersive nonlinear media, Opt. Lett. **21**, 65-67 (1996).

27. **Chernev, P. and V. Petrov**, Self-focusing of light pulses in the presence of normal group-velocity dispersion, Opt. Lett. **17**, 172-174 (1992).

28. **Chiao, R. Y., E. Garmire, and C. H. Townes**, Self-trapping of optical beams, Phys. Rev. Lett. **13**, 479-482 (1964).

29. **Chien, C. Y., B. La Fontaine, A. Desparois, Z. Jiang, T. W. Johnston, J. C. Kieffer, H. Pépin, F. Vidal, and H. P. Mercure**, Single-shot chirped-pulse spectral interferometry used to measure the femtosecond ionization dynamics of air, Opt. Lett. **25**, 578-580 (2000).

30. **Chin, S. L., A. Brodeur, S. Petit, O. G. Kosareva, and V. P. Kandidov**, Filamentation

and supercontinuum generation during the propagation of powerful ultrashort laser pulses in optical media (white light laser), J. Nonlinear Opt. Phys. & Materials **8**, 121-146 (1999).

31. **Chin, S. L. and K. Miyazaki**, A comment on lightning control using a femtosecond laser, Jpn. J. Appl. Phys. **38**, 2011-2012 (1999).

32. **Chin, S. L., S. Petit, F. Borne, and K. Miyazaki**, The white light supercontinuum is indeed an ultrafast white light laser, Jpn. J. Appl. Phys. **38**, L126-L128 (1999).

33. **Chiron, A., H. R. Lange, J.-F. Ripoche, B. Lamouroux, M. Franco, B. Prade, and A. Mysyrowicz**, Numerical simulations of the nonlinear propagation of femtosecond optical pulses in gases, Eur. Phys. J. D **6**, 383-396 (1999).

34. **Christov, I. P., H. C. Kapteyn, M. M. Murnane, C.-P. Hang, and J. Zhou**, Space-time focusing of femtosecond pulses in a Ti:sapphire laser, Opt. Lett. **20**, 309-311 (1995).

35. **Clark, T. R. and H. M. Milchberg**, Time and space-resolved density evolution of the plasma waveguide, Phys. Rev. Lett. **78**, 2373-2376 (1997).

36. **Comtois, D., C. Y. Chien, A. Desparois, F. Génin, G. Jarry, T. W. Johnston, J.-C. Kieffer, B. La Fontaine, F. Martin, R. Mawassi, H. Pépin, F. A. M. Rizk, F. Vidal, P. Couture, H. P. Mercure, C. Potvin, A. Bondiou-Clergerie, and I. Gallimberti**, Triggering and guiding leader discharges using a plasma channel created by an ultrashort laser pulse, Appl. Phys. Lett. **76**, 819-821 (2000).

37. **Corkum, P. B. and C. Rolland**, Femtosecond continua produced in gases, IEEE J. Quantum Electron. **25**, 2634-2639 (1989).

38. **Corkum, P. B., C. Rolland, and T. Srinivasan-Rao**, Supercontinuum generation in gases, Phys. Rev. Lett. **57**, 2268-2271 (1986).

39. **Couairon, A. and L. Bergé**, Modeling the filamentation of ultra-short pulses in ionizing media, Phys. Plasmas **7**, 193-209 (2000).

40. **Couairon, A., S. Tzortzakis, L. Bergé, M. Franco, B. Prade, and A. Mysyrowicz**, Infrared femtosecond light filaments in air: simulations and experiments, J. Opt. Soc. Am. B (submitted).

41. **Côté, C. Y., J. C. Kieffer, and O. Peyrusse**, Picosecond time-resolved spectroscopy of a controlled preformed plasma heated by an intense subpicosecond laser pulse, Phys. Rev. E 56, 992-1000 (1997).

42. **Diddams, S. A., H. K. Eaton, A. A. Zozulya, and T. S. Clement**, Amplitude and phase measurements of femtosecond pulse splitting in nonlinear dispersive media, Opt. Lett. **23**, 379-381 (1998).

43. **Diels, J.-C. and W. Rudolph**, Ultrashort laser pulse phenomena. Academic Press (1996).

44. **Durfee III, C. G. and H. M. Milchberg**, Light pipe for high intensity laser pulses, Phys. Rev. Lett. **71**, 2409-2412 (1993).

45. **Edmundson, D. E. and R. H. Enns**, Fully three-dimensional collisions of bistable light bullets, Opt. Lett. **18**, 1609-1611 (1993).

46. **Esarey, E., P. Sprangle, J. Krall, and A. Ting**, Self-focusing and guiding of short laser pulses in ionized gases and plasmas, IEEE J. Quantum Electron. **33**, 1879 (1997).

47. **Esarey, E., P. Sprangle, M. Pilloff, and J. Krall**, Theory and group velocity of ultrashort, tightly focused laser pulses, J. Opt. Soc. Am. B **12**, 1695-1703 (1995).

48. **Feit, M. D. and J. A. Fleck Jr.**, Beam nonparaxiality, filament formation, and beam breakup in the self-focusing of optical beams, J. Opt. Soc. Am. B **5**, 633-640 (1988).

49. **Fibich, G. and B. Ilan**, Self-focusing of elliptic beams: an example of the failure of the aberrationless approximation, J. Opt. Soc. Am. B **17**, 1749-1758 (2000).

50. **Fibich, G. and G. C. Papanicolaou**, Self-focusing in the presence of small time dispersion and nonparaxiality, Opt. Lett. **15**, 1379-1381 (1997).

51. **Gaeta, A. L.**, Catastrophic collapse of ultrashort pulses, Phys. Rev. Lett. **84**, 3582-3585 (2000).

52. **Greig, J. R., D. W. Koopman, R. F. Fernsler, R. E. Pechacek, I. M. Vitkovitsky, and A. W. Ali**, Electrical discharges guided by pulsed CO_2 laser radiation, Phys. Rev. Lett. **41**, 174-177 (1978).

53. **Henz, S. and J. Herrmann**, Two-dimensional spatial optical solitons in bulk kerr-media stabilized by self-induced multi-photon ionization: variational approach, Phys. Rev. E **53**, 4092-4097 (1996).

54. **Henz, S. and J. Herrmann**, Self-channeling and pulse shortening of femtosecond pulses in multiphoton-ionized dispersive dielectric solids, Phys. Rev. A **59**, 2528-2531 (1999).

55. **Hercher, M. A.**, Laser induced damage in trasparent media, J. Opt. Soc. Am. **54**, 563 (1964).

56. **Hijikawa, M., H. Tamura, H. Arishima, K. Horioka, and K. Kasuya**, Electrical discharge channel in cesium vapor initiated by a XeCl laser, Appl. Phys. Lett. **45**, 234-236 (1984).

57. **Honda, C., K. Muraoka, T. Takuma, M. Akazaki, F. Kinoshita, and O. Katahira**, Characteristics of discharge induced by laser-generated plasmas in atmospheric air, Electr. Eng. Jap. **114**, 994-1002 (1994).

58. **Hutchinson, I. H.**, Principles of plasma diagnostics. Cambridge University Press (1994).

59. **Hüller, S., Ph. Mounaix, V. T. Tikhonchuk, and D. Pesme**, Interaction of two neighboring laser beams taking into account the effects of plasma hydrodynamics, Phys. Plasmas **4**, 2670-2680 (1997).

60. **Kandidov, V. P., O. G. Kosareva, and S. A. Shilyonov**, Spatial-temporal evolution of a

femtosecond ionizing pulse in gases, Nonlinear Opt. **12**, 119-135 (1994).

61. **Kandidov, V. P., O. G. Kosareva, and S. A. Shlenov**, Influence of transient self-defocusing on the propagation of high-power femtosecond laser pulses in gases under ionization conditions, Quantum Electron. **24**, 905-911 (1994).

62. **Kasparian, J., R. Sauerbrey, and S. L. Chin**, The critical laser intensity of self-guided light filaments in air, Appl. Phys. B **71**, 877-879 (2000).

63. **Kasparian, J., R. Sauerbrey, D. Mondelain, S. Niedermeier, J. Yu, J.-P. Wolf, Y.-B. André, M. Franco, B. Prade, S. Tzortzakis, A. Mysyrowicz, M. Rodriguez, H. Wille, and L. Wöste**, Infrared extension of the supercontinum generated by femtosecond terawatt laser pulses propagating in the atmosphere, Opt. Lett. **25**, 1397-1399 (2000).

64. **Keldysh, L. V**., Ionization in the field of a strong electromagnetic wave, Sov. Phys. JETP **20**, 1307-1314 (1965).

65. **Kempe, M. and W. Rudolph**, Femtosecond pulses in the focal region of lenses, Phys. Rev. A **48**, 4721-4729 (1993).

66. **Koprinkov, I. G., A. Suda, P. Wang, and K. Midorikawa**, Self-compression of high-intensity femtosecond optical pulses and spatiotemporal soliton generation, Phys. Rev. Lett. **84**, 3847-3850 (2000).

67. **Kosareva, O. G., V. P. Kandidov, A. Brodeur, C. Y. Chien, and S. L. Chin**, Conical emission from laser-plasma interaction in the filamentation of powerful ultrashort laser pulses in air, Opt. Lett. **22**, 1332-1334 (1997).

68. **Kosareva, O. G., V. P. Kandidov, A. Brodeur, and S. L. Chin**, From filamentation in condenced media to filamentation in gases, J. Nonlinear Opt. Phys. & Materials **6**, 485-494 (1997).

69. **Kosareva, O. G., V. P. Kandidov, and S. A. Shlenov**. 1996. Dynamics of the stimulated Raman Scattering of subpicosecond laser pulse in the self-produced plasma, p. 489-502. *In* Super Intense Laser Atom Physics . Kluver Academic Publishers, Netherlands.

70. **Kühlke, D., U. Herpers, and D. Von der Linde**, Spectral broadening if intense femtosecond pulses in atmospheric air, Opt. Commun. **63**, 275-277 (1987).

71. **L. Wöste *et al.***, Femtosecond atmospheric lamp, Laser und Optoelectronik **29**, 51 (1997).

72. **La Fontaine, B., F. Vidal, D. Comtois, C. Y. Chien, A. Desparois, T. W. Johnston, J. C. Kieffer, H. P. Mercure, H. Pépin, and F. A. M. Rizk**, The influence of electron density on the formation of streamers in electrical discharges triggered with ultrashort laser pulses, IEEE Trans. Plasma Sci. **27**, 688-700 (2000).

73. **La Fontaine, B., F. Vidal, Z. Jiang, C. Y. Chien, D. Comtois, A. Desparois, T. W. Johnston, J. C. Kieffer, H. Pépin, and H. P. Mercure**, Filamentation of ultrashort pulse laser beams resulting from their propagation over long distances in air, Phys. Plasmas **6**,

1615-1621 (1999).

74. **Ladouceur, H. D., A. P. Baronavski, D. Lohrmann, P. W. Grounds, and P. G. Girardi**, Electrical conductivity of a femtosecond laser generated plasma channel in air, Opt. Commun. **189**, 107-111 (2001).

75. **Lange, H. R.**, Autoguidage dans l'air d'impulsion ultracourtes, *Thesis*, Ecole Polytechnique, (1998).

76. **Lange, H. R., A. Chiron, J.-F. Ripoche, A. Mysyrowicz, P. Breger, and P. Agostini**, High-order harmonic generation and quasiphase matching in Xenon using self-guided femtosecond pulses, Phys. Rev. Lett. **81**, 1611-1613 (1998).

77. **Lange, H. R., G. Grillon, J.-F. Ripoche, M. Franco, B. Lamouroux, B. Prade, A. Mysyrowicz, E. T. J. Nibbering, and A. Chiron**, Anomalous long-range propagation of femtosecond laser pulses through air: moving focus or pulse self-guiding?, Opt. Lett. **23**, 120-122 (1998).

78. **Lange, H. R., J.-F. Ripoche, A. Chiron, B. Lamouroux, M. Franco, B. Prade, E. T. J. Nibbering, and A. Mysyrowicz**, Temporal evolution of selfguided femtosecond laser pulses in the presence of Kerr-nonlinearity and ionisation, XIth International Conference on Ultrafast Phenomena 115 (1998).

79. **Larochelle, S. F. J., A. Talebpour, and S. L. Chin**, Coulomb effect in multiphoton ionization of rare-gas atoms, J. Phys. B. **31**, 1215-1224 (1998).

80. **Lenzner, M., J. Krüger, S. Sartania, Z. Cheng, Ch. Spielmann, G. Mourou, W. Kautek, and F. Krausz**, Femtosecond Optical Breakdown in Dielectrics, Phys. Rev. Lett. **80**, 4076-4079 (1998).

81. **Li, M., S. Menon, J. P. Nibarger, and G. N. Gibson**, Ultrafast Electron Dynamics in Femtosecond Optical Breakdown of Dielectrics, Phys. Rev. Lett. **82**, 2394-2397 (1999).

82. **Liu, X., L. J. Qian, and F. W. Wise**, Generation of optical spatiotemporal solitons, Phys. Rev. Lett. **82**, 4631-4634 (1999).

83. **Loeb, L. B.**, Basic Processes of Gaseous Electronics. University of California Press, Berkley (1960).

84. **Losev, L. L. and V. I. Soskov**, Characteristic features of the ionization of air by ultrashort ultraviolet laser pulses, Sov. J. Quantum Electron. **19**, 46-49 (1989).

85. **Luther, G. G., J. V. Moloney, and A. C. Newell**, Self-focusing threshold in normally dispersive media, Opt. Lett. **19**, 862-864 (1994).

86. **Luther, G. G., A. C. Newell, J. V. Moloney, and E. M. Wright**, Short-pulse conical emission and spectral broadening in normally dispersive media, Opt. Lett. **19**, 789-791 (1994).

87. **Manassah, J., P. Baldeck, and R. Alfano**, Self-focusing, self-phase modulation and

diffraction in bulk homogeneous material, Opt. Lett. **13**, 1090-1092 (1988).

88. **Marburger, J.**, Self-focusing: theory, Prog. Quantum Electron. **4**, 35 (1975).

89. **Miki, M. , T. Shindo, and Y. Aihara**, Mechanisms of guiding ability of CO_2 laser produced plasmas on pulsed discharges, J. Phys. D **29**, 1984-1996 (1996).

90. **Miki, M. and A. Wada**, Guiding of electrical discharges under atmospheric air by ultraviolet laser-produced plasma channel, J. Appl. Phys. **80**, 3208-3214 (1996).

91. **Mlejnek, M., M. Kolesik, J. V. Moloney, and E. M. Wright**, Optically turbulent femtosecond light guide in air, Phys. Rev. Lett. **83**, 2938-2941 (1999).

92. **Mlejnek, M., M. Kolesik, E. M. Wright, and J. V. Moloney**, A dynamic spatial replenishment scenario for femtosecond pulses propagating in air - a route to optical turbulence, Laser Phys. **10**, 107-110 (2000).

93. **Mlejnek, M., E. M. Wright, and J. V. Moloney**, Dynamic spatial replenishment of femtosecond pulses propagating in air, Opt. Lett. **23**, 382-384 (1998).

94. **Mlejnek, M., E. M. Wright, and J. V. Moloney**, Femtosecond pulse propagation in argon: a pressure dependence study, Phys. Rev. E **58**, 4903-4910 (1998).

95. **Mlejnek, M., E. M. Wright, and J. V. Moloney**, Moving-focus versus self-waveguiding model for long distance propagation of femtosecond pulses in air, IEEE J. Quantum Electron. **35**, 1771-1776 (1999).

96. **Mlejnek, M., E. M. Wright, and J. V. Moloney**, Power dependence of dynamic spatial replenishment of femtosecond pulses propagating in air, Opt. Express **4**, 223-228 (1999).

97. **Muller, H. G., P. Agostini, and G. Petite**. 1992. Multiphoton ionization, *In* M. Gavrila (ed.), Atoms in intense laser fields. Academic Press.

98. **Nibbering, E. T. J., P. F. Curley, G. Grillon, B. Prade, M. Franco, F. Salin, and A. Mysyrowicz**, Conical emission from self-guided femtosecond pulses in air, Opt. Lett. **21**, 62-64 (1996).

99. **Nishioka, H., W. Odajima, K.-I. Ueda, and H. Takuma**, Ultrabroadband flat continuum generation in multichannel propagation of terrawatt Ti:sapphire laser pulses, Opt. Lett. **20**, 2503-2507 (1995).

100. **Petit, S., A. Talebpour, A. Proulx, and S. L. Chin**, Polarization dependence of the propagation of intense laser pulses in air, Opt. Commun. **175**, 323-327 (2000).

101. **Petit, S., A. Talebpour, A. Proulx, and S. L. Chin**, Some consequences during the propagation of an intense femtosecond laser pulse in trasparent optical media: a strongly deformed white-light laser, Laser Phys. **10**, 93-100 (2000).

102. **Proulx, A., A. Talebpour, S. Petit, and S. L. Chin**, Fast pulsed electric field created from the self-generated filament of a femtosecond Ti:Sapphire laser pulse in air, Opt.

Commun. **174**, 305-309 (2000).

103. **Qin, Y.-D., H. Yang, C.-J. Zhu, and Q. Gong**, Intense femtosecond laser-induced second-harmonic generation in atmospheric-pressure air, Appl. Phys. B **71**, 581-584 (2000).

104. **Rairoux, P., H. Schillinger, S. Niedermeier, M. Rodriguez, F. Ronneberger, R. Sauerbrey, B. Stein, D. Waite, C. Wedekind, H. Wille, L. Wöste, and C. Ziener**, Remote sensing of the atmosphere using ultrashort laser pulses, Appl. Phys. B **71**, 573-580 (2000).

105. **Raizer, Yu. P.**, Gas discharge physics. Springer (1997).

106. **Ranka, J. K. and A. L. Gaeta**, Breakdown of the slowly varying envelope approximation in the self-focusing of ultra-short pulses, Opt. Lett. **23**, 534-536 (1998).

107. **Ranka, J. K., R. W. Schirmer, and A. L. Gaeta**, Observation of pulse splitting in nonlinear dispersive media, Phys. Rev. Lett. **77**, 3783-3786 (1996).

108. **Ranka, J. K., R. W. Schirmer, and A. L. Gaeta**, Coherent spectroscopic effects in the propagation of ultrashort pulses through a two-level system, Phys. Rev. A **57**, R36-R39 (1998).

109. **Rasmussen, J. J. and K. Rypdal**, Blow-up in nonlinear Schödinger equations - I, Phys. Scripta **33**, 481 (1986).

110. **Remoissenet, M.**, Waves called solitons. Springer (1999).

111. **Ren, C. , R. G. Hemker, R. A. Fonseca, B. J. Duda, and W. B. Mori**, Mutual attraction of laser beams in plasmas: braided light, Phys. Rev. Lett. **85**, 2124-2127 (2000).

112. **Ripoche, J.-F.**, Mesure du profil temporel exact d'impulsions laser femtosecondes intenses, *Thesis*, Ecole Polytechnique, (1998).

113. **Ripoche, J.-F., G. Grillon, B. Prade, M. Franco, E. Nibbering, R. Lange, and A. Mysyrowicz**, Determination of the time dependence of n_2 in air, Opt. Commun. **135**, 310-314 (1997).

114. **Rothenberg, J. E.**, Pulse splitting during self-focusing in normally dispersive media, Opt. Lett. **17**, 583-585 (1992).

115. **Rothenberg, J. E.**, Space-time focusing: breakdown of the slowly varying envelope approximation in the self-focusing of femtosecond pulses, Opt. Lett. **17**, 1340-1342 (1992).

116. **Ryan, A. T. and G. P. Agrawal**, Pulse compression and spatial phase modulation in normally dispersive nonlinear Kerr media, Opt. Lett. **20**, 306-308 (1995).

117. **Sanhu, A. S., S. Banerjee, and D. Goswami**, Suppression of supercontinuum generation with circularly polirized light, Opt. Commun. **181**, 101-107 (2000).

118. **Schillinger, H. and R. Sauerbrey**, Electrical conductivity of long plasma channels in air generated by self-guided femtosecond laser pulses, Appl. Phys. B **68**, 753-756 (1999).

119. **Schwarz, J., P. Rambo, and J.-C. Diels**, Measurements of multiphoton ionization coefficients with ultrashort ultraviolet laser pulses, Appl. Phys. B (2001).

120. **Schwarz, J., P. Rambo, J.-C. Diels, M. Kolesik, E. M. Wright, and J. V. Moloney**, Ultraviolet filamentation in air, Opt. Commun. **180**, 383-390 (2000).

121. **Sekikawa, T., T. Kumazaki, Y. Kobayashi, Y. Nabekawa, and S. Watanabe**, Femtosecond extreme-ultraviolet quasi-continuum generation by an intense femtosecond Ti:sapphire laser, J. Opt. Soc. Am. B **15**, 1406-1409 (1998).

122. **Sergeev, A., E. Vanin, L. Stenflo, D. Anderson, M. Lisak, and M. L. Quiroga-Teixeiro**, Nonlinear shaping of a two-dimensional ultrashort ionizing pulse, Phys. Rev. A **46**, 7830-7836 (1992).

123. **Shen, Y. R.**, The principles of nonlinear optics. John Wiley & Sons (1984).

124. **Silberberg, Y.**, Collapse of optical pulses, Opt. Lett. **15**, 1282-1284 (1990).

125. **Skarka, V., V. I. Berezhiani, and R. Miklaszewki**, Spatiotemporal soliton propagation in saturating nonlinear optical media, Phys. Rev. E **56**, 1080-1087 (1997).

126. **Streltsov, A. M. and N. F. Borrelli**, Fabrication and analysis of a directional coupler written in glass by nanojoule femtosecond laser pulses, Opt. Lett. **26**, 42-43 (2001).

127. **Strickland, D. and P. B. Corkum**, Resistance of short pulses to self-focusing, J. Opt. Soc. Am. B **11**, 492-497 (1994).

128. **Szatmari, S. and F. P. Schäfer**, Simplified laser system for the generation of 60 fs pulses at 248 nm, Opt. Commun. **68**, 196-202 (1988).

129. **Talebpour, A., M. Abdel-Fattah, and S. L. Chin**, Focusing limits of intense ultrafast laser pulses in a high pressure gas: road to new spectroscopic source, Opt. Commun. **183**, 479-484 (2000).

130. **Talebpour, A., C.-Y. Chien, and S. L. Chin**, The effects of dissociative recombination in multiphoton ionization of O_2, J. Phys. B **29**, L677-L680 (1996).

131. **Talebpour, A., S. Petit, and S. L. Chin**, Re-focusing during the propagation of a focused femtosecond Ti:Sapphire laser pulse in air, Opt. Commun. **171**, 285-290 (1999).

132. **Talebpour, A., J. Yang, and S. L. Chin**, Semi-empirical model for the rate of tunnel ionization of N_2 and O_2 molecule in an intense Ti:sapphire laser pulse, Opt. Commun. **163**, 29-32 (1999).

133. **Tikhonenko, V., J. Jason Christou, and B. Luther-Davies**, Three Dimensional Bright Spatial Soliton Collision and Fusion in a Saturable Nonlinear Medium, Phys. Rev. Lett. **76**, 2698-2701 (1996).

134. **Tohmon, R., H. Mizuno, Y. Ohki, K. Sasagane, K. Nagasawa, and Y. Hama**, **Correlation of the 5.0 and 7.6 eV absorption bands in SiO_2 with oxygen vacancy, Phys. Rev. B 39**, 1337-1345 (1989).

135. **Tzortzakis, S., L. Bergé, A. Couairon, M. Franco, B. Prade, and A. Mysyrowicz**, Break-up, and fusion of self-guided femtosecond light pulses in air, Phys. Rev. Lett. **86**, 5470 (2001).

136. **Tzortzakis, S., M. Franco, Y.-B. André, A. Chiron, B. Lamouroux, B. Prade, and A. Mysyrowicz**, Formation of a conducting channel in air by self-guided femtosecond laser pulses, Phys. Rev. E **60**, R3505-R3507 (1999).

137. **Tzortzakis, S., B. Lamouroux, A. Chiron, M. Franco, B. Prade, A. Mysyrowicz, and S. D. Moustaizis**, Nonlinear propagation of subpicosecond ultraviolet laser pulses in air, Opt. Lett. **25**, 1270-1272 (2000).

138. **Tzortzakis, S., B. Lamouroux, A. Chiron, S. D. Moustaizis, D. Anglos, M. Franco, B. Prade, and A. Mysyrowicz**, Femtosecond and picosecond ultraviolet laser filaments in air: experiments and simulations, Opt. Commun. (to appear 2001).

139. **Tzortzakis, S., B. Prade, M. Franco, and A. Mysyrowicz**, Time-evolution of the plasma channel at the trail of a self-guided IR femtosecond laser pulse in air, Opt. Commun. **181**, 123-127 (2000).

140. **Tzortzakis, S., B. Prade, M. Franco, A. Mysyrowicz, S. Hüller, and P. Mora**, Femtosecond Laser-guided Electric Discharge in Air, Phys. Rev. E. (submitted).

141. **Tzortzakis, S., L. Sudrie, M. Franco, B. Prade, A. Mysyrowicz, A. Couairon, and L. Bergé**, Self-guided propagation of ultrashort IR laser pulses in fused silica, Phys. Rev. Lett. (submitted).

142. **Vidal, F., D. Comtois, C. Y. Chien, A. Desparois, B. La Fontaine, T. W. Johnston, J.-C. Kieffer, H. P. Mercure, H. Pépin, and F. A. M. Rizk**, Modeling the triggering of streamers in air by ultrashort laser pulses, IEEE Trans. Plasma Sci. **28**, 418-433 (2000).

143. **Vidal, F. and T. W. Johnston**, Electromagnetic beam breakup: multiple filaments, single beam equilibria, and radiation, Phys. Rev. Lett. **77**, 1282-1285 (1996).

144. **Wang, D., T. Ushio, Z. I. Kawasaki, K. Matsuura, Y. Shimada, S. Uchida, C. Yamanaka, Y. Izawa, Y. Sonoi, and N. Simokura**, A possible way to trigger lightning using a laser, J. Atmos. Terr. Phys. **57**, 459-466 (1995).

145. **Yamada, K., W. Watanabe, T. Toma, K. Itoh, and J. Nishii**, In situ observation of photoinduced refractive-index changes in filaments formed in glasses by femtosecond laser pulses, Opt. Lett. **26**, 19-21 (2001).

146. **Yang, G. and Y. R. Shen**, Spectral broadening of ultrashort pulses in a nonlinear medium, Opt. Lett. **9**, 510-512 (1984).

147. **Zhao, X. M.**, Femtosecond ultraviolet pulses triggering of ground to cloud lightning,

Thesis, University of New Mexico, (1993).

148. **Zhao, X. M., J.-C. Diels, A. Braun, X. Liu, D. Du, G. Korn, G. Mourou , and J. M. Elizondo**, Use of self-trapped filaments in air to trigger lightning, Ultrafast phenomena IX, 233-235 (1994).

149. **Zhao, X. M., J. C. Diels, C. Y. Wang, and J. M. Elizondo**, Femtosecond ultraviolet laser pulse induced lightning discharges in gases , IEEE J. Quantum Electron. 31, 599-612 (1995).

150. **Zhao, X. M., R. Jason Jones, C. E. M. Strauss, D. J. Funk, J. P. Roberts, and A. J. Taylor**, Control of femtosecond pulse filament formation in air through variation of the initial chirp of the pulse, CLEO 377 (1997).

151. **Zhao, X. M., P. Rambo, and J.-C. Diels**, Filamentation of femtosecond UV pulses in air, QELS **16**, 178-179 (1995).

152. **Zozulya, A., S. A. Diddams, A. G. Van Engen, and T. S. Clement**, Propagation dynamics of intense femtosecond pulses: multisplitings, coalescence, and continuum generation, Phys. Rev. Lett. **82**, 1430-1433 (1999).

153. **Zozulya, A. A., S. A. Diddams, and T. S. Clement**, Investigations of nonlinear femtosecond pulse propagation with the inclusion of Raman, shock, and third-order phase effects, Phys. Rev. A **58**, 3303-3310 (1998).

Personal References

Publications

[1] S. Tzortzakis, B. Lamouroux, A. Chiron, S. D. Moustaizis, D. Anglos, M. Franco, B. Prade, and A. Mysyrowicz, *"Femtosecond and picosecond ultraviolet laser filaments in air: experiments and simulations"*, Opt. Commun. (to appear, 2001).

[2] A. Couairon, S. Tzortzakis, L. Bergé, M. Franco, B. Prade, and A. Mysyrowicz, *"Infrared femtosecond light filaments in air: simulations and experiments"*, J. Opt. Soc. Am. B (submitted, 2001).

[3] S. Tzortzakis, L. Sudrie, M. Franco, B. Prade, A. Mysyrowicz, A. Couairon, and L. Bergé, *"Self-guided propagation of ultrashort IR laser pulses in fused silica"*, Phys. Rev. Lett. (submitted, 2001).

[4] S. Tzortzakis, B. Prade, M. Franco, A. Mysyrowicz, S. Hüller, and P. Mora, *"Femtosecond Laser-guided Electric Discharge in Air"*, Phys. Rev. E. (submitted, 2001).

[5] S. Tzortzakis, L. Bergé, A. Couairon, M. Franco, B. Prade, and A. Mysyrowicz, *"Break-up and fusion of self-guided femtosecond light pulses in air"*, Phys. Rev. Lett. **86**, 5470 (2001).

[6] S. Tzortzakis, B. Lamouroux, A. Chiron, M. Franco, B. Prade, A. Mysyrowicz, and S. D. Moustaizis, *"Non-linear propagation of sub-picosecond UV laser pulses in air"*, Opt. Lett. **25**, 1270 (2000).

[7] J. Kasparian, R. Sauerbrey, D. Mondelain, S. Niedermeier, J. Yu, J.-P. Wolf, Y.-B. André, M. Franco, B. Prade, S. Tzortzakis, A. Mysyrowicz, M. Rodriguez, H. Wille, L. Wöste, *"Infrared extension of the supercontinuum generated by femtosecond terawatt laser pulses propagating in the atmosphere"*, Opt. Lett. **25**, 1397 (2000).

[8] S. Tzortzakis, B. Prade, M. Franco, and A. Mysyrowicz, *"Time-evolution of the plasma channel at the trail of a self-guided IR femtosecond laser pulse in air"*, Opt. Commun. **181**, 123 (2000).

[9] S. Tzortzakis, M. A. Franco, Y.-B. André, A. Chiron, B. Lamouroux, B. S. Prade, and A. Mysyrowicz, *"Formation of a conducting channel in air by self-guided femtosecond laser pulses"*, Phys. Rev. E **60**, R3505 (1999).

International Conferences

[1] CLEO/Europe-EQEC, Focus Meetings 2001, International Congress Centre Munich, 18–22 June 2001, Munich, Germany.
S. Tzortzakis, L. Sudrie, M. Franco, B. Prade, A. Mysyrowicz, A. Couairon, L. Bergé *"Beam filamentation and pulse break-up of ultrashort IR laser pulses in fused Silica"*. (Oral Paper)

[2] CLEO/QELS 2001, Baltimore Convention Center, 6-11 May 2001,Baltimore, Maryland, USA.
L. Sudrie, S. Tzortzakis, M. Franco, B. Prade, A. Mysyrowicz, A. Couairon, L. Bergé *"Self-guided propagation of ultrashort IR laser pulses in fused Silica"*. (Oral Paper)

[3] Ultra-intense Laser Interactions and Applications - II, 29 September - 3 October 2000, Pisa, Italy.
S. Tzortzakis, S. D. Moustaizis, B. Lamouroux, A. Chiron, M. Franco, B. Prade, and A. Mysyrowicz, *"Ultra-short UV laser pulse filamentation in atmosphere"*. (Oral Paper)

[4] CLEO/Europe-IQEC 2000, Nice Acropolis, 10-15 September 2000, Nice, France.
S. Tzortzakis, B. Prade, Y.-B. André, M. Franco, and A. Mysyrowicz, *"Femtosecond Laser-guided Electric Discharge in Air"*. (Oral Paper)

[5] CLEO/Europe-IQEC 2000, Nice Acropolis, 10-15 September 2000, Nice, France.
S. Tzortzakis, S. D. Moustaizis, B. Lamouroux, A. Chiron, M. Franco, B. Prade, and A. Mysyrowicz, *"Sub-picosecond UV laser pulse filamentation in atmosphere"*. (Oral Paper)

[6] CLEO/Europe-IQEC 2000, Nice Acropolis, 10-15 September 2000, Nice, France.
J. Yu, M. Franco, J. Kasparian, D. Mondelain, A. Mysyrowicz, S. Niedermeier, B. Prade, M. Rodriguez, R. Sauerbrey, S. Tzortzakis, H. Wille, J.-P- Wolf, L. Wöste, *"Characterization and optimization of infrared emission from light filaments observed in a fs-TW laser beam propagating in the atmosphere"*. (Oral Paper)

[7] Lasers and their applications, 4-9 September 2000, Grodon (Minsk), Belarus.
J. Kasparian, Y.-B. André, M. Franco, D. Mondelain, A. Mysyrowicz, S. Niedermeier, B. Prade, P. Rairoux, M. Rodriguez, R. Sauerbrey, S. Tzortzakis, H. Wille, J.-P- Wolf, L. Wöste, J. Yu, *"White light continuum generation by fs-TW laser pulses in the atmosphere and application to Lidar"*. (Oral Paper)

[8] Nonlinear Optics 2000, 7-11 August 2000, Kauai-Lihue, Hawaii, USA
A. Couairon, L. Bergé, S. Tzortzakis, M. Franco, A. Chiron, B. Lamouroux, Y-B. André, B. Prade, and A. Mysyrowicz, *"Break-up, coalescence and self-guiding of femtosecond laser pulses in air"*. (Oral Paper)

[9] 9th International Laser Physics Workshop, Lphys2000, 17-21 July 2000, Bordeaux, France.
A. Mysyrowicz, S. Tzortzakis, Y.-B. André, M. Franco, and B. Prade, *"Self-Guided Propagation Of Intense Femtosecond Laser Pulses Through Atmosphere"*. (Oral Paper, **Invited**)

[10] 9th International Laser Physics Workshop, Lphys2000, 17-21 July 2000, Bordeaux, France.
R. Sauerbrey, S. Niedermeier, Y.-B. André, M. Franco, J. Kasparian, D. Mondelain, A. Mysyrowicz, B. Prade, M. Rodriguez, S. Tzortzakis, H. Wille, J.-P- Wolf, L. Wöste,

J. Yu, *"High Intensity Laser-Beam Propagation in the Earth Atmosphere"*. (Oral Paper, **Invited**)

[11] CLEO/QELS 2000, The Moscone Convention Center, 7-12 May 2000, San Francisco, California, USA.
S. Tzortzakis, S. D. Moustaizis, M. Franco, A. Chiron, B. Lamouroux, B. Prade, and A. Mysyrowicz, *"Long connected plasma channels in air produced by ultrashort UV laser pulses"*. (Oral Paper)

[12] CLEO/QELS 2000, The Moscone Convention Center, 7-12 May 2000, San Francisco, California, USA.
S. Tzortzakis, M. Franco, A. Chiron, B. Lamouroux, Y-B. André, B. Prade, A. Mysyrowicz, A. Couairon, and L. Bergé, *"Self-Guiding of IR femtosecond laser pulses in air: Experiments versus Simulations"*. (Oral Paper)

[13] CLEO/QELS 2000, The Moscone Convention Center, 7-12 May 2000, San Francisco, California, USA.
R. Sauerbrey, S. Niedermeier, M. Franco, J. Kasparian, D. Mondelain, A. Mysyrowicz, B. Prade, P. Rairoux, M. Rodriguez, F. Ronneberger, H. Schillinger, S. Tzortzakis, H. Wille, J.-P- Wolf, L. Wöste, J. Yu, *"Long range Propagation of Terawatt Laser Pulses in the Earth atmosphere"*. (Oral Paper, **Invited**)

[14] Advanced Solid-State Lasers, Fifteenth Topical Meeting and Tabletop Exhibit, 13-16 February 2000, Davos Congress Center, Davos, Switzerland.
S. Niedermeier, M. Franco, J. Kasparian, D. Mondelain, A. Mysyrowicz, B. Prade, P. Rairoux, M. Rodriguez, F. Ronneberger, R. Sauerbrey, H. Schillinger, S. Tzortzakis, H. Wille, J.-P. Wolf, L. Wöste, J. Yu, *"Light filaments generated by terawatt-laser pulses - conductivity, spectral content and LIDAR measurements"*. (Oral Paper)

[15] 30th Winter Colloquium on the Physics of Quantum Electronics, 9-12 January 2000, Snowbird, Utah, USA.
S. Tzortzakis, B. Prade, M. Franco, A. Chiron, and A. Mysyrowicz, *"Study of the propagation of intense femtosecond laser pulses through atmosphere"*. (Oral Paper, **Invited**)

[16] 8th International Laser Physics Workshop, Lphys'99, 2-6 July 1999, Budapest, Hungary.
A. Mysyrowicz, S. Tzortzakis, M. A. Franco, Y.-B. André, A. Chiron, B. Lamouroux, B. S. Prade, *" Formation of a conducting channel in air by self-guided femtosecond laser pulses "*. (Oral Paper, **Invited**)

[17] Ultra-intense Laser Interactions and Applications-1, 7-11 May 1999, Elounda, Crete, Greece.
S. Tzortzakis, M. A. Franco, Y.-B. André, A. Chiron, B. Lamouroux, B. S. Prade, and A. Mysyrowicz, *" Study of femtosecond filament propagation in air: electric and optical diagnostics"*. (Poster)

[18] Centre de Physique des Houches, Intense Laser Fields X-ray Generation and Applications, 8-11 March 1999, Les Houches, France.
S. Tzortzakis, M. A. Franco, Y.-B. André, A. Chiron, B. Lamouroux, B. S. Prade, and A. Mysyrowicz, *"Evidence for a conducting channel in air by self-guided femtosecond laser pulses"*. (Poster)